MULTISCALE MODELLING OF CO_2-CH_4 DISPLACEMENT IN SHALE GAS RESERVOIRS

A thesis submitted in fulfillment of the requirements for the degree of

Doctor of Philosophy

by

Jian Wu

Master of Applied Science (Civil Engineering)

Supervisor: **Prof. Luming Shen**

Auxiliary Supervisor: **A/Prof. Yixiang Gan**

School of Civil Engineering

Faculty of Engineering

The University of Sydney, NSW 2006 Australia

Live fast, be wild, and have fun.

Statement of Originality

This is to certify that to the best of my knowledge, the content of this thesis is my own work. This thesis has not been submitted for any degree or other purposes.

I certify that the intellectual content of this thesis is the product of my own work and that all the assistance received in preparing this thesis and sources have been acknowledged.

Jian Wu

Signature:

30/09/2023

Acknowledgements

I would like to express my deepest gratitude to my supervisor, Prof. Luming Shen, for his constant guidance and support throughout my PhD journey. His unwavering dedication, expertise, and mentorship have been instrumental and shaped not only my research but also my growth as a scholar. I am deeply grateful for the autonomy and encouragement he provided, allowing me to explore novel research ideas aligned with my own interests. The realisation of this PhD thesis would not have been possible without him. I am also indebted to my secondary supervisor, A/Prof. Yixiang Gan, for his invaluable insights, critical feedback, and firm support. His expertise and commitment to excellence have enriched the quality of this thesis significantly. I am grateful to Prof. Jingqiang Tan at Central South University in China for providing me with a visiting opportunity and a conducive academic environment for my research during the COVID-19 pandemic.

I would like to extend my sincere thanks to Dr. Pengyu Huang, Dr. Zhang Shi, and A/Prof. Federico Maggi for providing constructive discussions and necessary resources for my research. Their invaluable suggestions and comments have substantially enhanced the quality of this thesis and greatly contributed to the successful publication of the included manuscripts.

I gratefully acknowledge the Faculty of Engineering for providing the scholarship for my PhD study. I acknowledge the University of Sydney, the School of Civil Engineering, and Prof. Luming Shen for the extra funds to support me in conference travel and other research activities. I am also grateful to Daniela Entenmann for her valuable support to the HDR community.

I would like to thank my dearest friends in Sydney, Yuyao Zhang, Zhang Shi, Emily Nabong, Jordan Krahn, Andrés Escobar, Nabeela Nasim, Arvin Hadlos, Isaac Besarra, James Warner, Sabita Adhikari, for being a constant source of inspiration, collaboration, and camaraderie. They have enriched my experience outside of academic life immeasurably.

I would like to express my heartfelt thanks to my family for their unconditional love, support, and encouragement throughout this long and arduous journey. Their belief in me has always been my greatest motivation and strength.

Co-Author Agreements

The co-authors listed below certify that they have contributed to publications and/or manuscripts in this thesis and that they agree to the use of those publications and/or manuscripts in this thesis.

Luming Shen, School of Civil Engineering, The University of Sydney, NSW 2006, Australia

Signature:

Yixiang Gan, School of Civil Engineering, The University of Sydney, NSW 2006, Australia

Signature:

Federico Maggi, School of Civil Engineering, The University of Sydney, NSW 2006, Australia

Signature:

Zhang Shi, School of Civil Engineering, The University of Sydney, NSW 2006, Australia

Signature:

Pengyu Huang, CSIRO Mineral Resources, QCAT, Pullenvale, QLD 4069, Australia

Signature:

List of Publications

Published journal articles

1. **Wu, J.**, Huang, P., Maggi, F., & Shen, L.* (2022). Molecular investigation on CO_2-CH_4 displacement and kerogen deformation in enhanced shale gas recovery. *Fuel*, 315, 123208.
2. **Wu, J.**, Huang, P., Maggi, F., & Shen, L.* (2022). Effect of sorption-induced deformation on methane flow in kerogen slit pores. *Fuel*, 325, 124886.
3. **Wu, J.**, Shen, L.*, Huang, P., & Gan, Y. (2023). Selective adsorption and transport of CO_2-CH_4 mixture under nano-confinement. *Energy*, 273, 127224.
4. **Wu, J.**, Gan, Y., Shi, Z., Huang, P., & Shen, L.* (2023). Pore-scale lattice Boltzmann simulation of CO_2-CH_4 displacement in shale matrix. *Energy,* 278, 127991.

Journal article not included in this thesis

1. **Wu, J.**, Gan, Y., Huang, P., & Shen, L.* A coarse-grained approach to modelling gas transport in swelling porous media. To be submitted.
2. **Wu, J.**, Gan, Y., Huang, P., & Shen, L.* Gas permeability through swelling porous media: Insights from coarse-grained pore-scale simulations. To be submitted.

Conference presentations

1. **Wu, J.**, Gan, Y., Shi, Z., Huang, P., & Shen, L. A numerical study of CO_2-CH_4 displacement in shale using lattice Boltzmann method, *15th Annual Meeting of the International Society for Porous Media (InterPore)*, 2023, Edinburgh, United Kingdom
2. **Wu, J.**, Huang, P., Shen, L. & Gan, Y. Selective adsorption and transport of CO_2-CH_4 mixture in shale's organic nanopores, *AGU Fall Meeting*, 2022, Chicago, United States

3. **Wu, J.**, Huang, P., & Shen, L. Molecular investigation on sorption-induced kerogen deformation and its impact on gas flow, *14th Annual Meeting of the International Society for Porous Media (InterPore)*, 2022, Abu Dhabi, United Arab Emirates

Authorship attribution statement

I have performed all the numerical work and the analysis of the results, and am the primary author of the above articles. In addition to the statements above, in cases where I am not the corresponding author of a published item, permission to include the published material has been granted by the corresponding author.

Jian Wu

Signature:

30/09/2023

As supervisor for the candidature upon which this thesis is based, I can confirm that the authorship attribution statements above are correct.

Luming Shen

Signature:

30/09/2023

Abstract

Shale gas is becoming an increasingly important source in the global energy sector. Australia has one of the largest shale gas reserves globally, but the exploration is still in the very early stage. Shale reservoirs are characterised by small porosity and ultra-low permeability, with gas production from natural fractures rapidly decaying over time. CO_2 injection can potentially be utilised to recover adsorbed gas from the organic matrix and achieve carbon sequestration in the meantime, known as CO_2-enhanced gas recovery (EGR). As shale is mainly composed of nanopores, the gas flow and transport can significantly differ from that described by conventional theories. During CO_2-CH_4 displacement, shale can also deform in response to gas adsorption/desorption like many other nanoporous materials, which may affect gas permeability during production. Therefore, the fundamental physics occurring during CO_2-CH_4 displacement in nanoporous media must be better understood, including the multiscale gas transport process and gas-gas/solid interactions.

In this study, a hybrid method of grand canonical Monte Carlo (GCMC) and molecular dynamics (MD) is first used to investigate CO_2-CH_4 displacement in a realistic, flexible kerogen matrix (i.e., shale's primary organic matter) that can change volume according to swelling/shrinking strain. A non-linear adsorption-strain model is derived mathematically to describe the relationship between the gas adsorption amount and the volumetric strain. In the second and third parts, single-component methane and binary CO_2-CH_4 mixture flows are simulated by non-equilibrium molecular dynamics (NEMD) in kerogen slit nanopores. The pure methane flux and the apparent gas permeability are summarised as a function of pore pressure and compared between the deformable and non-deformable kerogen pores. In the binary mixture simulations, varied gas molar compositions are simulated to address gas-gas/solid interactions under nano-confinement, which are translated into selective mass transport and competitive adsorption. Since MD is not suitable for investigating large-scale systems for a long duration, a novel lattice Boltzmann (LB) model coupling multiphysics is

developed based on results from previous MD simulations to conduct a sensitivity study of various pore-scale parameters affecting the displacement of CH_4 by CO_2.

Gas adsorption can induce a swelling volumetric strain up to 7.4% and 5.1% for pure CO_2 and CH_4 at ~20 MPa and 300 K in the kerogen matrix. CO_2 injection can cause further swelling in the depleted reservoir with residual CH_4. The sorption-induced swelling constraints methane mass flux by narrowing the slit pore size under the constant volume condition, which also reduces the apparent gas permeability. When CO_2 and CH_4 flow as a mixture, gas velocity decreases logarithmically with the increase of the CO_2 molar ratio. The competitive adsorption and selective transport between CO_2 and CH_4 are strongly correlated to gas pressure and slit pore size but not to gas composition. The upscaled LB modelling study shows that CO_2-CH_4 displacement is controlled by the inter-/intra-solid mass transfer and the mass exchange rate between pore space and solid matrix. The gas diffusion coefficients, Langmuir rate constants, and pore geometry are all important factors affecting the concentration and adsorption/desorption evolutions of CO_2 and CH_4.

Table of Contents

List of Figures

List of Tables

List of Abbreviations

2D	Two-dimensional
3D	Three-dimensional
ADE	Advection-diffusion equations
BGK	Bhatnagar-Gross-Krook
CNT	Carbon nanotube
CVFF	Consistent valence force field
DEM	Discrete element method
DFT	Density functional theory
EGR	Enhanced gas recovery
EIA	U.S. Energy Information Administration
EMD	Equilibrium molecular dynamics
EOS	Equation of state
GA	Geoscience Australia
GAFF	General AMBER force field
GCMC	Grand canonical Monte Carlo
GHG	Greenhouse gases
HSDM	Homogeneous solid diffusion model
IEA	International Energy Agency
LB	Lattice Boltzmann

LBM	Lattice Boltzmann method
MD	Molecular dynamics
MMT	Montmorillonite
NEMD	Non-equilibrium molecular dynamics
NIST	U.S. National Institute of Standards and Technology
NMR	Nuclear magnetic resonance
NRC	Natural Resources Canada
NSE	Navier-Stokes equations
PES	Potential energy surface
PR-EOS	Peng-Robinson equation of state
QSGS	Quartet structure generation set
RMS	Root mean square
USGS	United States Geological Survey

Chapter 1 Introduction

1.1 Background

As the energy demand keeps growing for global industrialisation, conventional oil and gas are depleting and no longer meet our needs with the current exploitation (IEA, 2022). This supply-demand imbalance leads to the active search for unconventional resources, referring to hydrocarbons found in low-permeable tight reservoirs (< 0.1 mD) (Alfarge et al., 2020). Oil and natural gas cannot be directly produced from such reservoirs using the standard methods employed in the conventional reservoirs (Alfarge et al., 2020). As a common type of unconventional resource, shale gas exists between 1 and 5 km below the earth's surface (Zendehboudi and Bahadori, 2016). It has abundant reserves in basins globally, with the total estimated at 7577 trillion cubic feet (Figure 1.1). Despite the exploitation challenges, the rapid development of long horizontal wells drilling and hydraulic fracturing has dramatically encouraged gas production from unconventional reservoirs (Rahm, 2011). In 2022, shale gas accounted for 28.5 trillion cubic feet, approximately 80% of the total dry natural gas production in the United States (EIA, 2022).

Australia has substantial unconventional gas resources. Although coal seam gas (primarily located in Queensland and New South Wales) has always been considered as Australia's most important unconventional gas resource, the total estimate of recoverable shale gas is among the world's highest, ranking 7th in the world after China, Argentina, Algeria, United States, Canada, and Mexico (GA, 2022; EIA, 2015). Prospective shale gas resources are distributed in basins onshore, such as Cooper, Eromanga, and Georgina (GA, 2022). Until today Australia's shale gas exploration is still in the very early stage, with 75% of natural gas production contributed by conventional gas and the rest nearly all from coal seam gas (GA, 2022).

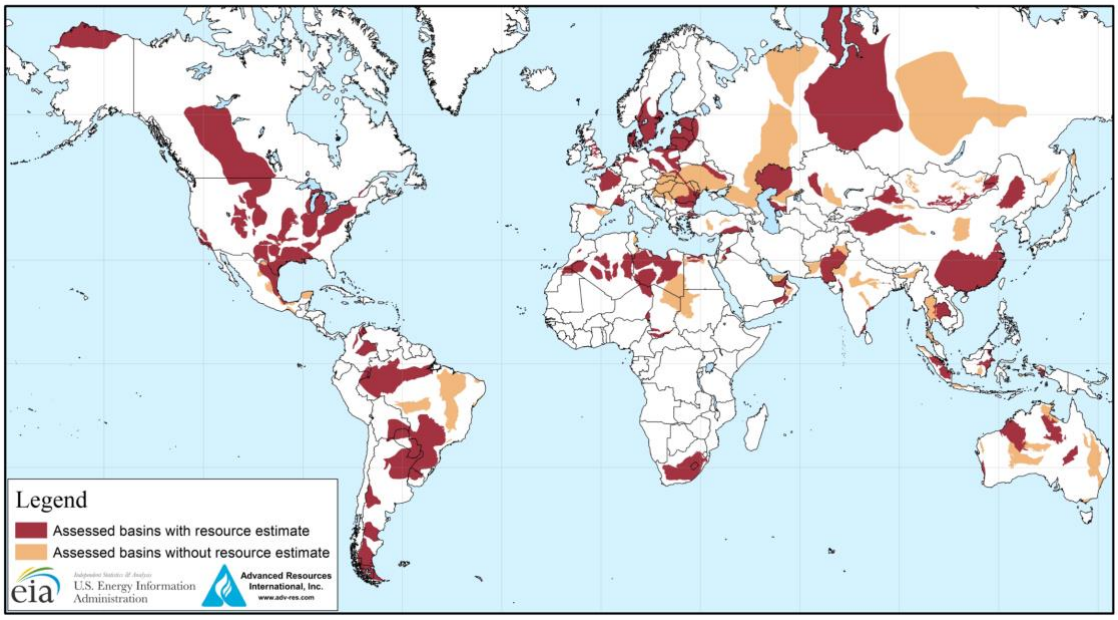

Figure 1.1 Locations of assessed basins with shale oil and gas by May 2013 (EIA, 2015).

Shale gas has a similar composition as natural gas found in conventional reservoirs (Zendehboudi and Bahadori, 2016). It typically contains over 85% of methane, 3-8% ethane, 1-5% of propane, 1-2% of butane, 1-5% of pentane, and a small portion of other non-hydrocarbon gases such as carbon dioxide and nitrogen (Speight, 2013). Gas in shale reservoirs has three different forms: free gas in natural fractures, adsorbed gas on organic matter surfaces, and dissolved gas in kerogen bulk (Pan and Connell, 2015). Unlike other reservoirs, shale acts as both the source and storage sites for gas (Zendehboudi and Bahadori, 2016). After the gas is generated from organic matter, it immediately becomes trapped inside nanopores under high confining pressure (Swami et al., 2013). The characteristic well production pattern in shale reservoirs involves an initial rapid gas production phase from natural fractures, succeeded by a sudden decline attributed to the exhaustion of free gas (Hyman et al., 2016; Neil et al., 2020). With the decline in reservoir pressure, the shale matrix initiates gas desorption, which then becomes the dominant production process. The total gas recovery by these two processes is around 28-40% (Sharma and Chopra, 2013; Speight, 2013). Conventional recovery methods such as hydraulic fracturing and horizontal drilling can stimulate gas production by up to 60%

subject to reservoir properties and surrounding geological conditions (Iddphonce et al., 2020). Achieving a further recovery from the large portion of unproduced gas in shale reservoirs remains an essential but challenging topic for the oil and gas industry. In addition, there are some environmental issues concerning the traditional production method of shale gas. For example, using hydraulic fracturing liquid can cost a high amount of water and introduce toxic chemical contaminants into the subsurface groundwater system (Zendehboudi and Bahadori, 2016). The increasing government regulations also lead to the active search for alternative sustainable solutions.

CO_2-enhanced gas recovery (CO_2-EGR) shows great potential in recovering adsorbed gas and sequestrating CO_2 in shale reservoirs (Alfarge et al., 2017; Fathi and Akkutlu, 2014; Huang et al., 2020; Louk et al., 2017). As a fracturing liquid, CO_2 is more environmental-friendly and exerts less pressure on the global water situation in contrast to water usage. Supercritical CO_2 can also dissolve organic matter and minerals as well as generate secondary fractures through phase change (Iddphonce et al., 2020; Memon et al., 2022). These unique characteristics promote complex fracture networks in the shale reservoirs, creating more available fluid flow pathways for the gas production (Lan et al., 2019). Figure 1.2 provides a schematic illustration of CO_2-EGR operations. Firstly, the captured CO_2 is pressurised, liquefied, and mixed with proppants. Next, the CO_2 mixture is injected into the target reservoir through a wellbore, generating fractures along the horizontal well. CO_2 enters the shale gas production zone and displaces CH_4 along the way, which eventually flows toward the horizontal well under a pressure gradient. The CO_2-CH_4 gas mixture flows back to the wellbore and is separated on the ground. The recovered CH_4 is sent to market, and unused CO_2 can be recycled for the next fracturing event. Although the feasibility of CO_2-EGR has been widely recognised, it is not yet a wholly commercialised technique for the production enhancement in shale gas reservoirs, and issues such as possible injectivity decrease due to reduced reservoir permeability remain to be solved (Wu et al., 2017; Zhou et al., 2020). As nano-confinement can greatly affect gas dynamics, the multiscale gas transport and gas-gas/gas-solid interactions in nanoporous media need to be studied thoroughly to provide fundamental insights into CO_2-EGR in shale

reservoirs for the development of accurate reservoir models.

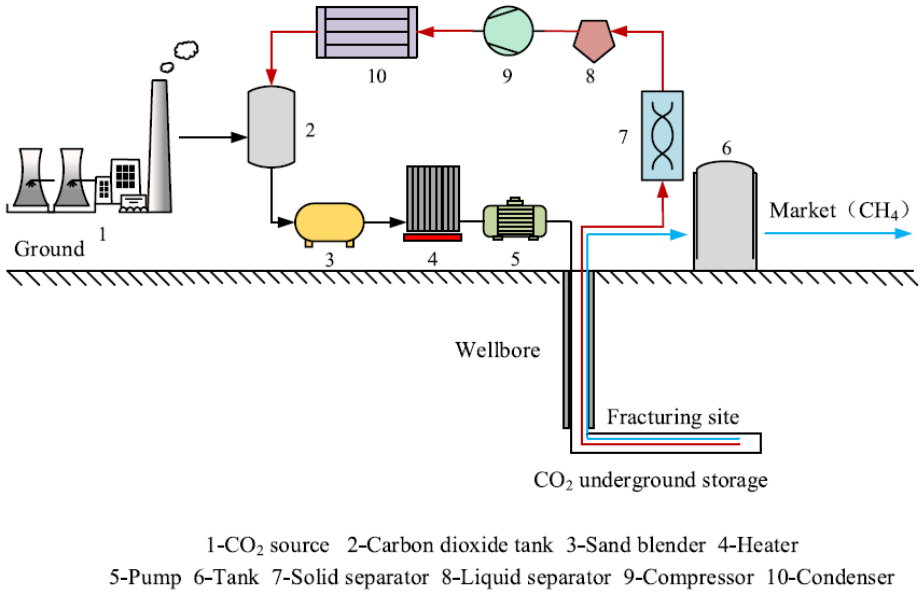

Figure 1.2 Illustration of CO_2 fracturing operations (Lan et al., 2019).

1.2 Research objectives

The aim of this thesis is to study the fundamental physics of CO_2-CH_4 displacement within shale matrix, including gas adsorption/desorption, gas transport, CO_2-CH_4 interaction, and sorption-induced solid deformation. With the successful construction of a realistic overmature kerogen (i.e., shale's primary organic matter) model, grand canonical Monte Carlo (GCMC) and molecular dynamics (MD) are used to study CO_2 and CH_4 adsorption in kerogen and its corresponding volumetric deformation. Using non-equilibrium molecular dynamics (NEMD), single-component methane flow and transport under nano-confinement are investigated in kerogen slit pores to address the diffusion-enhanced mass transfer and experimental-observed permeability reduction from sorption-induced deformation. The binary CO_2-CH_4 mixture is further investigated in the kerogen slit pores to reveal the selective transport (i.e., separation) of the two gas components under nano-confinement. Although molecular simulation is a valuable tool for studying the fundamental mechanisms at atomic and nanopore scales, it is

computationally expensive and cannot be directly adopted for large simulation sizes and long duration. For such reasons, a pore-scale multiphysics model has been developed using the lattice Boltzmann method (LBM) to study the CO_2-CH_4 displacement efficiency in various porous geometries. The objectives of this research can be summarised as follows:

- Obtain the optimal conditions for CH_4 production and CO_2 sequestration in the kerogen matrix under various reservoir depletion and CO_2 injection pressures using a hybrid GCMC-MD method.
- Analyse sorption-induced deformation as a function of gas pressure or total adsorption amount and describe such relations by a mathematical model.
- Investigate the enhanced gas transport under nano-confinement and quantify the effect of sorption-induced deformation on permeability using NEMD and an analytical model.
- Study the flow velocity and selective transport of CO_2-CH_4 mixture as a function of pore pressure, pore size, and molar ratio in kerogen slit pores.
- Develop an upscaled lattice Boltzmann (LB) model based on MD results and conduct a sensitivity analysis of CO_2-CH_4 displacement efficiency subject to pore geometry and other essential parameters.

1.3 Thesis outline

The thesis is prepared in the "thesis by publications" format. Chapters 3-6 present the main results of this research and are self-contained. Each of Chapters 3-6 is prefaced by the main motivation and general descriptions of the research work in this thesis. Chapters 3-6 have been published as peer-reviewed journal articles. The supporting materials are included at the end of each corresponding chapter.

This thesis conducts a systematic multiscale investigation into the fundamental physics

occurring during the process of CO_2-CH_4 displacement at nano- and micro-scales. Rather than using simplified graphene and mineral models, a realistic kerogen model is constructed to investigate gas-gas and gas-solid interactions, with mathematic models derived to explain the simulation results. A novel LB multi-lattice coupling scheme is also introduced to study multicomponent gas displacement at the pore-scale. The simulation results and mathematical relationships either can directly provide insights into the optimal selection of operational conditions for CO_2-EGR or may be indirectly implemented in existing reservoir models for more accurate predictions.

The thesis is organised as follows. Chapter 1 presents the background and objectives of the research. Chapter 2 first reviews the fundamental theories of nanoscale gas transport, followed by the summary of current experimental and nano/micro-scale numerical studies on CO_2-CH_4 systems in the context of CO_2-EGR. Chapter 3 presents the CO_2-CH_4 displacement in the kerogen matrix and the sorption-induced kerogen deformation under various reservoir conditions using a hybrid GCMC-MD method. Chapter 4 reports a NEMD study of the nanoscale methane transport with the consideration of kerogen deformation in slit pores. Chapter 5 explores the flow velocity and selective mass transport of CO_2-CH_4 mixtures as a function of nanopore size and pressure. Chapter 6 introduces the development of a novel pore-scale CO_2-CH_4 displacement model in the LBM framework and conducts a sensitivity study of gas displacement efficiency. The conclusions of this research and recommendations for future work are summarised in Chapter 7.

References

1. Alfarge, D., Wei, M., & Bai, B. (2017). Feasibility of CO_2-EOR in shale-oil reservoirs: Numerical simulation study and pilot tests. *Carbon Management Technology Conference*, CMTC-485111-MS.

2. Alfarge, D., Wei, M., & Bai, B. (2020). Developments in petroleum science. *Elsevier, 67*,

1-13.

3. EIA. (2015). https://www.eia.gov/analysis/studies/worldshalegas.

4. EIA. (2022). https://www.eia.gov/tools/faqs/faq.php?id=907&t=8.

5. Fathi, E., & Akkutlu, I. Y. (2014). Multi-component gas transport and adsorption effects during CO_2 injection and enhanced shale gas recovery. *International Journal of Coal Geology, 123*, 52-61.

6. GA. (2022). https://www.ga.gov.au/digital-publication/aecr2022/gas.

7. Huang, J., Jin, T., Barrufet, M., & Killough, J. (2020). Evaluation of CO_2 injection into shale gas reservoirs considering dispersed distribution of kerogen. *Applied Energy, 260*, 114285.

8. Hyman, J., Jiménez-Martínez, J., Viswanathan, H. S., Carey, J. W., Porter, M. L., Rougier, E., . . . Chen, L. (2016). Understanding hydraulic fracturing: A multi-scale problem. *Philosophical Transactions of the Royal Society A: Mathematical, Physical and Engineering Sciences, 374(2078)*, 20150426.

9. Iddphonce, R., Wang, J., & Zhao, L. (2020). Review of CO_2 injection techniques for enhanced shale gas recovery: Prospect and challenges. *Journal of Natural Gas Science and Engineering, 77*, 103240.

10. IEA. (2022). https://www.iea.org/news/world-energy-outlook-2022-shows-the-global-energy-crisis-can-be-a-historic-turning-point-towards-a-cleaner-and-more-secure-future.

11. Lan, Y., Yang, Z., Wang, P., Yan, Y., Zhang, L., & Ran, J. (2019). A review of microscopic seepage mechanism for shale gas extracted by supercritical CO_2 flooding. *Fuel, 238*, 412-424.

12. Louk, K., Ripepi, N., Luxbacher, K., Gilliland, E., Tang, X., Keles, C., . . . Michael, K. (2017). Monitoring CO_2 storage and enhanced gas recovery in unconventional shale reservoirs: Results from the Morgan County, Tennessee injection test. *Journal of Natural*

Gas Science and Engineering, 45, 11-25.

13. Memon, S., Feng, R., Ali, M., Bhatti, M. A., Giwelli, A., Keshavarz, A., . . . Sarmadivaleh, M. (2022). Supercritical CO_2-Shale interaction induced natural fracture closure: Implications for $scCO_2$ hydraulic fracturing in shales. *Fuel, 313*, 122682.

14. Neil, C. W., Mehana, M., Hjelm, R. P., Hawley, M. E., Watkins, E. B., Mao, Y., . . . Xu, H. (2020). Reduced methane recovery at high pressure due to methane trapping in shale nanopores. *Communications Earth & Environment, 1*, 49.

15. Pan, Z., & Connell, L. D. (2015). Reservoir simulation of free and adsorbed gas production from shale. *Journal of Natural Gas Science and Engineering, 22*, 359-370.

16. Rahm, D. (2011). Regulating hydraulic fracturing in shale gas plays: The case of Texas. *Energy Policy, 39*(5), 2974-2981.

17. Sharma, R. K., & Chopra, S. (2013). Conventional approach for characterising unconventional reservoirs. *CSEG RECORDER, 38*, 34-38.

18. Speight, J. G. (2013). Shale gas production processes. *Gulf Professional Publishing*.

19. Swami, V., Settari, A. T., & Javadpour, F. (2013). A numerical model for multi-mechanism flow in shale gas reservoirs with application to laboratory scale testing. *EAGE Annual Conference & Exhibition incorporating SPE Europec*, SPE-164840-MS.

20. Wu, W., Zoback, M. D., & Kohli, A. H. (2017). The impacts of effective stress and CO_2 sorption on the matrix permeability of shale reservoir rocks. *Fuel, 203*, 179-186.

21. Zendehboudi, S., & Bahadori, A. (2016). Shale oil and gas handbook: Theory, technologies, and challenges. *Gulf Professional Publishing*.

22. Zhou, J., Tian, S., Zhou, L., Xian, X., Yang, K., Jiang, Y., . . . Guo, Y. (2020). Experimental investigation on the influence of sub- and super-critical CO_2 saturation time on the permeability of fractured shale. *Energy, 191*, 116574

Chapter 2 Literature review

2.1 Gas flow and transport in shale reservoirs

Shale gas is stored in various forms within nanoporous and microporous media, with kerogen acting as the main storage site of hydrocarbons that contains roughly half of the adsorbed gas (Kang et al., 2021; Rani et al., 2019). As shown in Figure 2.1, gas flowing in shale is a multiscale interconnected process and involves a network of natural/stimulated fractures and pores of different sizes ranging from nanometres to micrometres (Javadpour et al., 2007; Wang et al., 2020). Free gas is firstly produced from the large fractures after a new wellbore is drilled, and then from the micro-fractures and inorganic pores. With the free gas depleting, the equilibrium between the shale matrix and the fractures/micropores no longer holds. Gas desorbs from the kerogen surface and flows towards the fractures to replenish the free gas phase. Once gas molecules on the kerogen surface desorb, the gas concentration gradient comes into play and drives the diffusion from the kerogen bulk nanopores to the surface (Memon et al., 2020; Neil et al., 2020; Savage, 2014). The nanopores in kerogen make gas production in shale considerably different from conventional reservoirs, which are generally modelled by Darcy's law (Swami et al., 2012). For example, the no-slip boundary does not always hold at such a length scale as the gas molecule size is comparable to pore size, and the gas-wall interaction increases under strong nano-confinement.

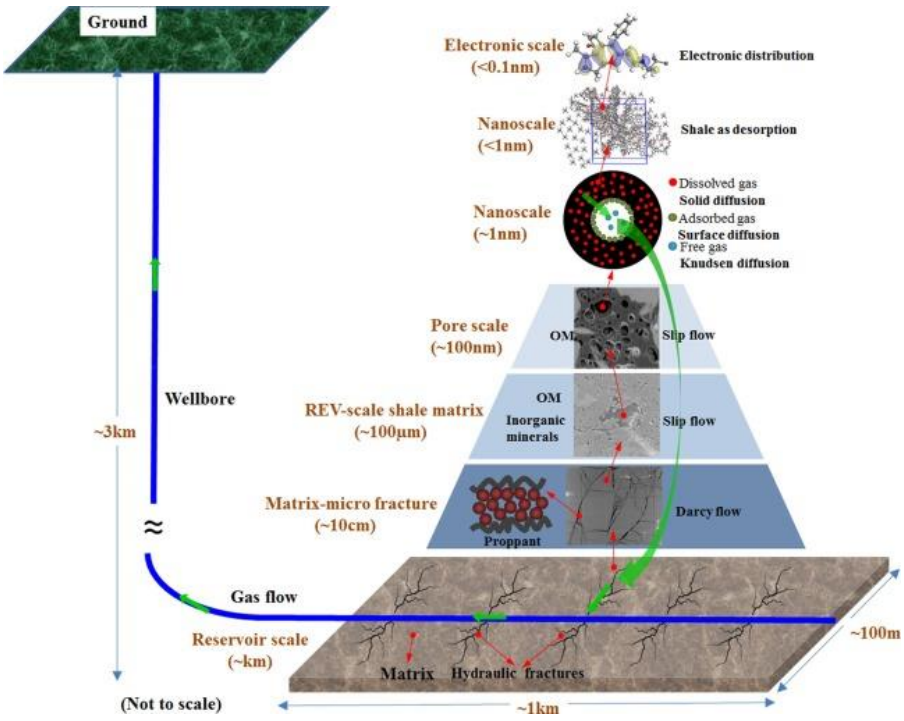

Figure 2.1 Investigation of shale gas production as a multiscale process (Wang et al., 2020).

Knudsen number is used as a criterion to decide the pore-wall boundary condition, which is simply the ratio between the molecular mean free path λ and the characteristic pore length L, where λ is a function of temperature and pressure

$$K_n = \frac{\lambda}{L} \tag{2.1}$$

Four different gas flow regimes can be summarised based on Knudsen Number (Darabi et al., 2012; Javadpour et al., 2007; Swami et al., 2012)

(1) Darcy flow (i.e., viscous flow): $K_n < 0.001$. Gas molecules have negligible interactions with pore walls; hence Darcy's law is still valid for use.

(2) Slip flow: $0.001 < K_n < 0.1$. Gas molecular interactions with pore walls need to be considered, and the flow velocity is non-zero at pore walls. The most popular slip models are first-order Maxwell slip (Maxwell, 1879), second-order slip (Beskok and Karniadakis, 1999), and Langmuir slip (Myong, 2001a; Myong, 2001b; Myong, 2004).

Klingenberg's slippage factor (Klinkenberg, 2012) can be used to modify the calculation for gas permeability.

(3) Transitional flow: $0.1 < K_n < 10$. Both the collision with pore walls and intermolecular interaction become essential. It is the most challenging region to model but commonly seen in tight reservoirs such as shale.

(4) Molecular free flow: $K_n > 10$. The mean free path of gas molecules dominates. The flow regimes are also related to the pore size and pressure as shown in Figure 2.2.

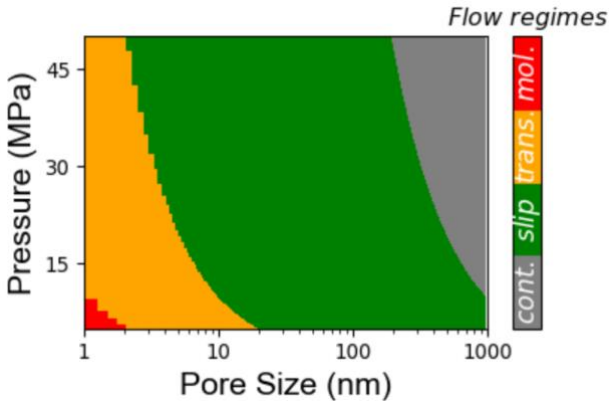

Figure 2.2 Flow regimes as a function of pore size and pressure (Javadpour et al., 2021).

Gas fluxes from these four flow regimes should be considered individually by their own mathematical expressions. As the pore size distribution varies in shale, the total mass flux during shale gas production can be estimated as a weighted combination of these individual mass fluxes by taking diffusive transport into account, including bulk diffusion (i.e., Fick's diffusion), surface diffusion, and Knudsen diffusion (Cussler, 2009; Javadpour et al., 2021; Wu et al., 2016). Transitional diffusion can be described as an intermediate form with characteristics of both Knudsen diffusion and Fick's diffusion (Cai et al., 2019; Pollard and Present, 1948). Fick's diffusion coefficient D_F and Knudsen diffusion coefficient D_k are expressed as

$$D_F = \frac{k_B T}{3\sqrt{2}\pi d^2 P}\sqrt{\frac{8RT}{\pi M}} \tag{2.2}$$

$$D_k = \frac{H}{3}\sqrt{\frac{8RT}{\pi M}} \tag{2.3}$$

where k_B is the Boltzmann constant, T is the temperature, P is the pressure, d is the diameter of gas molecule, R is the ideal gas constant, M is the gas molar mass, and H is the pore size. A lumped transitional diffusion coefficient may be expressed as a function of Knudsen number (Cai et al., 2019; Pollard and Present, 1948)

$$D_t = \frac{1}{Kn+1}D_F = \frac{Kn}{Kn+1}D_k \tag{2.4}$$

The transitional diffusion coefficient becomes pure Fick's diffusion and Knudsen diffusion coefficients as Kn approaches 0.1 and 10, respectively. The surface diffusion coefficient D_s increases with adsorbed gas concentration, which is expressed based on the random walk/hopping mechanism (Chen and Yang, 1991)

$$D_s = D_o \frac{1-\theta+\frac{\kappa}{2}\theta(2-\theta)+H(1-\kappa)(1-\kappa)\frac{\kappa}{2}\theta^2}{\left(1-\theta+\frac{\kappa}{2}\theta\right)^2} \tag{2.5}$$

The Heaviside function is dependent on $\kappa = \frac{\kappa_B}{\kappa_M}$

$$H(1-\kappa) = \begin{cases} 0, & \kappa > 1 \\ 1, & 0 \le \kappa \le 1 \end{cases} \tag{2.6}$$

where D_o is the surface diffusivity at zero surface coverage, θ is the fractional gas coverage, κ_B is the backward rate constant, and κ_M is the forward rate constant. It is important to note that the contribution from each gas flow regime is dynamically changeable concerning pore radius and pressure during the production process (Shen et al., 2017; Yu et al., 2018). With the addition of another gas component in the operation of CO_2-EGR, the multiscale and multiphysics system further complicates due to the gas-gas interaction and competitive adsorption., etc. Therefore, a systematic understanding of the coupling physics is required to successfully predict the gas transport and production characteristics in shale reservoirs at multiscale.

2.2 Enhanced gas recovery

Enhanced gas recovery (EGR) techniques are utilised during the drilling, stimulation and production phases of shale gas exploitation (Hasan et al., 2017). Horizontal wells and hydraulic fracturing are the most well-known EGR techniques and have shown excellent efficiency in recovering shale gas (Rahm, 2011). Horizontal drilling is the practice of drilling non-vertical bores, which can be extended to a few kilometres in the target formation to increase the contact between the reservoir and the wellbore (Hasan et al., 2017; Ma et al., 2016). Hydraulic fracturing, also referred to as fracking, is a process of injecting water, sand, and chemicals into a well to create a connecting network of fractures within the reservoir to increase oil and gas flow (USGS, 2019). Sands, used as proppants, facilitate the initiation of fractures and keep them open during the gas production process (Gandossi and Von Estorff, 2013). Water-based fracturing liquids often contain alcohol, oil, acid and a variety of additives (< 2%) (Aadnoy and Looyeh, 2019). After the fracking operation, the viscosity of the fracturing liquid in the shale formations needs to be reduced for clean-up prior to gas production (Ma and Holditch, 2015).

Despite the great success of hydraulic fracturing in enhancing shale gas production, there are two major concerns: the extensive usage of water and the negative environmental impact of additive chemicals. Besides, around 40% of gas still remains unproduced mostly in the form of adsorbed phase (Iddphonce et al., 2020). As a sustainable alternative to water-based fracturing, CO_2 has been introduced to increase shale gas production, contributing to the carbon net-zero goal by sequestrating CO_2 in depleted reservoirs (Hamza et al., 2021; Omari et al., 2022). The number one reason why CO_2 can be used to recover shale gas potentially is the high CO_2/CH_4 adsorption selectivity in organic matter. In other words, CO_2 is much preferentially adsorbed over CH_4 when the shale reservoir is exposed to a binary mixture of them. The CO_2/CH_4 selectivity typically decreases with increasing total bulk gas pressure and temperature but always stays greater than one (Ho et al., 2018b; Huang et al., 2018; Sui et al., 2020; Wang

et al., 2018a). The underlying mechanism of competitive adsorption can be summarised as follows (Cui et al., 2004; Lan et al., 2019; Li et al., 2009; Pathak et al., 2018; Sui and Yao, 2016): (1) CO_2 has a smaller molecule size and can enter smaller pores; (2) The critical temperature of CO_2 is higher than CH_4, which promotes the exothermic adsorption process; (3) CO_2 has higher quadrupole and dipole moments and interacts more strongly with kerogen; (4) The diffusivity of CO_2 is weaker than CH_4 and thus CO_2 is more likely to remain in kerogen upon gas displacement. Such difference in adsorption ability makes it theoretically possible for the injected CO_2 to displace adsorbed CH_4 on the kerogen surface and achieve a high gas production ratio. The first pilot CO_2-EGR test conducted in Morgan County, Tennessee (US) has evidenced the strong potential of enhanced shale gas recovery and CO_2 storage in depleted shale reservoirs, as the daily gas production increased over eight times following CO_2 injection (Louk et al., 2017). To investigate CO_2-EGR in shale reservoirs, three main stages need to be included (Fathi and Akkutlu, 2014): (1) convective/dispersive flow of the injected CO_2 and displaced CH_4 in the fractures; (2) dispersive gas transport in the secondary fractures and micropores; (3) multicomponent competitive gas adsorption and desorption in kerogen nanopores.

2.3 Experimental studies of CO_2/CH_4 in shale

In laboratory settings, researchers often investigate single-component CO_2 or CH_4 adsorption in the shale matrix by constructing sorption isotherms. This process entails measuring the free and adsorbed phases of either gas components within a crushed shale sample under a wide range of controlled temperature and pressure conditions (Klewiah et al., 2020). It is widely reported that the gas adsorption data in shale can be accurately described by the Langmuir model, which assumes monolayer adsorption at either low or high pressure (Hong et al., 2016; Ji et al., 2012; Klewiah et al., 2020; Liu et al., 2019; Yuan et al., 2014). The gas adsorption capacities of CO_2 and CH_4 are linearly correlated to the organic matter content, with CO_2

consistently showing higher adsorption capacities than CH_4 (Hong et al., 2016). Increasing the temperature reduces the amounts of both CO_2 and CH_4 adsorption in shale (Chen et al., 2021; Duan et al., 2016; Hu et al., 2021; Xie et al., 2021).

A number of experimental studies have been performed on the displacement between CO_2 and CH_4 regardless of the difficulty in separating the free and adsorbed gas components. Low-field nuclear magnetic resonance (NMR) is an effective method to directly measure methane (hydrogen-contained) adsorption based on a relaxation time difference between the gas inside and outside the shale nanopores (Zeng et al., 2023). For instance, Liu et al. (2017) employed the NMR technique to assess the dynamic desorption of adsorbed methane in a crushed Longmaxi shale sample. Their results show that CO_2 injection can further improve the residual gas recovery by 25% after pressure drawdown. By adopting a similar method with a gas supply system, Liu et al. (2019) measured CO_2/CH_4 competitive adsorption under equimolar and non-equimolar conditions. They found that the CO_2/CH_4 selectivity was distributed between 3-6 at a total gas pressure of 2-10 MPa, and the EGR efficiency reached ~80% when the CO_2/CH_4 pressure ratio was 2.5. The adsorbed CO_2 in the shale sample was calculated using the volumetric method and NMR measurements. Lu et al. (2022) developed an experimental system that combined low-field NMR and gas chromatography to analyse CO_2 and CH_4 compositions in situ during their competitive adsorption in shale. The CO_2/CH_4 selectivity was estimated at 8-3 as the total gas pressure increased from 1 to 11 MPa.

Various experimental studies suggest that shale permeability can change upon CO_2 and CH_4 adsorption, likely related to sorption-induced deformation and chemical reaction of minerals. For example, Zhao et al. (2019) simultaneously measured the adsorption and permeability of shale core samples. They observed that the intrinsic permeability of the shale core sample decreased by threefold from 9.66×10^{-19} to 3.24×10^{-19} m^2 as the methane adsorption pressure increased from 0.76 to 6.79 MPa under constant effective stress. It is found that permeability and sorption-induced swelling strain are approximately linearly correlated. Zhou et al. (2020) investigated the impact of gas-phase (6 MPa) and supercritical (8 MPa) CO_2 on the

permeability reduction of artificially fractured shale samples regarding saturation time. They argued that supercritical CO_2 injection could induce a higher and longer permeability decrease than gas-phase CO_2. Shale permeability is influenced by the swelling resulting from gas adsorption and the effective stress change from the injection pressure. Wu et al. (2017) studied the separated effects of effective stress and CO_2 adsorption on the Utica shale through pressure pulse-decay experiments. When the initial shale permeability was lower than the threshold of 10^{-20} m^2, the permeability reduction was dominated by adsorption-indued strain since gas mainly exists in nanopores. Otherwise, effective stress controlled the permeability reduction due to flow paths dominated by microfractures. A similar balance between adsorption and effective stress has also been reported with respect to pressure. Sheng et al. (2019) developed a scheme to upscale the pore size change due to poromechanical response, adsorption layer thinning, and adsorption-indued strain into a dynamic apparent permeability. The dividing pore pressure was reported as 20 MPa, below which the adsorption effect became the governing mechanism of permeability change. A great number of studies have been focusing on deriving a relationship to address the competition between the above two effects as a function of pressure and how they impact the permeability evolution, which can be applied to more scenarios such as gas extraction and CO_2 injection (Clarkson et al., 2010; Cui et al., 2018; Li et al., 2020; Liu et al., 2011). Although much work is initially developed for coal seam, the knowledge can be easily extended to shale reservoirs considering the similarities between the two (Kumar et al., 2016).

2.4 Molecular simulations

Numerical models are useful tools to describe shale gas adsorption and transport, including the density functional theory (DFT), grand canonical Monte Carlo (GCMC), molecular dynamics (MD), lattice Boltzmann method (LBM), finite volume method (FVM), and empirical correlation method (Wang et al., 2020). MD is a computer simulation method for analysing the

trajectories of atoms and molecules by numerically solving Newton's equations of motion, where forces between the particles and their potential energies are calculated from pre-defined force fields (Wikipedia, 2023). GCMC performs Monte Carlo insertion, deletion, and movement under the grand canonical ensemble, assuming an imaginary reservoir of given chemical potential is connected to the simulation box. In nanoporous media, a hybrid method of GCMC and MD has been developed to study fluid adsorption under the unjacketed condition, where the simulation box volume can change under zero effective stress by setting the confining pressure equal to the fluid pressure. This hybrid method allows the adsorption isotherm and sorption-induced deformation to be simulated at the same time. Several studies have shown that ignoring the sorption-induced deformation of the solid matrix will result in an underestimated sorption loading (Ho et al., 2018a; Potier et al., 2023; Wu and Firoozabadi, 2019). For example, Ho et al. (2018a) observed that pure CO_2 and CH_4 adsorption loadings (6.2 and 4.1 mmol/g) in swollen overmature kerogen were 1.5-1.8 times higher than that in rigid kerogen at ~20 MPa. Potier et al. (2023) found that the adsorbed Argon in a mature kerogen with atomic H/C ~0.5 could be lower by 19% if swelling was not included and 28% if both swelling and internal deformations were not considered. In addition, kerogen maturity increases both CO_2 and CH_4 sorption capacities, while moisture content reduces their adsorption amounts (Huang et al., 2019).

A summarised CO_2/CH_4 adsorption dataset from the literature is presented as Figure 2.3. Consistent with experimental data, pure CO_2 always shows higher adsorption capacity than CH_4 in MD simulations. This is because CO_2 adsorbed onto the kerogen surface has greater isosteric heat than CH_4 (Sun et al., 2017; Wang et al., 2018a). Moreover, the estimated interaction energies of CO_2 and CH_4 molecules with the type II-D kerogen surface are -6.2 kcal/mol and -4.2 kcal/mol, respectively (Ho and Wang, 2021). Higher affinity to CO_2 is also observed for pyrophyllite, gibbsite, and montmorillonite surfaces (Ho and Wang, 2021). To further investigate the adsorption behaviours of CO_2 and CH_4 as a mixture, Huang et al. (2018) and Sui et al. (2020) studied the adsorption of CO_2-CH_4 binary mixtures in kerogen matrix of various organic types and water saturations, suggesting that gas adsorption capacity followed

the order of kerogen type I < II < III. Interestingly, they found that specific moisture contents could increase the CO_2/CH_4 selectivity. Ho et al. (2018b) calculated the selectivity of CO_2 over CH_4 at 3-6 in overmature kerogen matrix using equimolar binary mixtures and found it decreased with increasing pressure. Wang et al. (2018a, 2018b) reported that the CO_2/CH_4 selectivity decreased with increasing temperature in kerogen, and the pressure-dependence became weaker at higher temperatures. In summary, environmental variables (e.g., pressure and temperature) and kerogen properties (e.g., organic type, maturity, and moisture content) can all affect the competitive adsorption between CO_2 and CH_4.

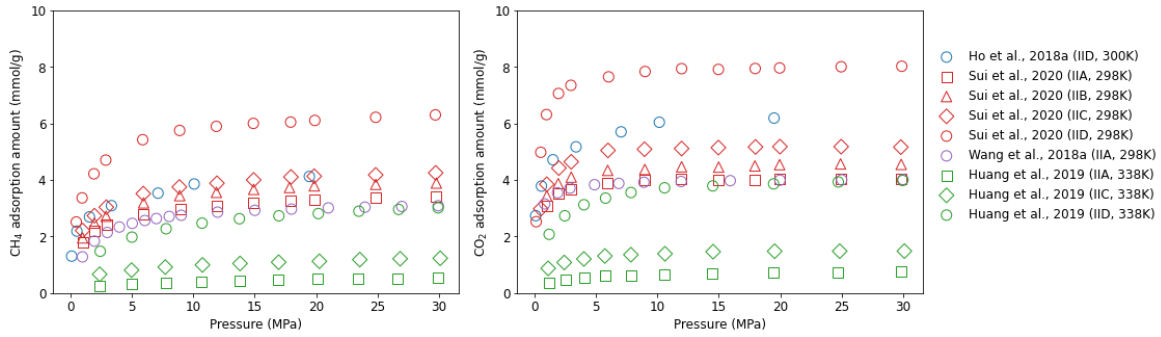

Figure 2.3 CH_4 and CO_2 adsorption amounts as a function of pressure. Data are summarised from the literature.

A few studies have investigated the displacement between CO_2 and CH_4 in a slit nanopore using GCMC or MD at various geological temperatures and pressures (Gong et al., 2020; Shi et al., 2019; Zhang and Cao, 2016; Zhang et al., 2019, 2020). GCMC investigates CO_2-CH_4 displacement assuming the simulation box is connected to two imaginary gas reservoirs, while MD initiates gas displacement by controlling the bulk gas reservoir at the ends of the slit nanopore. These studies suggest that the displacement efficiency and final adsorbed CO_2/CH_4 amounts vary with geological depth (i.e., pressure, temperature) and slit pore size. Over 90% of gas recovery can possibly be achieved by supercritical CO_2 displacement under high-pressure condition (Sun et al., 2017; Sun et al., 2016), much greater than using N_2 (Gong et al., 2020; Shi et al., 2019). To look into the gas displacement mechanisms, Yuan et al. (2015)

compared the process of CH_4 desorption caused by pressure drawdown and CO_2 displacement in a carbon nanotube (CNT). Ho et al. (2018b) found that the CO_2 could penetrate through water blockage at the pore entrance to displace CH_4 molecules in a CNT and graphene slit.

Gas flow and transport can also be investigated by molecular simulations, including dual control-volume grand canonical Monte Carlo (DCV-GCMC) (Jin, 2017; Sun et al., 2019), boundary-driven non-equilibrium molecular dynamics (BD-NEMD) (Collell et al., 2015; Wu and Firoozabadi, 2019), and non-equilibrium molecular dynamics (NEMD) (Yu et al., 2018). Methane flow has been studied in inorganic and organic nanopores to address the effects of pressure, temperature, pore size, surface roughness, and mineral composition, etc. Yu et al. (2018) and Yu et al. (2020b) found that methane transport in slit nanopores strongly depended on pressure and consisted of viscous flow, Knudsen diffusion, and surface diffusion. Gas slippage, as a common and widespread phenomenon in nanopores, decreases with the increase of gas pressure (Nan et al., 2020; Sun et al., 2020), pore size (Nan et al., 2020), and surface roughness (Castez et al., 2017; Huang et al., 2022; Yu et al., 2020a; Zhao et al., 2022). However, some studies show slippage is only present in the organic (e.g., graphene) nanopores rather than the inorganic (e.g., quartz, calcite, and montmorillonite) nanopores (Wang et al., 2017; Zhan et al., 2021).

Selective transport and separation are essential features for gas mixtures flowing through nanopores (Firouzi and Wilcox, 2013; Ho and Wang, 2020; Kazemi and Takbiri-Borujeni, 2017; Liu et al., 2018; Liu et al., 2022; Wu and Firoozabadi, 2018). For example, Firouzi and Wilcox (2013) observed a discrepancy between CO_2 and CH_4 gas velocity profiles when the two gases were flowing as an equimolar mixture in a single carbon slit pore, which might be attributed to the different strengths of gas-wall interaction. The separation of binary gas mixtures is mainly a function of pore size, as it weakens with the increasing pore size and becomes neglectable when pore size is above a critical value (Ho and Wang, 2020; Wu and Firoozabadi, 2018). Moreover, the gas mixture composition may also affect the separation factor since self-diffusion and Fick's diffusion coefficients of CO_2 and CH_4 increase with the partial pressure

(Kazemi and Takbiri-Borujeni, 2017; Liu et al., 2018).

2.5 Lattice Boltzmann simulations

The lattice Boltzmann method (LBM) serves as a mesoscopic numerical tool for solving fluid flow that connects the nano- and macroscales. It operates by evolving a discrete-velocity distribution function representing a fictitious particle population through collision and streaming (Krüger et al., 2017; Wang et al., 2020). LBM is especially adept at handling complex geometries, such as porous media, and it enables simulations of multiphase and multicomponent flow by adding an interaction force (e.g., Shan-Chen model) between different phases or components (Krüger et al., 2017; Sheikholeslami et al., 2013; Yan et al., 2021). Several modifications have been developed and implemented in LBM to capture unique characteristics of nanoporous flow in shale, such as slip flow boundary conditions, Knudsen layer, and surface adsorption/desorption (Wang et al., 2020). Three boundary conditions – bounce-back (BB), Maxwellian diffuse reflection (MDR), and Langmuir slip (LS) (Wang et al., 2020; Wang et al., 2016), are often combined to simulate slip flow more accurately (Liu et al., 2021; Wang et al., 2017b; Zhou et al., 2022). Using a local relaxation time calculated from the gas-solid distance and adding a gas-solid interaction force, the Knudsen effect and surface adsorption can be implemented in LBM, respectively (Wang et al., 2022; Wang et al., 2016; Wang et al., 2017a; Zhao et al., 2016).

Navier-Stokes (NSE) and advection-diffusion (ADE) equations can be solved in LBM using different equilibrium distributions to simulate viscous flow and mass transfer. They are often coupled together in multi-lattices to investigate gas migration in porous media (Lei et al., 2021; Peng et al., 2021; Peng et al., 2018; Zakirov and Khramchenkov, 2022; Zhang and Sun, 2019; Zhou et al., 2015; Zhou et al., 2016). Moreover, the Langmuir adsorption boundary scheme developed by Zhou et al. (2015) allows simulating gas adsorption at gas-solid interfaces, which further evolves into the solid (i.e., dual porosity model). This LBM coupling scheme can be

combined with the pore network modelling (Zhang and Sun, 2019) and the quartet structure generation set (QSGS) method (Zhou et al., 2016) to study gas flow in randomly disordered pore structures. The LBM NSE-ADE coupling is also utilised for handling scenarios involving multiphase and multicomponent flow (Jiang and Xu, 2021; Mansoubi et al., 2023; Wang et al., 2018; Xia, 2016). For instance, Jiang and Xu (2021) utilised the Shan-Chen model to address immiscible CO_2-water flow with mass and heat transfer. Wang et al. (2018) coupled two ADE lattices to a single NSE lattice to investigate the separation between CO_2 and CH_4 mixtures in porous membranes. Moreover, the discrete element method (DEM) is often coupled with LBM to study fluid-solid interaction, such as stress-dependent permeabilities in porous media (Huang et al., 2021) and solid particle movement under fluid flow (Jiang et al., 2022; Kano et al., 2020). Based on the versatility of LBM and its ability to couple with other numerical methods, more advanced models can be built to simulate shale gas flow in nanoporous media where strong gas-gas/solid interactions are encountered.

2.6 Summary of literature review and research gaps

This chapter reviews theories, experimental and multiscale numerical studies relevant to CO_2-enhanced gas recovery in shale reservoirs. In the presence of nanopores, gas transport largely deviates from that described by conventional theories due to the strong gas-solid interaction. As CO_2 displaces CH_4, competitive adsorption and selective mass transport take place as a function of nanopore size. Moreover, gas adsorption can induce swelling of the organic matrix (i.e., kerogen), further reducing gas permeability by narrowing the pore size. MD simulations are fundamentally based on particle interaction potentials after defining a proper force field. Therefore, it is a perfect tool to help us understand the physical behaviours arising from gas-gas and gas-solid interactions at an atomistic scale. LBM is suitable to upscale from a single pore to a complex porous structure as it is convenient to achieve multiphysics coupling of gas flow, transport, and adsorption, which occurs during CO_2-CH_4 displacement. The main research

gaps are summarised as

- Although much research focuses on CO_2/CH_4 adsorption and flows at nano- and micro-scales, the realistic kerogen model is rarely utilised and the studies across different scales are not bridged together. Since kerogen is the main generation and storage sites of CH_4, its interaction with gases plays the determining role in ensuring the success of enhanced shale gas recovery.
- Sorption-induced swelling is an important feature of nanoporous materials such as kerogen. Shale matrix is largely composed of kerogen. The effect of sorption-induced swelling on nano-confined gas transport remains to be better understood as it can greatly affect the CO_2-CH_4 displacement efficiency. Correlations between kerogen swelling and gas adsorption and between gas permeability and kerogen swelling need to be established, which can be potentially extended for use in continuum-scale reservoir simulations.
- The displacement of CH_4 by CO_2 is a multiscale and multiphysics process. Prior to predicting with large-scale models, it is imperative to gain a more profound comprehension of the underlying interplays of gas-gas and gas-solid interactions that steer the effectiveness of CO_2-EGR.

References

1. Aadnoy, B. S., & Looyeh, R. (2019). Petroleum rock mechanics: Drilling operations and well design. *Gulf Professional Publishing*.
2. Beskok, A., & Karniadakis, G. E. (1999). Report: A model for flows in channels, pipes, and ducts at micro and nano scales. *Microscale Thermophysical Engineering, 3*(1), 43-77.
3. Cai, J., Lin, D., Singh, H., Zhou, S., Meng, Q., & Zhang, Q. (2019). A simple permeability

model for shale gas and key insights on relative importance of various transport mechanisms. *Fuel, 252*, 210-219.

4. Castez, M. F., Winograd, E. A., & Sánchez, V. M. (2017). Methane flow through organic-rich nanopores: The key role of atomic-scale roughness. *The Journal of Physical Chemistry C, 121*(51), 28527-28536.

5. Chen, L., Liu, K., Jiang, S., Huang, H., Tan, J., & Zuo, L. (2021). Effect of adsorbed phase density on the correction of methane excess adsorption to absolute adsorption in shale. *Chemical Engineering Journal, 420*, 127678.

6. Chen, Y. D., & Yang, R. T. (1991). Concentration dependence of surface diffusion and zeolitic diffusion. *AIChE Journal, 37*(10), 1579-1582.

7. Clarkson, C. R., Pan, Z., Palmer, I. D., & Harpalani, S. (2010). Predicting sorption-induced strain and permeability increase with depletion for coalbed-methane reservoirs. *SPE Journal, 15*(01), 152-159.

8. Collell, J., Galliero, G., Vermorel, R., Ungerer, P., Yiannourakou, M., Montel, F., & Pujol, M. (2015). Transport of multicomponent hydrocarbon mixtures in shale organic matter by molecular simulations. *The Journal of Physical Chemistry C, 119*(39), 22587-22595.

9. Cui, G., Liu, J., Wei, M., Feng, X., & Elsworth, D. (2018). Evolution of permeability during the process of shale gas extraction. *Journal of Natural Gas Science and Engineering, 49*, 94-109.

10. Cui, X., Bustin, R. M., & Dipple, G. (2004). Selective transport of CO_2, CH_4, and N_2 in coals: Insights from modelling of experimental gas adsorption data. *Fuel, 83*(3), 293-303.

11. Cussler, E. L. (2009). Diffusion: Mass transfer in fluid systems. *Cambridge University Press*.

12. Darabi, H., Ettehad, A., Javadpour, F., & Sepehrnoori, K. (2012). Gas flow in ultra-tight shale strata. *Journal of Fluid Mechanics, 710*, 641-658.

13. Duan, S., Gu, M., Du, X., & Xian, X. (2016). Adsorption equilibrium of CO_2 and CH_4 and their mixture on Sichuan Basin shale. *Energy & Fuels, 30*(3), 2248-2256.

14. Fathi, E., & Akkutlu, I. Y. (2014). Multi-component gas transport and adsorption effects during CO_2 injection and enhanced shale gas recovery. *International Journal of Coal Geology, 123*, 52-61.

15. Firouzi, M., & Wilcox, J. (2013). Slippage and viscosity predictions in carbon micropores and their influence on CO_2 and CH_4 transport. *The Journal of Chemical Physics, 138*(6), 064705.

16. Gandossi, L., & Von Estorff, U. (2013). An overview of hydraulic fracturing and other formation stimulation technologies for shale gas production – Updated 2015. *Publications Office of the European Union*.

17. Gong, L., Zhang, Y., Li, N., Gu, Z.-K., Ding, B., & Zhu, C.-Y. (2020). Molecular investigation on the displacement characteristics of CH_4 by CO_2, N_2 and their mixture in a composite shale model. *Energies, 14*(1), 2.

18. Hamza, A., Hussein, I. A., Al-Marri, M. J., Mahmoud, M., Shawabkeh, R., & Aparicio, S. (2021). CO_2 enhanced gas recovery and sequestration in depleted gas reservoirs: A review. *Journal of Petroleum Science and Engineering, 196*, 107685.

19. Hasan, M., Eliebid, M., Mahmoud, M., Elkatatny, S., & Shawabkeh, R. (2017). Enhanced gas recovery (EGR) methods and production enhancement techniques for shale & tight gas reservoirs. *SPE Kingdom of Saudi Arabia Annual Technical Symposium and Exhibition*, SPE-188090-MS.

20. Ho, T. A., & Wang, Y. (2020). Pore size effect on selective gas transport in shale nanopores. *Journal of Natural Gas Science and Engineering, 83*, 103543.

21. Ho, T. A., & Wang, Y. (2021). Molecular origin of wettability alteration of subsurface porous media upon gas pressure variations. *ACS Applied Materials & Interfaces, 13*(34),

41330-41338.

22. Ho, T. A., Wang, Y., & Criscenti, L. J. (2018a). Chemo-mechanical coupling in kerogen gas adsorption/desorption. *Physical Chemistry Chemical Physics, 20*(18), 12390-12395.

23. Ho, T. A., Wang, Y., Xiong, Y., & Criscenti, L. J. (2018b). Differential retention and release of CO_2 and CH_4 in kerogen nanopores: Implications for gas extraction and carbon sequestration. *Fuel, 220*, 1-7.

24. Hong, L., Jain, J., Romanov, V., Lopano, C., Disenhof, C., Goodman, A., . . . Dilmore, R. (2016). An investigation of factors affecting the interaction of CO_2 and CH_4 on shale in Appalachian Basin. *Journal of Unconventional Oil and Gas Resources, 14*, 99-112.

25. Hu, R., Wang, W., Tan, J., Chen, L., Dick, J., & He, G. (2021). Mechanisms of shale gas adsorption: Insights from a comparative study on a thermodynamic investigation of microfossil-rich shale and non-microfossil shale. *Chemical Engineering Journal, 411*, 128463.

26. Huang, J., Xiao, F., Labra, C., Sun, J., & Yin, X. (2021). DEM-LBM simulation of stress-dependent absolute and relative permeabilities in porous media. *Chemical Engineering Science, 239*, 116633.

27. Huang, L., Ning, Z., Wang, Q., Qi, R., Cheng, Z., Wu, X., . . . Qin, H. (2019). Molecular insights into kerogen deformation induced by CO_2/CH_4 sorption: Effect of maturity and moisture. *Energy & Fuels, 33*(6), 4792-4805.

28. Huang, L., Ning, Z., Wang, Q., Zhang, W., Cheng, Z., Wu, X., & Qin, H. (2018). Effect of organic type and moisture on CO_2/CH_4 competitive adsorption in kerogen with implications for CO_2 sequestration and enhanced CH_4 recovery. *Applied Energy, 210*, 28-43.

29. Huang, P., Shen, L., Maggi, F., Chen, Z., & Pan, Z. (2022). Influence of surface roughness on methane flow in shale kerogen nano-slits. *Journal of Natural Gas Science and Engineering, 103*, 104650.

30. Iddphonce, R., Wang, J., & Zhao, L. (2020). Review of CO_2 injection techniques for enhanced shale gas recovery: Prospect and challenges. *Journal of Natural Gas Science and Engineering, 77*, 103240.

31. Javadpour, F., Fisher, D., & Unsworth, M. (2007). Nanoscale gas flow in shale gas sediments. *Journal of Canadian Petroleum Technology, 46*(10), PETSOC-07-10-06.

32. Javadpour, F., Singh, H., Rabbani, A., Babaei, M., & Enayati, S. (2021). Gas flow models of shale: A Review. *Energy & Fuels, 35*(4), 2999-3010.

33. Ji, L., Zhang, T., Milliken, K. L., Qu, J., & Zhang, X. (2012). Experimental investigation of main controls to methane adsorption in clay-rich rocks. *Applied Geochemistry, 27*(12), 2533-2545.

34. Jiang, F., Liu, H., Chen, X., & Tsuji, T. (2022). A coupled LBM-DEM method for simulating the multiphase fluid-solid interaction problem. *Journal of Computational Physics, 454*, 110963.

35. Jiang, M., & Xu, Z. G. (2021). Pore-scale investigation on reactive flow in non-uniform dissolved porous media considering immiscible phase by lattice Boltzmann method. *Journal of Natural Gas Science and Engineering, 96,* 104280.

36. Jin, Z. (2017). Effect of nano-confinement on high pressure methane flow characteristics. *Journal of Natural Gas Science and Engineering, 45*, 575-583.

37. Kang, D., Wang, X., Zheng, X., & Zhao, Y.-P. (2021). Predicting the components and types of kerogen in shale by combining machine learning with NMR spectra. *Fuel, 290*, 120006.

38. Kano, Y., Sato, T., & Oyama, H. (2020). Numerical study on the formations of gas channels and subsequent bubbles in unconsolidated sandy seabed sediment using a coupled LBM-DEM method. *Journal of Natural Gas Science and Engineering, 74*, 103101.

39. Kazemi, M., & Takbiri-Borujeni, A. (2017). Selective adsorption and transport diffusion of CO_2-CH_4 binary mixture in carbon-based organic nanopores. S*PE Western Regional*

Meeting, SPE-185623-MS.

40. Klewiah, I., Berawala, D. S., Alexander Walker, H. C., Andersen, P. Ø., & Nadeau, P. H. (2020). Review of experimental sorption studies of CO_2 and CH_4 in shales. *Journal of Natural Gas Science and Engineering, 73*, 103045.

41. Klinkenberg, L. J. (2012). The permeability of porous media to liquids and gases. *Drilling and Production Practice*, 200-213.

42. Krüger, T., Kusumaatmaja, H., Kuzmin, A., Shardt, O., Silva, G., & Viggen, E. M. (2017). The lattice Boltzmann method. *Springer International Publishing*.

43. Kumar, H., Elsworth, D., Mathews, J. P., & Marone, C. (2016). Permeability evolution in sorbing media: Analogies between organic-rich shale and coal. *Geofluids, 16*(1), 43-55.

44. Lan, Y., Yang, Z., Wang, P., Yan, Y., Zhang, L., & Ran, J. (2019). A review of microscopic seepage mechanism for shale gas extracted by supercritical CO_2 flooding. *Fuel, 238*, 412-424.

45. Lei, J., Ding, R., & Zhang, J. (2021). Study on seepage and adsorption characteristics of porous media containing adsorbent based on lattice Boltzmann. *AIP Advances, 11*(4), 045126.

46. Li, J. R., Kuppler, R. J., & Zhou, H. C. (2009). Selective gas adsorption and separation in metal-organic frameworks. *Chemical Society Reviews, 38*(5), 1477-1504.

47. Li, Y., Wang, J., Wang, Z., & Pan, Z. (2020). Variation in permeability during CO_2-CH_4 displacement in coal seams. Part 2: Modelling and simulation. *ACS Omega, 5*(29), 18432-18440.

48. Liu, B., Qi, C., Mai, T., Zhang, J., Zhan, K., Zhang, Z., & He, J. (2018). Competitive adsorption and diffusion of CH_4/CO_2 binary mixture within shale organic nanochannels. *Journal of Natural Gas Science and Engineering, 53*, 329-336.

49. Liu, J., Wang, J., Chen, Z., Wang, S., Elsworth, D., & Jiang, Y. (2011). Impact of transition

from local swelling to macro swelling on the evolution of coal permeability. *International Journal of Coal Geology, 88*(1), 31-40.

50. Liu, J., Xie, L., Elsworth, D., & Gan, Q. (2019). CO_2/CH_4 competitive adsorption in shale: Implications for enhancement in gas production and reduction in carbon rmissions. *Environmental Science & Technology, 53*(15), 9328-9336.

51. Liu, J., Yao, Y., Liu, D., & Elsworth, D. (2017). Experimental evaluation of CO_2 enhanced recovery of adsorbed-gas from shale. *International Journal of Coal Geology, 179*, 211-218.

52. Liu, L., Nieto-Draghi, C., Lachet, V., Heidaryan, E., & Aryana, S. A. (2022). Bridging confined phase behaviour of CH_4-CO_2 binary systems across scales. *The Journal of Supercritical Fluids, 189*, 105713.

53. Liu, L., Wang, Y., & Aryana, S. A. (2021). Insights into scale translation of methane transport in nanopores. *Journal of Natural Gas Science and Engineering, 96*, 104220.

54. Louk, K., Ripepi, N., Luxbacher, K., Gilliland, E., Tang, X., Keles, C., . . . Michael, K. (2017). Monitoring CO_2 storage and enhanced gas recovery in unconventional shale reservoirs: Results from the Morgan County, Tennessee injection test. *Journal of Natural Gas Science and Engineering, 45*, 11-25.

55. Lu, T., Zeng, K., Jiang, P., Zhou, B., & Xu, R. (2022). Competitive adsorption in CO_2 enhancing shale gas: Low-field NMR measurement combined with molecular simulation for selectivity and displacement efficiency model. *Chemical Engineering Journal, 440*, 135865.

56. Ma, T., Chen, P., & Zhao, J. (2016). Overview on vertical and directional drilling technologies for the exploration and exploitation of deep petroleum resources. *Geomechanics and Geophysics for Geo-Energy and Geo-Resources, 2*, 365-395.

57. Ma, Y. Z., & Holditch, S. (2015). Unconventional oil and gas resources handbook: Evaluation and development. *Gulf Professional Publishing*.

58. Mansoubi, H., Mansourpour, Z., & Fatemi, S. (2023). Investigation of CO_2 and CH_4 capture from syngas in adsorption process and breakthrough modelling by modified Lattice-Boltzmann mesoscale method. *Chemosphere, 325*, 138366.

59. Maxwell, J. C. (1879). VII. On stresses in rarified gases arising from inequalities of temperature. *Philosophical Transactions of the Royal Society of London*, *170*, 231-256.

60. Memon, A., Li, A., Memon, B. S., Muther, T., Han, W., Kashif, M., . . . Akbar, I. (2020). Gas adsorption and controlling factors of Shale: Review, application, comparison and challenges. *Natural Resources Research, 30*(1), 827-848.

61. Myong, R. (2001). A computational method for Eu's generalised hydrodynamic equations of rarefied and microscale gas dynamics. *Journal of Computational Physics, 168*(1), 47-72.

62. Myong, R. (2001). Velocity-slip effect in low-speed microscale gas flows. *The 35th AIAA Thermophysics Conference*.

63. Myong, R. (2004). Gaseous slip models based on the Langmuir adsorption isotherm. *Physics of Fluids, 16*(1), 104-117.

64. Nan, Y., Li, W., & Jin, Z. (2020). Slip length of methane flow under shale reservoir conditions: Effect of pore size and pressure. *Fuel, 259*, 116237.

65. Neil, C. W., Mehana, M., Hjelm, R. P., Hawley, M. E., Watkins, E. B., Mao, Y., . . . Xu, H. (2020). Reduced methane recovery at high pressure due to methane trapping in shale nanopores. *Communications Earth & Environment, 1*, 49.

66. Omari, A., Wang, C., Li, Y., & Xu, X. (2022). The progress of enhanced gas recovery (EGR) in shale gas reservoirs: A review of theory, experiments, and simulations. *Journal of Petroleum Science and Engineering, 213*, 110461.

67. Pathak, M., Huang, H., Meakin, P., & Deo, M. (2018). Molecular investigation of the interactions of carbon dioxide and methane with kerogen: Application in enhanced shale gas recovery. *Journal of Natural Gas Science and Engineering, 51*, 1-8.

68. Peng, Z., Deng, Z., Feng, H., Liu, S., & Li, Y. (2021). Multiscale lattice Boltzmann simulation of the kinetics process of methane desorption-diffusion in coal. *ACS Omega, 6*(30), 19789-19798.

69. Peng, Z., Liu, S., Tang, S., Zhao, Y., & Li, Y. (2018). Multicomponent lattice Boltzmann simulations of gas transport in a coal reservoir with dynamic adsorption. *Geofluids, 2018*, 1-13.

70. Pollard, W., & Present, R. D. (1948). On gaseous self-diffusion in long capillary tubes. *Physical Review, 73*(7), 762.

71. Potier, K., Ariskina, K., Obliger, A., & Leyssale, J. M. (2023). Molecular simulation of argon adsorption and diffusion in a microporous carbon with poroelastic couplings. *Langmuir*, *39*(27), 9384-9395.

72. Rahm, D. (2011). Regulating hydraulic fracturing in shale gas plays: The case of Texas. *Energy Policy, 39*(5), 2974-2981.

73. Rani, S., Padmanabhan, E., & Prusty, B. K. (2019). Review of gas adsorption in shales for enhanced methane recovery and CO_2 storage. *Journal of Petroleum Science and Engineering, 175*, 634-643.

74. Savage, F. (2014). Effect of dry-wet cycles on fracture propagation in shale and gas production mechanism. *University of Louisiana at Lafayette*.

75. Sheikholeslami, M., Gorji-Bandpy, M., & Ganji, D. (2013). Numerical investigation of MHD effects on Al_2O_3-water nanofluid flow and heat transfer in a semi-annulus enclosure using LBM. *Energy, 60*, 501-510.

76. Shen, W., Li, X., Xu, Y., Sun, Y., & Huang, W. (2017). Gas flow behaviour of nanoscale pores in shale gas reservoirs. *Energies, 10*(6), 751.

77. Sheng, G., Javadpour, F., & Su, Y. (2019). Dynamic porosity and apparent permeability in porous organic matter of shale gas reservoirs. *Fuel, 251*, 341-351.

78. Shi, J., Gong, L., Sun, S., Huang, Z., Ding, B., & Yao, J. (2019). Competitive adsorption phenomenon in shale gas displacement processes. *RSC Advances, 9*(44), 25326-25335.

79. Sui, H., & Yao, J. (2016). Effect of surface chemistry for CH_4/CO_2 adsorption in kerogen: A molecular simulation study. *Journal of Natural Gas Science and Engineering, 31*, 738-746.

80. Sui, H., Zhang, F., Wang, Z., Wang, D., & Wang, Y. (2020). Effect of kerogen maturity, water content for carbon dioxide, methane, and their mixture adsorption and diffusion in kerogen: A computational investigation. *Langmuir, 36*(33), 9756-9769.

81. Sun, H., Zhao, H., Qi, N., & Li, Y. (2017). Molecular insights into the enhanced shale gas recovery by carbon dioxide in kerogen slit nanopores. *The Journal of Physical Chemistry C, 121*(18), 10233-10241.

82. Sun, H., Zhao, H., Qi, N., Qi, X., Zhang, K., Sun, W., & Li, Y. (2016). Mechanistic insight into the displacement of CH_4 by CO_2 in calcite slit nanopores: The effect of competitive adsorption. *RSC Advances, 6*(106), 104456-104462.

83. Sun, J., Liu, Z., & Cao, D. (2019). A permeation model of shale gas in cylindrical-like kerogen pores at geological conditions. *Chemical Engineering Science, 207*, 457-463.

84. Sun, Z., Li, X., Liu, W., Zhang, T., He, M., & Nasrabadi, H. (2020). Molecular dynamics of methane flow behaviour through realistic organic nanopores under geologic shale condition: Pore size and kerogen types. *Chemical Engineering Journal, 398*, 124341.

85. Swami, V., Clarkson, C. R., & Settari, A. (2012). Non-Darcy flow in shale nanopores: Do we have a final answer? *SPE Canadian Unconventional Resources Conference*, SPE-162665-MS.

86. USGS. (2019). https://usgs.gov/mission-areas/water-resources/science/hydraulic-fracturing.

87. Wang, H., Chen, L., Qu, Z., Yin, Y., Kang, Q., Yu, B., & Tao, W.-Q. (2020). Modelling of multi-scale transport phenomena in shale gas production — A critical review. *Applied*

Energy, 262, 114575.

88. Wang, H., Qu, Z. G., & Zhou, L. (2018). Coupled GCMC and LBM simulation method for visualisations of CO_2/CH_4 gas separation through Cu-BTC membranes. *Journal of Membrane Science, 550*, 448-461.

89. Wang, H., Su, Y., Wang, W., Jin, Z., & Chen, H. (2022). CO_2-oil diffusion, adsorption and miscible flow in nanoporous media from pore-scale perspectives. *Chemical Engineering Journal, 450*, 137957.

90. Wang, J., Chen, L., Kang, Q., & Rahman, S. S. (2016). The lattice Boltzmann method for isothermal micro-gaseous flow and its application in shale gas flow: A review. *International Journal of Heat and Mass Transfer, 95*, 94-108.

91. Wang, J., Kang, Q., Chen, L., & Rahman, S. S. (2017a). Pore-scale lattice Boltzmann simulation of micro-gaseous flow considering surface diffusion effect. *International Journal of Coal Geology, 169*, 62-73.

92. Wang, J., Kang, Q., Wang, Y., Pawar, R., & Rahman, S. S. (2017b). Simulation of gas flow in micro-porous media with the regularised lattice Boltzmann method. *Fuel, 205*, 232-246.

93. Wang, S., Feng, Q., Javadpour, F., Zha, M., & Cui, R. (2017). Multiscale modelling of shale apparent permeability: An integrated study of molecular dynamics and pore network model. *SPE Annual Technical Conference and Exhibition*, SPE-187286-PA.

94. Wang, T., Tian, S., Li, G., & Sheng, M. (2018a). Selective adsorption of supercritical carbon dioxide and methane binary mixture in shale kerogen nanopores. *Journal of Natural Gas Science and Engineering, 50*, 181-188.

95. Wang, T., Tian, S., Li, G., Sheng, M., Ren, W., Liu, Q., & Zhang, S. (2018b). Molecular simulation of CO_2/CH_4 competitive adsorption on shale kerogen for CO_2 sequestration and enhanced gas recovery. *The Journal of Physical Chemistry C, 122*(30), 17009-17018.

96. Wikipedia. (2023). https://en.wikipedia.org/wiki/Molecular_dynamics.

97. Wu, K., Li, X., Guo, C., Wang, C., & Chen, Z. (2016). A unified model for gas transfer in nanopores of shale-gas reservoirs: Coupling pore diffusion and surface diffusion. *SPE Journal, 21*(05), 1583-1611.

98. Wu, T., & Firoozabadi, A. (2018). Molecular simulations of binary gas mixture transport and separation in slit nanopores. *The Journal of Physical Chemistry C, 122*(36), 20727-20735.

99. Wu, T., & Firoozabadi, A. (2019). Effect of microstructural flexibility on methane flow in kerogen matrix by molecular dynamics simulations. *The Journal of Physical Chemistry C, 123*(17), 10874-10880.

100. Wu, W., Zoback, M. D., & Kohli, A. H. (2017). The impacts of effective stress and CO_2 sorption on the matrix permeability of shale reservoir rocks. *Fuel, 203*, 179-186.

101. Xia, M. (2016). Pore-scale simulation of miscible displacement in porous media using the lattice Boltzmann method. *Computers & Geosciences, 88*, 30-40.

102. Xie, W., Wang, M., & Wang, H. (2021). Adsorption characteristics of CH_4 and CO_2 in shale at high pressure and temperature. *ACS Omega, 6*(28), 18527-18536.

103. Yan, M., Zhou, M., Li, S., Lin, H., Zhang, K., Zhang, B., & Shu, C.-M. (2021). Numerical investigation on the influence of micropore structure characteristics on gas seepage in coal with lattice Boltzmann method. *Energy, 230*, 120773.

104. Yu, H., Fan, J., Chen, J., Zhu, Y., & Wu, H. (2018). Pressure-dependent transport characteristic of methane gas in slit nanopores. *International Journal of Heat and Mass Transfer, 123*, 657-667.

105. Yu, H., Xu, H., Fan, J., Wang, F., & Wu, H. (2020a). Roughness factor-dependent transport characteristic of shale gas through amorphous kerogen nanopores. *The Journal of Physical Chemistry C, 124*(23), 12752-12765.

106. Yu, H., Xu, H., Xia, J., Fan, J., Wang, F., & Wu, H. (2020b). Nanoconfined transport

characteristic of methane in organic shale nanopores: The applicability of the continuous model. *Energy & Fuels, 34*(8), 9552-9562.

107. Yuan, Q., Zhu, X., Lin, K., & Zhao, Y. P. (2015). Molecular dynamics simulations of the enhanced recovery of confined methane with carbon dioxide. *Physical Chemistry Chemical Physics, 17*(47), 31887-31893.

108. Yuan, W., Pan, Z., Li, X., Yang, Y., Zhao, C., Connell, L. D., . . . He, J. (2014). Experimental study and modelling of methane adsorption and diffusion in shale. *Fuel, 117*, 509-519.

109. Zakirov, T. R., & Khramchenkov, M. G. (2022). Effect of pore space heterogeneity on the adsorption dynamics in porous media at various convection-diffusion and reaction conditions: A lattice Boltzmann study. *Journal of Petroleum Science and Engineering, 212*, 110300.

110. Zeng, K., Xu, R., Lu, T., Tian, Z., & Jiang, P. (2023). NMR measurements for gas adsorption characterisation on shale: State of the art and perspectives. *Energy & Fuels*, *37*(13), 8824-8835.

111. Zhan, S., Su, Y., Lu, M., Cai, M., Fu, J., Liu, Z., . . . Li, G. (2021). Effect of surface type on the flow characteristics in shale nanopores. *Geofluids, 2021*, 1-12.

112. Zhang, H., & Cao, D. (2016). Molecular simulation of displacement of shale gas by carbon dioxide at different geological depths. *Chemical Engineering Science, 156*, 121-127.

113. Zhang, H., Diao, R., Mostofi, M., & Evans, B. (2019). Monte Carlo simulation of the adsorption and displacement of CH_4 by CO_2 injection in shale organic carbon slit micropores for CO_2 enhanced shale gas recovery. *Energy & Fuels, 34*(1), 150-163.

114. Zhang, H., Diao, R., Mostofi, M., & Evans, B. (2020). Molecular simulation of enhanced CH_4 recovery and CO_2 storage by CO_2–N_2 mixture injection in deformable organic

micropores. *Journal of Natural Gas Science and Engineering, 84*, 103658.

115. Zhang, T., & Sun, S. (2019). A coupled Lattice Boltzmann approach to simulate gas flow and transport in shale reservoirs with dynamic sorption. *Fuel, 246*, 196-203.

116. Zhao, J., Yao, J., Zhang, L., Sui, H., & Zhang, M. (2016). Pore-scale simulation of shale gas production considering the adsorption effect. *International Journal of Heat and Mass Transfer, 103*, 1098-1107.

117. Zhao, Y., Luo, M., Liu, L., Wu, J., Chen, M., & Zhang, L. (2022). Molecular dynamics simulations of shale gas transport in rough nanopores. *Journal of Petroleum Science and Engineering, 217*, 110884.

118. Zhao, Y., Wang, C., Zhang, Y., & Liu, Q. (2019). Experimental study of adsorption effects on shale permeability. *Natural Resources Research, 28*(4), 1575-1586.

119. Zhou, J., Tian, S., Zhou, L., Xian, X., Yang, K., Jiang, Y., . . . Guo, Y. (2020). Experimental investigation on the influence of sub- and super-critical CO_2 saturation time on the permeability of fractured shale. *Energy, 191*, 116574.

120. Zhou, L., Qu, Z. G., Chen, L., & Tao, W. Q. (2015). Lattice Boltzmann simulation of gas–solid adsorption processes at pore scale level. *Journal of Computational Physics, 300*, 800-813.

121. Zhou, L., Qu, Z. G., Ding, T., & Miao, J. Y. (2016). Lattice Boltzmann simulation of the gas-solid adsorption process in reconstructed random porous media. *Physical Review E, 93*, 043101.

122. Zhou, W., Yang, X., & Liu, X. (2022). Multiscale modelling of gas flow behaviours in nanoporous shale matrix considering multiple transport mechanisms. *Physical Review E, 105*(5-2), 055308.

Chapter 3 Molecular investigation on CO_2-CH_4 displacement and kerogen deformation in enhanced shale gas recovery

Since it is challenging to investigate the displacement between CO_2 and CH_4 in kerogen experimentally, numerical simulations using a hybrid method of MD and GCMC are performed in this chapter. MD is proposed for kerogen deformation, and GCMC realises gas adsorption and desorption through continuous insertion and deletion of molecules. This hybrid method enables tracking the swelling and shrinkage of the kerogen matrix due to gas adsorption and desorption, which are commonly seen in nanoporous materials. In the first part, kerogen's adsorption and swelling volumetric strain are studied as a function of CO_2 or CH_4 pressure and compared with a sorption-induced swelling model derived from surface energy change. In the second part, CO_2 is injected into kerogen matrix with residual methane. The displacement efficiency and CO_2 sequestration are investigated as a function of CO_2 injection and depleted reservoir pressures. Lastly, kerogen deformation is analysed, and a non-linear correlation is observed between gas adsorption amount and swelling. This chapter aims to establish a relationship between CH_4 recovery ratio and CO_2 injection/reservoir depletion pressure at the nanoscale, which provides information for selecting proper injection conditions to maximise gas production during CO_2-EGR. This chapter is presented in the form of a manuscript that has been published in *Fuel*:

Wu, J., Huang, P., Maggi, F., & Shen, L. (2022). Molecular investigation on CO_2-CH_4 displacement and kerogen deformation in enhanced shale gas recovery. *Fuel, 315*, 123208.

The PhD candidate has performed all the numerical work and the analysis of the results, and is the primary author of the above article.

Molecular investigation on CO_2-CH_4 displacement and kerogen deformation in enhanced shale gas recovery

Jian Wu, Pengyu Huang, Federico Maggi, Luming Shen*

School of Civil Engineering, The University of Sydney, NSW 2006, Australia

*Corresponding author. Email: luming.shen@sydney.edu.au

Abstract

CO_2-enhanced gas recovery (EGR) is a promising method that can not only improve the production of adsorbed shale gas but also achieve the geological storage of CO_2. During the injection of CO_2, shale is expected to deform due to both CH_4 desorption-induced shrinkage and CO_2 adsorption-induced swelling. Regardless of the potential effects on gas permeability and transport, the sorption-induced deformation remains poorly understood and is generally overlooked in large-scale simulations of CO_2-EGR. In this paper, Monte Carlo and molecular dynamics simulations are performed to study the CO_2-CH_4 displacement in the type II-D overmature kerogen (i.e., the primary organic matter in shale). Our results indicate that the CO_2-CH_4 displacement efficiency increases with the increase of the CO_2 injection pressure but decreases linearly with the increase of the reservoir depletion pressure. Moreover, the sorption-induced deformation is measured as volumetric strain and analysed after initial CH_4 saturation, pressure drawdown, and CO_2 injection. It is observed that CO_2 injection can induce a volume expansion of the original CH_4-saturated kerogen up to 5%. In addition, a novel non-linear adsorption-strain model is derived to provide a theoretical basis for kerogen deformation by taking the gas adsorption and deformation coupling into consideration. Different from the conventional linear theory, the increment of volumetric strain induced by gas adsorption becomes much faster when close to adsorption saturation. The derived model can accurately

capture the observed non-linearity and predict deformation caused by single-component gas and gas mixtures. Since swelling can further reduce shale permeability, these results imply that CO_2 injectivity and CH_4 production rate may both decline faster than expected in CO_2-EGR.

3.1 Introduction

Shale reservoirs are common formation types holding unconventional oil and gas resources within their extremely fine-grained sedimentary rocks (Alfarge et al., 2020). The reservoir permeability is usually in the range of 0.001-0.0001 mD, leading to a very low gas production (NRC, 2019). However, the recent development of long horizontal wells drilling and hydraulic fracturing has dramatically improved gas production in unconventional reservoirs (Zendehboudi and Bahadori, 2016). As one of the cleanest and most efficient energy sources, shale gas is believed to help reduce greenhouse gas emissions over the long term (Wang et al., 2011; Karagöz et al., 2021). In 2019, shale gas accounted for 27.77 trillion cubic feet in the US, estimated at 67.9% of their total natural gas production (EIA, 2020).

Shale's typical well production profile is characterised by the initial rapid gas production from natural fractures and a soon-to-follow decline due to free gas depletion (Neil et al., 2020). As reservoir pressure drops, gas desorption starts in the shale matrix and becomes the primary process for production, after which the total gas recovery is only around 28-40% (Sharma and Chopra, 2013; Speight, 2013). CO_2-Enhanced Gas Recovery (CO_2-EGR) is a promising method that can further improve adsorbed gas production and achieve geological storage of CO_2 in shale reservoirs (Alfarge et al., 2017; Fathi and Akkutlu, 2014; Huang et al., 2020; Louk et al., 2017). As a fracturing liquid replacing the commonly used water, CO_2 is environmental-friendly and can reduce the pressure on the global water crisis facing us today (Lan et al., 2019). The CO_2-CH_4 displacement is a dynamic process governed by pressure gradient and competitive adsorption (Iddphonce et al., 2020). During the displacement, shale permeability is changeable with production time due to the deformation (i.e., fracture and pore size change)

induced by repetitive gas adsorption and desorption (Alfarge et al., 2017; Li et al., 2020a; Li et al., 2020b). Therefore, a comprehensive understanding is required for the CO_2-CH_4 displacement with the consideration of shale deformation.

During gas adsorption and desorption in porous organic matter, deformation (i.e., swelling and shrinkage) is expected to take place (Gor et al., 2017). According to experimental observations, this sorption-induced swelling can reach 2%, significantly reducing shale permeability by one order of magnitude (Ao et al., 2017; Zhou et al., 2020). Several molecular simulation studies have been performed focusing on the kerogen volumetric strain either as a function of gas pressure or adsorption amount (Ho et al., 2018a; Chong et al., 2021; Tesson and Firoozabadi, 2019; Yu et al., 2021; Huang et al., 2019). For single-component gas, a Langmuir-like relationship was observed between volumetric strain and gas pressure (Chong et al., 2021; Ho et al., 2018a; Tesson and Firoozabadi, 2019). After studying different adsorbate gases, Tesson and Firoozabadi (2019) suggested that small gas molecules could induce greater kerogen swelling at the same pressure (i.e., CO_2 > CH_4 > C_2H_6 > C_3H_8). Yu et al. (2021) proposed a simple linear-relationship model between the volumetric strain and total adsorption amount, in which the correlation coefficient was associated with the adsorbent type and the kinetic diameter of gas molecules. They concluded that the same molar amount of large molecule-sized gas would have a more significant swelling effect (C_2H_6 > CH_4 > CO_2). In addition, deformation induced by single-component gases was also investigated against kerogen maturity and moisture content, and the total volumetric strain under the same gas pressure was found the highest in the type II-D overmature kerogen without moisture (Huang et al., 2019b).

Grand canonical Monte Carlo (GCMC) and grand canonical Monte Carlo-molecular dynamics (GCMC-MD) are the two most common methods used to investigate gas adsorption in kerogen matrix and slit nanopores (Ho et al., 2018a; Chong et al., 2021; Tesson and Firoozabadi, 2019; Yu et al., 2021; Huang et al., 2019; Huang et al., 2018; Sui et al., 2020; Wang et al., 2018b; Zhang et al., 2019). Mixed gas adsorption is usually accomplished by applying a fixed bulk gas pressure and a known mole fraction of CO_2 and CH_4 (e.g., 0.5/0.5) (Huang et al., 2018; Sui et

al., 2020; Wang et al., 2018b; Zhang et al., 2019). For example, Huang et al. (2018) and Sui et al. (2020) studied the effects of organic type and moisture content on CO_2-CH_4 binary adsorption in the kerogen matrix. Their results showed that gas adsorption capacity was in the order of kerogen type I < II < III and increased with kerogen maturity. Despite the negative effect on gas adsorption, moisture, salinity, and ethane increased the CO_2/CH_4 selectivity (Huang et al., 2018; Sui et al., 2020; Li et al., 2021). Wang et al. (2018b) constructed a slit pore between kerogen matrices to study CO_2 injection under different geological conditions (i.e., pressure and temperature) and suggested that the optimal injection depth for CO_2-EGR projects is in the buried range of 1000-2500 m. Zhang et al. (2019) simulated the competitive adsorption and gas density distribution profiles at various CO_2-CH_4 mole fractions and bulk gas pressures. For the smaller pore of 0.65 nm, they found that increasing the CO_2 mole fraction from 20% to 70% had a negligible impact on both adsorbed CO_2 and recovered CH_4 densities. Sun et al. (2021) discovered that the CO_2/CH_4 selectivity in the kerogen matrix was higher than that in the slit, indicating CH_4 might be more easily displaced out of shale formations with fewer fractures.

There is a limited number of experimental studies on the direct CO_2-CH_4 displacement due to the difficulty of separating the free and adsorbed gas phases in shale (Du et al., 2019; Liu et al., 2017). Liu et al. (2017) used the nuclear magnetic resonance (NMR) to evaluate the dynamic desorption process of adsorbed CH_4 in a black shale core sample collected from the Lower Silurian Longmaxi Formation. Their results illustrated that CO_2 injection could improve the residual gas recovery by an additional 25% after pressure drawdown. In contrast, a more popular choice would be molecular simulations (Shi et al., 2019; Zhang and Cao, 2016; Gong et al., 2020; Sun et al., 2016; Sun et al., 2017; Yuan et al., 2015; Ho et al., 2018b). For example, GCMC was performed to study the CO_2-CH_4 displacement in a slit nanopore between two sheets composed of organic and inorganic matter at various geological temperatures and pressures (Gong et al., 2020; Shi et al., 2019; Zhang and Cao, 2016). The results indicated that geological depth and pore size significantly affected the final equilibrium CO_2 and CH_4 adsorption amounts. MD, as an alternative molecular simulation method, has also been widely

employed to investigate binary gas displacement in slit nanopores (Gong et al., 2020; Sun et al., 2016; Sun et al., 2017; Yuan et al., 2015; Ho et al., 2018b). In such simulations, CO_2 displacement can be carried out by changing the bulk gas reservoir pressure emplaced at two ends of the slit nanopore. It was observed that adsorbed CH_4 could be more easily displaced by high-pressure supercritical CO_2 than gaseous CO_2, with over 90% of gas recovery achieved (Sun et al., 2017; Sun et al., 2016). However, a recovery limit was reported by Gong et al. (2020) where the displacement efficiency of CH_4 gradually slowed down at the CO_2 injection pressure greater than 10 MPa, and a further increase of pressure had little impact on enhancing gas recovery. To study the gas displacement mechanisms, Yuan et al. (2015) compared the CH_4 desorption evolutions during pressure drawdown and CO_2 injection in a single carbon nanotube (CNT). Ho et al. (2018b) performed GCMC-MD in a CNT and graphene slit with water blockage. They confirmed the preferential adsorption of CO_2 over CH_4 and determined that highly-soluble CO_2 could even successfully penetrate through the water to displace CH_4 molecules.

Deformation induced by the gas mixture is a more complicated process and has been studied with molecular simulations and poromechanical models (Brochard et al., 2012a; Brochard et al., 2012b; Huang et al., 2019a). Brochard et al. (2012b) derived a poroelastic equation that could relate volumetric strain to the sorption-pressure dependency in nanomaterials. Subsequently, their group successfully validated the model against experimental data for pure CO_2 and CH_4 in a coal sample and applied it to estimate the coal strain difference between exposure to the CO_2-CH_4 mixture and pure CH_4 at the same bulk pressure (Brochard et al., 2012a). More recently, Huang et al. (2019a) used the poromechanical model to calculate kerogen volumetric strain under the CO_2-CH_4 mixture along with the adsorption isotherms obtained from GCMC-MD simulations. Their results indicated that increasing the CO_2 composition in the binary gas mixture could generate a more considerable amount of volumetric strain, especially when the total bulk gas pressure was high. So far there has been no direct molecular simulations on kerogen deformation during the CO_2-CH_4 displacement in the literature. However, it is important to understand the swelling/shrinkage behaviour of the

kerogen matrix in order to better predict the permeability evolution and gas production characteristics when practising CO_2-EGR on site.

Despite of previous efforts, the investigation of kerogen deformation associated with gas adsorption remains focused on single-component gases, from which several mathematical models can be derived and validated. The deformation from pre-designed gas mixtures is often indirectly calculated with those poromechanical models mentioned above by substituting in the adsorption isotherms. So far, there have been no direct molecular simulations on kerogen deformation in the process of CO_2-CH_4 displacement (i.e., initial CH_4 desorption and subsequent CO_2 adsorption) with controlled injection parameters. However, it is essential to understand the swelling/shrinkage behaviour of the kerogen matrix in order to better predict the permeability evolution and gas production characteristics when practising CO_2-EGR on site. This study used the GCMC-MD hybrid method to simulate the CO_2-CH_4 displacement in the kerogen matrix under various reservoir conditions. The simulations were intended to mimic real-life engineering practices and followed a complete procedure of gas saturation, pressure drawdown, and gas displacement. The deformation of the kerogen matrix was measured as a volumetric strain after each stage. Additionally, a novel theoretical adsorption-strain model was proposed based on the coupling effect between adsorption and strain. This model successfully captured the non-linearity between the total adsorption amount and volumetric strain observed in our simulations.

3.2 Computational methods

3.2.1 Model of kerogen structure

The type II-D kerogen unit ($C_{175}H_{102}O_9N_4S_2$) developed by Ungerer et al. (2014) was used in this study. The PCFF+ fore field was originally used to describe the intramolecular and intermolecular interactions in Ungerer et al. (2014). It should be noted that PCFF+ uses the 9/6

Lennard-Jones potential for the intermolecular interaction of kerogen molecules, while the interaction of CH_4 and CO_2 gas molecules is often described by the 12/6 Lennard-Jones potential (Ho et al., 2016). Different force fields, such as consistent valence force field (CVFF) and general AMBER force field (GAFF), were also used for kerogen molecules (Ho et al., 2016; Vasileiadis et al., 2017). CVFF and GAFF use the 12/6 Lennard-Jones potential, which is more suitable to simulate the intermolecular interaction between kerogen and gas molecules. Since GAFF is applicable to most organic molecules (Wang et al., 2004), it is chosen to simulate the kerogen structure in this work. The electrostatic potentials can be calculated at HF/6-31G* level of theory along with the geometry optimisation from the initial molecular configuration of Ungerer et al. (2014) using the GAUSSIAN16 code (Frisch et al., 2016), similar to the process in Vasileiadis et al. (2017). Then, the partial atomic charges can be calculated and assigned with the antechamber tool (Wang et al., 2006) from the AmberTools19 compilation (Case et al., 2019). As a result, a conclusive Amber data file including the assigned GAFF force field parameters and atomic charges was successfully generated. It could then be converted to a LAMMPS data file by InterMol (Shirts et al., 2017) for molecular dynamics simulations.

To create the kerogen matrix for adsorption simulations, a total of 27 kerogen units were emplaced in a simulation box of 100 Å × 100 Å × 100 Å with periodic boundary conditions applied in all three dimensions. A dummy Lennard-Jones particle ($\varepsilon = 0.4$ Kcal/mol, $\sigma = 20$ Å) was fixed in the middle of the simulation box during relaxation in order to create a relatively large porosity in the kerogen matrix (Michalec and Lísal, 2017). The complete relaxation process is summarised in Table 3.1 with a timestep size of 1 fs, similar to the procedure suggested by Ungerer et al. (2014). The final kerogen structure has a density of 1.106 g/cm^3. The total porosity was computed as 14.9% with a helium probe using the Monte Carlo method suggested by Herrera et al. (2010). Pore size distributions (PSDs) are in the range of 2.1-7.4 Å (Figure 3.1), measured by a CO_2 molecule in PSDsolv (Bhattacharya and Gubbins, 2006; Gelb and Gubbins, 1999). The relaxation of kerogen molecules without the dummy particle was also simulated for the validation of the force field. The average density of three relaxed kerogen samples is calculated as 1.23 ± 0.02 g/cm^3, which is consistent with the values calculated using

PCFF+ and CVFF (Ho et al., 2016; Ungerer et al., 2014).

Table 3.1 Detailed construction steps of the kerogen matrix model.

Step	Ensemble	Pressure (MPa)	Temperature (K)	Simulation time (ps)
1	NVT	-	1000	100
2	NPT	15	1000	500
3	NPT	15	1000 – 900	100
4	NPT	15	900 – 700	200
5	NPT	15	700 – 500	200
6	NPT	15	500 – 400	200
7	NPT	15	400 – 300	200
8	NVT	-	300	200
9	NPT	15 – 0.1	300	200
10	NPT	0.1	300	200
11	NPT (with dummy particle removed)	0.1	300	1000

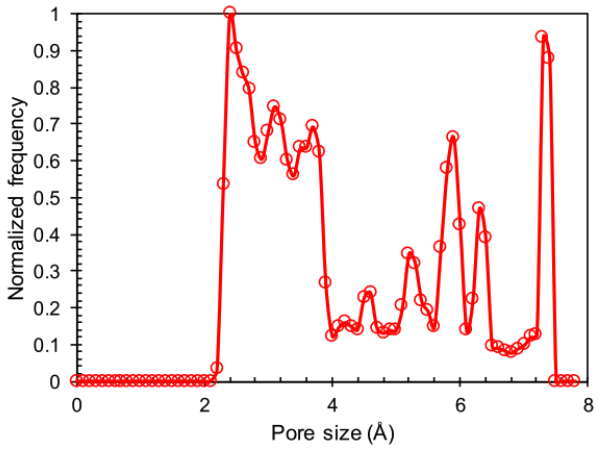

Figure 3.1 Pore size distribution of the initial kerogen matrix model.

3.2.2 GCMC-MD

Our molecular simulations were carried out in the open-source LAMMPS Molecular Dynamics

Simulator (Thompson, 2022). The hybrid GCMC-MD method was implemented to model gas adsorption in the type II-D kerogen with periodic boundary conditions in the three directions. In single-component gas simulations, the simulation box was assumed in connection with an imaginary reservoir with the specific temperature and chemical potential as described by Frenkel and Smit (2001). The chemical potentials of both CO_2 and CH_4 were previously decided as a function of pressure at 300 K by running pure gas simulations under the NVT ensemble. The gas adsorption isotherms in the kerogen could then be determined with different chemical potentials under the NPT ensemble, where the kerogen structure was free to swell and shrink. In the CO_2-CH_4 displacement simulations, the simulation box was separately connected to two individual imaginary gas reservoirs filled with either CO_2 or CH_4. The displacement of CH_4 by CO_2 was investigated by GCMC-MD simulations in the following steps. First, the kerogen matrix was saturated with CH_4 up to a pressure of 15 MPa, corresponding to the initial reservoir pressure at a shallow geological depth of 1 km. Then the CH_4 pressure was decreased to several pressure levels (0.1 MPa, 0.9 MPa, 1.8 MPa, 3.6 MPa, 5.1 MPa), mimicking the primary gas production by pressure drawdown. After the CH_4 production had ceased, CO_2 was injected into the kerogen matrix with a specific pressure (1.9 MPa, 4.3 MPa, 6 MPa, 8.7 MPa) to displace residual CH_4. The chemical potential of CH_4 was kept the same when connecting the new CO_2 imaginary reservoir. According to Ho et al. (2018b), it is assumed that the chemical potential in the binary mixture is close to its pure gas chemical potential. Hence, we did not consider the chemical potential of binary mixtures, and the gas pressure we are referring to here is the individual pressure of pure gas reservoirs.

GCMC exchanges were conducted 100 times after every 100 MD steps with a 50%/50% chance of insertion and deletion of gas molecules. Several test simulations were also run with frequencies of 500 and 1000 MD steps between GCMC exchanges and converged results were obtained. In the case of CO_2-CH_4 displacement, the 100 GCMC exchanges were equally split with respect to each imaginary gas reservoir. No extra MC moves were performed (i.e., translations and rotations) since the inserted molecules already had random locations and orientations and MD steps were used to relax the system. In this study, the NPT ensemble

pressure was always set equal to the total gas pressure. This led to the observation of the maximum swelling and shrinkage of the kerogen structure under zero effective stress (Ho et al., 2018a). In other words, the effect of mechanical compression could then be ignored, and the volumetric strain was induced by gas adsorption alone. A simulation was stopped when the number of gas molecules and the simulation box volume had reached a stable state. This usually takes a total of 4×10^6 MD timesteps and GCMC exchanges for single-component gases and $6\text{-}8 \times 10^6$ steps for the CO_2-CH_4 gas mixture.

3.2.3 Force field

The total potential energy consists of bonding and nonbonding interactions. Bonding interactions exist only within each kerogen macro-molecule and are described by the GAFF force field. Nonbonding potentials are calculated for intramolecular atom pairs separated by more than two bonds and all intermolecular interactions (i.e., kerogen-kerogen, gas-gas, kerogen-gas) according to the standard 12/6 Lennard-Jones potential with long-range Coulombic interactions. The potential energy between non-bonded particles *i* and *j* is expressed as

$$\mathrm{E}(r_{ij}) = 4\epsilon_{ij}\left[\left(\frac{\sigma_{ij}}{r_{ij}}\right)^{12} - \left(\frac{\sigma_{ij}}{r_{ij}}\right)^{6}\right] + \frac{q_i q_j}{4\pi\epsilon_0 r_{ij}} \tag{3.1}$$

where r_{ij} is the distance between the two non-bonded particles *i* and *j*, ϵ_{ij} is the depth of the Lennard-Jones potential well, σ_{ij} is the Lennard-Jones radius, q_i and q_j are the charges on the two particles, and ϵ_0 is the dielectric constant. The global cut-off distance was set as 14 Å, and interactions outside this range were calculated in K-space with the particle-particle particle-mesh (PPPM) solver (Hockney and Eastwood, 1988).

Table 3.2 provides a summary of the Lennard-Jones parameters of gas molecules used for intermolecular potential calculations. CO_2 molecules were simulated by the TraPPE force field

as rigid bodies. There were no intramolecular interactions as both bond angle (180°) and length (1.16 Å) were fixed (Potoff and Siepmann, 2001). CH_4 molecules were simulated by the TraPPE-UA force field, in which each molecule was treated as a united atom (Martin and Siepmann, 1998). Therefore, three types of gas particles (i.e., CH_4, C of CO_2, and O of CO_2) can interact with each other and with kerogen via Lennard-Jones and Coulomb forces. Pair coefficients for interactions between particles of different types were calculated by the Lorentz-Berthelot mixing rule

$$\sigma_{ij} = \frac{1}{2}\left(\sigma_{ii} + \sigma_{jj}\right) \tag{3.2}$$

$$\epsilon_{ij} = \sqrt{\epsilon_{ii}\epsilon_{jj}} \tag{3.3}$$

Within the temperature and pressure range that we are interested in, the force fields for CO_2 and CH_4 have both been verified to successfully simulate the equilibrium properties after comparing them with the Peng-Robinson equation of state (PR-EOS) (Peng and Robinson, 1976) as shown in Figure 3.2. However, discrepancies are also noticeable when the CO_2 density increases sharply (i.e., gas to liquid state) from 5 MPa to 6 MPa, which needs to be considered in the adsorption simulations.

Table 3.2 Lennard-Jones parameters of gas molecules.

Molecule	Interaction type	ϵ (Kcal/mol)	σ (Å)	q (e)
CH_4	CH_4-CH_4	0.2941	3.73	0
CO_2	C-C	0.0536	2.80	0.70
	O-O	0.1570	3.05	-0.35

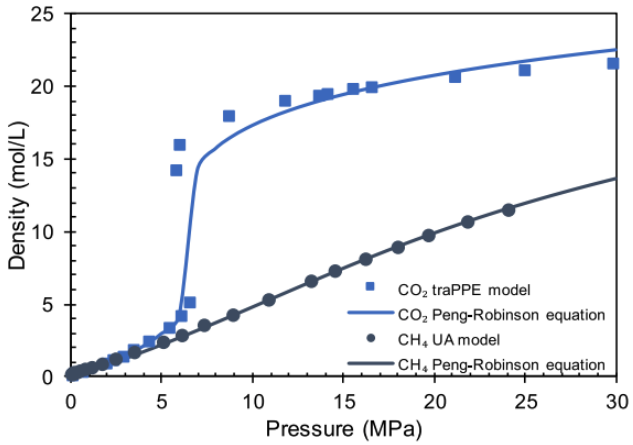

Figure 3.2 Validation of equation of state (EOS) for CO_2 TraPPE and CH_4 TraPPE-UA models at the temperature of 300 K.

3.2.4 Kerogen deformation

In the simulation, the flexible kerogen structure was allowed to swell and shrink freely due to gas adsorption and desorption. The sorption-induced kerogen deformation was quantitatively measured by volumetric strain during the gas adsorption and desorption process

$$V_\varepsilon = \frac{V - V_o}{V_o} \tag{3.4}$$

where V_o and V are the initial and final equilibrated average volume of the kerogen simulation box, respectively. In addition to the direct simulations, we derived an adsorption-strain mathematical model using the surface energy approach to provide some profound insights into the kerogen deformation as well.

Bangham's law is the first to introduce the adsorption-induced deformation being proportional to the decrease in the solid surface energy (Gor et al., 2017). Based on a series of experiments they conducted with charcoal, the linear strain ε of the adsorbent was found to be related to the change of surface free energy $\Delta\gamma$ by (Bangham and Razouk, 1938)

$$\varepsilon = \lambda\Delta\gamma \tag{3.5}$$

where λ is a constant that can be calculated according to the adsorbent properties (Maggs, 1946; Tian and Liu, 2020)

$$\lambda = \frac{\rho A}{E_s} \tag{3.6}$$

where ρ is the density of the adsorbent, A is the specific surface area per unit mass of the adsorbent, and E_s is the swelling modulus and is generally smaller than Young's modulus (Maggs, 1946). Furthermore, the Gibbs adsorption equation in terms of surface excess is expressed as (Bangham, 1937)

$$\Delta\gamma = -\Gamma d\mu = RT\int_0^p \Gamma d(\ln p) \tag{3.7}$$

where Γ is the surface excess (i.e., the adsorption amount per unit area of surface), μ is the chemical potential of the adsorbate fluid, R is the gas constant, T is the temperature, and p is the pressure of the adsorbate fluid. In the case of gas adsorption in porous media, the density of the adsorbate gas is assumed homogeneous in the bulk phase and zero within the solid. The total adsorption amount on the surface N_e (i.e., excess adsorption) is expressed as (Myers, 2002)

$$N_e = N_{ab} - V_g\rho_g \tag{3.8}$$

where N_{ab} is the total moles of gas adsorption (i.e., absolute adsorption) in the system, and V_g and ρ_g are the volume and molar density of the gas, respectively. When the adsorbent can swell during gas adsorption, assuming a marginal porosity change (i.e., constant), the excess adsorption amount per unit mass of the adsorbent can be further detailed as (Yu et al., 2021)

$$n_e = n_{ab} - \frac{\phi V_o(1+V_\varepsilon)\rho_g}{m} \tag{3.9}$$

where n_{ab} is the absolute adsorption amount per unit mass of the adsorbent, and ϕ, V_o, m are the porosity, initial volume, and mass of the adsorbent, respectively. The volumetric strain V_ε is approximated as 3ε under the assumption of isotropic deformation for the small block of kerogen matrix we are interested in here. Combining equations (3.5)-(3.7) and (3.9), the

adsorption-induced linear strain of the adsorbent is derived as

$$\varepsilon = \frac{\rho_o A}{E_s(1+3\varepsilon)} RT \int_0^p \frac{n_{ab} - \phi V_o(1+3\varepsilon)\frac{p}{mRT}}{Ap} dp$$

$$= \frac{\rho_o RT}{E_s(1+3\varepsilon)} \int_0^p \frac{n_{ab}}{p} - \frac{\phi V_o(1+3\varepsilon)}{mRT} dp \tag{3.10}$$

where ρ_o is the initial density of the adsorbent before any adsorption takes place, and the specific surface area A is assumed as a constant that is not affected by gas adsorption. For binary gas adsorption, the above Equation (3.10) is extended as

$$\varepsilon = \frac{\rho_o RT}{E_s(1+3\varepsilon)} \left(\int_0^{p_1} \frac{n_1^{ab}}{p_1} - \frac{\phi V_o(1+3\varepsilon)}{mRT} dp_1 + \int_0^{p_2} \frac{n_2^{ab}}{p_2} - \frac{\phi V_o(1+3\varepsilon)}{mRT} dp_2 \right) \tag{3.11}$$

where ε, n_1^{ab} and n_2^{ab} are dependent variables on both p_1 and p_2. Considering the complexity of solving Equation (3.11), this paper has used the single-component gas equation as an alternative assuming the total kerogen deformation is the sum of the individual effect by CO_2 and CH_4. With a fitting of the Langmuir adsorption isotherm $n_{ab} = \frac{n_L p}{p_L + p}$, an ordinary differential equation (ODE) is derived from Equation (3.10) as

$$\frac{d\varepsilon}{dp} = \frac{\rho_o RT}{E_s(1+6\varepsilon)} \left(\frac{n_L}{p_L + p} - \frac{\phi V_o(1+3\varepsilon)}{mRT} \right) \tag{3.12}$$

where n_L and p_L are the Langmuir adsorption density and Langmuir pressure, respectively. Although the pore size distribution is not explicitly considered here, it is expected to be related to the deformation as well and this effect might have been reflected indirectly from the Langmuir fitting parameters. Note that fugacity should be used instead when pressure is higher than ~3 MPa due to deviation from the ideal gas behaviour. Conclusively, the relationship between the adsorption-induced volumetric strain and gas pressure can be obtained with Equation (3.12). This adsorption-strain model can also be applied to calculate the volumetric strain from the measured gas adsorption amount.

In theory, the residing fluid pressure can also apply stress on the kerogen skeleton and cause a

volumetric strain expressed as $-p/K_s$, where K_s is the kerogen bulk modulus devoid of any cavities (Nur and Byerlee, 1971). The K_s can be measured from high-density kerogen structures (i.e., minimise the porosity). As reported by Kashinath et al. (2020), the bulk modulus of dense type II-D kerogen at a density of 1.6 g/cm^3 can reach 40 GPa at 300 K. Within our interested pressure range, the volumetric strain induced by the fluid pressure is less than 0.05%. Therefore, it is not considered in the following discussion.

3.3 Results and discussion

3.3.1 Single-component gas adsorption

The kerogen matrix was first investigated for single-component gas adsorption by either CO_2 or CH_4. The absolute adsorption isotherms were determined by averaging the total gas molecule numbers in the kerogen after the GCMC-MD simulations had reached a stable state. Langmuir adsorption isotherms can well fit the simulated adsorption data as shown in Figure 3.3a. The type II-D overmature kerogen has a much higher ability of gas adsorption compared with type II-A, II-B and II-C because of its large porosity (Huang et al., 2019b; Sui et al., 2020). Our absolute adsorption data are compared to the literature and lie within the range of other simulation results reported for type II-D kerogen. For example, the maximum absolute adsorption amount was around 6 mmol/g and 4 mmol/g for CO_2 and CH_4 at 20 MPa and 300 K in the study by Ho et al. (2018a), and 8 mmol/g and 6 mmol/g at 20 MPa and 298 K in Sui et al. (2020). The adsorption isotherm for CO_2 is always above CH_4, suggesting that more CO_2 molecules can be adsorbed in the kerogen matrix under the same pressure. This is mainly because of the higher affinity of kerogen with CO_2 than with CH_4 as the interaction energies of CO_2 and CH_4 molecules with type II-D kerogen surfaces were calculated at -6.2 kcal/mol and -4.2 kcal/mol, respectively, by MD simulation (Ho and Wang, 2021). In addition, CO_2 density becomes much higher than CH_4 after reaching the pressure of 6 MPa, contributing a significant

portion to the total gas molecules in the kerogen as the free phase. From Figure 3.3a, it is also observed that the absolute adsorption amounts for both CO_2 and CH_4 increase fast with pressure before reaching a plateau at 3 MPa, indicating the majority of available adsorption sites are filled up at the outset of gas adsorption.

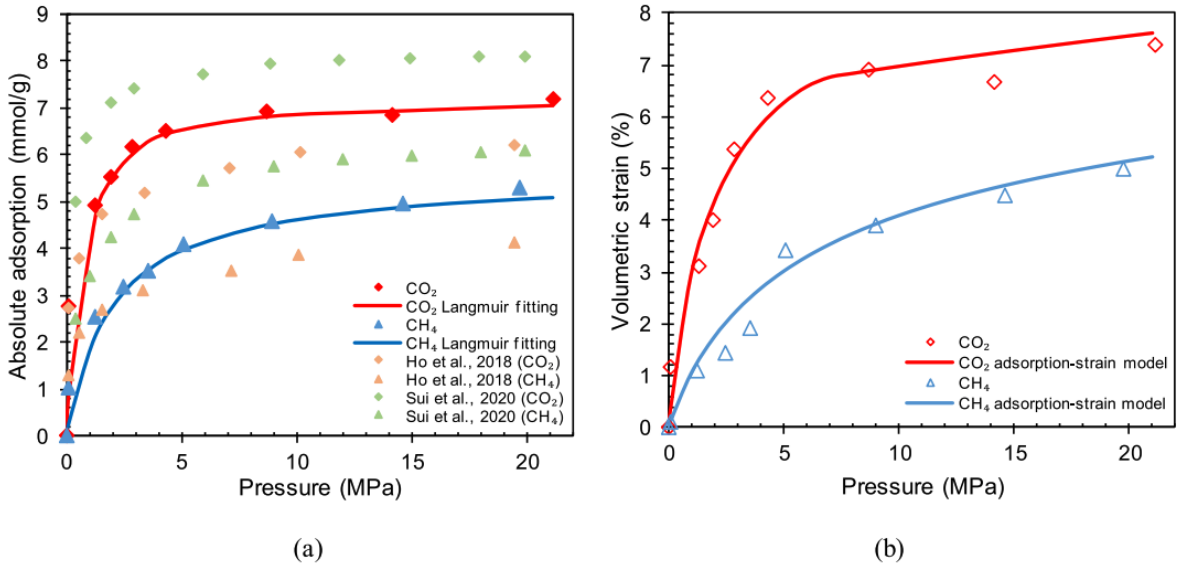

Figure 3.3 (a) Absolute adsorption isotherms for pure CO_2 and CH_4 at 300 K with Langmuir fitting curves. (b) Volumetric strain included by single-component gas adsorption (i.e., pure CO_2 or CH_4) at different pressures with solid lines showing predictions from the adsorption-strain model (the fitting parameter $E_s = 1700$ MPa is close to experimentally reported values for San Juan and Longmaxi shale samples (Tian and Liu, 2020).

The volumetric strain was also calculated from the simulation box volume after gas adsorption at each pressure level. As shown in Figure 3.3b, the volumetric strain shows a similar trend as the adsorption isotherms for CO_2 and CH_4. This result can be explained by the fact that the adsorption-induced volumetric strain is closely associated with the gas adsorption amount, as already elaborated when deriving the adsorption-strain model. The maximum strains are 7.4% and 5.1% for CO_2 and CH_4, respectively, at 20 MPa and 300 K. With the Langmuir fitting parameters obtained from the adsorption isotherms, our adsorption-strain model successfully

predicts the volumetric strain as a function of pressure during single-component gas adsorption.

3.3.2 CH_4 displacement by CO_2 injection

The CO_2-enhanced recovery of CH_4 was achieved by introducing a new imaginary GCMC gas reservoir of CO_2. The complete CO_2-CH_4 process is illustrated in Figure 3.4. There are a few reasons why CO_2 can displace CH_4 in shale (Lan et al., 2019). First and foremost, the CO_2/CH_4 adsorption selectivity is far greater than one in the kerogen matrix, such as 5-16 at 300 K in the study of Wang et al. (2018a). Shale is more likely to adsorb CO_2 when exposed to a binary mixture of CO_2 and CH_4. Because of the difference of initial CH_4 adsorption amounts before injecting CO_2, the total CH_4 recovery and the CO_2 displacement efficiency are used to evaluate the role of CO_2 in facilitating CH_4 desorption. The CH_4 recovery R_r is defined as

$$R_\mathrm{r} = \frac{n_{sat} - n_\mathrm{res}}{n_\mathrm{sat}} \tag{3.13}$$

where n_sat is the CH_4 total adsorption amount when saturated at 15 MPa, and n_res is the residual CH_4 adsorption amount after CO_2 injection. In the case of no CO_2 injection, n_p is used to represent the remaining CH_4 adsorption amount after each pressure drawdown (i.e., $R_\mathrm{r} = \frac{n_{sat} - n_\mathrm{p}}{n_\mathrm{sat}}$). Meanwhile, the CO_2 displacement efficiency R_d is defined as

$$R_\mathrm{d} = \frac{n_\mathrm{p} - n_\mathrm{res}}{n_\mathrm{p}} \tag{3.14}$$

Both R_r and R_d are calculated and summarised in Figure 3.5. As the reservoir pressure is decreased, more CH_4 is recovered from the kerogen matrix. However, the maximum CH_4 recovery can only reach as high as ~80% at 0.1 MPa reservoir pressure without the help of CO_2 injection. As can be seen clearly from Figure 3.5a, the effect of CO_2 is significant in terms of enhancing the recovery of CH_4. For example, the introduction of CO_2 at 8.7 MPa can increase the CH_4 recovery by five times from 16.7% to 83.1% when the reservoir depletion pressure is 5.1 MPa. Even the most minor CO_2 injection pressure at 1.9 MPa can increase the CH_4 recovery by four times up to 66.9%. Remarkably, almost all the CH_4 in the kerogen matrix can be

recovered by CO_2 injection when the reservoir depletion pressure is 0.1 MPa, but achieving such a low depletion pressure may be unrealistic in actual engineering practices. Based on the number of gas molecules within the kerogen matrix, it is estimated that 0.13~0.6 mmol/g CH_4 can be recovered for every 1 mmol/g CO_2 sequestrated.

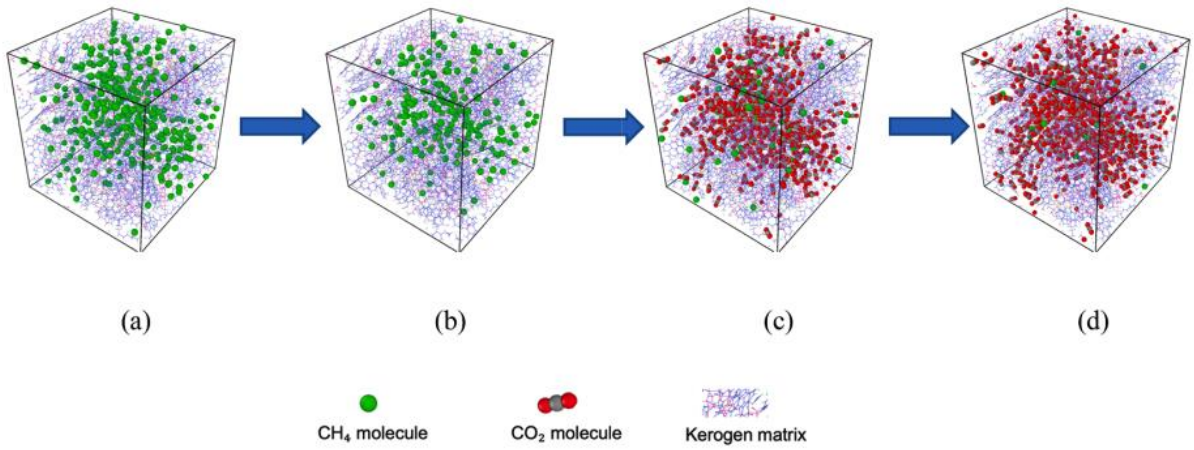

Figure 3.4 OVITO (Stukowski, 2009) visualisation of different CO_2-CH_4 displacement stages in the kerogen matrix: (a) Initial kerogen configuration saturated with CH_4 at 15 MPa; (b) After desorption by pressure drawdown to 1.8 MPa; (c) During CO_2-CH_4 displacement with P_{CO2} = 4.3 MPa; (d) Displacement completed.

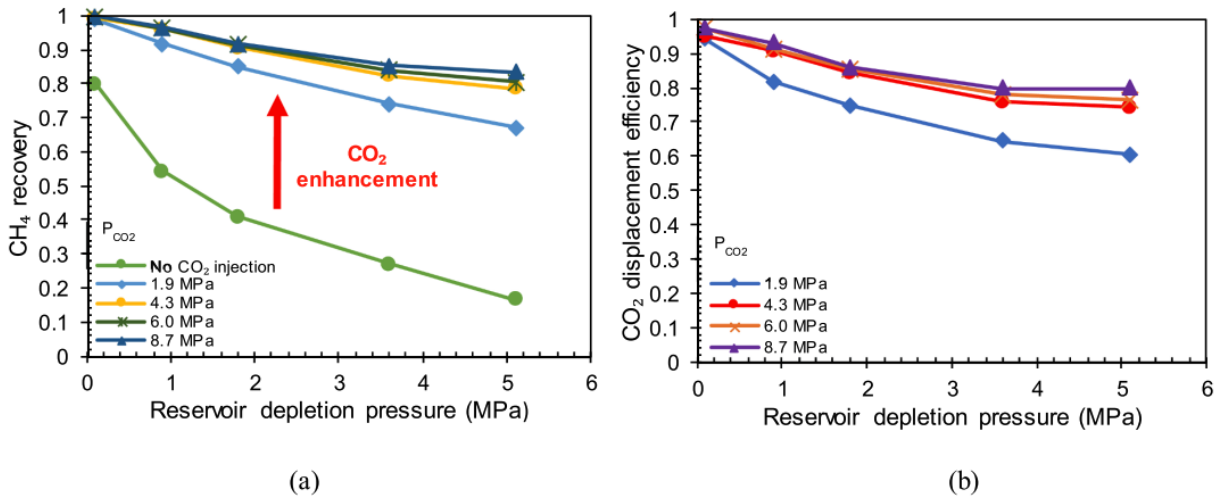

(a) (b)

Figure 3.5 (a) Comparison of CH_4 recovery by pressure drawdown and CO_2 injection at different

pressures (P_{CO2}). (b) The efficiency of CO_2 displacing CH_4 at different reservoir depletion pressures.

A comparison of various CO_2 injection pressures can be found in Figure 3.5b. It is noted that the high CO_2 injection pressure generally increases the production of CH_4. However, the rate of increase does not continue as the CO_2 injection pressure increases. For example, increasing injection pressure from 1.9 MPa to 4.3 MPa has improved the displacement efficiency by 20%, while an additional increase from 4.3 MPa to 8.7 MPa can merely raise the efficiency by 8%. Similar bottlenecks of displacement efficiency growth were reported in slit pores as well (Gong et al., 2020). This phenomenon is likely to be related to the CO_2/CH_4 selectivity which decreases gradually with the increasing total bulk gas pressure. The selectivity will remain unchanged after the total bulk gas pressure reaches a certain point (Wang et al., 2018a; Wang et al., 2016). Overall, these results suggest that an optimum CO_2 injection pressure should be considered when practising CO_2-EGR because injecting CO_2 at high pressure may not always benefit the CH_4 production as much. The cost can outweigh the gain under those circumstances.

3.3.3 CO_2 sequestration after displacement

Apart from effectively displacing residual CH_4, CO_2-EGR has the potential to become a major option for carbon capture, utilisation, and storage as well as to reduce the water usage for fracking (Middleton et al., 2015). Therefore, it is essential to study the sequestration amount of CO_2 besides the enhanced production of CH_4. The CO_2 adsorption amounts after each displacement process are summarised in Figure 3.6. As can be expected, the CO_2 injection at high pressure can lead to more CO_2 adsorption in the kerogen matrix. Comparing the final CO_2 and CH_4 amounts in the kerogen matrix, the CO_2 adsorption amount (4.21-7.61 mmol/g) is much more significant than the residual CH_4 amount (0.03-1.64 mmol/g). This significant difference results from the preferable CO_2 adsorption over CH_4, as discussed in Section 3.3.2. Likewise, a slowdown of CO_2 sequestration is observed at high CO_2 injection pressure due to the CO_2/CH_4 adsorption selectivity plateau. In addition, it can be seen that more CO_2 is

adsorbed in the kerogen matrix when the reservoir pressure is lower and there are more available adsorption sites. Interestingly, the CO_2 adsorption data collapse at the 4.3 MPa injection pressure for various reservoir depletion pressures of 1.8 MPa, 3.6 MPa, and 5.1 MPa. A possible explanation for this may be that CO_2 is experiencing a quick phase transition into liquid near 5 MPa. The CO_2-TraPPE model can not perfectly catch the sharp increase of CO_2 density (Figure 3.2), especially in the presence of another gas. Another important finding is that at the same CO_2 pressure (or chemical potential), more CO_2 is adsorbed in the kerogen matrix from the CO_2-CH_4 binary mixture compared with the pure CO_2. For example, the CO_2 adsorption amount is 7.4 mmol/g and 6.9 mmol/g for the binary mixture and pure gas, respectively, under the same CO_2 pressure at 8.7 MPa. This discrepancy may be attributed to the existence of CH_4, which opens up more pore spaces through the adsorption-induced swelling. The swelling may not be fully recoverable even after CH_4 desorption by pressure drawdown.

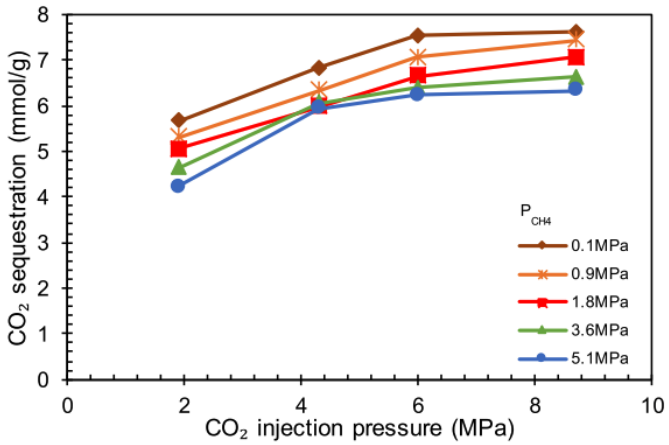

Figure 3.6 Sequestrated CO_2 adsorption amount after CO_2-CH_4 displacement subject to different reservoir depletion pressures (P_{CH4}). With a kerogen volume percentage of 27.97% and 11.09% (Pang et al., 2019b), the CO_2 storage capacity is estimated at 57.6 m^3/m^3 and 22.8 m^3/m^3 for the Barnett and Eagle Ford shales, respectively.

3.3.4 Adsorption-induced strain

The kerogen matrix has undergone different degrees of shrinkage when the initial CH_4 pressure is decreased from 15 MPa to the depletion pressure, as indicated in Table 3.3. With the injection of CO_2, the kerogen matrix quickly swells, although CH_4 is being displaced out during this process. The net increase of volume suggests that the swelling caused by CO_2 adsorption is greater than the shrinkage by CH_4 desorption. The volumetric strain is plotted as a function of CO_2 injection pressure and reservoir depletion pressure in Figure 3.7. Surprisingly, the swelling effect is so substantial that even at the lowest CO_2 injection pressure and reservoir depletion pressure, CO_2 can increase the volumetric strain from 0.6% to 4.0%, slightly below the initial volumetric strain of 5% when saturated with CH_4 at 15 MPa. It seems that the volumetric strain is proportional to the CO_2 injection pressure as high injection pressure usually results in more significant deformation of the kerogen matrix because of the higher CO_2 sequestration amount. The most considerable volumetric strain is 9.81% when the CO_2 injection pressure is at the highest 8.7 MPa. It is much larger than the highest volumetric strain that can be induced by pure CO_2 (7.4%) or CH_4 (5.1%) adsorption because of the stronger combining effect of both gases (i.e., each gas can cause swelling upon adsorption). It is worth noting that the kerogen matrix volume has exceeded above the 15 MPa CH_4 saturation baseline after CO_2 injection in almost all the presented cases. Different from the assumption of zero effective stress in this study for the purpose of observing the maximum swelling, the real-life kerogen is usually confined in the inorganic matrix of shale reservoirs and the volumetric swelling of kerogen will turn into the decrease of pore and fracture size in the inorganic matrix. Therefore, it is possible that one would expect a permeability and injectivity reduction compared to the original reservoir in the CO_2-EGR operations.

Table 3.3 Kerogen shrinkage by pressure drawdown from 15 MPa.

Reservoir depletion pressure (MPa)	0.1	0.9	1.8	3.6	5.1
Shrinkage (%)	-3.71	-3.27	-2.91	-2.06	-0.96

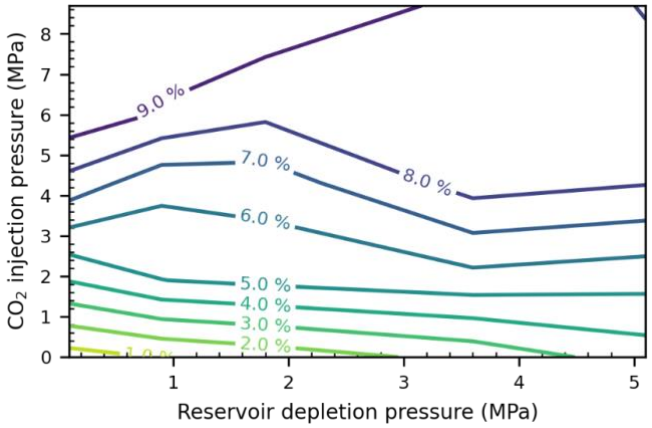

Figure 3.7 Summary of the volumetric strain of the kerogen matrix after displacement at different CO_2 injection pressures and reservoir depletion pressures.

The volumetric strain is often considered as a linear function of the total adsorption amount in the literature (Cui et al., 2007; Pang et al., 2019a; Tian and Liu, 2020; Yu et al., 2021). However, the pore volume change due to adsorption-induced strain can have a back effect on the adsorption amount, resulting in a complicated coupling relationship between each other. As can be seen from Figure 3.8, the volumetric strain increases much faster after the total gas adsorption amount reaches ~3 mmol/g in the CO_2-CH_4 displacement. The correlational analysis between the total absolute gas adsorption and volumetric strain is summarised in Figure 3.8, along with the predictions from the adsorption-strain model. For single-component gas, the volumetric strain induced by CO_2 and CH_4 follows a very similar path at low gas adsorption amount but then deviates from each other as gas adsorption increases. This inconsistency may be due to the different molecular sizes of CO_2 and CH_4 because large gas molecules are

expected to cause deformation more greatly (Tesson and Firoozabadi, 2019). Such an effect can be more pronounced when there are a large number of molecules. A similar non-linear trend between the volumetric strain and the total gas sorption was reported by Ho et al. (2018a), where a quadratic function was used to fit the data ($y = ax^2 + bx + c$) by assuming the volume expansion is proportional to the square of adsorbed gas amount. The same fitting method is adopted and $y = 0.2136x^2 - 0.6865x + 1.4278$ (R^2 = 0.99) and $y = 0.1991x^2 - 0.0667x - 0.0715$ (R^2 = 0.98) are obtained to fit our data for CO_2 and CH_4, respectively. This suggests a simple quadratic function can provide a good approximation for the sorption-induced strain, but the fitting parameters are expected to depend on properties such as kerogen porosity and gas type. In comparison, our proposed adsorption-strain model is derived with physical meaning and can estimate kerogen deformation from its adsorption isotherm.

For the CO_2-CH_4 binary mixture, the relationship between volumetric strain and total gas adsorption is similar to pure CO_2. Those data points are scattered between the CO_2 and CH_4 curves. This result may be explained by the fact that CO_2 adsorption consists over 70% of the total gas adsorption amount after CO_2-CH_4 displacement. With the non-linear function between volumetric strain and total gas adsorption for pure CO_2 and CH_4, the volumetric strain induced by their binary mixture can be estimated as a weighted sum $x_{CH_4}V_\varepsilon^{CH_4} + x_{CO_2}V_\varepsilon^{CO_2}$ according to the final adsorption compositions *x*. The strain approximations calculated from the model are compared with the simulations, and this simplified approach is shown to provide a reasonable estimation of the final volumetric strain induced by the CO_2-CH_4 binary gas mixture with R^2 = 0.94.

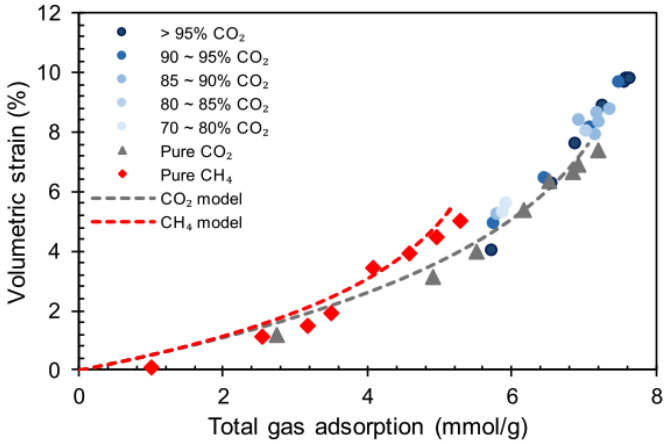

Figure 3.8 Volumetric strain of kerogen as a function of total adsorption amount under single-component gas and binary gas mixture. Dotted lines show predictions from the adsorption-strain model.

3.3.5 Implications for CO_2-EGR

This work suggests that both CO_2 injection pressure and reservoir depletion pressure are important factors affecting the final recovery of CH_4. CO_2 injection can probably achieve better performance after the reservoir pressure drops to a certain level because both CH_4 recovery and CO_2 displacement efficiency are found to be negatively correlated with the reservoir depletion pressure. Although a high percentage of CH_4 recovery is generally accomplished under high CO_2 injection pressure, the CH_4 recovery eventually stabilises with the continuously rising CO_2 injection pressure. That being said, super high CO_2 injection pressure may have limited improvement on the recovery compared with low CO_2 injection pressure. Therefore, it is crucial to decide the optimum pressure conditions for CO_2-EGR before operations so that the benefits are maximised.

Shale reservoirs have extremely low permeability, in the range of 0.0001-0.001 Md (NRC, 2019). Volumetric matrix swelling induced by gas adsorption can further significantly reduce the shale permeability by narrowing the size of pores and fractures where gas flow occurs (Wu et al., 2017; Zhao et al., 2019; Zhou et al., 2020). For example, Zhao et al. (2019) reported that

the intrinsic permeability of the shale core sample decreased threefold from 9.66×10^{-19} m^2 to 3.24×10^{-19} m^2 as the CH_4 adsorption pressure increased from 0.76 MPa to 6.79 MPa. This work suggests that swelling induced by CO_2 sequestration is likely to surpass shrinkage by CH_4 desorption after CO_2-CH_4 displacement. The net volumetric strain can even become drastically higher than the original CH_4-saturated reservoir. In the presence of the binary gas mixture, the maximum strain is 9.8%, greater than 7.4% and 5.1% for the single-component CO_2 and CH_4 in the type II-D overmature kerogen at a temperature of 300 K. Consequently, a stepwise decrease in CO_2 injectivity and CH_4 production rate is expected when practising CO_2-EGR. Future reservoir models should also pay attention to the dynamic evolution of shale permeability in the assessments of CO_2-EGR since it can significantly change gas transport behaviours.

3.4 Conclusions

The hybrid GCMC-MD method was applied to study the CO_2-CH_4 displacement and the adsorption-induced deformation in the type II-D overmature kerogen. A non-linear adsorption–strain relationship was derived according to the change of surface free energy and compared with the simulation results. Main simulation results are summarised below

- In single-component gas adsorption, the maximum strain is 7.4% and 5.1% for CO_2 and CH_4 at ~20 MPa and 300 K, corresponding to the absolute adsorption of 7.20 mmol/g and 5.29 mmol/g, respectively.
- CO_2 injection can greatly enhance the residual CH_4 recovery after pressure drawdown, up to five times from 16.7% to 83.1%. The displacement efficiency increases with the CO_2 injection pressure but decreases with the increasing reservoir depletion pressure.
- After displacement, the kerogen matrix contains over 70% of CO_2 under the studied conditions. High CO_2 injection pressure and low reservoir pressure promote CO_2

sequestration. The maximum CO_2 sequestration amount is 7.61 mmol/g at 8.7 MPa injection pressure.

- The swelling by CO_2 adsorption far outweighs the shrinkage by CH_4 desorption during displacement. The net volumetric strain can be much higher than the original CH_4-saturated reservoir. The maximum strain is 9.8% when the CO_2 injection pressure is 8.7 MPa, greater than that induced by single-component CO_2 or CH_4.
- Absolute gas adsorption has a non-linear relationship with volumetric strain. The derived mathematical equation can accurately capture the observed non-linearity and provide reasonable predictions for the volumetric strain after CO_2-CH_4 displacement.

Acknowledgments

This work was supported in part by the Australian Research Council through Discovery Projects (DP200101919 and DP190102954). The authors acknowledge the use of the National Computational Infrastructure (NCI) which is supported by the Australian Government, and accessed through the Sydney Informatics Hub HPC Allocation Scheme, which is supported by the Deputy Vice-Chancellor (Research), University of Sydney and the ARC LIEF, 2019: Smith, Muller, Thornber et al., Sustaining and strengthening merit-based access to National Computational Infrastructure (LE190100021).

References

1. Alfarge, D., Wei, M., & Bai, B. (2017). Feasibility of CO_2-EOR in shale-oil reservoirs: Numerical simulation study and pilot tests. *Carbon Management Technology Conference*, CMTC-485111-MS.

2. Alfarge, D., Wei, M., & Bai, B. (2020). Developments in petroleum science. *Elsevier, 67*,

1-13.

3. Ao, X., Lu, Y., Tang, J., Chen, Y., & Li, H. (2017). Investigation on the physics structure and chemical properties of the shale treated by supercritical CO_2. *Journal of CO_2 Utilisation, 20*, 274-281.

4. Bangham, D. (1937). The Gibbs adsorption equation and adsorption on solids. *Transactions of the Faraday Society, 33*, 805-811.

5. Bangham, D., & Razouk, u. R. (1938). The saturation and immersion expansions and the heat of wetting. *Proceedings of the Royal Society of London. Series A. Mathematical and Physical Sciences, 166*(927), 572-586.

6. Bhattacharya, S., & Gubbins, K. E. (2006). Fast method for computing pore size distributions of model materials. *Langmuir, 22*(18), 7726-7731.

7. Brochard, L., Vandamme, M., & Pellenq, R. J. M. (2012b). Poromechanics of microporous media. *Journal of the Mechanics and Physics of Solids, 60*(4), 606-622.

8. Brochard, L., Vandamme, M., Pellenq, R. J., & Fen-Chong, T. (2012a). Adsorption-induced deformation of microporous materials: Coal swelling induced by CO_2-CH_4 competitive adsorption. *Langmuir, 28*(5), 2659-2670.

9. Case, D.A., Ben-Shalom, I.Y., Brozell, S.R., Cerutti, D.S., Cheatham III, T.E., Cruzeiro, V.W.D., Darden, T.A., Duke, R.E., Ghoreishi, D., Giambasu, G., Giese, T., Gilson, M.K., Gohlke, H., Goetz, A.W., Greene, D., Harris, R., Homeyer, N., Huang, Y., Izadi, S., Kovalenko, A., Krasny, R., Kurtzman, T., Lee, T.S., LeGrand, S., Li, P., Lin, C., Liu, J., Luchko, T., Luo, R., Man, V., Mermelstein, D.J., Merz, K.M., Miao, Y., Monard, G., Nguyen, C., Nguyen, H., Onufriev, A., Pan, F., Qi, R., Roe, D.R., Roitberg, A., Sagui, C., Schott-Verdugo, S., Shen, J., Simmerling, C.L., Smith, J., Swails, J., Walker, R.C., Wang, J., Wei, H., Wilson, L., Wolf, R.M., Wu, X., Xiao, L., Xiong, Y., York, D.M., & Kollman, P.A. (2019). AMBER 2019. *University of California, San Francisco*.

10. Chong, L., Sanguinito, S., Goodman, A. L., & Myshakin, E. M. (2021). Molecular characterisation of carbon dioxide, methane, and water adsorption in micropore space of kerogen matrix. *Fuel, 283*, 119254.

11. Cui, X., Bustin, R. M., & Chikatamarla, L. (2007). Adsorption-induced coal swelling and stress: Implications for methane production and acid gas sequestration into coal seams. *Journal of Geophysical Research, 112,* B10202.

12. Du, X., Gu, M., Liu, Z., Zhao, Y., Sun, F., & Wu, T. (2019). Enhanced shale gas recovery by the injections of CO_2, N_2, and CO_2/N_2 mixture gases. *Energy & Fuels, 33*(6), 5091-5101.

13. EIA (2020). https://www.eia.gov/naturalgas/annual/.

14. Fathi, E., & Akkutlu, I. Y. (2014). Multi-component gas transport and adsorption effects during CO_2 injection and enhanced shale gas recovery. *International Journal of Coal Geology, 123*, 52-61.

15. Frenkel, D., & Smit, B. (2001). Understanding molecular simulation: From algorithms to applications. *Elsevier*.

16. Frisch, M. J., Trucks, G. W., Schlegel, H. B., Scuseria, G. E., Robb, M. A., Cheeseman, J. R., . . . Fox, D. J. (2016). Gaussian 16 Rev. C.01. Wallingford, CT.

17. Gelb, L. D., & Gubbins, K. (1999). Pore size distributions in porous glasses: A computer simulation study. *Langmuir, 15*(2), 305-308.

18. Gong, L., Zhang, Y., Li, N., Gu, Z.-K., Ding, B., & Zhu, C.-Y. (2020). Molecular investigation on the displacement characteristics of CH_4 by CO_2, N_2 and their mixture in a composite shale model. *Energies, 14*(1), 2.

19. Gor, G. Y., Huber, P., & Bernstein, N. (2017). Adsorption-induced deformation of nanoporous materials – A review. *Applied Physics Reviews, 4*(1), 011303.

20. Herrera, L., Do, D. D., & Nicholson, D. (2010). A Monte Carlo integration method to determine accessible volume, accessible surface area and its fractal dimension. *Journal of*

Colloid and Interface Science, 348(2), 529-536.

21. Ho, T. A., & Wang, Y. (2021). Molecular origin of wettability alteration of subsurface porous media upon gas pressure variations. *ACS Applied Materials & Interfaces, 13*(34), 41330-41338.

22. Ho, T. A., Criscenti, L. J., & Wang, Y. (2016). Nanostructural control of methane release in kerogen and its implications to wellbore production decline. *Scientifc Report, 6*, 28053.

23. Ho, T. A., Wang, Y., & Criscenti, L. J. (2018a). Chemo-mechanical coupling in kerogen gas adsorption/desorption. *Physical Chemistry Chemical Physics, 20*(18), 12390-12395.

24. Ho, T. A., Wang, Y., Xiong, Y., & Criscenti, L. J. (2018b). Differential retention and release of CO_2 and CH_4 in kerogen nanopores: Implications for gas extraction and carbon sequestration. *Fuel, 220*, 1-7.

25. Hockney, R. W., & Eastwood, J. W. (1988). Computer simulation using particles. *CRC Press*.

26. Huang, J., Jin, T., Barrufet, M., & Killough, J. (2020). Evaluation of CO_2 injection into shale gas reservoirs considering dispersed distribution of kerogen. *Applied Energy, 260*, 114285.

27. Huang, L., Ning, Z., Wang, Q., Qi, R., Cheng, Z., Wu, X., . . . Qin, H. (2019a). Kerogen deformation upon CO_2/CH_4 competitive sorption: Implications for CO_2 sequestration and enhanced CH_4 recovery. *Journal of Petroleum Science and Engineering, 183*, 106460.

28. Huang, L., Ning, Z., Wang, Q., Qi, R., Cheng, Z., Wu, X., . . . Qin, H. (2019b). Molecular insights into kerogen deformation induced by CO_2/CH_4 sorption: Effect of maturity and moisture. *Energy & Fuels, 33*(6), 4792-4805.

29. Huang, L., Ning, Z., Wang, Q., Zhang, W., Cheng, Z., Wu, X., & Qin, H. (2018). Effect of organic type and moisture on CO_2/CH_4 competitive adsorption in kerogen with implications for CO_2 sequestration and enhanced CH_4 recovery. *Applied Energy, 210*, 28-43.

30. Iddphonce, R., Wang, J., & Zhao, L. (2020). Review of CO_2 injection techniques for enhanced shale gas recovery: Prospect and challenges. *Journal of Natural Gas Science and Engineering, 77*, 103240.

31. Karagöz, Y., Balcı, Ö., Gezer, O., Köten, H., & Işın, Ö. (2021). Performance and emissions of spark-ignition engines fuelled with petrol and methane. *Proceedings of the Institution of Civil Engineers-Energy*, *174*(4), 156-169.

32. Kashinath, A., Szulczewski, M., & Dogru, A. H. (2020). Modelling the effect of maturity on the elastic moduli of kerogen using atomistic simulations. *Energy & Fuels, 34*(2), 1378-1385.

33. Lan, Y., Yang, Z., Wang, P., Yan, Y., Zhang, L., & Ran, J. (2019). A review of microscopic seepage mechanism for shale gas extracted by supercritical CO_2 flooding. *Fuel, 238*, 412-424.

34. Li, J., Wang, Y., Chen, Z., & Rahman, S. S. (2021). Insights into the molecular competitive adsorption mechanism of CH_4/CO_2 in a kerogen matrix in the presence of moisture, salinity, and ethane. *Langmuir*, *37*(43), 12732-12745.

35. Li, Y., Wang, J., Wang, Z., & Pan, Z. (2020). Variation in permeability during CO_2-CH_4 displacement in coal seams. Part 2: Modelling and simulation. *ACS omega*, *5*(29), 18432-18440.

36. Li, Y., Wang, Y., Wang, J., & Pan, Z. (2020). Variation in permeability during CO_2-CH_4 displacement in coal seams: Part 1 – Experimental insights. *Fuel*, *263*, 116666.

37. Liu, J., Yao, Y., Liu, D., & Elsworth, D. (2017). Experimental evaluation of CO_2 enhanced recovery of adsorbed-gas from shale. *International Journal of Coal Geology, 179*, 211-218.

38. Louk, K., Ripepi, N., Luxbacher, K., Gilliland, E., Tang, X., Keles, C., . . . Michael, K. (2017). Monitoring CO_2 storage and enhanced gas recovery in unconventional shale reservoirs: Results from the Morgan County, Tennessee injection test. *Journal of Natural*

Gas Science and Engineering, 45, 11-25.

39. Maggs, F. (1946). The adsorption-swelling of several carbonaceous solids. *Transactions of the Faraday Society, 42*, B284-B288.

40. Martin, M. G., & Siepmann, J. I. (1998). Transferable potentials for phase equilibria. 1. United-atom description of n-alkanes. *The Journal of Physical Chemistry B, 102*(14), 2569-2577.

41. Michalec, L., & Lísal, M. (2017). Molecular simulation of shale gas adsorption onto overmature type II model kerogen with control microporosity. *Molecular Physics, 115*(9-12), 1086-1103.

42. Middleton, R. S., Carey, J. W., Currier, R. P., Hyman, J. D., Kang, Q., Karra, S., . . . Viswanathan, H. S. (2015). Shale gas and non-aqueous fracturing fluids: Opportunities and challenges for supercritical CO_2. *Applied Energy, 147*, 500-509.

43. Myers, A. (2002). Thermodynamics of adsorption in porous materials. *AIChE Journal, 48*(1), 145-160.

44. Neil, C. W., Mehana, M., Hjelm, R. P., Hawley, M. E., Watkins, E. B., Mao, Y., . . . Xu, H. (2020). Reduced methane recovery at high pressure due to methane trapping in shale nanopores. *Communications Earth & Environment, 1*(1), 49.

45. NRC. (2019). https://www.nrcan.gc.ca/energy/sources/shale-tight-resources/17675.

46. Nur, A., & Byerlee, J. D. (1971). An exact effective stress law for elastic deformation of rock with fluids. *Journal of Geophysical Research, 76*(26), 6414-6419.

47. Pang, Y., He, Y., & Chen, S. (2019a). An innovative method to characterise sorption-induced kerogen swelling in organic-rich shales. *Fuel, 254*, 115629.

48. Pang, Y., Tian, Y., Soliman, M. Y., & Shen, Y. (2019b). Experimental measurement and analytical estimation of methane absorption in shale kerogen. *Fuel, 240*, 192-205.

49. Peng, D.-Y., & Robinson, D. B. (1976). A new two-constant equation of state. *Industrial & Engineering Chemistry Fundamentals, 15*(1), 59-64.

50. Potoff, J. J., & Siepmann, J. I. (2001). Vapour-liquid equilibria of mixtures containing alkanes, carbon dioxide, and nitrogen. *AIChE Journal, 47*(7), 1676-1682.

51. Sharma, R. K., & Chopra, S. (2013). Conventional approach for characterising unconventional reservoirs. *CSEG RECORDER, 38*, 34-38.

52. Shi, J., Gong, L., Sun, S., Huang, Z., Ding, B., & Yao, J. (2019). Competitive adsorption phenomenon in shale gas displacement processes. *RSC Advances, 9*(44), 25326-25335.

53. Shirts, M. R., Klein, C., Swails, J. M., Yin, J., Gilson, M. K., Mobley, D. L., . . . Zhong, E. D. (2017). Lessons learned from comparing molecular dynamics engines on the SAMPL5 dataset. *Journal of Computer-aided Molecular Design, 31*(1), 147-161.

54. Speight, J. G. (2013). Shale gas production processes. *Gulf Professional Publishing*.

55. Stukowski, A. (2009). Visualisation and analysis of atomistic simulation data with OVITO – the Open Visualisation Tool. *Modelling and Simulation in Materials Science and Engineering, 18*(1), 015012.

56. Sui, H., Zhang, F., Wang, Z., Wang, D., & Wang, Y. (2020). Effect of kerogen maturity, water content for carbon dioxide, methane, and their mixture adsorption and diffusion in kerogen: A Computational Investigation. *Langmuir, 36*(33), 9756-9769.

57. Sun, H., Zhao, H., Qi, N., & Li, Y. (2017). Molecular insights into the enhanced shale gas recovery by carbon dioxide in kerogen slit nanopores. *The Journal of Physical Chemistry C, 121*(18), 10233-10241.

58. Sun, H., Zhao, H., Qi, N., Qi, X., Zhang, K., Sun, W., & Li, Y. (2016). Mechanistic insight into the displacement of CH_4 by CO_2 in calcite slit nanopores: The effect of competitive adsorption. *RSC Advances, 6*(106), 104456-104462.

59. Sun, Q., Liu, W., & Zhang, N. (2021). Molecular insights into recovery of shale gas by CO_2

injection in kerogen slit nanopores. *Journal of Natural Gas Science and Engineering*, *90*, 103903.

60. Tesson, S., & Firoozabadi, A. (2019). Deformation and swelling of kerogen matrix in light hydrocarbons and carbon dioxide. *The Journal of Physical Chemistry C, 123*(48), 29173-29183.

61. Thompson, A. P., Aktulga, H. M., Berger, R., Bolintineanu, D. S., Brown, W. M., Crozier, P. S., ... & Plimpton, S. J. (2022). LAMMPS-a flexible simulation tool for particle-based materials modelling at the atomic, meso, and continuum scales. *Computer Physics Communications*, *271*, 108171.

62. Tian, W., & Liu, H. (2020). Insight into the adsorption of methane on gas shales and the induced shale swelling. *ACS Omega, 5*(49), 31508-31517.

63. Ungerer, P., Collell, J., & Yiannourakou, M. (2014). Molecular modelling of the volumetric and thermodynamic properties of kerogen: Influence of organic type and maturity. *Energy & Fuels, 29*(1), 91-105.

64. Vasileiadis, M., Peristeras, L. D., Papavasileiou, K. D., & Economou, I. G. (2017). Modelling of bulk kerogen porosity: Methods for control and characterisation. *Energy & Fuels, 31*(6), 6004-6018.

65. Wang, J., Ryan, D., & Anthony, E. J. (2011). Reducing the greenhouse gas footprint of shale gas. *Energy Policy*, *39*(12), 8196-8199.

66. Wang, J., Wang, W., Kollman, P. A., & Case, D. A. (2006). Automatic atom type and bond type perception in molecular mechanical calculations. *Journal of Molecular Graphics and Modelling, 25*(2), 247-260.

67. Wang, J., Wolf, R. M., Caldwell, J. W., Kollman, P. A., & Case, D. A. (2004). Development and testing of a general amber force field. *Journal of Computational Chemistry, 25*(9), 1157-1174.

68. Wang, T., Tian, S., Li, G., & Sheng, M. (2018a). Selective adsorption of supercritical carbon dioxide and methane binary mixture in shale kerogen nanopores. *Journal of Natural Gas Science and Engineering, 50*, 181-188.

69. Wang, T., Tian, S., Li, G., Sheng, M., Ren, W., Liu, Q., & Zhang, S. (2018b). Molecular simulation of CO_2/CH_4 competitive adsorption on shale kerogen for CO_2 sequestration and enhanced gas recovery. *The Journal of Physical Chemistry C, 122*(30), 17009-17018.

70. Wang, X., Zhai, Z., Jin, X., Wu, S., Li, J., Sun, L., & Liu, X. (2016). Molecular simulation of CO_2/CH_4 competitive adsorption in organic matter pores in shale under certain geological conditions. *Petroleum Exploration and Development, 43*(5), 841-848.

71. Wu, W., Zoback, M. D., & Kohli, A. H. (2017). The impacts of effective stress and CO_2 sorption on the matrix permeability of shale reservoir rocks. *Fuel, 203*, 179-186.

72. Yu, X., Li, J., Chen, Z., Wu, K., Zhang, L., Yang, S., . . . Yang, M. (2021). Determination of CH_4, C_2H_6 and CO_2 adsorption in shale kerogens coupling sorption-induced swelling. *Chemical Engineering Journal, 410*, 127690.

73. Yuan, Q., Zhu, X., Lin, K., & Zhao, Y. P. (2015). Molecular dynamics simulations of the enhanced recovery of confined methane with carbon dioxide. *Physical Chemistry Chemical Physics, 17*(47), 31887-31893.

74. Zendehboudi, S., & Bahadori, A. (2016). Shale oil and gas handbook: Theory, technologies, and challenges. *Gulf Professional Publishing*.

75. Zhang, H., & Cao, D. (2016). Molecular simulation of displacement of shale gas by carbon dioxide at different geological depths. *Chemical Engineering Science, 156*, 121-127.

76. Zhang, H., Diao, R., Mostofi, M., & Evans, B. (2019). Monte Carlo simulation of the adsorption and displacement of CH_4 by CO_2 injection in shale organic carbon slit micropores for CO_2 enhanced shale gas recovery. *Energy & Fuels, 34*(1), 150-163.

77. Zhao, Y., Wang, C., Zhang, Y., & Liu, Q. (2019). Experimental study of adsorption effects

on shale permeability. *Natural Resources Research, 28*(4), 1575-1586.

78. Zhou, J., Tian, S., Zhou, L., Xian, X., Yang, K., Jiang, Y., . . . Guo, Y. (2020). Experimental investigation on the influence of sub- and super-critical CO_2 saturation time on the permeability of fractured shale. *Energy, 191*, 116574.

Chapter 4 Effect of sorption-induced deformation on methane flow in kerogen slit pores

Although sorption-induced swelling greatly reduces shale permeability by narrowing pore size, it is rarely considered in nanoscale gas transport studies. During CO_2-EGR, the desorption of methane and adsorption of CO_2 lead to a dynamic evolution of gas permeability, which affects CO_2 injectivity and methane production and plays a vital role in accurate reservoir modelling. Chapter 4 addresses the effect of sorption-induced deformation on nanoscale gas transport by comparing methane flow in a kerogen slit pore ranging from 1-4 nm with rigid and flexible pore walls (i.e., non-deformable and deformable upon gas adsorption). Consistent with previous studies, nanoscale gas transport is enhanced under strong confinement, consisting of contributions from viscous flow and various modes of diffusion. As kerogen swelling increases with the gas uptake in the matrix, the mass flux reduction through the slit pore is analysed as a function of gas pressure and validated against a theoretical model incorporating swelling-induced pore size change. The apparent gas permeability ratio is also calculated between the rigid and flexible kerogen slit pores, which strongly correlates with gas pressure and pore size. This chapter aims to derive a mathematical expression based on MD results to describe gas transport in nano-confined kerogen slit pores considering the sorption-induced swelling, which can be potentially extended and incorporated into continuum models to improve accuracy in simulating CO_2-EGR. This chapter is presented in the form of a manuscript that has been published in *Fuel*:

Wu, J., Huang, P., Maggi, F., & Shen, L. (2022). Effect of sorption-induced deformation on methane flow in kerogen slit pores. *Fuel, 325*, 124886.

The PhD candidate has performed all the numerical work and the analysis of the results, and is the primary author of the above article.

Effect of sorption-induced deformation on methane flow in kerogen slit pores

Jian Wu, Pengyu Huang, Federico Maggi, Luming Shen*

School of Civil Engineering, The University of Sydney, NSW 2006, Australia

*Corresponding author. Email: luming.shen@sydney.edu.au

Abstract

Shale gas production relies on the movement of methane through nanopores which are characterised by extra-low permeability in shale formations. However, there is a lack of understanding on methane transport in realistic organic nanopores, especially in relation to sorption-induced swelling. Here, using Monte Carlo and molecular dynamics simulations, the effect of kerogen deformation on gas transport is investigated by comparing the flow rate differences in slit pores with rigid (non-deformable) and flexible (deformable) kerogen matrices, constructed from 27 type II-D kerogen units. Simulation results show that sorption-induced swelling reduces methane mass flux significantly in large slit pores (20-40 Å) as pressure increases. By incorporating kerogen deformation into a diffusive-viscous gas flow model, it is concluded that the observed mass flux decrease is likely attributed to the narrowing pore size which mainly suppresses the viscous flux component. Further calculations suggest that kerogen swelling may decrease the apparent permeability of the slit pore by up to ~40% within pore pressure of 50 MPa. Additional findings show that diffusion can enhance the maximum gas velocity in the slit pores threefold compared with the Hagen-Poiseuille equation when pore pressure is ~2 MPa, and the diffusion and the viscous flow dominate the total mass flux when $Kn > 10$ and $Kn < 0.1$, respectively.

4.1 Introduction

In recent decades, shale gas has played an increasingly significant role in the global energy sector due to the abundant reserve and fast-developing extraction technologies (Alfarge et al., 2020; Speight, 2013; Zendehboudi and Bahadori, 2016). As a form of natural gases, shale gas is generated from living organisms buried in the deep subsurface by pressure and heat (Zendehboudi and Bahadori, 2016). It is one of the cleanest and most efficient sources of energy (EIA, 2021), with the potential to reduce greenhouse gas emissions over the long term (Wang et al., 2011). Large-scale natural gas production from shale began in the early 2000s in the United States (EIA, 2022). The US Energy Information Administration (EIA) predicts that shale gas will occupy 46% of the total energy production in the country by 2035 (Stevens, 2012).

The porosity of shale formations is generally lower than 10% (Speight, 2013). It has the lowest permeability of about 0.0001 mD among all conventional and unconventional reservoirs (Rahim et al., 2012). In order to characterise shale's pore structure in detail, a variety of methods, such as scanning electron microscopy, small-angle/ultrasmall-angle neutron scattering, mercury intrusion porosimetry, and low-pressure adsorption experiments, have been implemented by researchers (Yu et al., 2020c). Loucks et al. (2009) reported that the Barnett shale was characterised by a wide range of pore sizes from as small as 5 nm. Based on the analysis of Bakken shale samples, Liu et al. (2017) demonstrated the coexistence of micropores (< 2 nm), mesopores (2-50 nm), and macropores (> 50 nm). However, they found that micropores and mesopores composed the majority of shale's porosity.

The tight confinement of fluids and interactions between solids and fluids can change the fluid's physical properties and transport in nanoscale pores (Bao and Zhao, 2021; Salahshoor et al., 2018; Sun et al., 2020). The conventional continuum theory (i.e., Hagen-Poiseuille equation) breaks down for nanoscale gas transport due to high slip velocity at pore walls and various forms of gas diffusion (Behrang et al., 2016; Liu et al., 2021; Sun et al., 2020; Yu et al.,

2020d). The Knudsen number (Kn) describes the competition between gas-gas and gas-wall molecular collisions (i.e., the ratio of the molecular mean free path to the characteristic pore length) and is often used to distinguish different flow regimes, namely, molecular free flow ($Kn > 10$), transitional flow ($0.1 < Kn < 10$), slip flow ($0.001 < Kn < 0.1$), and viscous flow ($Kn < 0.001$) (Javadpour et al., 2007; Wu et al., 2016). The Klinkenberg correction captures the gas-wall interaction and recovers the slip velocity when gas-gas interaction can be ignored (i.e., slip flow regime) (Bravo, 2007).

Gas transport in shale nanopores is mostly studied with molecular simulations, proven to be a powerful tool in revealing the underlying mechanisms (Wang et al., 2020). Several approaches are applicable to perturb the molecular system for flow generation, such as molecular dynamics (MD) (Fang et al., 2019; Yan et al., 2017), dual control-volume grand canonical Monte Carlo (DCV-GCMC) (Jin, 2017; Sun et al., 2019), boundary-driven non-equilibrium molecular dynamics (BD-NEMD) (Collell et al., 2015; Wu and Firoozabadi, 2019), and non-equilibrium molecular dynamics (NEMD) (Yu et al., 2018; Nan et al., 2020; Wang et al., 2017; Zhan et al., 2021; Yu et al., 2020a; Ho et al; 2018b). Yu et al. (2018) simulated methane flow in a calcite slit pore (2-10 nm) under pressure from 0.5 to 50 MPa. They argued that the transport characteristic of methane in slit nanopores was mainly dependent on pressure, with pore size significantly affecting the individual flux contribution from viscous flow, Knudsen diffusion, and surface diffusion. Nan et al. (2020) investigated the effect of nanopore size (2-20 nm) and pressure (10-60 MPa) on the gas slippage in a three-layered graphene slit pore, indicating that the slip length decreased with the increase of both pressure and pore size hyperbolically. Interestingly, Wang et al. (2017) and Zhan et al. (2021) observed that methane slippage only occurred in the organic (graphene) nanopores and disappeared in the inorganic (quartz, calcite, and montmorillonite) nanopores. By measuring the potential energy surface (PES) map of both organic and inorganic walls, Yu et al. (2020a) argued that the absence of slippage was ascribed to the large PES fluctuation of inorganic walls. In other words, the molecule-wall interaction forces were inhomogeneously distributed at those inorganic surfaces. It is important to note that the aforementioned solid models are all idealised with a perfectly organised lattice

structure and smooth surfaces, which may not be good representations of many actual nanofluidic systems (Ho et al., 2018b). As Castez et al. (2017) suggested, the flow enhancement over Hagen-Poiseuille flow could be mainly due to the surface smoothness that promoted the mobility of gas adsorption layers. Therefore, further studies should be performed on shale with realistic and deformable amorphous pore structures.

Since several kerogen units of different organic types and maturities were built from the elemental and functional group analysis by Ungerer et al. (2014), shale gas molecular simulations have been greatly encouraged in applications of adsorption and swelling (Chong et al., 2021; Ho et al., 2018a; Huang et al., 2018; Tesson and Firoozabadi, 2019; Wu et al., 2022; Yu et al., 2021), diffusion (Sui et al., 2020; Tesson and Firoozabadi, 2018), and fluid transport (Sun et al., 2020; Wu and Firoozabadi, 2019; Yu et al., 2020d). Based on the kerogen units, Sun et al. (2020) studied methane's density distribution and transport capacity in a kerogen-based circular nanopore (1-8.1 nm), suggesting that the average gas density confined in nanopores was 1.2 to 2.6 times of its bulk density and the conventional B-K model (Beskok and Karniadakis, 1999) underestimated the mass flux by 41-88%. In contrast, Yu et al. (2020d) observed parabolic velocity profiles with no slippage in a kerogen slit pore under a wide range of reservoir conditions, including pressure drop of 0.25-1 MPa, pore size of 2-8 nm, pore pressure of 5-50 MPa, and temperature of 300-390 K. They found that the no-slip continuum model could still provide accurate predictions for the simulated velocities, possibly related to the atomic-scale roughness and heterogenous potential energy of kerogen surfaces. Their additional results showed that gas velocity in organic nanopores declined dramatically with surface roughness increase and quickly reached no-slip condition when the relative roughness factor (i.e., the ratio of the maximum fluctuating height of surface atoms to the pore size) was as small as 2.5% (Yu et al., 2020b).

Similar to many nanoporous organic matter (Gor et al., 2017), kerogen will swell or shrink subject to gas adsorption and desorption, respectively. The sorption-induced deformation is likely more sensitive in shale considering its ultra-low permeability (Lyu et al., 2021).

According to the results from core flooding experiments, CH_4-induced swelling decreased shale's permeability threefold with adsorption pressure increased from 0.76 to 6.79 MPa (Zhao et al., 2019), and CO_2 injection even more significantly reduced the permeability by one order of magnitude (Ao et al., 2017; Zhou et al., 2020). This deformation could also cause variation of CO_2-injectivity during CO_2-CH_4 displacement (Hamza et al., 2021; Li et al., 2020). These experimental studies have the limitation of giving us insights into the underlying pore-scale mechanisms of the permeability change. MD simulations, however, can overcome this limitation and present us the detailed fluid-solid interactions at nanoscale which are not accessible from core-scale experiments. With MD and GCMC simulations, the deformation induced by gas adsorption has been quantified in the kerogen matrix as a function of pressure, which varies according to kerogen type and maturity (Huang et al., 2019). The typical kerogen matrix swelling resulting from CH_4 adsorption is 2-5% (Chong et al., 2021; Ho et al., 2018a; Wu et al., 2022; Yu et al., 2021). In addition, the flexibility of the kerogen matrix is closely associated with higher gas adsorption and pore structure alteration (Ho et al., 2018a; Obliger et al., 2018; Tesson and Firoozabadi, 2018). These aspects may lead to different gas transport regimes in the non-rigid kerogen nanopores when performing molecular simulations. For instance, Wu and Firoozabadi (2019) discovered that gas transport through a flexible kerogen matrix was partially blocked since adsorption narrowed the main flow path under nano-confinement.

As kerogen deformation and gas flow are usually studied separately, it remains challenging to understand their coupling relationship. Therefore, a molecular study combining these two behaviours is needed to reveal the underlying mechanisms of sorption-induced deformation on gas flow at nanoscale, including changes of pore size and morphology as well as transport properties. In this study, we first constructed a series of kerogen slit pores with sizes of 10 to 40 Å within the kerogen matrix. Subsequently, GCMC and EMD simulations were performed to achieve different pore pressures in the slit pores with rigid and flexible kerogen structures depending on whether deformation is allowed. Furthermore, the pressure-driven methane flow was simulated by NEMD in the rigid and flexible kerogen slit pores to identify the effect of

sorption-induced deformation. The total gas flux and apparent gas permeability were calculated and analysed against pore pressure and pore size. Lastly, a diffusive-viscous gas flow model was developed by incorporating the newly developed adsorption-strain relationship to gain insights into the reduced gas flux in the deformable kerogen nanopores.

4.2 Computational methods

4.2.1 Construction of kerogen slit pores

The kerogen matrix (45.24 Å × 45.61 Å × 48.61 Å), composed of 27 type II-D kerogen units ($C_{175}H_{102}O_9N_4S_2$) (Ungerer et al., 2014) was chosen as the starting structure to build the kerogen slit pores in this study. A large dummy particle of 20 Å was first used to generate some relatively large pores within the matrix. Consequently, the relaxed final structure has a density of 1.106 g/cm^3 and a porosity of 14.9%. The general AMBER force field (GAFF) was used with the 12/6 Lennard-Jones potential to describe the intramolecular and intermolecular interactions (Wang et al., 2004). The detailed process of building the kerogen matrix from molecular units can be found in our previous paper (Wu et al., 2022). In order to construct the slit pores, the simulation box was first extended to 100 Å in the *z*-direction. Then, a wall of dummy particles (σ = 1 Å) was emplaced at one end of the simulation box. All the atoms were translated to bring the wall of dummy particles to the middle of the simulation box, leading to the separation of the two kerogen matrix pieces as shown in Figure 4.1a. A subsequent simulation in the NVT and NPT (P controlled only in the *z*-direction) ensembles was performed with a timestep of 1 fs for 2000 ps to minimise the total energy and gradually bring the system to 300 K and 1 atm (Figure 4.1b, detailed relaxation procedure provided in Table 4.S1). The final simulation box has a size of 45.24 Å × 45.61 Å × 45.31 Å. Finally, the wall of dummy particles was removed so that the desired pore size could be successfully set up with artificially flattened surfaces (Figure 4.1c). The kerogen slit pore can be further relaxed to produce rough

surfaces (Figure 4.1d). The procedure to create kerogen slit pores from a kerogen matrix was based on Tesson and Firoozabadi (2018).

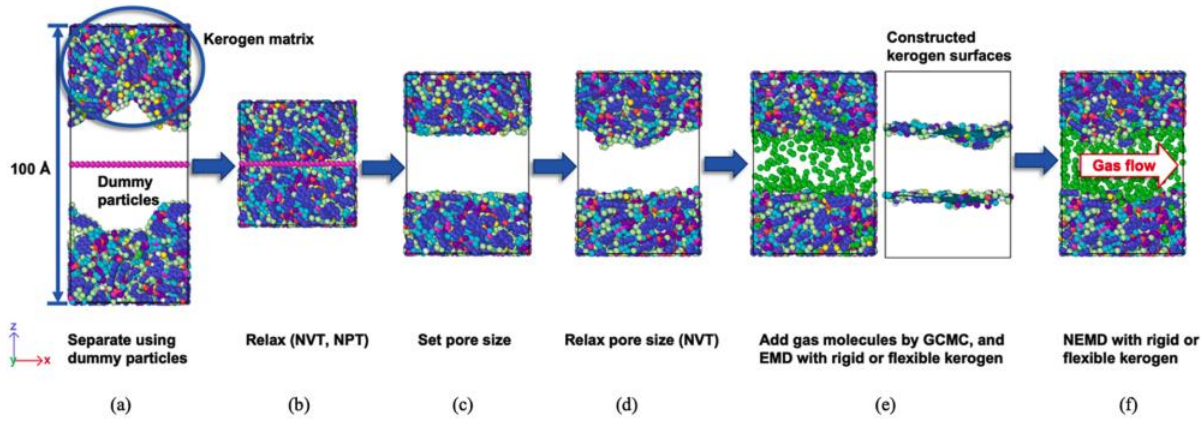

Figure 4.1 Illustration of constructing a kerogen slit pore and flow simulations with rigid and flexible kerogen slit pores.

4.2.2 Methane flow in kerogen slit pores

The methane molecules were added into the simulation box by GCMC to achieve the initial gas pressure (Figure 4.1e). Each methane molecule was treated as a united atom by the TraPPE-UA force field (Potoff and Siepmann, 2001). A total of 100,000 trials were conducted with a half-half chance of random insertion and deletion of gas molecules to ensure convergence. The resulting configuration after GCMC was further relaxed in the NVT ensemble (T = 300 K) for 5 ns with a timestep of 1 fs to ensure the complete equilibrium of methane in the kerogen matrix and slit pore (Figure 4.1e), which is the so-called EMD simulation. The kerogen matrix was set either rigid or flexible in the EMD stage, according to whether the kerogen atoms were frozen in place or could update their locations during time integration. In the flexible kerogen simulations, the kerogen atoms were able to respond to gas pressure and sorption-induced stress. However, their overall linear and angular momentums were removed so that the macroscopic position of the kerogen matrix remained unchanged. In the last 2.5 ns of the production run, the equilibrated gas pressure was calculated from per-atom stresses (x- and y-direction) in the

pore centre to minimise the effect from interaction forces between gas molecules and kerogen walls. The density profile was measured from gas molecule counts in the *z*-direction using the spatial binning method, where the simulation box was divided into several one-dimensional slabs (0.5-1 Å). To identify the slit pore boundaries, the alpha-shaped algorithm (Stukowski, 2014) was employed in OVITO (Stukowski, 2009) after EMD to construct a surface representation formed by a few kerogen atoms at each side of the slit pore (Figure 4.1e). The coordinates of these kerogen wall atoms were then extracted and assigned into the upper and lower groups. The upper and lower boundaries were defined by averaging the *z*-coordinates (i.e., the centre of mass location) of the wall atoms belonging to each group. Additionally, the calculated boundary locations were translated towards the inner-pore direction for 4 Å in consideration of the kerogen atomic sizes, which is about twice the van der Waals radius of a carbon atom (Batsanov, 2001).

The NEMD simulation was subsequently conducted (Figure 4.1f) with a force of 0.001 kcal/(mol·A) applied on each methane molecule in the *x*-direction within the slit pore to mimic the gas flow under a specific pressure gradient (Sun et al., 2020)

$$\nabla P = \frac{nF}{AL} \tag{4.1}$$

where n is the number of gas molecules in the slit pore, F is the force applied on each gas molecule, A is the cross-section area of the slit pore, and L is the slit pore length in the flow direction. The simulation was run in the NVT ensemble at 300 K for 25-30 ns with a timestep of 1 fs. In the beginning, gas molecules were accelerated to overcome the thermal velocity. After the gas flow had reached a stable state, the last 12 to 15 ns were used for sampling and velocity profile calculations with a sampling frequency of 10-100 fs. Methane molecules in the slit pore region were assigned to multiple chunks along the *z*-direction. The per-atom (i.e., CH_4 molecule) velocities were reduced as a collective average for each chunk (i.e., chunk velocity), which could be subsequently time-averaged to produce the final velocity profile across the slit pore. Note that the atom velocity in the *x*-direction was excluded from the temperature calculation and the Nosé-Hoover thermostat. Nonbonding potentials were calculated by the

standard 12/6 Lennard-Jones potential with long-range Coulombic interactions. Pair coefficients σ and ϵ for interactions between the particles of different types were calculated by the Lorentz-Berthelot mixing rule as the arithmetic and geometric means, respectively (essential coefficients provided in Table 4.S2). All the simulations were carried out by the large-scale open-source LAMMPS Molecular Dynamics Simulator (Thompson et al., 2021). As summarised in Table 4.1, two different schemes were implemented in the simulations with either the rigid or flexible kerogen structure. The flexible kerogen matrix swells upon gas adsorption, narrowing the slit pore in between. This is expected to result in a lower mass flux compared to the rigid matrix due to shrinkage of the gas flow channel. Therefore, we can identify the effect of sorption-induced deformation on gas flow by comparing their difference.

Table 4.1 Schemes for the kerogen structure during EMD and NEMD simulations.

Scheme	Kerogen surface	Kerogen flexibility	Sorption-induced swelling?
Sc1	Rough	Flexible	Yes
Sc2	Rough	Rigid	No

4.3 Results and discussion

4.3.1 Adsorption in kerogen slit pores

To identity the difference of gas transport due to sorption-induced kerogen swelling, a series of simulations have been performed at different pressures (2-50 MPa) and pore sizes (10-40 Å) with either the rigid or flexible kerogen matrix. It covers a wide range of Knudsen numbers from 0.03 to 3. The pressure range also represents reservoir conditions in different production stages. The absolute adsorption amount calculated from the number of methane molecules inside the rigid and flexible kerogen matrix follows a Langmuir isotherm trend and plateau at high pressure as the kerogen matrix becomes saturated with methane molecules (Figure 4.2).

The response of adsorption on deformation and pressure were analysed using a combination of ANOVA and linear regression. Results show that pressure positively impacts gas adsorption ($p < 2e\text{-}16$) and there is strong evidence that rigid kerogen matrix has a negative effect on the impact of pressure ($p = 0.00463$). Similar to previous studies (Ho et al., 2018a; Wu and Firoozabadi, 2019), we found that the flexible kerogen matrix manifests a stronger gas adsorption ability by ~1.5 times compared with the rigid one. This is because gas molecules can impose tensile stress along the circumference of the pore upon adsorption, resulting in the overall expansion of the kerogen matrix when given flexibility (Ho et al., 2018a). The change of the kerogen matrix will further create more pore spaces for gas adsorption inside the matrix. Moreover, the evolution of the flexible kerogen structure can facilitate gas flow into those isolated pores and lead to more active diffusion (Wu and Firoozabadi, 2019).

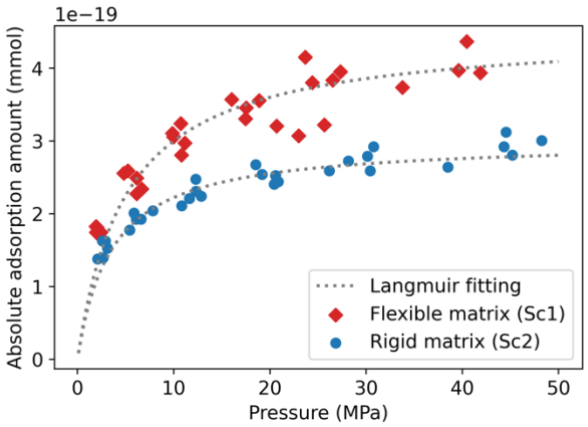

Figure 4.2 Adsorption isotherms in the rigid and flexible kerogen matrix.

Gas pressure and density are important factors affecting the mass flow capacity in the slit pores. Their dependence on each other is also used for the purpose of model validation as done in earlier works (Sun et al., 2020; Yu et al., 2018). After the EMD simulations, the bulk gas pressure and density are measured in the centre of the slit pore (5-10 Å) to minimise the influence from the kerogen walls. However, it is difficult to identify a bulk gas region from the density profile in the narrow slit pores below 15 Å due to the short distance and strong influence

from the upper and lower kerogen walls. Therefore, only the bulk gas density data of slit pores larger than 15 Å are presented in Figure 4.3 and compared with the US National Institute of Standards and Technology (NIST) data at 300 K (Linstrom and Mallard, 2022). Although the nanoscale confinement and surface adsorption near the kerogen walls can strongly affect the pressure-density relationship in the slit pore, it can be seen that the EMD simulation results in the bulk region are still consistent with the conventional EOS with minor deviations. Furthermore, it is found that the equilibrium pore pressure after EMD is generally higher when the kerogen matrix is set rigid than flexible even though they have comparable total amount of gas molecules in the system after GCMC. This is likely due to the fact that the flexible kerogen matrix swells upon gas adsorption, and thus more gas molecules can enter the kerogen matrix with fewer of them left in the slit pore.

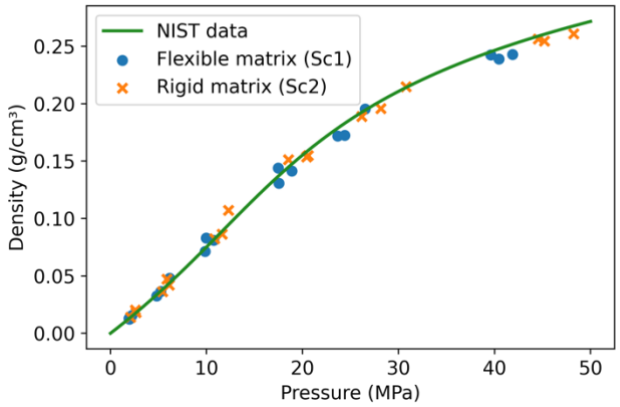

Figure 4.3 Comparison between EMD-simulated bulk density at pore centre and NIST data (Linstrom and Mallard, 2022).

4.3.2 Kerogen deformation and pore size reduction

During the EMD simulations, gas diffuses inside the kerogen matrix and slit pore until a new equilibrium is reached. The flexible kerogen matrix swells due to adsorption while the slit pore is compressed in size. Under the constant volume condition, the volume decrease of the slit

pore must be equal to the volume increase of the kerogen matrix (Cui et al., 2018). Considering one half of the kerogen matrix-slit system as shown in Figure 4.4a, the decrease of the slit pore size due to sorption-induced swelling may be expressed as (Wang et al., 2012)

$$\Delta H_s = SV_\varepsilon \tag{4.2}$$

where S is the kerogen matrix size normal to the slit pore length and V_ε is the sorption-induced volumetric strain. Our previous study has simulated the volumetric strain of the type II-D kerogen matrix induced by methane adsorption. It is shown that the volumetric strain can be estimated from the gas adsorption isotherms following the relationship (Wu et al., 2022)

$$\frac{dV_\varepsilon}{dP} = \frac{3\rho_o RT}{E_s(1+2V_\varepsilon)}\left[\frac{n_L}{P_L+P} - \frac{\phi V_o(1+V_\varepsilon)}{mRT}\right] \tag{4.3}$$

where R is the ideal gas constant, T is the temperature, P is the gas pressure, m, V_o and ρ_o are the mass, initial volume, and initial density of the adsorbing matrix, E_s is the swelling modulus, ϕ is the porosity, and n_L and P_L are the Langmuir adsorption density and pressure, respectively. On the other hand, the pore pressure in the slit pore also leads to the increase of pore size through mechanical compression of the kerogen matrix. Assuming that gas pressure has diffused uniformly between the kerogen matrix and the slit pore, the pore size change induced by mechanical expansion is expressed as (Wang et al., 2012)

$$\Delta H_p = \frac{(\alpha_f - \alpha_m)}{(1 + K_f S/K_s)}\frac{SP}{K_s} \tag{4.4}$$

where α_f and α_m are the Biot coefficients of the slit pore and matrix, respectively, K_f is the slit pore stiffness, K_s is the bulk modulus of the matrix. In summary, the pore size change is a competing process between swelling and poromechanical responses, and controls the gas transport rate in the slit pore. In the present study, however, ΔH_p (< 0.07 Å) is assumed to be negligible compared with the value of ΔH_s (~1.5 Å) with $\alpha_f = 1, \alpha_m = 0.7$ and $K_s = 5$ GPa (Kashinath et al., 2020; Wang et al., 2012) in the pressure range of 50 MPa. Thus, the size of the deformed kerogen slit pore can be simply calculated as

$$H' = H - 2\Delta H_s = H - 2SV_\varepsilon \tag{4.5}$$

As described in Section 4.2.2, the slit pore size after EMD with gas molecules is calculated from a few extracted surface atoms and compared with the initial pore size that has no gas in place. In Figure 4.4b, the change of slit pore size subject to kerogen matrix swelling is plotted as a function of pore pressure. Within the pressure range of 50 MPa, the swelling of the kerogen matrix can reach 6.6% as per Equation (4.3) and reduce the slit pore size by 3 Å. As the slit pore size decrease is closely related to the swelling of the kerogen matrix, the slit pore size change is sharp in the beginning but slows down with the increase of pressure when the maximum swelling is approached. The prediction line roughly passes through the average slit pore size data measured from the EMD simulations. Since the kerogen matrix structure is fully flexible, the surface atoms can move randomly in any direction during swelling and form different geometries, which likely causes the large deviations of measured pore size from case to case. The kerogen physical properties and fitting parameters (E_s, n_L and P_L) used for calculations are given in Table 4.2.

Table 4.2 Kerogen physical properties and fitting parameters in the calculations of kerogen slit pore size.

m (g)	ρ_o (g/cm^3)	V_o (Å^3)	ϕ (%)	S (Å)	E_s (GPa)	n_L (mmol/g)	P_L (MPa)
1.109×10^{-19}	1.106	100315	14.9	22.65	1.7	5.8	2.1

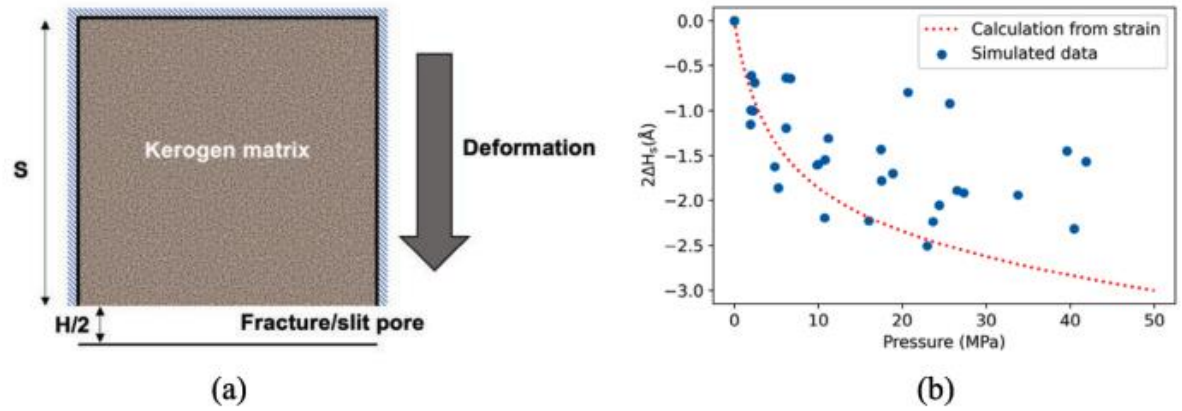

Figure 4.4 (a) A schematic drawing of kerogen matrix deformation. (b) The evolution of pore size change $2\Delta H_s$ calculated from Equations (4.2) and (4.3) as a function of pore pressure.

4.3.3 Gas velocity and density profiles in kerogen slit pores

Methane flow in the kerogen slit pore is studied against a variety of slit pore sizes and pressures. The velocity profile is obtained from the continuous sampling average after the gas flow has reached a stable state. The calculated velocities are normalised by the pressure drop across the slit pore ($\nabla P = 0.022$ MPa/Å) in all the simulated cases. The scaling method is applicable as gas velocity is found to be linearly related to pressure drop (Figure 4.S1). As shown in Figures 4.5a and 4.5c, gas velocity decreases with the increase of pore pressure. The maximum velocity drops fast at low gas pressure, for example, by over twice from ~2 to ~5 MPa in the slit pore of size 40 Å. Such velocity difference gradually becomes smaller and smaller as pressure increases. To measure the deviation of nanoscale gas velocity from what predicted by the conventional theory, the velocity data are fitted with a parabolic function $az^2 + bz + c$, from which the maximum velocity can be retrieved and divided by that calculated from the Hagen-Poiseuille equation ($V_{max} = \frac{H^2 \nabla P}{8\mu}$) at different pore sizes and pressure (Figure 4.6). At ~2 MPa, the simulated results are much greater than calculations from the continuum model due to the additional diffusion effect, with a ratio up to 3. As pressure increases, the ratio reduces fast and

approaches unity when pressure exceeds ~5 MPa. The turning point is close to methane's critical pressure of 4.6 MPa at 300 K, where it changes from vapour to supercritical phase. It is observed that the ratio goes slightly below one occasionally, which may be attributed to the overestimation of the slit pore size (i.e., *H* in the Hagen-Poiseuille equation) calculated from the alpha-shaped method.

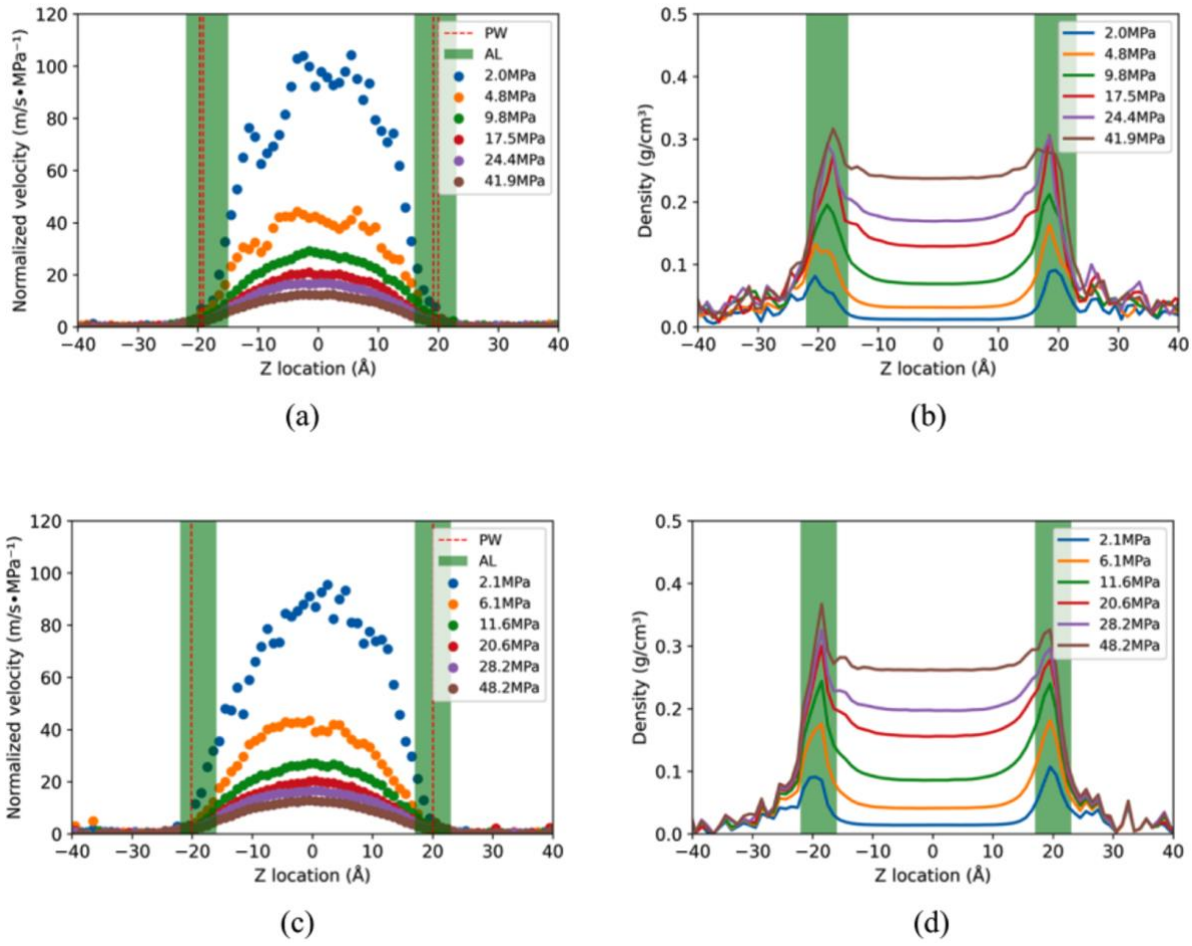

Figure 4.5 Normalised transport velocity profiles and density distributions of methane molecules in (a-b) flexible (Sc1) and (c-d) rigid (Sc2) slit nanopores of 40 Å under different pore pressures. The red dashed lines show the pore walls (PW) determined from the alpha-shaped method and the green shades represent the adsorption layers (AL) determined from the density peaks in the adsorption profiles.

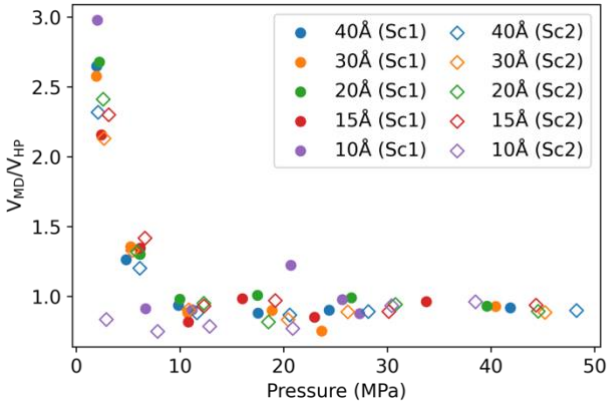

Figure 4.6 The ratio of the MD-simulated maximum velocity V_{MD} to the calculated by the Hagen-Poiseuille equation V_{HP} at different pore pressure.

Surprisingly, the velocity profiles demonstrate a parabolic shape without apparent slippage at both sides of the slit pore in the studied pressure range regardless of the rigid or flexible condition. Although slip velocities are not entirely zero at the pore walls, this is still quite different from the common observation that velocity profiles are plug-shaped along with a high slip velocity under nanoscale confinement and small gas pressure (Nan et al., 2020; Sun et al., 2020). This result may be explained by the fact that the kerogen surface can exert strong interaction forces on those methane molecules. It is reported that the interaction energy of methane molecules with the kerogen surface is much higher than with some other commonly-seen mineral surfaces, such as pyrophyllite, gibbsite, and montmorillonite (Ho and Wang, 2021). Note that gas slippage is absent in montmorillonite slit pores, as reported in several studies (Wang et al., 2017; Yu et al., 2020a). Using a single methane probing molecule, the interaction energy map is calculated at a distance of 3 Å (the equilibrium distance between methane and type II-D kerogen (Ho and Wang, 2021)) from the flat kerogen surface (Figure 4.1c) across a randomly picked area of 20 Å × 20 Å. The interaction energy is quite inhomogeneous and lies in the range of -0.3 to -2.7 kcal/mol (Figure 4.S2). Such large fluctuation of interaction energy can significantly diminish the slip velocity at the pore walls (Yu et al., 2020a; Yu et al., 2020d). In addition, several studies have shown that slip velocity is

extremely sensitive to atomic-scale roughness (Castez et al., 2017; Yu et al., 2020b). In this study, the kerogen surface's root-mean-square (RMS) roughness is estimated at 1-2.5 Å. This is clearly different from the majority of studies of shale gas transport in organic pores, where large slip velocity is observed in ideally smooth slit pores consisting of regular lattice structure and monoatomic surface layers (e.g., graphene sheets) with RMS roughness being exactly zero.

The gas distribution also affects the mass flow capacity in the slit pore. As shown in Figures 4.5b and 4.5d, gas adsorption peaks are observed near the kerogen pore surfaces. Gas velocity decreases continuously inside this adsorption layer. The velocity enhancement by gas diffusion, however, is not particularly observed here. The reason may be that methane's self-diffusion is not constant across the slit pore. The higher gas density causes more frequent molecule-wall collisions, especially with the rough surface, resulting in decreased methane mobility near the wall (Chen et al., 2017). Specifically, the self-diffusion coefficient can decrease by two orders of magnitude from the slit pore centre to the matrix (Tesson and Firoozabadi, 2018). By comparing Sc1 and Sc2, kerogen deformation does not show an obvious influence on the pattern of gas velocity and density profiles. Therefore, mass fluxes are further quantified in the rigid and flexible kerogen slit pores to reveal the effect of deformation in the next section.

4.3.4 Effect of deformation on mass flux

Gas transport characteristics in nanopores are determined by the intermolecular collision among gas molecules as well as the gas-wall interaction (Cai et al., 2019; Yu et al., 2018). They usually coexist during gas transport so that the total gas mass flux in the kerogen slit pore can be approximated as the sum of viscous flow and gas diffusion (Cai et al., 2019; Geng et al., 2016; Shen et al., 2017; Zhang et al., 2015). In the NEMD simulations, the total mass flux can be calculated from the integration of the density and velocity profiles in the x-direction (ρ_{MD} and v_x)

$$J_{MD} = \int \rho_{MD} v_x dA \tag{4.6}$$

Mathematically, the viscous flux is calculated from the Hagen-Poiseuille equation

$$J_v = \rho y \int_0^H v_x dz = \rho y \int_0^H \frac{1}{2\mu} \frac{dP}{dx} (Hz - z^2)\, dz$$

$$= \frac{\rho y H^3}{12\mu} \frac{dP}{dx} \tag{4.7}$$

where *y* is the slit pore thickness perpendicular to the flow direction, μ is the bulk gas viscosity, and dP/dx is the pressure gradient. Gas diffusion in nanopores is highly dependent on the Knudsen number, defined as the ratio of the molecular mean free path (λ) to the characteristic pore length (L) (Javadpour et al., 2007)

$$Kn = \frac{\lambda}{L} = \frac{k_B T}{\sqrt{2}\pi d^2 PH} \tag{4.8}$$

where k_B is the Boltzmann constant, and d is the diameter of gas molecule. Consequently, three different diffusion regimes can be defined including Knudsen diffusion (Kn > 10), transition diffusion (0.1 < Kn < 10), and Fick's diffusion (Kn < 0.1) (Cai et al., 2019). Knudsen diffusion is derived from frequent gas-wall collisions in small pores. Fick's diffusion is activated under a mass concentration gradient in large pores due to gas-gas collisions. Transitional diffusion is a mixed-mode of collision that lies between Knudsen diffusion and Fick's diffusion. By considering a combined collision frequency of a gas molecule with another molecule and with the pore wall, the transition diffusion coefficient may be expressed as (Cai et al., 2019; Pollard and Present, 1948)

$$D_t = \frac{1}{Kn + 1} D_F = \frac{Kn}{Kn + 1} D_k \tag{4.9}$$

where D_F is the Fick's diffusion coefficient, and D_k is the Knudsen diffusion coefficient. D_t is a function of Kn and it approaches D_F and D_k as $Kn \rightarrow 0.1$ and $Kn \rightarrow 10$, respectively. The detailed expressions of D_F and D_k are given as follows (Cai et al., 2019)

$$D_F = \frac{k_B T}{3\sqrt{2}\pi d^2 P}\sqrt{\frac{8RT}{\pi M}} \tag{4.10}$$

$$D_k = \frac{H}{3}\sqrt{\frac{8RT}{\pi M}} \tag{4.11}$$

where M is the gas molar mass. In conjunction with the compact definition of D_t, the diffusion flux can be calculated irrespective of the diffusion regime

$$J_d = -AD_t\frac{dC}{dx} = yH\frac{D_t M}{RT}\frac{dP}{dx} \tag{4.12}$$

where dC/dx is the mass concentration gradient of gas and is converted to the pressure gradient by ideal gas law. The mass flux contribution from surface diffusion is assumed negligible compared with the total mass flux. Therefore, the total gas mass flux is expressed as

$$J_t = J_v + J_d = \frac{\rho y H^3}{12\mu}\frac{dP}{dx} + yH\frac{D_t M}{RT}\frac{dP}{dx} \tag{4.13}$$

The total mass flux J_t is calculated for a broad range of gas pressures and pore sizes in Figure 4.7a by taking the kerogen deformation into consideration. It shows a nonmonotonic trend with pressure and tends to stabilise at ~20 MPa. The calculated results are in good agreement with the NEMD simulations from Sc1. The Kolmogorov-Smirnov test has been performed to confirm the normality of the residuals between observations and predictions (D = 0.14, p = 0.56). The total mass flux in the flexible kerogen slit pores (Sc1) is generally less than that in the rigid kerogen slit pores (Sc2) because of the sorption-induced pore size decrease. The absolute difference is more pronounced when the initial slit pore size is relatively large. To further shed light on the underlying mechanisms of kerogen deformation on methane transport, the viscous flux and the diffusion flux are plotted separately as a function of pressure by Equations (4.7) and (4.12) with and without coupling deformation. In Figure 4.7b, the viscous flux and the diffusion flux demonstrate opposite trends with the increasing gas pressure. The diffusion flux greatly contributes to the total flux at low gas pressure but becomes less and less significant as pressure further increases. The deformation of the kerogen slit pore has a

negligible effect on the diffusion flux. Instead, it mainly affects the viscous flux that is proportional to the cubic of pore size. The reduction of the viscous flux due to kerogen swelling increases with both increasing gas pressure and pore size.

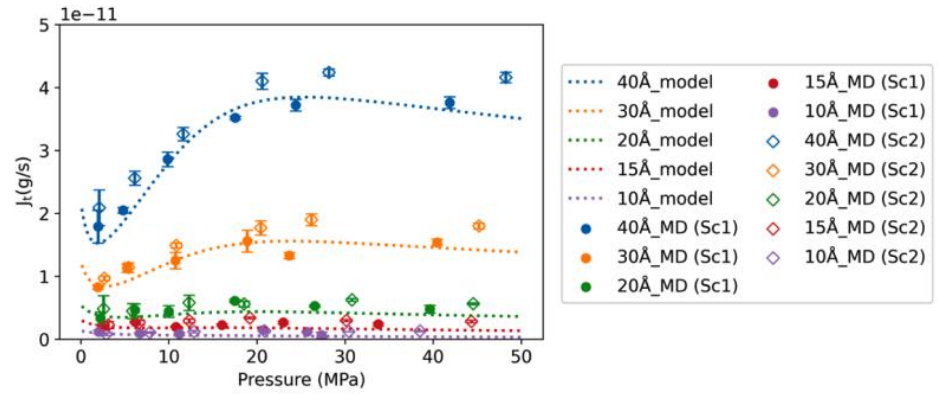

(a)

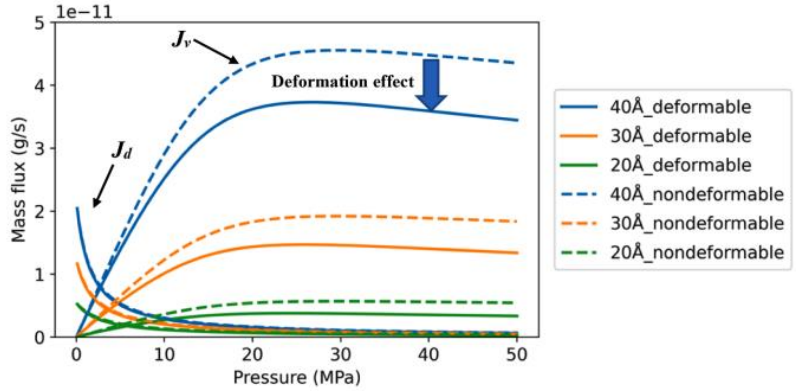

(b)

Figure 4.7 (a) The total mass flux J_t obtained from the NEMD simulations and the proposed theoretical model. Error bars are calculated as the standard deviation for each data point based on three sampling intervals divided from the production timesteps. (b) Comparison of the viscous flux J_v (increasing curves) and the diffusion flux J_d (reducing curves) calculated from the theoretical model with and without coupling kerogen deformation.

The calculated ratio of the diffusion flux to the total mass flux is analysed against the Knudsen number as summarised in Figure 4.8. When the Knudsen number is greater than one, this ratio does not show a noticeable difference for various pore sizes, and the diffusion flux contributes

over 60% of the total mass flux. As *Kn* further increases to 10 and above (i.e., Knudsen diffusion region), the diffusion flux entirely dominates (J_d/J_t approaches one) the total mass flux while the contribution of the viscous flux becomes marginal. On the contrary, the diffusion flux is negligible when *Kn* is smaller than 0.1 in the Fick's diffusion region, and the total mass flux can be estimated with the viscous flux alone at this time. If the pore is small enough (e.g., smaller than 10 Å), *Kn* may never reach the Fick's diffusion region, and the diffusion flux will always contribute a great portion to the total mass flux.

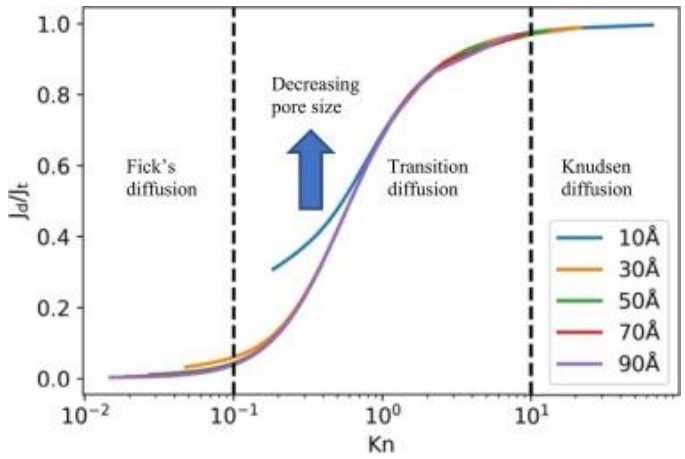

Figure 4.8 The ratio of the diffusion flux J_d to the total mass flux J_t as a function of *Kn* for pore sizes ranging from 10 to 90 Å.

4.3.5 Effect of deformation on permeability

The apparent permeability is another frequently-used property when describing the gas flow capacity in shale reservoirs. Due to the flow enhancement from diffusion, the apparent permeability may be significantly higher than the intrinsic permeability (i.e., $H^2/12$) (Yu et al., 2018; Zhang et al., 2015). The apparent permeability can be calculated from the total mass flux by Darcy's law

$$K_a = \frac{J_t \mu}{\rho H \nabla P} \tag{4.14}$$

Substituting the total mass fluxes obtained from both the NEMD simulations and Equation (4.13) into Equation (4.14), the apparent permeabilities of the flexible kerogen slit pores are presented in Figure 4.9a. The apparent permeability is further compared with the intrinsic permeability in Figure 4.9b. Equations (4.13) and (4.14) coupled with deformation provide a good prediction of NEMD simulated apparent gas permeability in the flexible kerogen slit pores. The apparent permeability declines rapidly with gas pressure within 10 MPa before reaching a plateau. As can be seen from Figures 4.9a and 4.9b, the apparent permeability does not vary as to pore size when gas travels at low pressure, which is 1-3 orders of magnitude greater than at high pressure. As gas pressure increases, the apparent permeability starts to differentiate from each other according to the pore size and gradually approaches the intrinsic permeability. Similar to the total mass flux, kerogen deformation reduces the apparent permeability due to the narrowed flow path by swelling. It can be seen from Figure 4.9c that the kerogen deformation has a slight effect on the apparent permeability at low pressure since the apparent permeability reduction by deformation is always less than 10%. However, an overestimated permeability may sometimes occur if the kerogen deformation is not properly considered as the permeability reduction can be as large as 40% under 50 MPa. Therefore, it is more important to pay attention to the effect of kerogen deformation when dealing with gas flow in small pores under high pressure levels. It should also be noted that the kerogen matrix size S plays an important role in estimating permeability. In the case of a core sample, a large value of S suggests a higher content of kerogen and less fractures so that kerogen deformation may have a greater impact on the permeability.

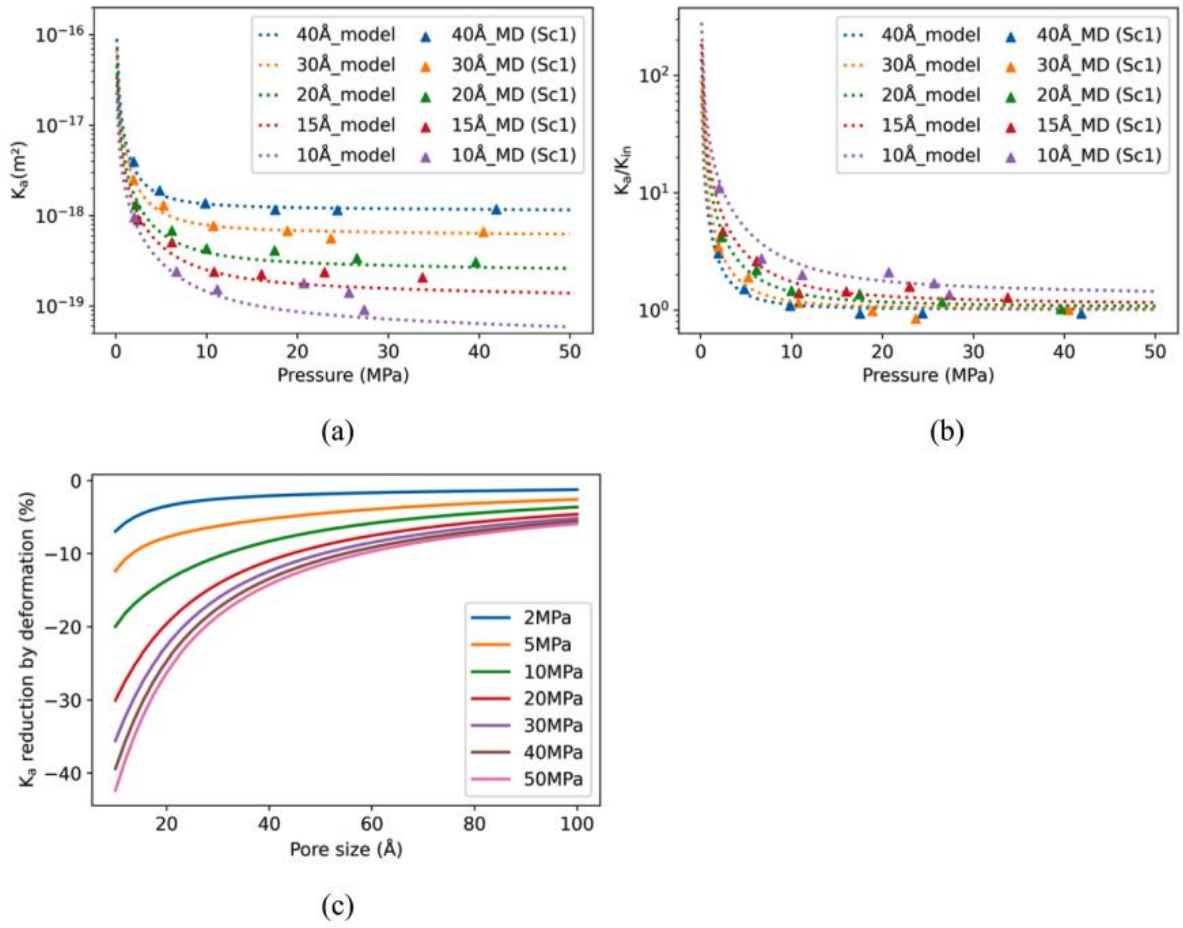

Figure 4.9 (a) The apparent permeability K_a obtained from the NEMD simulations in the flexible kerogen slit pores (Sc1) and the proposed theoretical model. (b) Deviations of K_a from the intrinsic permeability K_{in}. (c) The reduction of K_a by kerogen deformation calculated by the proposed model for various initial pore sizes and pressures.

4.4 Conclusions

In this study, we investigated the effect of sorption-induced deformation on methane transport at nanoscale using molecular simulations. In summary, gas adsorption can induce kerogen swelling and significantly narrow the associated slit pore size. In consideration of the kerogen flexibility, the narrowed flow path due to kerogen swelling mainly reduces viscous gas flow instead of diffusion. The mass flux reduction is insignificant at low pressure but becomes more

pronounced when pore pressure is high. Gas apparent permeability can be calculated from the total mass flux by Darcy's law. In the slit pore of size 10 Å, the apparent permeability reduction by kerogen swelling is 40% under pore pressure of 50 MPa. However, the effect of kerogen deformation on permeability becomes less significant as pore size increases. In addition, it is found that the ratio of the diffusion flux to the total mass flux is highly dependent on the Knudsen number. When $Kn > 10$, the diffusion flux dominates the total mass flux. When $Kn < 0.1$, the viscous flux makes the predominant contribution instead. The results are expected to enhance the understanding of dynamic permeability evolution of shale reservoirs and facilitate accurate predictions of gas production. Strategies such as pressure management and pore size optimization can be potentially implemented to minimise the negative effects of swelling on gas permeability.

Acknowledgments

This work was supported in part by the Australian Research Council through Discovery Projects (DP200101919 and DP190102954). The authors acknowledge the use of the National Computational Infrastructure (NCI) which is supported by the Australian Government, and accessed through the Sydney Informatics Hub HPC Allocation Scheme, which is supported by the Deputy Vice-Chancellor (Research), University of Sydney and the ARC LIEF, 2019: Smith, Muller, Thornber et al., Sustaining and strengthening merit-based access to National Computational Infrastructure (LE190100021). Statistical support from Jim Matthews of the Sydney Informatics Hub is gratefully acknowledged.

References

1. Alfarge, D., Wei, M., & Bai, B. (2020). Developments in petroleum science. *Elsevier, 67*,

1-13.

2. Ao, X., Lu, Y., Tang, J., Chen, Y., & Li, H. (2017). Investigation on the physics structure and chemical properties of the shale treated by supercritical CO_2. *Journal of CO_2 Utilisation, 20*, 274-281.

3. Bao, B., & Zhao, S. (2021). A review of experimental nanofluidic studies on shale fluid phase and transport behaviours. *Journal of Natural Gas Science and Engineering, 86*, 103745.

4. Batsanov, S. S. (2001). Van der Waals radii of elements. *Inorganic Materials, 37*(9), 871-885.

5. Behrang, A., Mohammadmoradi, P., Taheri, S., & Kantzas, A. (2016). A theoretical study on the permeability of tight media; effects of slippage and condensation. *Fuel, 181*, 610-617.

6. Beskok, A., & Karniadakis, G. E. (1999). Report: A model for flows in channels, pipes, and ducts at micro and nano scales. *Microscale Thermophysical Engineering, 3*(1), 43-77.

7. Bravo, M. C. (2007). Effect of transition from slip to free molecular flow on gas transport in porous media. *Journal of Applied Physics, 102*(7), 074905.

8. Cai, J., Lin, D., Singh, H., Zhou, S., Meng, Q., & Zhang, Q. (2019). A simple permeability model for shale gas and key insights on relative importance of various transport mechanisms. *Fuel, 252*, 210-219.

9. Castez, M. F., Winograd, E. A., & Sánchez, V. M. (2017). Methane flow through organic-rich nanopores: The key role of atomic-scale roughness. *The Journal of Physical Chemistry C, 121*(51), 28527-28536.

10. Chen, J., Yu, H., Fan, J., Wang, F., Lu, D., Liu, H., & Wu, H. (2017). Channel-width dependent pressure-driven flow characteristics of shale gas in nanopores. *AIP Advances, 7*(4), 045217.

11. Chong, L., Sanguinito, S., Goodman, A. L., & Myshakin, E. M. (2021). Molecular characterisation of carbon dioxide, methane, and water adsorption in micropore space of kerogen matrix. *Fuel, 283*, 119254.

12. Collell, J., Galliero, G., Vermorel, R., Ungerer, P., Yiannourakou, M., Montel, F., & Pujol, M. (2015). Transport of multicomponent hydrocarbon mixtures in shale organic matter by molecular simulations. *The Journal of Physical Chemistry C, 119*(39), 22587-22595.

13. Cui, G., Liu, J., Wei, M., Shi, R., & Elsworth, D. (2018). Why shale permeability changes under variable effective stresses: New insights. *Fuel, 213*, 55-71.

14. EIA. (2021). Natural gas explained: Natural gas and the environment, https://www.eia.gov/energyexplained/natural-gas/natural-gas-and-the-environment.

15. EIA. (2022). Natural gas explained: Where our natural gas comes from, https://www.eia.gov/energyexplained/natural-gas/where-our-natural-gas-comes- from.

16. Fang, T., Wang, M., Gao, Y., Zhang, Y., Yan, Y., & Zhang, J. (2019). Enhanced oil recovery with CO_2/N_2 slug in low permeability reservoir: Molecular dynamics simulation. *Chemical Engineering Science, 197*, 204-211.

17. Geng, L., Li, G., Zitha, P., Tian, S., Sheng, M., & Fan, X. (2016). A diffusion-viscous flow model for simulating shale gas transport in nano-pores. *Fuel, 181*, 887-894.

18. Gor, G. Y., Huber, P., & Bernstein, N. (2017). Adsorption-induced deformation of nanoporous materials – A review. *Applied Physics Reviews, 4*(1), 011303.

19. Hamza, A., Hussein, I. A., Al-Marri, M. J., Mahmoud, M., Shawabkeh, R., & Aparicio, S. (2021). CO_2 enhanced gas recovery and sequestration in depleted gas reservoirs: A review. *Journal of Petroleum Science and Engineering, 196*, 107685.

20. Ho, T. A., & Wang, Y. (2021). Molecular origin of wettability alteration of subsurface porous media upon gas pressure variations. *ACS Applied Materials & Interfaces, 13*(34), 41330-41338.

21. Ho, T. A., Wang, Y., & Criscenti, L. J. (2018a). Chemo-mechanical coupling in kerogen gas adsorption/desorption. *Physical Chemistry Chemical Physics, 20*(18), 12390-12395.

22. Ho, T. A., Wang, Y., Ilgen, A., Criscenti, L. J., & Tenney, C. M. (2018b). Supercritical CO_2-induced atomistic lubrication for water flow in a rough hydrophilic nanochannel. *Nanoscale, 10*(42), 19957-19963.

23. Huang, L., Ning, Z., Wang, Q., Qi, R., Cheng, Z., Wu, X., . . . Qin, H. (2019). Molecular insights into kerogen deformation induced by CO_2/CH_4 sorption: Effect of maturity and moisture. *Energy & Fuels, 33*(6), 4792-4805.

24. Huang, L., Ning, Z., Wang, Q., Zhang, W., Cheng, Z., Wu, X., & Qin, H. (2018). Effect of organic type and moisture on CO_2/CH_4 competitive adsorption in kerogen with implications for CO_2 sequestration and enhanced CH_4 recovery. *Applied Energy, 210*, 28-43.

25. Javadpour, F., Fisher, D., & Unsworth, M. (2007). Nanoscale gas flow in shale gas sediments. *Journal of Canadian Petroleum Technology, 46*(10), PETSOC-07-10-06.

26. Jin, Z. (2017). Effect of nano-confinement on high pressure methane flow characteristics. *Journal of Natural Gas Science and Engineering, 45*, 575-583.

27. Kashinath, A., Szulczewski, M., & Dogru, A. H. (2020). Modelling the effect of maturity on the elastic moduli of kerogen using atomistic simulations. *Energy & Fuels, 34*(2), 1378-1385.

28. Li, Y., Wang, Y., Wang, J., & Pan, Z. (2020). Variation in permeability during CO_2-CH_4 displacement in coal seams: Part 1 – Experimental insights. *Fuel, 263*, 116666.

29. Linstrom, P., & Mallard, W. (2022). NIST chemistry WebBook, NIST standard reference database number 69, National Institute of Standards and Technology, Gaithersburg MD, 20899.

30. Liu, K., Ostadhassan, M., Zhou, J., Gentzis, T., & Rezaee, R. (2017). Nanoscale pore

structure characterisation of the Bakken shale in the USA. *Fuel, 209*, 567-578.

31. Liu, L., Wang, Y., & Aryana, S. A. (2021). Insights into scale translation of methane transport in nanopores. *Journal of Natural Gas Science and Engineering, 96*, 104220.

32. Loucks, R. G., Reed, R. M., Ruppel, S. C., & Jarvie, D. M. (2009). Morphology, genesis, and distribution of nanometer-scale pores in siliceous mudstones of the Mississippian Barnett Shale. *Journal of Sedimentary Research, 79*(12), 848-861.

33. Lyu, Q., Tan, J., Li, L., Ju, Y., Busch, A., Wood, D. A., . . . Hu, R. (2021). The role of supercritical carbon dioxide for recovery of shale gas and sequestration in gas shale reservoirs. *Energy & Environmental Science, 14*(8), 4203-4227.

34. Nan, Y., Li, W., & Jin, Z. (2020). Slip length of methane flow under shale reservoir conditions: Effect of pore size and pressure. *Fuel, 259*, 116237.

35. Obliger, A., Valdenaire, P. L., Capit, N., Ulm, F. J., Pellenq, R. J., & Leyssale, J. M. (2018). Poroelasticity of methane-loaded mature and immature kerogen from molecular simulations. *Langmuir, 34*(45), 13766-13780.

36. Pollard, W., & Present, R. D. (1948). On gaseous self-diffusion in long capillary tubes. *Physical Review, 73*(7), 762.

37. Potoff, J. J., & Siepmann, J. I. (2001). Vapour–liquid equilibria of mixtures containing alkanes, carbon dioxide, and nitrogen. *AIChE Journal, 47*(7), 1676-1682.

38. Rahim, Z., Al-Anazi, H., & Al-Kanaan, A. (2012). Maximising postfrac gas flow rates from conventional, tight reservoirs. *Oil & Gas Journal, 110*(3), 76-85.

39. Salahshoor, S., Fahes, M., & Teodoriu, C. (2018). A review on the effect of confinement on phase behaviour in tight formations. *Journal of Natural Gas Science and Engineering, 51*, 89-103.

40. Shen, W., Li, X., Xu, Y., Sun, Y., & Huang, W. (2017). Gas flow behaviour of nanoscale pores in shale gas reservoirs. *Energies, 10*(6), 751.

41. Speight, J. G. (2013). Shale gas production processes. *Gulf Professional Publishing*.

42. Stevens, P. (2012). The shale gas revolution: Developments and changes. *Chatham House London*.

43. Stukowski, A. (2009). Visualisation and analysis of atomistic simulation data with OVITO – the Open Visualisation Tool. *Modelling and Simulation in Materials Science and Engineering, 18*(1), 015012.

44. Stukowski, A. (2014). Computational analysis methods in atomistic modelling of crystals. *Jom, 66*(3), 399-407.

45. Sui, H., Zhang, F., Wang, Z., Wang, D., & Wang, Y. (2020). Effect of kerogen maturity, water content for carbon dioxide, methane, and their mixture adsorption and diffusion in kerogen: A computational investigation. *Langmuir, 36*(33), 9756-9769.

46. Sun, C., Zhou, R., Zhao, Z., & Bai, B. (2020). Nanoconfined fluids: What can we expect from them? *The Journal of Physical Chemistry Letters, 11*(12), 4678-4692.

47. Sun, J., Liu, Z., & Cao, D. (2019). A permeation model of shale gas in cylindrical-like kerogen pores at geological conditions. *Chemical Engineering Science, 207*, 457-463.

48. Sun, Z., Li, X., Liu, W., Zhang, T., He, M., & Nasrabadi, H. (2020). Molecular dynamics of methane flow behaviour through realistic organic nanopores under geologic shale condition: Pore size and kerogen types. *Chemical Engineering Journal, 398*, 124341.

49. Tesson, S., & Firoozabadi, A. (2018). Methane adsorption and self-diffusion in shale kerogen and slit nanopores by molecular simulations. *The Journal of Physical Chemistry C, 122*(41), 23528-23542.

50. Tesson, S., & Firoozabadi, A. (2019). Deformation and swelling of kerogen matrix in light hydrocarbons and carbon dioxide. *The Journal of Physical Chemistry C, 123*(48), 29173-29183.

51. Thompson, A. P., Aktulga, H. M., Berger, R., Bolintineanu, D. S., Brown, W. M., Crozier,

P. S., . . . Nguyen, T. D. (2021). LAMMPS – A flexible simulation tool for particle-based materials modelling at the atomic, meso, and continuum scales. *Computer Physics Communications*, *271*, 108171.

52. Ungerer, P., Collell, J., & Yiannourakou, M. (2014). Molecular modelling of the volumetric and thermodynamic properties of kerogen: Influence of organic type and maturity. *Energy & Fuels, 29*(1), 91-105.

53. Wang, H., Chen, L., Qu, Z., Yin, Y., Kang, Q., Yu, B., & Tao, W.Q. (2020). Modelling of multi-scale transport phenomena in shale gas production — A critical review. *Applied Energy, 262*, 114575.

54. Wang, J., Ryan, D., & Anthony, E. J. (2011). Reducing the greenhouse gas footprint of shale gas. *Energy Policy, 39*(12), 8196-8199.

55. Wang, J., Wolf, R. M., Caldwell, J. W., Kollman, P. A., & Case, D. A. (2004). Development and testing of a general amber force field. *Journal of Computational Chemistry, 25*(9), 1157-1174.

56. Wang, S., Elsworth, D., & Liu, J. (2012). A mechanistic model for permeability evolution in fractured sorbing media. *Journal of Geophysical Research: Solid Earth, 117*, B06205.

57. Wang, S., Feng, Q., Javadpour, F., Zha, M., & Cui, R. (2017). Multiscale modelling of shale apparent permeability: An integrated study of molecular dynamics and pore network model. *SPE Annual Technical Conference and Exhibition*, SPE-187286-MS.

58. Wu, J., Huang, P., Maggi, F., & Shen, L. (2022). Molecular investigation on CO_2-CH_4 displacement and kerogen deformation in enhanced shale gas recovery. *Fuel, 315*, 123208.

59. Wu, K., Chen, Z., Li, X., Guo, C., & Wei, M. (2016). A model for multiple transport mechanisms through nanopores of shale gas reservoirs with real gas effect–adsorption-mechanic coupling. *International Journal of Heat and Mass Transfer, 93*, 408-426.

60. Wu, T., & Firoozabadi, A. (2019). Effect of microstructural flexibility on methane flow in

kerogen matrix by molecular dynamics simulations. *The Journal of Physical Chemistry C, 123*(17), 10874-10880.

61. Yan, Y., Li, C., Dong, Z., Fang, T., Sun, B., & Zhang, J. (2017). Enhanced oil recovery mechanism of CO_2 water-alternating-gas injection in silica nanochannel. *Fuel, 190*, 253-259.

62. Yu, H., Fan, J., Chen, J., Zhu, Y., & Wu, H. (2018). Pressure-dependent transport characteristic of methane gas in slit nanopores. *International Journal of Heat and Mass Transfer, 123*, 657-667.

63. Yu, H., Fan, J., Xia, J., Liu, H., & Wu, H. (2020a). Multiscale gas transport behaviour in heterogeneous shale matrix consisting of organic and inorganic nanopores. *Journal of Natural Gas Science and Engineering, 75*, 103139.

64. Yu, H., Xu, H., Fan, J., Wang, F., & Wu, H. (2020b). Roughness factor-dependent transport characteristic of shale gas through amorphous kerogen nanopores. *The Journal of Physical Chemistry C, 124*(23), 12752-12765.

65. Yu, H., Xu, H., Fan, J., Zhu, Y.-B., Wang, F., & Wu, H. (2020c). Transport of shale gas in microporous/nanoporous media: Molecular to pore-scale simulations. *Energy & Fuels, 35*(2), 911-943.

66. Yu, H., Xu, H., Xia, J., Fan, J., Wang, F., & Wu, H. (2020d). Nanoconfined transport characteristic of methane in organic shale nanopores: The applicability of the continuous model. *Energy & Fuels, 34*(8), 9552-9562.

67. Yu, X., Li, J., Chen, Z., Wu, K., Zhang, L., Yang, S., . . . Yang, M. (2021). Determination of CH_4, C_2H_6 and CO_2 adsorption in shale kerogens coupling sorption-induced swelling. *Chemical Engineering Journal, 410*, 127690.

68. Zendehboudi, S., & Bahadori, A. (2016). Shale oil and gas handbook: Theory, technologies, and challenges. *Gulf Professional Publishing*.

69. Zhan, S., Su, Y., Lu, M., Cai, M., Fu, J., Liu, Z., . . . Li, G. (2021). Effect of surface type on the flow characteristics in shale nanopores. *Geofluids, 2021*, 1-12.

70. Zhang, L., Li, D., Lu, D., & Zhang, T. (2015). A new formulation of apparent permeability for gas transport in shale. *Journal of Natural Gas Science and Engineering, 23*, 221-226.

71. Zhao, Y., Wang, C., Zhang, Y., & Liu, Q. (2019). Experimental study of adsorption effects on shale permeability. *Natural Resources Research, 28*(4), 1575-1586.

72. Zhou, J., Tian, S., Zhou, L., Xian, X., Yang, K., Jiang, Y., . . . Guo, Y. (2020). Experimental investigation on the influence of sub- and super-critical CO_2 saturation time on the permeability of fractured shale. *Energy, 191*, 116574.

Supplementary materials for

Effect of sorption-induced deformation on methane flow in kerogen slit pores

Jian Wu, Pengyu Huang, Federico Maggi, Luming Shen*

School of Civil Engineering, The University of Sydney, NSW 2006, Australia

*Corresponding author. Email: luming.shen@sydney.edu.au

Table 4.S1 Detailed construction steps of the kerogen slit pore.

Step	Ensemble	Temperature (K)	Pressure (atm)	Time (ps)
1	NVT	300	–	100
2	NVT	300 – 2000	–	100
3	NVT	2000	–	100
4	NPT	2000 – 1000	100	100
5	NPT	1000 – 2000	100	100
6	NPT	2000 – 1000	100	100
7	NPT	1000 – 2000	100	100
8	NPT	2000 – 300	100	400
9	NPT	300	100 – 1	100
10	NPT	300	1	300
11	NVT	300	–	500

Table 4.S2 Summary of pair coefficients for kerogen and methane models.

Interaction type	ϵ (kcal/mol)	σ (Å)
	Kerogen* (GAFF)	
os-os	0.1700	3.00
ca-ca	0.0860	3.40
na-na	0.1700	3.25
c3-c3	0.1094	3.40
h2-h2	0.0157	2.29
ha-ha	0.0150	2.60
h1-h1	0.0157	2.47

hc-hc	0.0157	2.65
ss-ss	0.2500	3.56
hn-hn	0.0157	1.07
nb-nb	0.1700	3.25
h4-h4	0.0150	2.51
	Methane (TraPPE-UA)	
CH_4-CH_4	0.2941	3.73

*Description of kerogen atoms in GAFF can be found in http://ambermd.org/antechamber/gaff.

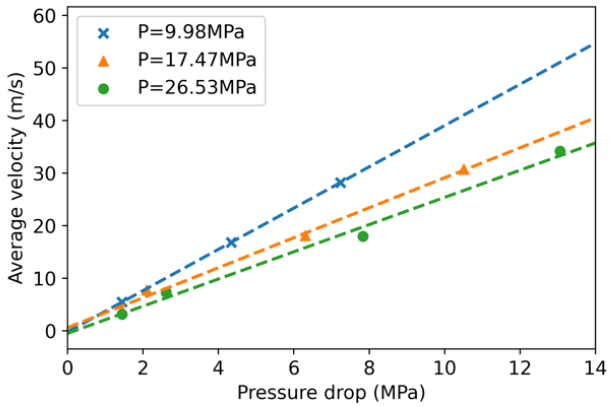

Figure 4.S1 The linear relationship between average gas velocity and pressure drop in the flexible kerogen slit pore (Sc1) of 20 Å.

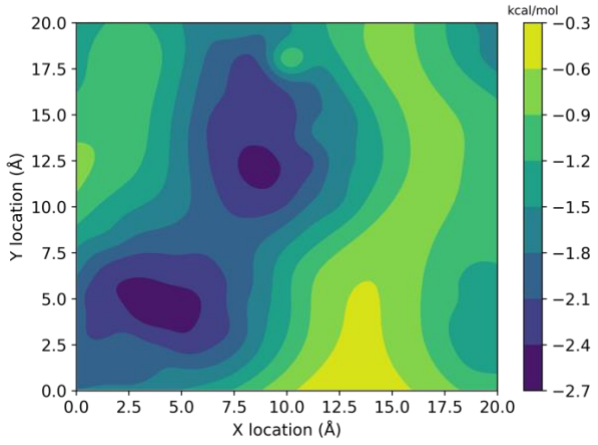

Figure 4.S2 The methane-kerogen surface interaction energy map measured by a single methane molecule at an average distance of 3 Å.

Python implementation of the diffusive-viscous gas flow model:

```
import numpy as np
import pandas as pd
from scipy.interpolate import interp1d

df1 = pd.read_csv('ch4_eos.csv')      #load isothermal properties for methane
x = df1.P
y1 = df1.density
y2 = df1.viscosity
f1 = interp1d(x, y1, kind='cubic')
f2 = interp1d(x, y2, kind='cubic')

df2 = pd.read_csv('ch4_adsorption_strain.csv')        #load methane pressure-strain relationship
x = df2.P
y = df2.Strain
f3 = interp1d(x, y, kind='cubic')

# fitting params
x = 45.2382     #A
y = 45.6134
z = 22.654    #half of kerogen matrix
alpha_f = 1
alpha_s = 0.65
kf = 0         #GPa/m
ks = 5         #GPa

def flux(p, H):
```

```
den = f1(p)*16.04/1000     #g/cm3
mu = f2(p)*1e-15
epsilon = f3(p)/100
delta_hs = epsilon*z
#delta_hp =(alpha_f-alpha_s)/(1+kf*z*1E-10/ks)*z*p*1e-3/ks
delta_hp = 0
H_new = H-2*(delta_hs-delta_hp)
kn =1.3805E-23*300/np.sqrt(2)/np.pi/3.8e-10**2/p*10000/H_new
Dk = H_new*1e-10/3*np.sqrt(8*8.314462*300/np.pi/0.01604)
Dt = Dk*kn/(kn+1)
Jd = Dt/8.314462/300*(1e6/4.52382E-9)*H_new*45.6134*1e-20*16.04
Jv = H_new**3*45.6134*1e-40/12/mu/1e9*(1e6/4.52382E-9)*den*1e6
Jtotal = Jd+Jv
ratio = Jd/Jtotal
ka = Jtotal*mu/H_new/y/den/(1/x)*1e7
return Jd, Jv, Jtotal, kn, H_new, ka, delta_hs, delta_hp
```

Chapter 5 Selective adsorption and transport of CO_2-CH_4 mixture under nano-confinement

The injection of CO_2 into a depleted reservoir with residual methane results in a gas flow system of a binary mixture, which is difficult to be separated in experimental investigations. As CO_2 and CH_4 have different interaction energies with the slit pore walls, the two components usually show great variances in gas adsorption amount and transport speed, known as selective adsorption and transport. Gas separation of the mixture components is most likely to occur under strong nano-confinement. Selective adsorption is the most important mechanism controlling CO_2-EGR and essentially affects the gas recovery rate. By simulating the pressure-driven flow of the CO_2-CH_4 binary mixture in a kerogen slit pore using NEMD, CO_2/CH_4 selectivity can be derived as a function of total gas pressure, molar composition, and pore size. On the other hand, CO_2 composition in the slit pore increases as the injection proceeds and methane depletes. Measuring the gas mixture velocity and mass transfer rate respecting the CO_2 molar ratio provides deep insights into the dynamic production of methane and CO_2 injection process. This chapter is presented in the form of a manuscript that has been published in *Energy*:

Wu, J., Shen, L., Huang, P., & Gan, Y. (2023). Selective adsorption and transport of CO_2-CH_4 mixture under nano-confinement. *Energy, 273*, 127224.

The PhD candidate has performed all the numerical work and the analysis of the results, and is the primary author of the above article.

Selective adsorption and transport of CO_2-CH_4 mixture under nano-confinement

Jian Wu[a], Luming Shen[a, *], Pengyu Huang[a, b], Yixiang Gan[a, c]

[a] School of Civil Engineering, The University of Sydney, NSW 2006, Australia

[b] Hard Rock Mining, CSIRO Mineral Resources, QCAT, 1 Technology Court, Pullenvale, QLD 4069, Australia

[c] Sydney Nano Institute, The University of Sydney, NSW 2006, Australia

[*]Corresponding author. Email: luming.shen@sydney.edu.au

Abstract

CO_2-enhanced gas recovery (EGR) is a promising technology to sequestrate CO_2 while enhancing CH_4 recovery simultaneously in shale reservoirs. During the process, the mixture of injected CO_2 and desorbed CH_4 of varied compositions flows within nanopores of shale. The nano-confinement is known to affect single-component gas flow and transport significantly but has not yet been properly addressed for non-equimolar gas mixtures. Herein, we use molecular dynamics to systematically investigate the selective adsorption and transport of CO_2-CH_4 mixture in kerogen slit nanopores. Results show that the gas mixture velocity decreases logarithmically with increasing CO_2 molar ratio. The CO_2/CH_4 adsorption and transport selectivities are generally greater than one and have a strong negative correlation with the total pore gas pressure and pore size. The transport selectivity becomes rather important (i.e., much greater than one) when pore size is below 20 Å. Analyses indicate that surface adsorption and diffusion are primarily responsible for the selective transport, with bulk diffusion also playing a role. These findings provide nanoscale insights into the CO_2-EGR in shale's organic matrix and suggest that the selective transport of CO_2-CH_4 mixture should be considered in large-scale

simulations under certain pore size and pressure conditions.

5.1 Introduction

The discovery and exploitation of shale gas are considered to have a positive impact on greenhouse gas (GHG) emissions in the global energy sector (Zendehboudi and Bahadori, 2016). Over the past decade, CO_2 geologic sequestration has also emerged from a concept to a commercially feasible component of the clean energy transition to mitigate global warming (GHD, 2022; Singh, 2013). Although saline aquifers can be popular options for the storage sites, depleted gas reservoirs such as shale may be more attractive for CO_2 storage as their pore pressure is below what existed before depletion, thus less likely to trigger earthquakes (Zoback and Gorelick, 2012). Moreover, shale gas production and CO_2 storage nowadays often come together, known as CO_2-EGR since shale gas production rate declines hyperbolically with time (Neil et al., 2020) and CO_2 injection can potentially enhance the limited transport of adsorbed gas from the matrix. The CO_2 storage potential of depleted unconventional shale reservoirs with enhanced CH_4 recovery has been confirmed by the first successful "huff-and-puff" CO_2 injection test conducted in Morgan County, Tennessee (US) where the daily gas production was over eight times the pre-injection average in the first month of flowback (Louk et al., 2017).

One of the most attractive aspects of CO_2 injection in shale reservoirs is the preferential adsorption of CO_2 over CH_4 in the organic matrix, which fundamentally differs from the storage mechanisms in saline aquifers (Liu et al., 2013). The competitive adsorption between CO_2 and CH_4 has been studied extensively by laboratory experiments (Liu et al., 2019; Liu et al., 2017; Qin et al., 2021b; Xie et al., 2022) and numerical simulations (Ho et al., 2018; Huang et al., 2018; Li and Sun, 2022; Sui et al., 2020; Sun et al., 2022; Wang et al., 2018; Yang et al., 2022). For example, Liu et al. (2017) confirmed that CO_2 injection could induce dynamic desorption of adsorbed CH_4 by additionally ~25% in a sample of black shale core after performing the low-field nuclear magnetic resonance (NMR) measurements. The results of Liu et al. (2019)

showed that increasing the CO_2/CH_4 partial pressure ratio in shale increased the adsorption capacity of CO_2 but decreased that of CH_4 logarithmically, and the competitive CO_2/CH_4 adsorption ratio (CAR) decreased logarithmically with the increasing total gas pressure as well. With the combination of gas chromatography and conventional sorption experimental setup, binary mixture gas adsorption measurements were conducted in shale samples with varied CO_2/CH_4 molar ratios, where the preferential adsorption of CO_2 over CH_4 was widely recognised and the selectivity of CO_2 was found to change with pressure (Klewiah et al., 2020).

Molecular dynamics (MD) simulation is a valuable tool to reveal the underlying mechanisms of competitive sorption without the difficulty of separating free and adsorbed gases as in the laboratory experiments (Liu et al., 2017). Using simplified organic and inorganic pore structures, Sun et al. (2022) performed MD simulations in graphene-montmorillonite (MMT) slit pores with both homogeneous and heterogeneous surfaces and argued that the partial pressures of CO_2 and CH_4 played the decisive role in competitive gas adsorption at a fixed temperature and pore size. Interestingly, they found that gas adsorption on MMT surfaces was not sensitive to the partial pressure of the gas component. Kerogen is the primary hydrocarbon source of shale gas holding approximately one half of the adsorbed gas (Kang et al., 2021). Ho et al. (2018) performed grand canonical Monte Carlo-molecular dynamics (GCMC-MD) simulations for equimolar CO_2-CH_4 mixtures under various pressures and found that the adsorption selectivity of CO_2 over CH_4 was 3-6 within the over-mature kerogen nanoporous structure. Kerogen's organic type, maturity and moisture content can affect the competitive adsorption of CO_2-CH_4 mixtures. For example, Huang et al. (2018) reported that the CO_2/CH_4 selectivity followed the order of kerogen type I < II < III in consistent with porosity values and changed nonmonotonically with moisture content. Sui et al. (2020) found that the CO_2/CH_4 selectivity decreased with kerogen maturity as the N-, S-, and O-containing groups in kerogen had a greater impact on CO_2 adsorption than CH_4. Wang et al. (2018) studied CO_2-CH_4 competitive adsorption in a kerogen slit pore under different geological pressure and temperature conditions, and inferred that the most proper injection depth for CO_2-EGR projects was 1.5-2.5 km below the surface. In theory, the greater isosteric heat of CO_2 than CH_4 adsorbed

on kerogen surfaces justified the stronger adsorption capacity of CO_2 in kerogen slit nanopores (Sun et al., 2017). More specifically, Ho and Wang (2021) measured the interaction energies of CO_2 with kerogen II-D, pyrophyllite, gibbsite, and MMT as -6.2, -2.9, -5, and -5 kcal/mol, respectively, higher than (more negative) that of CH_4 with all these surfaces. They also reported that the interaction of CO_2 with the overmature kerogen was stronger than that with other inorganic mineral surfaces.

Pores with size smaller than 50 nm constitute the majority of shale's porosity (Gou et al., 2021). The nano-confinement leads to a unique gas flow and transport behaviour distinct from the continuum scale, such as slip flow, Knudsen diffusion and surface diffusion (Hu et al., 2022; Javadpour et al., 2007; Javadpour et al., 2021; Sun et al., 2020; Wang and Aryana, 2021; Yang et al., 2020). In the context of gas mixtures, several studies have shown the selective transport and separation of gas components through nanopores (Firouzi and Wilcox, 2013; Ho and Wang, 2020; Kazemi and Takbiri-Borujeni, 2017; Liu et al., 2018; Liu et al., 2022; Wu and Firoozabadi, 2018). Liu et al. (2018) calculated the self-diffusion coefficients of CO_2 and CH_4 in both single-component and mixture gases, suggesting that the CH_4 and CO_2 self-diffusion coefficients could increase and decrease with the increase of CO_2 composition, respectively. However, the self-diffusion coefficients may not be appropriate for describing gas transport under a concentration gradient. Kazemi and Takbiri-Borujeni (2017) simulated CO_2-CH_4 mixture diffusion in a graphene slit pore and concluded that the overall CO_2/CH_4 selectivity was negatively correlated to the total gas pressure. Specifically, the Fick's diffusion coefficient of each gas component increased with its partial pressure. They also found that the off-diagonal diffusion (by the chemical potential gradient of the partner gas component) had the same magnitude as the diagonal terms (by its own chemical potential gradient), and thus should not be ignored. Firouzi and Wilcox (2013) examined the flow behaviour of pure CO_2, CH_4, and their mixture in a single carbon slit pore under an external driving force and suggested that the gas velocity profiles would not always match each other for the 1:1 CO_2-CH_4 mixture as the transport of CO_2 was impacted more significantly by the pore walls compared with CH_4. Even though the kinetic diameter of CO_2 is less than that of CH_4, the greater impact mainly results

from the higher affinity of CO_2 to the pore walls. For instance, the interaction energies of CO_2 and CH_4 molecules with a kerogen surface are -6.2 kcal/mol and -4.2 kcal/mol, respectively (Ho and Wang, 2021). Based on the dual control volume-grand canonical molecular dynamics (DCV-GCMD), Wu and Firoozabadi (2018) developed a new technique to simulate the transport and separation of the CH_4/He and CO_2/CH_4 mixtures in slit pores by controlling the pressure of the permeate side through random deletion of molecules. They found that the gas mixture separation factor (i.e., selectivity) decreased as pore size increased from 0.8 to 2 nm, and then approached unity. Similarly, Ho and Wang (2020) observed a critical pore size (~1.8 nm) below which the selective transport of equimolar C_2H_6-CH_4 mixture could occur and argued that surface adsorption and diffusion were responsible for the selective transport. In addition, they suggested further work should be conducted with varied gas compositions other than 1:1 in clay and kerogen-based pores.

The existing literature greatly focuses on the competitive adsorption of binary CO_2-CH_4 gases at the nanoscale, which are mostly found in the operation of CO_2-EGR. There is a lack of studies on the multicomponent gas transport, and such investigations are limited to equimolar binary mixtures through the simplified inorganic/organic nanoporous structures. In this paper, we aim to systemically investigate the selective adsorption and transport of CO_2-CH_4 mixtures in shale's organic kerogen nanopores, subject to the influence of pore pressure (~2-30 MPa), gas composition (~10%-80% of CO_2) and pore size (10-60 Å). Firstly, we perform GCMC-MD simulations to build the initial gas saturation inside a slit pore confined between two over-mature kerogen slabs. Non-equilibrium molecular dynamics (NEMD) is then employed to simulate the pressure-driven gas flow and transport. Gas mixture velocity is studied as a function of gas composition under varied pore sizes, while CO_2/CH_4 adsorption and transport selectivities are analysed as a function of pressure and pore size. The results can provide new insights into the gas production rate at different geological depths (i.e., pressure) as well as different stages (i.e., gas composition) of CO_2-EGR. Based on the adsorption and transport selectivities of CO_2/CH_4 mixtures, the gas compositions in shale reservoirs may be predicted from the produced gas compositions in real-time. The knowledge discussed here can also be

potentially implemented into continuum scale simulations by upscaling.

5.2 Computational methods

As the main organic matter in shale, the type II-D kerogen units (Ungerer et al., 2014) are used to build the slit pore model in this study, which is an overmature type from the Duvernay series and represents unconventional gas reserves such as the Barnett shale. Initially, 27 kerogen units are emplaced into an empty simulation box of 100 Å × 100 Å × 100 Å and relaxed by annealing in a few cycles. A wall of dummy particles is then added to the middle of the produced kerogen matrix, and the whole structure is relaxed again for separation (i.e., create two individual pieces of kerogen matrix). By adjusting the separation distance between two pieces of kerogen matrix in the *z*-dimension accordingly, different slit pore sizes can be created. As shown in Figure 5.1, the kerogen slit pore model of size 10 Å is contained in a simulation box with a size of 45.24 Å × 45.61 Å × 55.31 Å. At the nanoscale, the amorphous kerogen walls are considered rough surfaces and have heterogeneous interaction forces with gas molecules. Therefore, the constructed slit pores are not perfectly straight. Our previous study on the single-component gas flow has shown that sorption-induced swelling can greatly affect the absolute gas adsorption and mass flux through the kerogen slit pore (Wu et al., 2022a). Therefore, the kerogen slit model is considered fully flexible in the present study and all kerogen matrix deformations are coupled into the results discussed herein. The kerogen, CO_2 and CH_4 molecules are described by the general Amber (Huang et al., 2022; Wang et al., 2004), TraPPE (Eggimann et al., 2019; Potoff and Siepmann, 2001) and TraPPE-UA (Martin and Siepmann, 1998) force fields, respectively. The CO_2 molecule is rigidified with the C = O bond length fixed at 1.16 Å and the O = C = O angle at 180°. The non-bonded potential is calculated by the 12/6 Lennard-Jones potential with electrostatic force. Pair coefficients between different atom types are calculated by the Lorentz-Berthelot mixing rule. The cut-off is set at 14 Å and the long-range Coulombic term is calculated in the K-space by the particle-particle particle-mesh

solver (PPPM) (Hockney and Eastwood, 1988). More simulation details, including the kerogen model and slit pore construction processes, can be found in our previous work (Huang et al., 2022; Wu et al., 2022a, 2022b).

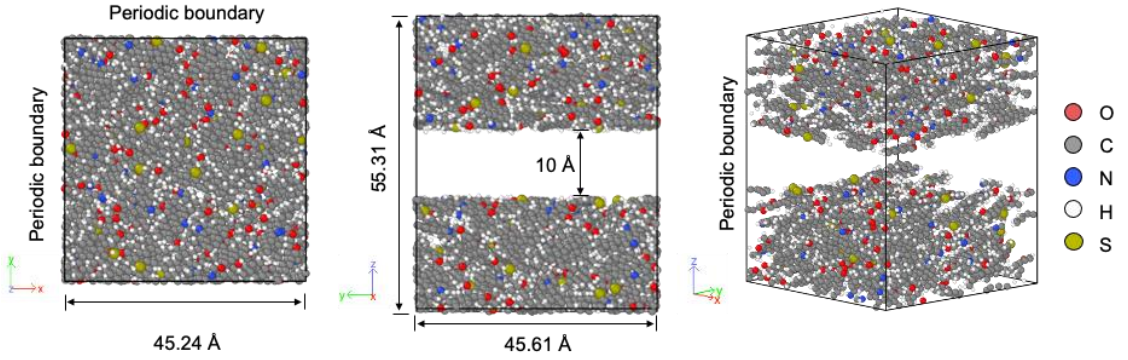

Figure 5.1 Schematic of the kerogen slit pore model with boundary conditions.

Hybrid GCMC-MD simulations are performed to achieve the initial state of gas saturation while allowing the kerogen matrix to deform sufficiently in the meantime. The GCMC input chemical potentials for various CO_2-CH_4 compositions and total gas pressures are calculated from the Peng-Robinson equation of state (Peng and Robinson, 1976) and have been testified in another set of GCMC-MD simulations with an empty simulation box in the absence of kerogen (see Table 5.S1 and Figure 5.S1 in the supplementary materials). GCMC exchanges of gas molecules are conducted 50 times for CO_2 and 50 times for CH_4, respectively, after every 100 MD steps. The simulation is ceased when the numbers of CO_2 and CH_4 molecules converge after a typical period of 4 ns of MD relaxation. The NEMD simulation is subsequently conducted to generate pressure-driven flow by applying a force of 0.001 kcal/(mol·Å) on each gas particle (i.e., C, O and united CH_4 atoms) in the *x*-direction within the slit. The pressure drop along the slit pore length is calculated as

$$\Delta p = \frac{n_a F_a + n_b F_b + \cdots}{A} \tag{5.1}$$

where n_a and n_b are the numbers of particles a and b, F_a and F_b are the forces applied on particles a and b, and A is the pore cross-section area. It has been shown that the pressure drop

only depends on the total force imposed on the gas particles and the same velocity profile can always be obtained no matter how the constant total force is distributed among them (Li et al., 2019). Given sufficient running time of ~15 ns, the gas molecules can eventually reach a steady flowing state. The data between simulation time of 15 and 30 ns (and beyond) are selected to produce the velocity and density profiles of both CO_2 and CH_4 through spatial binning every 0.5 Å across the *z*-direction with a sampling frequency of 10 fs. Although only one kerogen type is used in this study, the reported data points are averaged values from over 1500,000 statistical samples, which represent 1500,000 different configurations of kerogen structures under a designed gas pressure and composition with the kerogen flexibility.

All the simulations are performed using LAMMPS (Thompson et al., 2021) with a timestep of 1 fs under the NVT ensemble (constant atom number, volume, and temperature) at 300 K. Periodic boundary conditions are applied in the *x*-, *y*- and *z*-directions. OVITO (Stukowski, 2009) is used for the visualisation of kerogen matrix and gas molecules. The CO_2 and CH_4 partial pressures and bulk molar compositions of the 60 Å and 40 Å slit pores are measured in a prescribed pore central region of height 10 Å, where the interaction from the kerogen surfaces is minimised. However, the bulk region is no longer identifiable when the pore size becomes smaller than 20 Å and the gas pressure cannot be directly measured within the pore. As an approximation, the average pressure from the bulk gas (without kerogen in the box) and large pore (60 Å and 40 Å) simulations that have the same inputted chemical potentials are used (Table 5.S1).

5.3 Results and discussion

5.3.1 Density profiles

The CO_2-CH_4 mixture manifests different adsorption behaviours with respect to pore pressure, gas composition and pore size. A wide range of pore pressure is used here for a systematic

investigation of the selectivity dependence on pressure, which may occur at different geological depths and reservoir depletion/CO_2 injection conditions. Figure 5.2 provides an overview of the equimolar mixture adsorption in the kerogen slit pores of different sizes. It can be seen that in the 60 Å slit pore, a greater amount of CO_2 and CH_4 molecules distribute near the kerogen surfaces than in the pore centre, while the difference gradually disappears as the pressure increases. In contrast, the entire 10 Å slit pore seems to be filled with gas molecules even at low pressure.

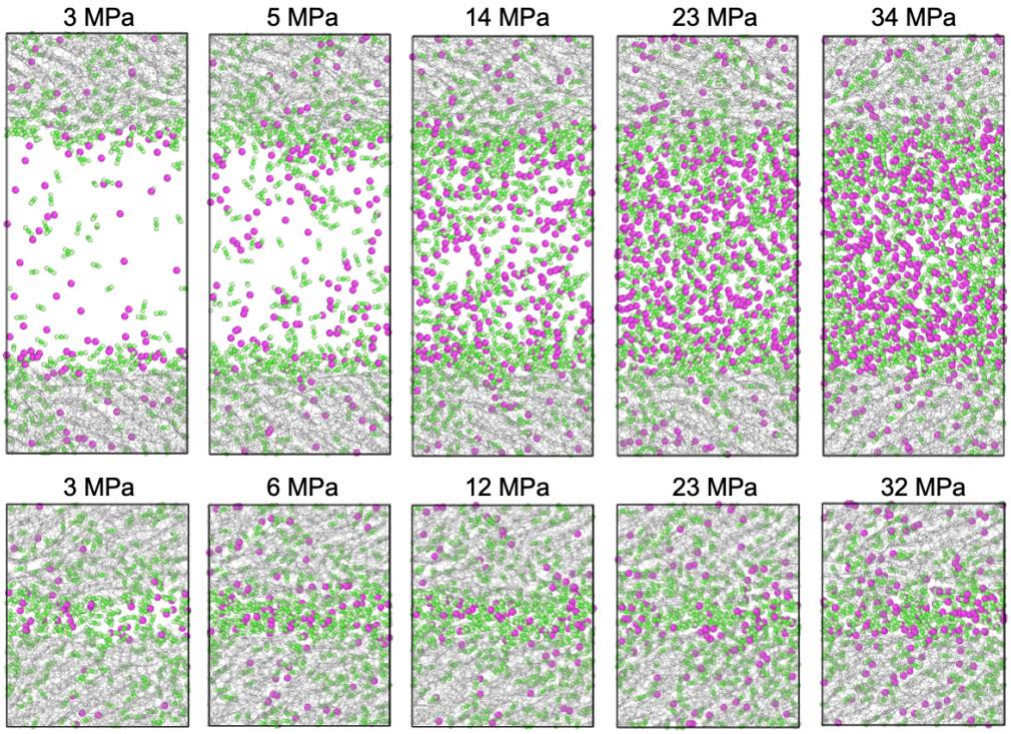

Figure 5.2 Illustration of CO_2 (green) and CH_4 (plum) distributions in kerogen (grey) slit pores of 60 Å (first row) and 10 Å (second row) under varied pore pressures. The CO_2 bulk molar ratio in the mixture ranges from 50% to 55% (close to 1:1 CO_2-CH_4 mixture).

As shown in Figure 5.3a, under the total gas pressure of ~3.0 MPa, both CO_2 and CH_4 form adsorption peaks close to the upper and lower kerogen surfaces in the 60 Å slit pore, and rise with the increase of the individual gas molar ratio in the bulk mixture. Compared with CH_4,

CO_2 has a much higher adsorption peak due to its stronger interaction force with the kerogen surface (Ho and Wang, 2021). The CO_2 peak is 13 times that of CH_4 under the CO_2:CH_4 bulk molar ratio of ~3:1 and three times under ~1:1. The results suggest that CO_2 can displace the CH_4 adsorbed at the kerogen surfaces even at low pressure and accumulate there before saturating the pore central region. With the gas pressure increase, the adsorption peaks start to ease out. This is evidenced in Figure 5.3b, where the relative difference between the adsorption peaks and the bulk densities is not as significant as that shown in Figure 5.3a. At 29% and 50% of CH_4 (i.e., 71% and 50% of CO_2), the adsorption peaks of CH_4 near the kerogen surfaces disappear entirely. The ratio of CO_2 and CH_4 adsorption peak heights also become smaller as a result of the high pressure: 3.6 under the CO_2:CH_4 bulk molar ratio of ~3:1 and 1.4 under ~1:1. It is also worth noting from Figure 5.3 that the adsorption layer is wider than one gas molecule size at the amorphous rough kerogen surfaces as indicated by the width of peaks in the density profiles.

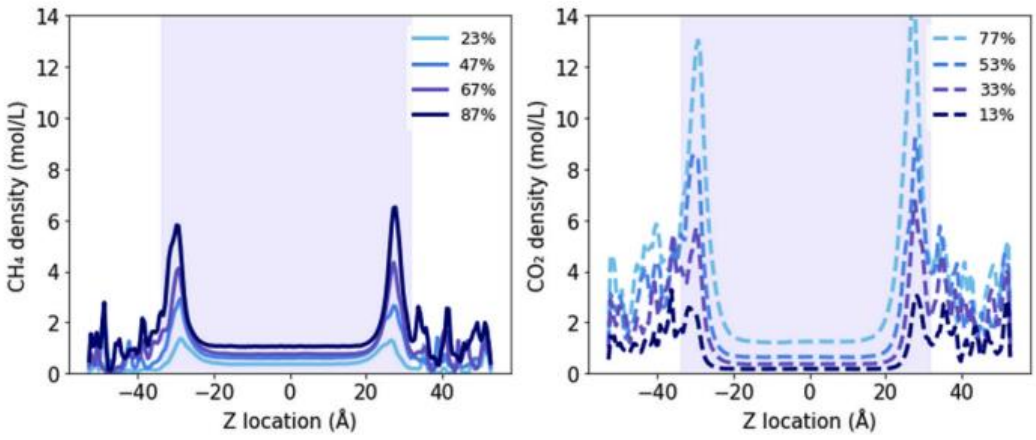

(a)

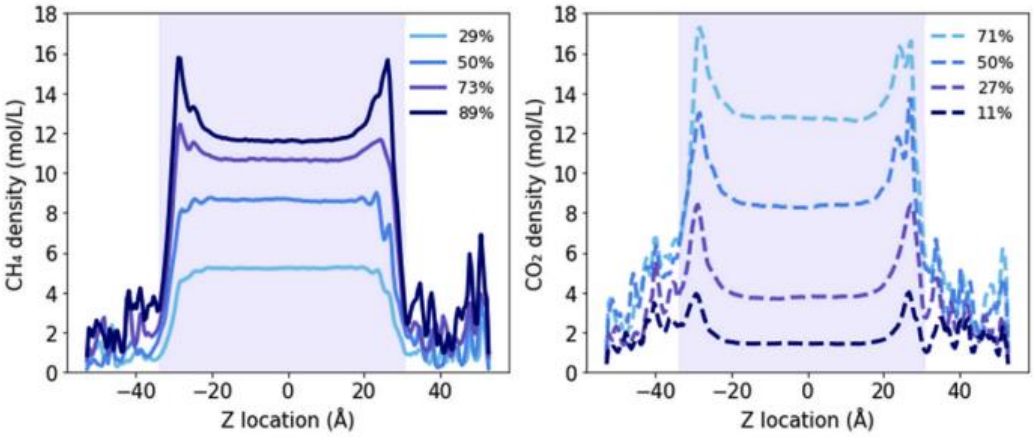

(b)

Figure 5.3 CH_4 and CO_2 density distributions in the kerogen slit pore of 60 Å. Two typical pressure levels of (a) 3.0 ± 0.4 MPa and (b) 31.3 ± 1.6 MPa with the characteristic difference in density profiles are chosen. The gas compositions are signified by the varied colours according to their bulk molar ratios.

In the 10 Å slit pore, the extreme nano-confinement leads to no distinction of the gas bulk region, with the two adsorption peaks at the upper and lower surfaces collapsing into one as shown in Figure 5.4 (also noticeable in Figure 5.2). The pore boundaries are difficult to identify as the kerogen surfaces are amorphous and move upon adsorption. The adsorption region somewhat extends into the kerogen matrix and looks wider than 10 Å, which is the initial shortest distance between the two kerogen surfaces. Similarly, the adsorption density increases with the increase in the individual gas molar ratio under the constant total gas pressure. When the gas pressure is close to 30 MPa, the CH_4 adsorption is greatly enhanced, but this is not clearly seen for the CO_2 adsorption by comparing Figures 5.4a and b. This indicates that the maximum CO_2 adsorption at the kerogen surfaces can be reached under a relatively small pressure. The slit pore gas adsorption amount is determined as the sum of the free gas in the bulk and the adsorbed gas at the surfaces from the density profiles, shown as the shaded area in Figures 5.3 and 5.4, and will be used for further discussions below.

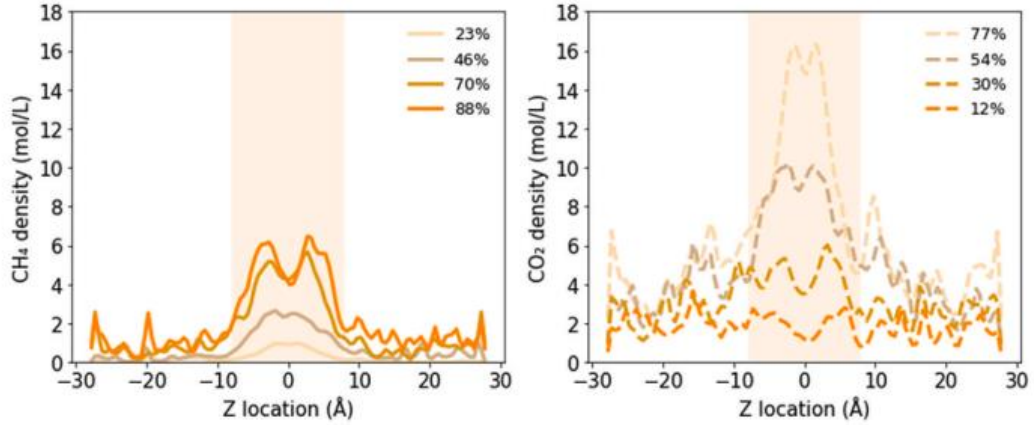

(a)

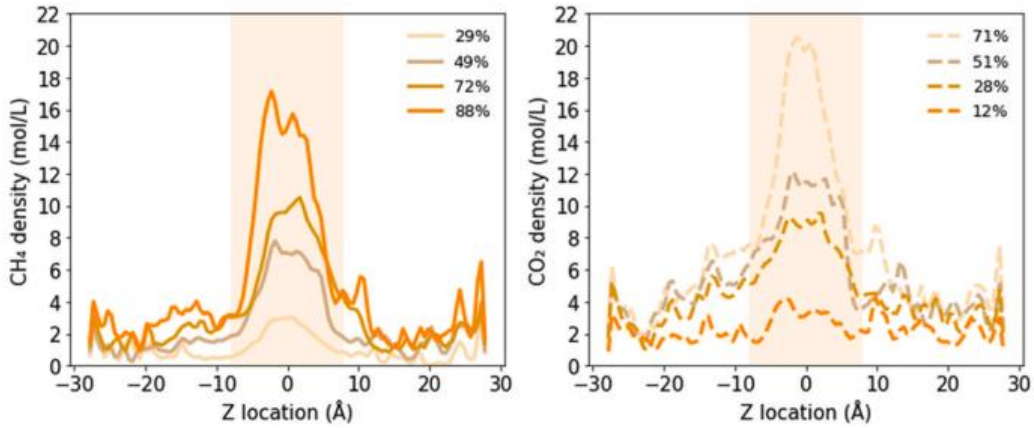

(b)

Figure 5.4 CH_4 and CO_2 density distributions in the kerogen slit pore of 10 Å. Two typical pressure levels of (a) 2.6 ± 0.2 MPa and (b) 29.9 ± 1.0 MPa with the characteristic difference in density profiles are chosen. The gas composition is signified by varied colours according to bulk molar ratios.

5.3.2 Velocity profiles and relationship with CO_2 composition

The mass transport velocity profiles are calculated as the multiplication of density and velocity profiles for CO_2 and CH_4, respectively, and presented in Figure 5.5. For easy comparison, they are normalised by the corresponding maximum mass velocity across the slit pore. A parabolic velocity profile is observed across the slit pore in all the simulated cases. The total mass flux

throughout the matrix is marginal (the tiny peaks near zero at two sides of the parabola) compared to the slit pore, suggesting that large slit nanopores are the main pathways for gas transport. Therefore, we only focus on the gas transport in the slit pore in this study. There is observable fast mass transport near the kerogen surfaces at lower pressures as shown in Figures 5.5a and b. This phenomenon is widely reported in the literature as surface diffusion (Liu et al., 2021; Yu et al., 2018; Zhao et al., 2022). As the gas pressure further increases to ~13 MPa and above, the diffusion-facilitated fast transport near kerogen surfaces becomes minimal and the mass transport is dominated by the viscous flow in the bulk gas region (Figure 5.5c). Another interesting aspect to notice is that CH_4 surface diffusion is not as highlighted as CO_2 because of the preferential adsorption of CO_2 over CH_4 at kerogen surfaces, which suggests the possible selective mass transport between CO_2 and CH_4 with CO_2 having a large contribution from the surface adsorption to the total mass flux (the total mass flux is the integration of the mass transport velocity profile). The CO_2 and CH_4 mass transport profiles tend to be identical at high pressure. According to Figure 5.5 overall, the CO_2-CH_4 composition does not seem to have any noticeable impact on the normalised mass transport profiles.

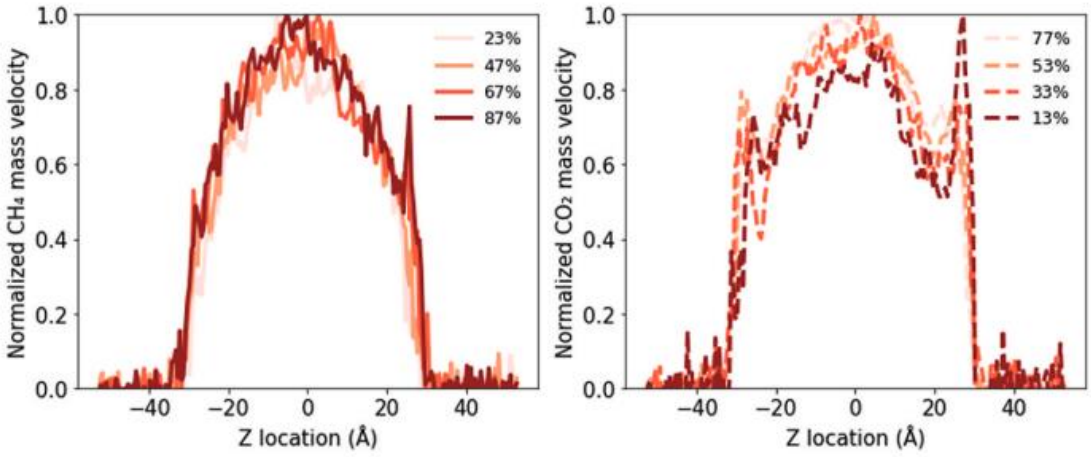

(a)

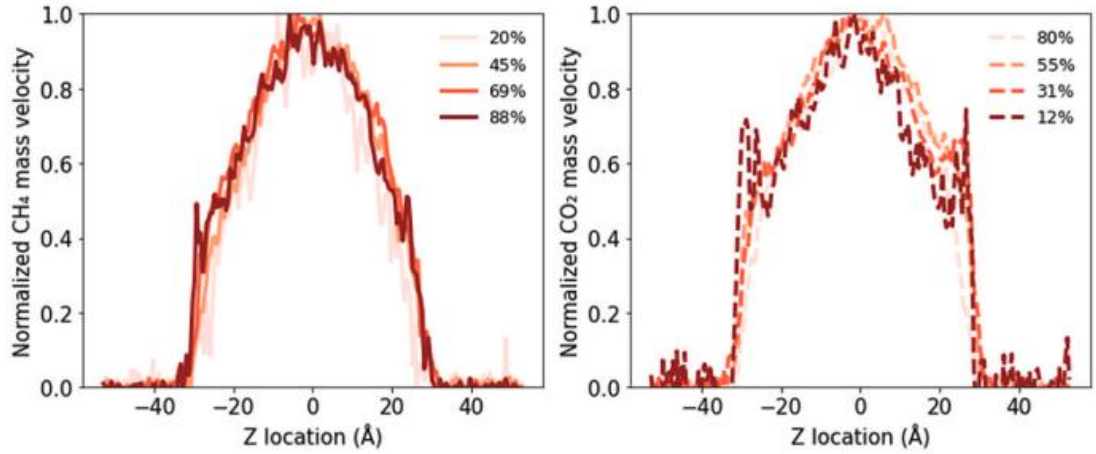

(b)

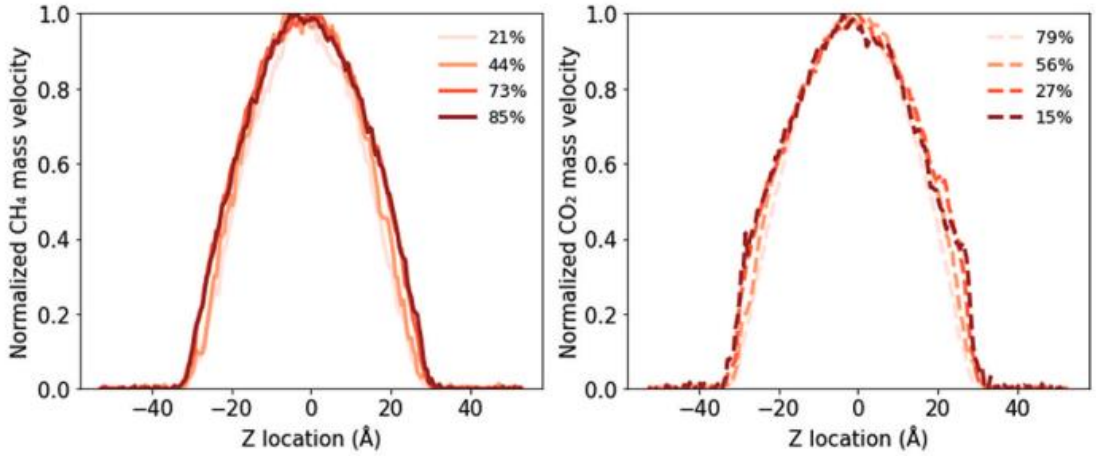

(c)

Figure 5.5 Representative normalised CH_4 and CO_2 mass velocity profiles in the 60 Å kerogen slit pore under a pore pressure of (a) 3.0 ± 0.4 MPa, (b) 6.0 ± 0.7 MPa and (c) 12.8 ± 0.7 MPa . The varied colours show the change in CH_4 and CO_2 compositions in the bulk.

The average gas mixture velocity (i.e., the volumetric flux divided by the initial pore size) under a unit pressure drop (i.e., normalised by the pressure drop) in the slit pores with size from 10 to 60 Å is plotted as a function of the CO_2 molar ratio in the bulk in Figure 5.6. In general, the gas velocity drops fast with the pore size decrease ($V_{ave} \propto H^2$ in Hagen-Poiseuille flow, where V_{ave} is the average gas velocity and H is the pore size). CO_2 is a more viscous fluid than

CH_4 at 300 K (Linstrom and Mallard, 2022). The addition of CO_2 increases the viscosity of the CO_2-CH_4 gas mixture, reducing the gas velocity under a given pressure by following a logarithmic decay (Figures 5.6a, b and c). The fitted declining slope seems sharp at low pore pressures and gradually levels off at higher pressures. As the CO_2 molar ratio further increases in the bulk mixture, the average gas velocity tends to converge to a constant value, especially when the gas pressure is above 6 MPa. The main reason can be ascribed to the high CO_2 viscosity that constrains the gas mixture velocity within a low range after it transfers from the vapour to liquid phase (~6.7 MPa for pure phase (Linstrom and Mallard, 2022)). The gas mixture velocity dependence on the CO_2 bulk molar ratio becomes weak in the slit pore of 10 Å as seen in Figure 5.6d. As discussed in Section 5.3.1, the free gas region completely disappears in the pore centre under the extreme confinement and the mass transport is dominated by the surface diffusion of the adsorbed phase. Therefore, the gas mixture velocity dependence on the CO_2 bulk ratio does not exactly follow the one in the 20-60 Å slit pores where the viscous flow is more pronounced (e.g., the case of 22.3 MPa). The noises are also likely related to the kerogen deformation since the adsorbed phase on the surfaces is affected more significantly by the kerogen surface morphology in the 10 Å slit pore. The average velocity in a single channel is usually calculated by the Hagen-Poiseuille equation ($V_{ave} = \frac{H^2 \nabla p}{12\mu}$, where μ is the viscosity). In the case of nano-confined CO_2-CH_4 mixtures, the viscosity greatly deviates from the bulk one due to the strong gas-gas and gas-solid interactions (Firouzi and Wilcox, 2013; Wang et al., 2016). As it will be difficult to mathematically derive the velocity dependence on gas composition and pressure, future research may consider looking into the logarithmic decrease observed from our MD simulations.

After CO_2 is injected into the shale reservoir, it flows through the fracture network and diffuses into the organic matrix. Through competitive adsorption, CH_4 starts to desorb while CO_2 adsorbs. The gas mixture flowing towards the production well initially contains a large portion of CH_4, while CO_2 gradually increases its percentage in the gas mixture as CH_4 is depleted. It can be inferred that the overall gas production rate may decrease during the described process

according to the dependence of gas velocity on the CO_2 ratio. In addition, the pressure sensitivity of the gas mixture velocity indicates that the CO_2 injection at a shallow geological depth under lower pressure may experience more fluctuation in recovery rate during the production process.

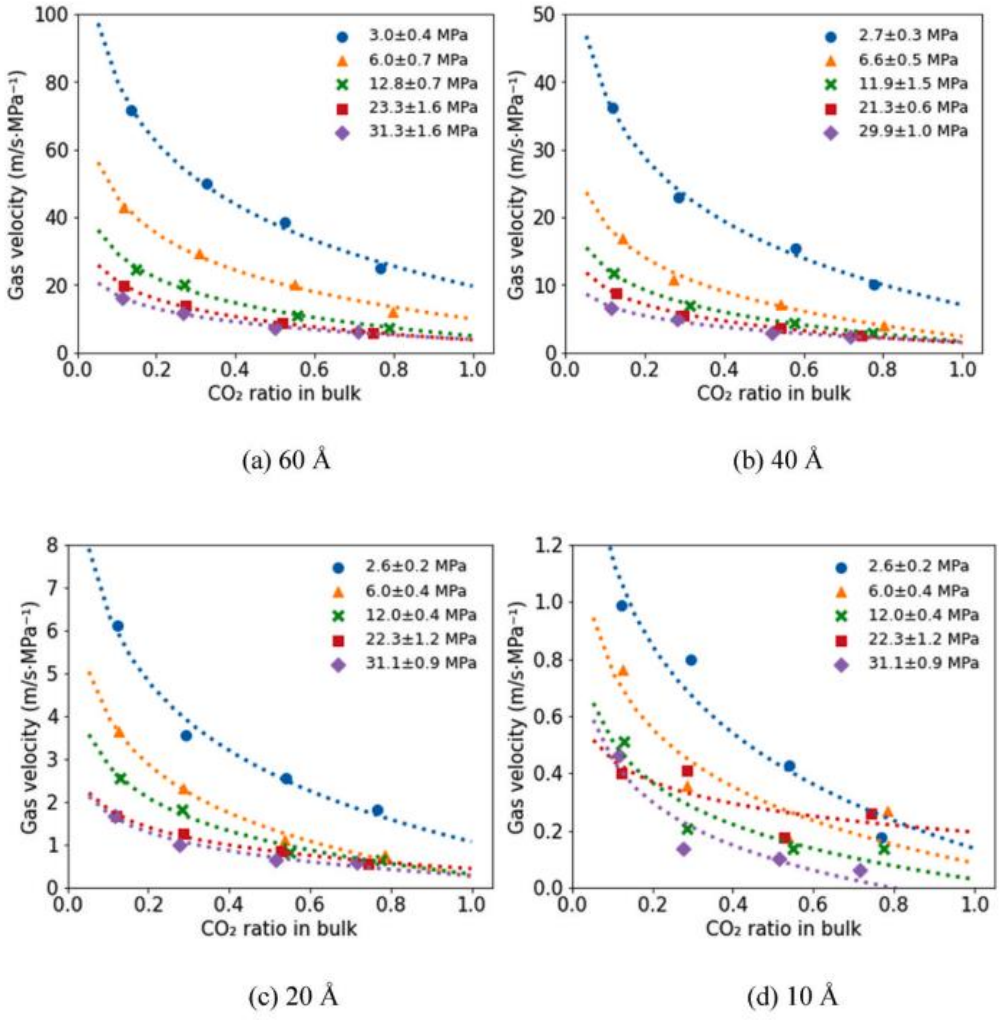

Figure 5.6 Normalised average CO_2-CH_4 gas mixture velocity as a function of the CO_2 molar ratio in the bulk phase across the kerogen slit pores of size (a) 60, (b) 40, (c) 20 and (d) 10 Å. The coloured symbols indicate varied total pore gas pressures, and the dotted lines are showing logarithmical fittings of the data.

5.3.3 Adsorption selectivity

The competitive adsorption between CO_2 and CH_4 is commonly described by the adsorption selectivity

$$S_{ad} = \frac{n_{CO2}/n_{CH4}}{y_{CO2}/y_{CH4}} \tag{5.2}$$

where n_{CO2} and n_{CH4} are the absolute adsorption amounts of CO_2 and CH_4 in the slit pores, and y_{CO2} and y_{CH4} are the bulk molar ratios of CO_2 and CH_4. It can be seen from Figure 5.7 that CO_2 is always preferentially adsorbed in the kerogen slit pore compared with CH_4 since the selectivity is greater than one in all the simulated cases. From 60 to 10 Å, the selectivity of CO_2 over CH_4 turns out to be more and more pronounced as the adsorbed density peaks at the lower and upper surfaces start to merge under the strong fluid-wall interactions: 1.1-2.0 in 60 Å (Figure 5.7a), 1.2-2.4 in 40 Å (Figure 5.7b), 1.5-2.9 in 20 Å (Figure 5.7c) and 1.7-6.5 in 10 Å (Figure 5.7d). The values generally agree well with experimental measurements. For example, the reported adsorption selectivities for organic-rich shale samples collected from the lower Silurian Longmaxi formation are 2.13-5.65 (323.15 K, < 20 MPa) (Xie et al., 2022), 3.43-5.81 (303.15 K, 2-10 MPa) (Liu et al., 2019), and 3-8 (300-330 K, 1-11 MPa) (Lu et al., 2022). The CO_2/CH_4 selectivity shows a linear-like decreasing trend (Ho et al., 2018; Huang et al., 2018) with the increase of the total gas pressure and the CO_2/CH_4 adsorption ratio approaches their ratio in the bulk phase (i.e., CO_2/CH_4 adsorption selectivity of ~1) at high pressures, possibly attributed to the smaller difference between the bulk gas density in the pore centre and adsorption density at the surfaces (e.g., the contribution from the surface adsorption peaks to the slit pore adsorption becomes less significant). In comparison, the adsorption sites can be quickly taken over by CO_2 molecules at a low pore pressure. The accumulation of CO_2 near the kerogen surfaces in a great number causes a large density difference from the less-saturated bulk, taking control of the total absolute gas adsorption amount in the slit pore. The adsorption selectivity seems not sensitive to the CO_2/CH_4 molar ratio. Theoretically, gas molecules will be adsorbed on the high-energy sites at low pressure, and the high-energy sites

become gradually occupied as the pressure increases (Li et al., 2019). In the case of CO_2 and CH_4 mixtures, we understand that CO_2 may always quickly take over the high-energy sites at low pressure, and CH_4 only starts competing with CO_2 for low-energy sites at high pressure (Huang et al., 2018). Since it is difficult for CH_4 to be adsorbed on the high-energy sites with CO_2 present, varying its ratio will not significantly affect the adsorption selectivity. In their experimental study, Qin et al. (2021a) also found that the CO_2/CH_4 adsorption selectivity varied slightly with the increasing CH_4 proportion in the mixed gas. The underlying mechanisms will be interesting for future investigations.

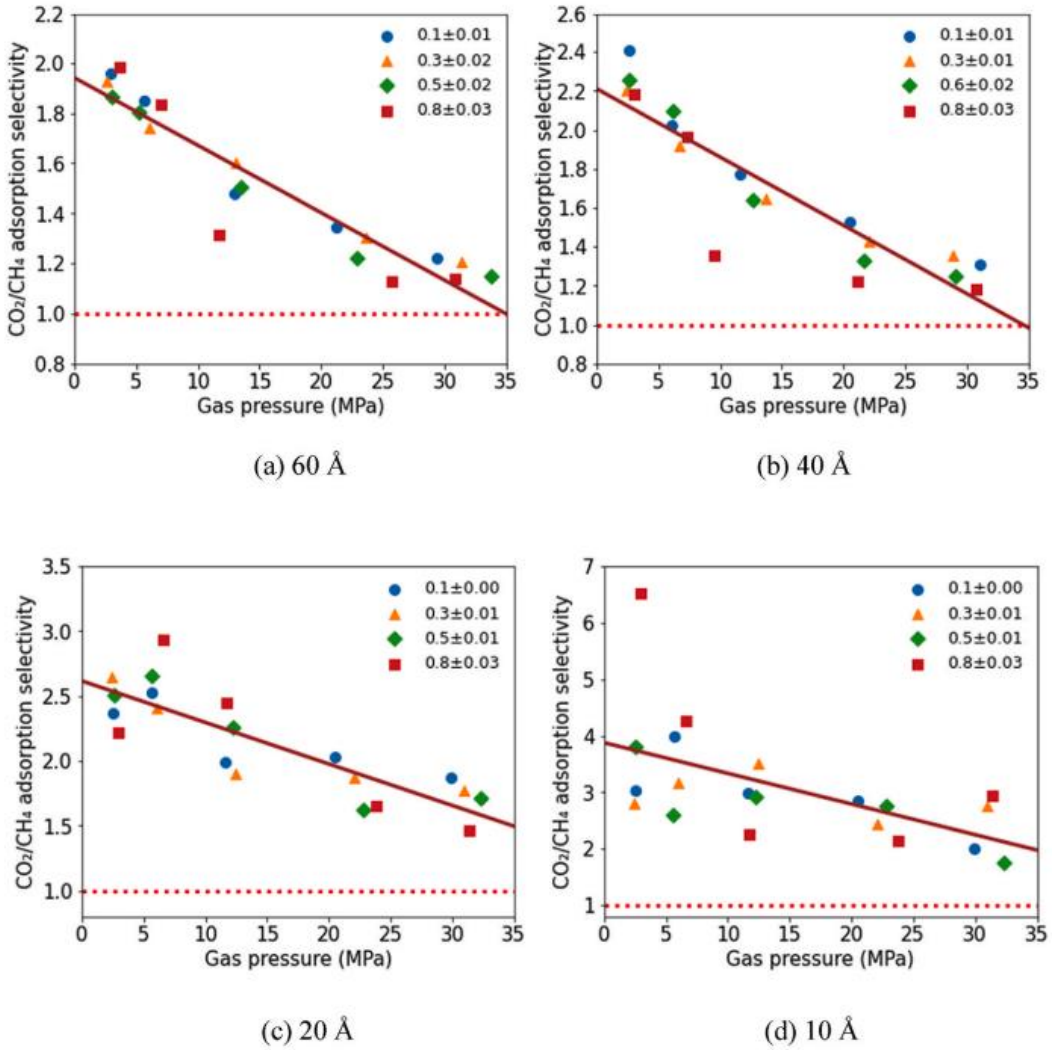

Figure 5.7 CO_2/CH_4 adsorption selectivity as a function of pore gas pressure in the kerogen slit pores of size (a) 60, (b) 40, (c) 20 and (d) 10 Å. The coloured symbols indicate varied CO_2 molar ratios in the

bulk mixture.

5.3.4 Mass transport selectivity

The selective mass transport of the CO_2-CH_4 mixture is analysed as the mass transport selectivity

$$S_{mt} = \frac{f_{CO2}/f_{CH4}}{y_{CO2}/y_{CH4}} \tag{5.3}$$

where f_{CO2} and f_{CH4} are the molar mass fluxes of CO_2 and CH_4 in the slit pores. Figure 5.8 presents the calculated mass transport selectivity as a function of gas pressure. It shows that the mass flux of CO_2 is generally higher than CH_4 regardless of their composition in the mixture and the slit pore size, with a maximum $S_{mt} = 7$ under ~3 MPa in the 10 Å slit pore. The CO_2/CH_4 mass flux selectivity follows a similar trend as their adsorption selectivity with respect to the total gas pressure. This is because the mass flux is calculated from the integral of the mass velocity profile, and the preferential adsorption of CO_2 near the kerogen surfaces significantly contributes to the transport difference in masses. When the pore size decreases, the CO_2/CH_4 mass flux selectivity is also magnified, similar to the pattern of the adsorption selectivity. In large-scale continuum models, the CO_2/CH_4 transport selectivity is not commonly considered when simulating CO_2-EGR. However, the results here suggest that CO_2-CH_4 mixtures can show significant separation in the nanoporous organic matrix, which may affect the overall performance of the CO_2 injection and CH_4 production. Since gas transport within the organic matrix is often approximated as a diffusion process, a lumped CO_2/CH_4 transport selectivity can be potentially calculated for the organic matrix according to its nanopore size distribution and incorporated into the continuum-scale model as a ratio of diffusion rates.

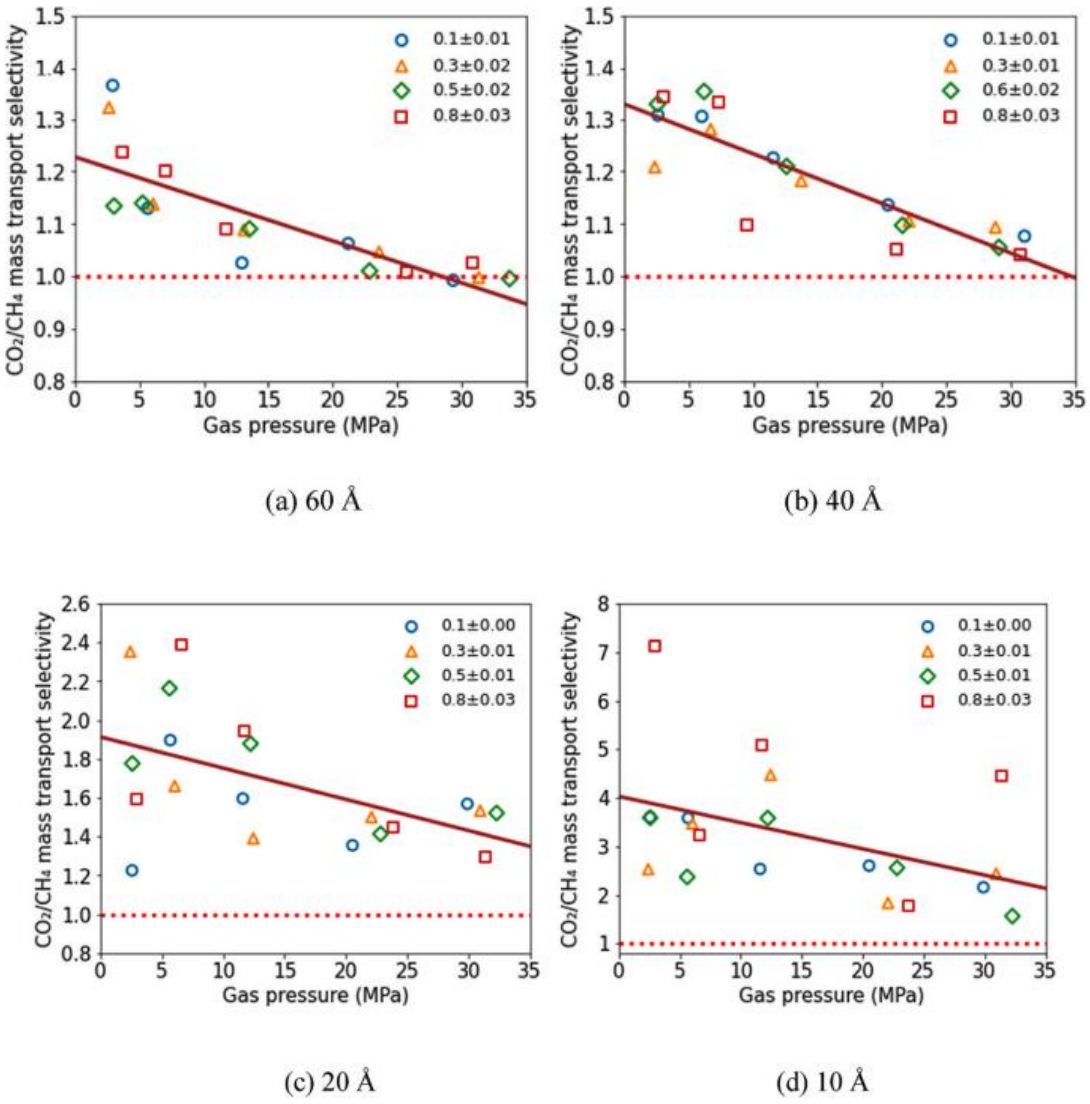

Figure 5.8 CO_2/CH_4 mass transport selectivity as a function of pore gas pressure in the kerogen slit pores of size (a) 60, (b) 40, (c) 20 and (d) 10 Å. The coloured symbols indicate the varied CO_2 molar ratios in the bulk mixture.

A summary of data with statistical analysis is provided in Figure 5.9 to highlight the impact from several factors such as pore size, gas composition and surface diffusion on the mass transport selectivity. As can be seen from Figure 5.9a, the CO_2/CH_4 mass flux selectivity goes down hyperbolically from 10 Å to 60 Å. In smaller nanopores, the CO_2/CH_4 mass flux selectivity spans over a much wider range (i.e., pressure-related variation). The variation of the

mass flux selectivity eventually converges to a value close to unity as the pore size reaches 40 Å and above. In terms of the mixture composition, there is no strong evidence showing that the CO_2/CH_4 mass flux selectivity is correlated with the CO_2 molar ratio, as reported in Figure 5.9b.

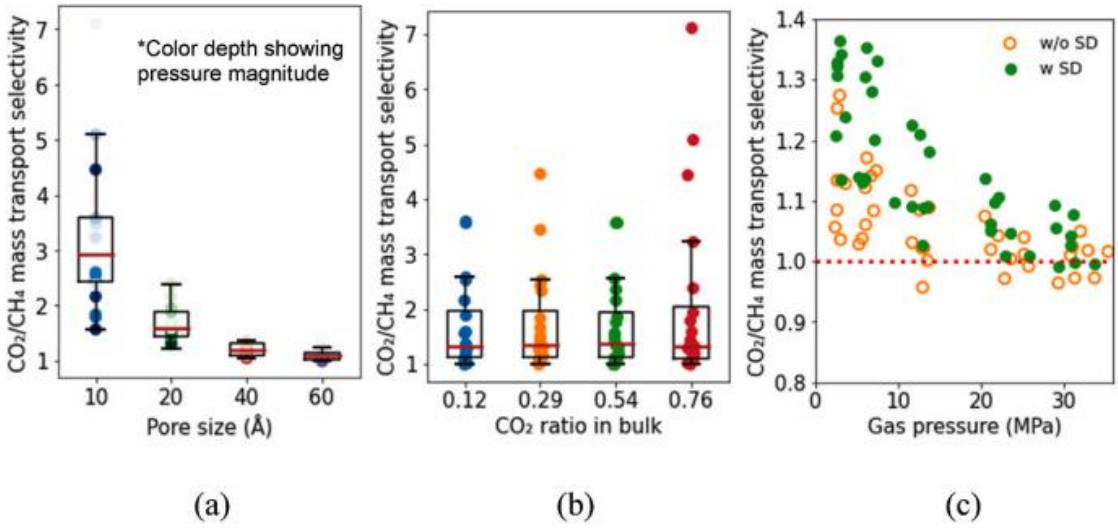

Figure 5.9 CO_2/CH_4 mass transport selectivity as a function of (a) pore size and (b) CO_2 molar ratio in the bulk mixture. (c) CO_2/CH_4 mass transport selectivity in the entire slit pore with surface diffusion (w SD) and bulk gas region without surface diffusion (w/o SD) (only showing the data in the 60 and 40 Å slit pores).

Coal has many similarities to kerogen as organic matter. Zhao et al. (2016) have found that the transport diffusivity of CO_2 is always greater than that of CH_4 in coal matrix and the diffusion selectivity drops monotonically with the increasing pressure. In small pores, the diffusion flux dominates over the viscous flux since there is no distinguishable bulk gas region so that the mass flux selectivity can reach very high. In large pores, the viscous flux would be more considerable than the diffusion flux. Viscous flow is driven by a pressure gradient and there is no selective transport when CO_2 and CH_4 are miscible gases flowing as a whole, and thus the mass flux selectivity would approach one. In order to evaluate the contribution of the surface

diffusion to the selective gas transport, the CO_2/CH_4 mass flux in the bulk region (60 Å and 40 Å pores) is isolated for the selectivity calculation as shown in Figure 5.9c. It can be seen that the CO_2/CH_4 mass flux selectivity becomes much closer to one after removing the contributions from the surface diffusion, suggesting the two individual components in the gas mixture flow at a similar rate in the bulk region of the slit pore. The effect of bulk diffusion can still be noticed when the pore gas pressure is smaller than 10 MPa, consistent with the findings in Zhao et al. (2016).

5.4 Conclusions

In this study, we have systematically investigated the selective adsorption and transport of CO_2-CH_4 mixture with varied compositions in kerogen slit pores. It is revealed that both CO_2/CH_4 adsorption and transport selectivities are negatively correlated with the pore gas pressure and pore size, while not strongly affected by the CO_2/CH_4 bulk ratio. Although bulk diffusion can cause CO_2/CH_4 velocity separation, the selective mass transport of CO_2-CH_4 mixture is mostly resulted from the stronger surface diffusion of CO_2 that has a significant adsorbed amount at the kerogen surfaces. It is also worth noting that the average velocity of CO_2-CH_4 mixture in the kerogen slit pore decreases logarithmically with the increase of CO_2 molar ratio in the bulk phase. Such decrease becomes especially significant when the gas pressure is low in large pores. These new results indicate that the selective mass transport of CO_2-CH_4 in low-porosity shale reservoirs is important and should not be neglected in the large-scale simulations of CO_2-EGR.

Acknowledgments

This work was supported in part by the Australian Research Council through Discovery Projects (DP200101919 and DP190102954). The authors acknowledge the use of the National

Computational Infrastructure (NCI) which is supported by the Australian Government, and accessed through the Sydney Informatics Hub HPC Allocation Scheme, which is supported by the Deputy Vice-Chancellor (Research), University of Sydney.

References

1. Eggimann, B. L., Sun, Y., DeJaco, R. F., Singh, R., Ahsan, M., Josephson, T. R., & Siepmann, J. I. (2019). Assessing the quality of molecular simulations for vapour-liquid equilibria: An analysis of the TraPPE database. *Journal of Chemical & Engineering Data, 65*(3), 1330-1344.

2. Firouzi, M., & Wilcox, J. (2013). Slippage and viscosity predictions in carbon micropores and their influence on CO_2 and CH_4 transport. *The Journal of Chemical Physics, 138*(6), 064705.

3. GHD. (2022). New global carbon capture, utilisation and storage team leads on world's largest project, https://www.ghd.com/en/news/new-global-carbon-capture-utilisation-and-storage-team-leads-on- world-s-largest-project.aspx.

4. Gou, Q., Xu, S., Hao, F., Yang, F., Shu, Z., & Liu, R. (2021). The effect of tectonic deformation and preservation condition on the shale pore structure using adsorption-based textural quantification and 3D image observation. *Energy, 219*, 119579.

5. Ho, T. A., & Wang, Y. (2020). Pore size effect on selective gas transport in shale nanopores. *Journal of Natural Gas Science and Engineering, 83*, 103543.

6. Ho, T. A., & Wang, Y. (2021). Molecular origin of wettability alteration of subsurface porous media upon gas pressure variations. *ACS Applied Materials & Interfaces, 13*(34), 41330-41338.

7. Ho, T. A., Wang, Y., Xiong, Y., & Criscenti, L. J. (2018). Differential retention and release

of CO_2 and CH_4 in kerogen nanopores: Implications for gas extraction and carbon sequestration. *Fuel, 220*, 1-7.

8. Hockney, R. W., & Eastwood, J. W. (1988). *Computer simulation using particles*. *CRC Press*.

9. Hu, Y., Liu, G., Luo, N., Gao, F., Yue, F., & Gao, T. (2022). Multi-field coupling deformation of rock and multi-scale flow of gas in shale gas extraction. *Energy, 238*, 121666.

10. Huang, L., Ning, Z., Wang, Q., Zhang, W., Cheng, Z., Wu, X., & Qin, H. (2018). Effect of organic type and moisture on CO_2/CH_4 competitive adsorption in kerogen with implications for CO_2 sequestration and enhanced CH_4 recovery. *Applied Energy, 210*, 28-43.

11. Huang, P., Shen, L., Maggi, F., Chen, Z., & Pan, Z. (2022). Influence of surface roughness on methane flow in shale kerogen nano-slits. *Journal of Natural Gas Science and Engineering*, *103*, 04650.

12. Javadpour, F., Fisher, D., & Unsworth, M. (2007). Nanoscale gas flow in shale gas sediments. *Journal of Canadian Petroleum Technology, 46*(10), PETSOC-07-10-06.

13. Javadpour, F., Singh, H., Rabbani, A., Babaei, M., & Enayati, S. (2021). Gas flow models of shale: A review. *Energy & Fuels, 35*(4), 2999-3010.

14. Kang, D., Wang, X., Zheng, X., & Zhao, Y.-P. (2021). Predicting the components and types of kerogen in shale by combining machine learning with NMR spectra. *Fuel, 290*, 120006.

15. Kazemi, M., & Takbiri-Borujeni, A. (2017). Selective adsorption and transport diffusion of CO_2-CH_4 binary mixture in carbon-based organic nanopores. S*PE Western Regional Meeting*, SPE-185623-MS.

16. Klewiah, I., Berawala, D. S., Alexander Walker, H. C., Andersen, P. Ø., & Nadeau, P. H. (2020). Review of experimental sorption studies of CO_2 and CH_4 in shales. *Journal of Natural Gas Science and Engineering, 73*, 103045.

17. Li, J., & Sun, C. (2022). Molecular insights on competitive adsorption and enhanced displacement effects of CO_2/CH_4 in coal for low-carbon energy technologies. *Energy, 261*, 125176.

18. Li, J., Wu, K., Chen, Z., Wang, W., Yang, B., Wang, K., . . . Yu, R. (2019). Effects of energetic heterogeneity on gas adsorption and gas storage in geologic shale systems. *Applied Energy, 251*, 113368.

19. Li, Z., Jun, Y., & Kou, J. (2019). Mixture composition effect on hydrocarbon-water transport in shale organic nanochannels. *The Journal of Physical Chemistry Letters, 10*(15), 4291-4296.

20. Linstrom, P., & Mallard, W. (2022). NIST chemistry WebBook, NIST standard reference database number 69, National Institute of Standards and Technology, Gaithersburg MD, 20899.

21. Liu, B., Qi, C., Mai, T., Zhang, J., Zhan, K., Zhang, Z., & He, J. (2018). Competitive adsorption and diffusion of CH_4/CO_2 binary mixture within shale organic nanochannels. *Journal of Natural Gas Science and Engineering, 53*, 329-336.

22. Liu, F., Ellett, K., Xiao, Y., & Rupp, J. A. (2013). Assessing the feasibility of CO_2 storage in the New Albany Shale (Devonian–Mississippian) with potential enhanced gas recovery using reservoir simulation. *International Journal of Greenhouse Gas Control, 17*, 111-126.

23. Liu, J., Xie, L., Elsworth, D., & Gan, Q. (2019). CO_2/CH_4 competitive adsorption in shale: Implications for enhancement in gas production and reduction in carbon emissions. *Environmental Science & Technology, 53*(15), 9328-9336.

24. Liu, J., Yao, Y., Liu, D., & Elsworth, D. (2017). Experimental evaluation of CO_2 enhanced recovery of adsorbed-gas from shale. *International Journal of Coal Geology, 179*, 211-218.

25. Liu, K., Ostadhassan, M., Zhou, J., Gentzis, T., & Rezaee, R. (2017). Nanoscale pore structure characterisation of the Bakken shale in the USA. *Fuel, 209*, 567-578.

26. Liu, L., Nieto-Draghi, C., Lachet, V., Heidaryan, E., & Aryana, S. A. (2022). Bridging confined phase behaviour of CH_4-CO_2 binary systems across scales. *The Journal of Supercritical Fluids, 189*, 105713.

27. Liu, L., Wang, Y., & Aryana, S. A. (2021). Insights into scale translation of methane transport in nanopores. *Journal of Natural Gas Science and Engineering, 96*, 104220.

28. Louk, K., Ripepi, N., Luxbacher, K., Gilliland, E., Tang, X., Keles, C., . . . Michael, K. (2017). Monitoring CO_2 storage and enhanced gas recovery in unconventional shale reservoirs: Results from the Morgan County, Tennessee injection test. *Journal of Natural Gas Science and Engineering, 45*, 11-25.

29. Lu, T., Zeng, K., Jiang, P., Zhou, B., & Xu, R. (2022). Competitive adsorption in CO_2 enhancing shale gas: Low-field NMR measurement combined with molecular simulation for selectivity and displacement efficiency model. *Chemical Engineering Journal, 440*, 135865.

30. Martin, M. G., & Siepmann, J. I. (1998). Transferable potentials for phase equilibria. 1. United-atom description of n-alkanes. *The Journal of Physical Chemistry B, 102*(14), 2569-2577.

31. Neil, C. W., Mehana, M., Hjelm, R. P., Hawley, M. E., Watkins, E. B., Mao, Y., . . . Xu, H. (2020). Reduced methane recovery at high pressure due to methane trapping in shale nanopores. *Communications Earth & Environment, 1*(1), 49.

32. Peng, D.-Y., & Robinson, D. B. (1976). A new two-constant equation of state. *Industrial & Engineering Chemistry Fundamentals, 15*(1), 59-64.

33. Potoff, J. J., & Siepmann, J. I. (2001). Vapour-liquid equilibria of mixtures containing alkanes, carbon dioxide, and nitrogen. *AIChE Journal, 47*(7), 1676-1682.

34. Qin, C., Jiang, Y., Zhou, J., Song, X., Liu, Z., Li, D., . . . Xie, C. (2021a). Effect of supercritical CO_2 extraction on CO_2/CH_4 competitive adsorption in Yanchang shale.

Chemical Engineering Journal, 412, 128701.

35. Qin, C., Jiang, Y., Zuo, S., Chen, S., Xiao, S., & Liu, Z. (2021b). Investigation of adsorption kinetics of CH_4 and CO_2 on shale exposure to supercritical CO_2. *Energy, 236*, 121410.

36. Singh, U. (2013). Carbon capture and storage: An effective way to mitigate global warming. *Current Science, 105*(7), 914-922.

37. Stukowski, A. (2009). Visualisation and analysis of atomistic simulation data with OVITO – the Open Visualisation Tool. *Modelling and Simulation in Materials Science and Engineering, 18*(1), 015012.

38. Sui, H., Zhang, F., Wang, Z., Wang, D., & Wang, Y. (2020). Effect of kerogen maturity, water content for carbon dioxide, methane, and their mixture adsorption and diffusion in kerogen: A computational investigation. *Langmuir, 36*(33), 9756-9769.

39. Sun, H., Zhao, H., Qi, N., & Li, Y. (2017). Molecular insights into the enhanced shale gas recovery by carbon dioxide in kerogen slit nanopores. *The Journal of Physical Chemistry C, 121*(18), 10233-10241.

40. Sun, J., Chen, C., Zhang, Y., Li, W., & Song, Y. (2022). Competitive adsorption characteristics based on partial pressure and adsorption mechanism of CO_2/CH_4 mixture in shale pores. *Chemical Engineering Journal, 430*, 133172.

41. Sun, Z., Li, X., Liu, W., Zhang, T., He, M., & Nasrabadi, H. (2020). Molecular dynamics of methane flow behaviour through realistic organic nanopores under geologic shale condition: Pore size and kerogen types. *Chemical Engineering Journal, 398*, 124341.

42. Thompson, A. P., Aktulga, H. M., Berger, R., Bolintineanu, D. S., Brown, W. M., Crozier, P. S., . . . Nguyen, T. D. (2021). LAMMPS – A flexible simulation tool for particle-based materials modelling at the atomic, meso, and continuum scales. *Computer Physics Communications*, *271*, 108171.

43. Ungerer, P., Collell, J., & Yiannourakou, M. (2014). Molecular modelling of the volumetric

and thermodynamic properties of kerogen: Influence of organic type and maturity. *Energy & Fuels, 29*(1), 91-105.

44. Wang, J., Wolf, R. M., Caldwell, J. W., Kollman, P. A., & Case, D. A. (2004). Development and testing of a general amber force field. *Journal of Computational Chemistry, 25*(9), 1157-1174.

45. Wang, S., Javadpour, F., & Feng, Q. (2016). Fast mass transport of oil and supercritical carbon dioxide through organic nanopores in shale. *Fuel, 181*, 741-758.

46. Wang, T., Tian, S., Li, G., Sheng, M., Ren, W., Liu, Q., & Zhang, S. (2018). Molecular simulation of CO_2/CH_4 competitive adsorption on shale kerogen for CO_2 sequestration and enhanced gas recovery. *The Journal of Physical Chemistry C, 122*(30), 17009-17018.

47. Wang, Y., & Aryana, S. A. (2021). Coupled confined phase behaviour and transport of methane in slit nanopores. *Chemical Engineering Journal, 404*, 126502.

48. Wu, J., Huang, P., Maggi, F., & Shen, L. (2022a). Effect of sorption-induced deformation on methane flow in kerogen slit pores. *Fuel, 325*, 124886.

49. Wu, J., Huang, P., Maggi, F., & Shen, L. (2022b). Molecular investigation on CO_2-CH_4 displacement and kerogen deformation in enhanced shale gas recovery. *Fuel, 315*, 123208.

50. Wu, T., & Firoozabadi, A. (2018). Molecular simulations of binary gas mixture transport and separation in slit nanopores. *The Journal of Physical Chemistry C, 122*(36), 20727-20735.

51. Xie, W., Wang, M., Chen, S., Vandeginste, V., Yu, Z., & Wang, H. (2022). Effects of gas components, reservoir property and pore structure of shale gas reservoir on the competitive adsorption behaviour of CO_2 and CH_4. *Energy, 254*, 124242.

52. Yang, X., Chen, Z., Liu, X., Xue, Z., Yue, F., Wen, J., . . . Xue, Y. (2022). Correction of gas adsorption capacity in quartz nanoslit and its application in recovering shale gas resources by CO_2 injection: A molecular simulation. *Energy, 240*, 122789.

53. Yang, X., Zhou, W., Liu, X., & Yan, Y. (2020). A multiscale approach for simulation of shale gas transport in organic nanopores. *Energy, 210*, 118547.

54. Yu, H., Fan, J., Chen, J., Zhu, Y., & Wu, H. (2018). Pressure-dependent transport characteristic of methane gas in slit nanopores. *International Journal of Heat and Mass Transfer, 123*, 657-667.

55. Zendehboudi, S., & Bahadori, A. (2016). Shale oil and gas handbook: Theory, technologies, and challenges. *Gulf Professional Publishing*.

56. Zhao, Y., Feng, Y., & Zhang, X. (2016). Selective adsorption and selective transport diffusion of CO_2-CH_4 binary mixture in coal ultramicropores. *Environmental Science & Technology, 50*(17), 9380-9389.

57. Zhao, Y., Luo, M., Liu, L., Wu, J., Chen, M., & Zhang, L. (2022). Molecular dynamics simulations of shale gas transport in rough nanopores. *Journal of Petroleum Science and Engineering, 217*, 110884.

58. Zoback, M. D., & Gorelick, S. M. (2012). Earthquake triggering and large-scale geologic storage of carbon dioxide. *Proceedings of the National Academy of Sciences of the United States of America, 109*(26), 10164-10168.

Supplementary materials for

Selective adsorption and transport of CO_2-CH_4 mixture under nano-confinement

Jian Wu[a], Luming Shen[a, *], Pengyu Huang[a, b], Yixiang Gan[a, c]

[a] School of Civil Engineering, The University of Sydney, NSW 2006, Australia

[b] Hard Rock Mining, CSIRO Mineral Resources, QCAT, 1 Technology Court, Pullenvale, QLD 4069, Australia

[c] Sydney Nano Institute, The University of Sydney, NSW 2006, Australia

[*]Corresponding author. Email: luming.shen@sydney.edu.au

Table 5.S1 Relationship between chemical potentials and simulated CO_2-CH_4 gas mixture pressure/composition by GCMC-MD.

CO_2 molar ratio	μCO_2 (kcal/mol)	μCH_4 (kcal/mol)	Pmix (MPa)	CO_2 molar ratio	Pmix (MPa)	CO_2 molar ratio	Pmix (MPa)	CO_2 molar ratio	Pmix (MPa)	CO_2 molar ratio
PR-EOS[1]			Bulk[2]		60 Å centre[3]		40 Å centre[4]		Mean	
2 MPa[1]										
0.1	-7.05	-9.19	2.16	0.12	2.91	0.13	2.61	0.12	2.56	0.12
0.25	-7.15	-8.68	2.25	0.27	2.63	0.33	2.37	0.28	2.42	0.29
0.5	-7.39	-8.3	2.15	0.52	3.02	0.53	2.58	0.58	2.58	0.54
0.75	-7.78	-8.07	2.25	0.76	3.62	0.77	3.09	0.78	2.99	0.77
5 MPa[1]										
0.1	-6.55	-8.74	5.37	0.12	5.66	0.12	6.02	0.15	5.68	0.13
0.25	-6.66	-8.24	5.36	0.27	6.06	0.31	6.71	0.27	6.04	0.28
0.5	-6.88	-7.87	5.4	0.52	5.25	0.55	6.20	0.54	5.62	0.54
0.75	-7.26	-7.65	5.42	0.75	7.05	0.80	7.35	0.80	6.61	0.78
10 MPa[1]										
0.1	-6.2	-8.47	10.27	0.12	12.95	0.15	11.57	0.12	11.60	0.13
0.25	-6.3	-7.98	10.51	0.27	13.11	0.27	13.74	0.31	12.45	0.28
0.5	-6.51	-7.64	10.54	0.51	13.54	0.56	12.61	0.58	12.23	0.55

0.75	-6.81	-7.46	10.59	0.77	11.68	0.79	12.81	0.77	11.69	0.78
20 MPa[1]										
0.1	-5.88	-8.25	19.93	0.12	21.20	0.12	20.48	0.13	20.54	0.12
0.25	-5.97	-7.79	20.58	0.29	23.59	0.27	22.09	0.30	22.09	0.29
0.5	-6.14	-7.5	20.38	0.52	22.86	0.52	25.22	0.54	22.82	0.53
0.75	-6.39	-7.36	20.48	0.74	25.74	0.75	25.21	0.74	23.81	0.74
30 MPa[1]										
0.1	-5.68	-8.12	29.3	0.12	29.34	0.11	31.07	0.11	29.90	0.11
0.25	-5.77	-7.68	29.49	0.28	31.34	0.27	32.03	0.28	30.95	0.28
0.5	-5.93	-7.4	30.2	0.52	33.72	0.50	32.93	0.52	32.28	0.51
0.75	-6.18	-7.26	27.96	0.72	30.81	0.71	35.37	0.72	31.38	0.72

[1] Under a fixed gas pressure, CO_2 and CH_4 chemical potentials (μCO_2 and μCH_4) are calculated from the Peng-Robinson equation of state with varied CO_2 molar ratio in the mixture,

[2] MD-simulated gas mixture pressure (Pmix = PCO_2 + PCH_4) and gas composition in an empty simulation box with μCO_2 and μCH_4 as input,

[3] MD-simulated gas mixture pressure (Pmix) and gas composition in the bulk region of the 60 Å kerogen slit pore,

[4] MD-simulated gas mixture pressure (Pmix) and gas composition in the bulk region of the 40 Å kerogen slit pore.

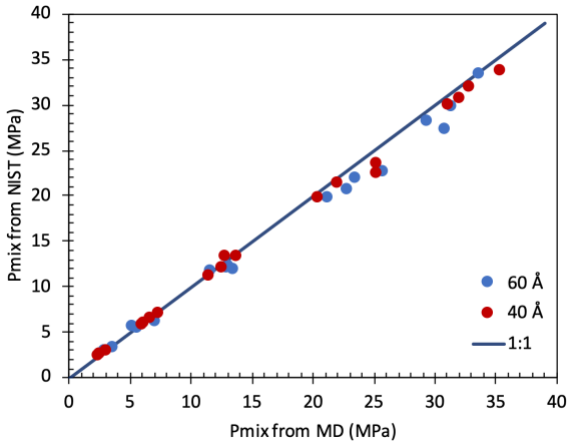

Figure 5.S1 Comparison of MD-simulated CO_2-CH_4 gas mixture pressure (measured in the pore central region) and NIST pressure data (derived from the gas mixture density and composition).

Chapter 6 Pore-scale lattice Boltzmann simulation of CO_2-CH_4 displacement in shale matrix

Although MD is a powerful tool for studying the fundamental aspects of nanoscale CO_2-CH_4 displacement, the high computational cost has limited it to a relatively small and simple domain. LBM relies on the collision and streaming of mesoscopic particle populations. By solving the Navier-Stokes and advection-diffusion equations in coupled lattices, gas flow and transport can be simulated in complex micropore geometries. In this chapter, a novel multi-lattice and multiphysics coupling scheme is developed to mimic the process of CO_2 displacing CH_4 in 2D porous media. The LB model is dual-porosity and includes interparticle and intraparticle mass transfer, driven by pressure and concentration gradients. A Langmuir adsorption boundary is implemented at the gas-solid interfaces to realise mass exchange between the pore space and solid matrix. The model is validated against several analytical solutions and compared with experimental data of a CO_2-CH_4 mixture passing through a reactive column. Subsequently, a sensitivity study is performed on diffusion coefficients, adsorption rates, and pore geometries to comprehensively evaluate the displacement efficiency, CO_2 storage capacity, and CH_4 production rate. This chapter is presented in the form of a manuscript that has been published in *Energy*:

Wu, J., Gan, Y., Shi, Z., Huang, P., & Shen, L. (2023). Pore-scale lattice Boltzmann simulation of CO_2-CH_4 displacement in shale matrix. *Energy 278*, 127991.

The PhD candidate has performed all the numerical work and the analysis of the results, and is the primary author of the above article.

Pore-scale lattice Boltzmann simulation of CO_2-CH_4 displacement in shale matrix

Jian Wu[a], Yixiang Gan[a, b], Zhang Shi[c], Pengyu Huang[a, d], Luming Shen[a, *]

[a] School of Civil Engineering, The University of Sydney, NSW 2006, Australia

[b] Sydney Nano Institute, The University of Sydney, NSW 2006, Australia

[b] School of Mechanical and Mining Engineering, The University of Queensland, St Lucia, QLD 4072, Australia

[d] Hard Rock Mining, CSIRO Mineral Resources, QCAT, 1 Technology Court, Pullenvale, QLD 4069, Australia

[*]Corresponding author. Email: luming.shen@sydney.edu.au

Abstract

This study couples the Navier-Stokes and multicomponent advection-diffusion equations within the lattice Boltzmann method (LBM) to innovatively simulate the CO_2-CH_4 displacement in nanoporous media of shale matrix, aiming to understand the gas flow and adsorption/desorption characteristics during CO_2-enhanced shale gas recovery. In the LBM simulations of CO_2 injection into heterogenous CH_4-saturated nanoporous media, gas movements are modelled by two separate advection-diffusion lattices driven by the velocity solved from the third Navier-Stokes lattice. Langmuir adsorption kinetics is employed at the fluid-solid interfaces to simulate the mass exchange between the bulk free space and the solid matrix. Mass transfer inside the solid matrix is also considered with adsorption and diffusion parameters obtained from molecular dynamics studies. CO_2 adsorption and CH_4 desorption, which occur in opposite directions, are simulated simultaneously. The coupling scheme is successfully validated for advection, diffusion, and surface adsorption. Results show that the

global mass transfer process is sensitive to intra-matrix diffusion. When the solid diffusion rate is ~10^{-4} of the bulk one (e.g., 6.71×10^{-11} m^2/s vs 5.66×10^{-7} m^2/s), selectivity can significantly impact the outflux concentration. Changing the CO_2 adsorption rate constant at the solid surfaces 0.1-10 times (e.g., 2.21×10^8 to 2.21×10^{10} $m^3/kmol/s$) nearly has no impact on gas adsorption in the solids. In comparison, the CH_4 desorption rate constant strongly correlates to the CH_4 desorption pathway. Further results from four algorithm-generated porous media suggest that increasing the particle size under a given porosity may benefit advection and lead to fast adsorption/desorption in the solids.

6.1 Introduction

Shale gas contributes to a significant portion of the global energy supply with a growing interest in more and more countries. One of the biggest challenges associated with shale gas exploitation is the production of adsorbed gas from nanopores within organic matrix, which consists of 20-80% of total gas held in the shale (Alfarge et al., 2020; Klewiah et al., 2020). Apart from horizontal drilling and hydraulic fracturing, CO_2 injection has shown great potential in enhancing the recovery of adsorbed CH_4 (Fathi and Akkutlu, 2014; Louk et al., 2017; Xie et al., 2022; Yang et al., 2022), leading up to 26% more CH_4 production after primary recovery and over 60% of injected CO_2 being sequestrated after flooding (Iddphonce et al., 2020). CO_2-enhanced gas recovery (EGR) is a dynamic displacement process governed by the pressure gradient and the competitive adsorption between CO_2 and CH_4 (Huo et al., 2017; Iddphonce et al., 2020; Klewiah et al., 2020; Qin et al., 2021). Therefore, it is important to understand the fundamental mechanisms of CO_2-CH_4 transport, displacement, and adsorption/desorption in nanoporous media consisting of complex geometries.

Gas flow and transport have been widely studied by molecular dynamics (MD) in a single slit pore, which focuses on molecular-level interactions of gas-gas, solid-solid, and gas-solid (Chen et al., 2019; Zhang et al., 2022). MD has the advantage of capturing nanopore-scale gas

characteristics (e.g., adsorption, diffusion, and surface slip) naturally by only defining the atomic force fields. Pore pressure and slit size are the two most important factors controlling nanoscale gas transport. Yu et al. (2018) simulated methane flow in 2 nm, 6 nm, and 10 nm calcite slit pores and found that pore pressure and slit size determined the individual flux contribution from viscous flow, Knudsen diffusion, and surface diffusion. Nan et al. (2020) observed that the gas slip length decreased hyperbolically with increasing pore pressure and size in 2-20 nm graphene slit pores. Gas-solid interaction energies at the pore walls impact gas slip flow as well. It is reported that gas slippage may be absent in the inorganic (e.g., quartz, calcite, and montmorillonite) nanopores due to the large fluctuation of the gas-solid interaction energy (Wang et al., 2017; Yu et al., 2020a; Zhan et al., 2021). Similarly, surface roughness causes heterogeneous gas-solid interaction forces and can diminish gas slippage at the pore walls (Castez et al., 2017; He et al., 2019; Huang et al., 2022; Yu et al., 2020b; Zhao et al., 2022). Moreover, MD is extended to investigate multiphase and multicomponent flow, such as the gas-liquid displacement in CO_2/N_2 flooding for enhanced oil recovery (Fang et al., 2019), miscible CO_2-octane flow (Zhang et al., 2021), and hydrocarbon mixture transport (Collell et al., 2015), etc. Despite the fact that MD has been a very successful tool in revealing the fundamental mechanisms of gas transport in nanopores, it is limited by the simulation size and duration due to its high computational cost. It cannot be used to study gas flow and transport in complex pore structures at the microscale.

The lattice Boltzmann method (LBM), as a mesoscopic method bridging the nano- and macro-scales, is fundamentally based on the evolution of the discrete-velocity distribution function (i.e., particle population) (Krüger et al., 2017; Wang et al., 2020). It is well suited to deal with irregular geometries like porous media and can achieve multiphysics coupling to simulate multiphase and multicomponent flow (Krüger et al., 2017; Sheikholeslami et al., 2013; Yan et al., 2021). For instance, Zhou et al. (2022) upscaled the results from MD simulations into the LBM through a local adsorption density parameter to investigate the effects of adsorption layer and surface diffusion on gas flow and transport in nanoporous shale matrix. There are various strategies to simulate shale gas flow in the LBM, which usually involve the development of

slip flow boundary conditions, Knudsen layer, and surface adsorption/desorption (Wang et al., 2020). The major types of boundary conditions for gas slippage are bounce-back (BB), Maxwellian diffuse reflection (MDR), and Langmuir slip (LS) (Wang et al., 2020; Wang et al., 2016). They are often implemented in a combined form to control the boundary slip with more accuracy (Liu et al., 2021; Wang et al., 2017b; Zhou et al., 2022). The Knudsen layer effect is generally mimicked by deriving local relaxation time from the Knudsen number considering the gas distance from the solid walls (Wang et al., 2016; Wang et al., 2017a). Surface adsorption in shale can be simulated by adding an extra gas-solid interaction force into the particle evolution function (Wang et al., 2022; Zhao et al., 2016).

The Navier-Stokes (NSE) and advection-diffusion equations (ADE) are often coupled in the LBM to investigate single-component gas migration and gas-solid adsorption in 2D porous media (Lei et al., 2021; Peng et al., 2021; Peng et al., 2018; Zakirov and Khramchenkov, 2022; Zhang and Sun, 2019; Zhou et al., 2015; Zhou et al., 2016). Zakirov and Khramchenkov (2022) investigated the effect of pore-scale heterogeneity on the dynamic gas adsorption coupled with Peclet number, porosity, adsorption rate constant, and absolute permeability, respectively. Peng et al. (2021) studied the desorption-diffusion of methane from coal matrix and gas migration within fractures/micro-pores. Their results indicated that the increased specific surface area and average pore size by hydraulic fracturing could lead to more efficient gas production. Zhou et al. (2015) developed three typical kinetic concentration boundary conditions (i.e., Dirichlet, constant concentration-flux, and mixed condition) to simulate the adsorption process at gas-solid interfaces. With the Langmuir adsorption kinetics, they found that the solid adsorption was nearly independent of porosity but changed with pore size in a simplified 2D porous structure composed of squares. They further investigated the gas-solid adsorption process in random porous media with varying porosities and particle sizes reconstructed by the quartet structure generation set (QSGS) method (Zhou et al., 2016) and argued that external and internal mass transfer resistances were crucial factors controlling the overall adsorption process. Zhang and Sun (2019) modified the NSE-ADE LBM coupling scheme by subtracting the adsorbed gas amount from the NSE lattice distribution function to consider the impact of

dynamic adsorption on flow velocity. In addition, they proposed to link this LBM coupling scheme with pore network modelling so that the disordered rock pore structures could be preserved in flow simulation.

The NSE-ADE coupling scheme in the LBM is only adopted for multiphase and multicomponent flow in a few cases (Jiang and Xu, 2021; Wang et al., 2018; Xia, 2016). For example, Jiang and Xu (2021) employed the Shan-Chen model to solve the immiscible CO_2-water flow field and coupled it with mass and heat transfer equations. Wang et al. (2018) extended the coupled single-component NSE-ADE LB model to study the separation and selectivity of CO_2-CH_4 gas mixtures in copper(II)-benzene-1,3,5-tricarboxylate (CU-BTC) membranes. They used the grand canonical Monte Carlo (GCMC) method to obtain the Langmuir adsorption parameters for CO_2 and CH_4, which could then be incorporated into the LB model to calculate the selectivity subject to porous media structure. Xia (2016) built a coupled model of fluid flow, heat transfer, and mass transport to investigate the viscous fingering during miscible displacement in porous media generated from micro-CT images.

To our knowledge, the coupled NSE-ADE scheme is still limited to single-component gas transport and has not yet been implemented into the LBM to investigate the dynamic CO_2-CH_4 displacement process in complex porous media. Single-component gas transport is suitable for the investigation of microscale shale gas flow. However, in the case of CO_2-EGR, CO_2 adsorption and CH_4 desorption usually take place simultaneously. It is needed to understand the relation between CH_4 production and CO_2 storage. In this study, we have implemented the NSE-ADE coupling scheme into the LBM to realise CO_2 injection into heterogenous CH_4-saturated porous media. An NSE lattice is coupled to two ADE lattices (one for each gas component) through the advective flow velocity, and the two ADE lattices are coupled in a simple way to achieve the competitive adsorption/desorption of CO_2 and CH_4. The LB model is first validated against three representative mass transfer problems with analytical solutions and compared with an experiment of CO_2-CH_4 mixture flow through a reaction bed. It is then adopted to simulate the CO_2-CH_4 displacement in porous media of varied pore structures. The

CO_2 adsorption and CH_4 desorption pathways in bulk free space and solids are examined in response to several selected parameters.

6.2 Computational methods

6.2.1 Navier-Stokes flow

The CO_2-CH_4 gas mixture is driven by an external flow field, which is simulated as a fictitious carrier fluid that conserves mass and momentum. The fluid flow of the CO_2-CH_4 mixture is described by the Navier-Stokes equations as

$$\partial_t \rho + \nabla \cdot (\rho \boldsymbol{u}) = 0 \tag{6.1}$$

$$\partial_t (\rho \boldsymbol{u}) + \nabla \cdot (\rho \boldsymbol{u}\boldsymbol{u}) = -\nabla p + \nabla \cdot \boldsymbol{\sigma} \tag{6.2}$$

where $\boldsymbol{u}$, p, ρ are fluid velocity, pressure and density, respectively, and $\boldsymbol{\sigma}$ is the viscous stress tensor. The physical space is discretised into a set of lattice nodes in the LBM solutions and the D2Q9 (two-dimensional and nine-velocity) lattice model is adopted to solve the discrete lattice velocity sets in the nine directions shown by the following vectors

$$\begin{cases} \text{Central: } \boldsymbol{e_0} = (0,0) \\ \text{Othogonal: } \boldsymbol{e_1} = (1,0);\ \boldsymbol{e_2} = (0,1);\ \boldsymbol{e_3} = (-1,0);\ \boldsymbol{e_4} = (0,-1) \\ \text{Diagnoal: } \boldsymbol{e_5} = (1,1);\ \boldsymbol{e_6} = (-1,1);\ \boldsymbol{e_7} = (-1,-1);\ \boldsymbol{e_8} = (1,-1) \end{cases}$$

Utilising the single-relaxation time Bhatnagar-Gross-Krook (BGK) collision operator (Bhatnagar et al., 1954), the evolution of the particle distribution function f_i with time t is calculated as

$$f_i(\boldsymbol{r} + \Delta t \boldsymbol{e}_i, t + \Delta t) - f_i(\boldsymbol{r}, t) = -\frac{1}{\tau_f}\left[f_i(\boldsymbol{r}, t) - f_i^{eq}(\boldsymbol{r}, t)\right] \tag{6.3}$$

$$f_i^{eq}(\boldsymbol{r}, t) = \rho w_i \left[1 + \frac{\boldsymbol{e}_i \cdot \boldsymbol{u}}{c_s^2} + \frac{(\boldsymbol{e}_i \cdot \boldsymbol{u})^2}{2c_s^4} - \frac{\boldsymbol{u}^2}{2c_s^2}\right] \tag{6.4}$$

where $\boldsymbol{r}$ is the lattice node position and can be expressed in the Cartesian coordinate system

as (*x, y*), Δt is the time step, i is the direction index from 0 to 8, $f_i^{eq}(\boldsymbol{r}, t)$ is the Boltzmann equilibrium distribution, τ_f is the relaxation time for the Navier-Stokes flow, and c_s is the sound speed of the fluid and equals to $1/\sqrt{3}$ in dimensionless lattice unit. The weight factors are $w_0 = 4/9$, $w_{1-4} = 1/9$, and $w_{5-8} = 1/36$, respectively, in the D2Q9 model. The fluid density and velocity at each lattice node can be calculated by summing up the particle distribution functions in all the directions

$$\rho = \sum_i f_i \tag{6.5}$$

$$\rho \boldsymbol{u} = \sum_i f_i \boldsymbol{e}_i \tag{6.6}$$

The kinematic viscosity of fluid v is related to the lattice relaxation time as

$$v = c_s^2(\tau_f - 0.5)\Delta t \tag{6.7}$$

and the fluid pressure p is related to density as

$$p = \rho c_s^2 \tag{6.8}$$

6.2.2 Mass transfer

The mass transfer processes of CO_2 (denoted as 1) and CH_4 (denoted as 2) are simulated by two individual advection-diffusion equations

$$\partial_t C_1 + \nabla(C_1 \boldsymbol{u}) = \nabla \cdot (D_1 \nabla C_1) + R_1 \tag{6.9}$$

$$\partial_t C_2 + \nabla(C_2 \boldsymbol{u}) = \nabla \cdot (D_2 \nabla C_2) + R_2 \tag{6.10}$$

where *C* is the gas concentration, *D* is the bulk diffusion coefficient in the free space (i.e., bulk pore space), and *R* is the source/sink term implemented at the gas-solid boundary lattice nodes to mimic the surface adsorption/desorption and is set to zero in the free space. Assuming the typical Langmuir adsorption kinetics, the CO_2 adsorption R_1 can be expressed as an

adsorption-desorption equilibrium (He et al., 2000)

$$R_1 = \frac{\partial N_1}{\partial t} = k_{\mathrm{a}1} C_1 (N_{m1} - N_1) - k_{\mathrm{d}1} N_1 \tag{6.11}$$

where N_m is the maximum gas adsorption amount, N is the current adsorption amount, and k_{a} (concentration^{-1}s^{-1}) and k_{d} (s^{-1}) are the adsorption and desorption rate constants, respectively. In the case of CO_2-CH_4 displacement, the solid matrix is initially saturated with CH_4 at the maximum N_{m2}. In the presence of CO_2, competitive adsorption takes place and the saturated CH_4 adsorption amount will be largely decreased to N_{m2}' due to the limited available adsorption sites and preferential adsorption of CO_2 (Wu et al., 2022). The competitive adsorption process is simulated as fast CH_4 desorption that will decrease the CH_4 adsorption amount N_2 from N_{m2} to N_{m2}' when CO_2 reaches the lattice node, followed by a subsequent adsorption-desorption equilibrium

$$\begin{cases} R_2 = \dfrac{\partial N_2}{\partial t} = -k_{\mathrm{d}2} N_2 \quad if\ N_2 > N_{m2}' \\ R_2 = \dfrac{\partial N_2}{\partial t} = k_{\mathrm{a}2} C_2 (N_{m2}' - N_2) - k_{\mathrm{d}2} N_2 \quad if\ N_2 \le N_{m2}' \end{cases} \tag{6.12}$$

The threshold CO_2 concentration to trigger the competitive adsorption (i.e., when N_{m2} starts decreasing to N_{m2}') is set at 0.1 (lattice unit) in the simulations. The use of a small finite value of concentration instead of zero is to avoid the artificial non-zero concentration during numerical calculation. The Langmuir adsorption kinetics acts as the mass exchange between the free space and the solid matrix at the gas-solid boundary. Subsequently, the adsorbed gas evolves in a fully diffusive manner (i.e., advection velocity is zero) and propagates from the gas-solid boundary into the solid matrix interior under a concentration gradient for CO_2 and oppositely for CH_4 during desorption. The intra-matrix transport of adsorbed gas is described by the homogeneous solid diffusion model (HSDM) as (Chahbani et al., 2002)

$$\frac{\partial N_1}{\partial t} = D_{s1} \left(\frac{\partial^2 N_1}{\partial x^2} + \frac{\partial^2 N_1}{\partial y^2} \right) \tag{6.13}$$

$$\frac{\partial N_2}{\partial t} = D_{s2} \left(\frac{\partial^2 N_2}{\partial x^2} + \frac{\partial^2 N_2}{\partial y^2} \right) \tag{6.14}$$

where D_s is the gas diffusion coefficient in the solid matrix. The D2Q5 (two-dimensional and five-velocity) lattice model is used to solve the gas concentration in the following five directions

$$\begin{cases} \text{Central: } \boldsymbol{e_0} = (0,0) \\ \text{Othogonal: } \boldsymbol{e_1} = (1,0);\ \boldsymbol{e_2} = (0,1);\ \boldsymbol{e_3} = (-1,0);\ \boldsymbol{e_4} = (0,-1) \end{cases}$$

The particle evolution function g_i at a time step is calculated as

$$g_i(\boldsymbol{r} + \Delta t \boldsymbol{e}_i, t + \Delta t) - g_i(\boldsymbol{r}, t) = -\frac{1}{\tau_c}\left[g_i(\boldsymbol{r}, t) - g_i^{eq}(\boldsymbol{r}, t)\right] \tag{6.15}$$

$$g_i^{eq}(\boldsymbol{r}, t) = C w_i \left(1 + \frac{\boldsymbol{e}_i \cdot \boldsymbol{u}}{c_s^2}\right) \tag{6.16}$$

where i is the direction index from 0 to 4, $g_i^{eq}(\boldsymbol{r}, t)$ is the Boltzmann equilibrium distribution, and τ_c is the relaxation time for advection-diffusion. The viscous gas flow velocity $\boldsymbol{u}(t)$ is retrieved from the Navier-Stokes lattice solution at each time step. The weight factors are $w_0 = 1/3$ and $w_{1-4} = 1/6$, respectively. The gas diffusion coefficient is related to the relaxation time according to

$$D = c_s^2(\tau_c - 0.5)\Delta t \tag{6.17}$$

The gas concentration at each lattice node is obtained by summing up the particle distribution functions

$$C = \sum_i g_i \tag{6.18}$$

In order to take the source/sink term into account at the gas-solid boundary for mass exchange, the particle evolution function and related equations are simply modified as (Seta, 2013)

$$g_i(\boldsymbol{r} + \Delta t \boldsymbol{e}_i, t + \Delta t) - g_i(\boldsymbol{r}, t) = -\frac{1}{\tau_c}\left[g_i(\boldsymbol{r}, t) - g_i^{eq}(\boldsymbol{r}, t)\right] + q_i \Delta t \tag{6.19}$$

$$q_i = \left(1 - \frac{1}{2\tau_c}\right) w_i R \tag{6.20}$$

$$C = \sum_i g_i + \frac{1}{2} R \Delta t \tag{6.21}$$

where q_i is the discrete source/sink term for gas adsorption/desorption. It should be noted that each gas component has a set of solution lattices as described above. For the HSDM gas adsorption evolution inside the solid matrix, it is simply required to replace the concentration C by the gas adsorption amount N, and τ_c by the relaxation time of D_s in Equations (6.15)-(6.18) with $\boldsymbol{u}$ set to zero. The surface adsorption amount at the gas-solid boundary is recalculated at each time step according to Equations (6.11) and (6.12), and further acts as the boundary condition for gas adsorption evolution inside the solid matrix. The updated surface adsorption amount at the boundary after propagation into the solid matrix also has feedback on the Langmuir adsorption kinetics by changing the adsorption and desorption rates. Therefore, surface adsorption/desorption only ceases when the entire solid matrix is saturated/desaturated with gas.

The above equations are implemented into OpenLB (Krause et al., 2021), an open-source numerical framework for LBM simulations. OpenLB provides a variety of 2D and 3D models with multiphysics coupling and can be easily executed on a parallel machine with distributed memory. Data visualisation is conduced in ParaView (Henderson, 2007). The proposed LBM coupling scheme is concluded in four steps:

a. The Navier-Stokes equations are solved in the bulk free space and each lattice node generates a velocity vector $\boldsymbol{u}$ for the CO_2 and CH_4 mixture.

b. In the free space, the advection-diffusion equations are solved for CO_2 and CH_4 on two separate lattices using the carrier fluid velocity $\boldsymbol{u}$ determined from the Navier-Stokes lattice.

c. At the gas-solid boundary, the dynamic surface gas adsorption amount is calculated through the source/sink term by the Langmuir adsorption kinetics.

d. The adsorbed CO_2 diffuses from the gas-solid boundary into the solid matrix interior while CH_4 diffuses in the opposite direction during the desorption process.

To validate the LB model developed, we present three typical benchmark cases (Inamuro et al.,

2002; Zhou et al., 2015) for the coupled NSE-ADE scheme along with the prescribed boundary conditions. The first example illustrates the mass transfer process of Poiseuille flow through a plate channel with a reactive boundary (Figure 6.S1). The second example examines the pure diffusion process driven by a concentration gradient at zero velocity inside the solid matrix (Figure 6.S2). The third example validates the proposed model in simulating the stable counter-diffusion of a binary mixture between two parallel porous plates (Figure 6.S3). In the fourth example, we compare simulation results with experimental data where a CO_2-CH_4 mixture flows through a 26 cm-long dispersive packed bed column of activated carbon (Figure 6.S4) (Mansoubi et al., 2023). The LB model successfully reproduces results from the analytical solutions and the experiment. The validations are detailed in the supplementary material.

6.2.3 Boundary conditions

Boundary conditions are essential aspects to consider in the LBM simulations. As described in Section 6.2.2, the simulation domain comprises one Navier-Stokes lattice that solves the velocity field and two advection-diffusion lattices that solve the CO_2 and CH_4 concentrations, respectively. Therefore, each lattice requires a set of boundary conditions. The boundary conditions used in the simulations are summarised in Table 6.1 with a schematic drawing in Figure 6.1. Except for the Langmuir adsorption kinetics at the solid surfaces and the fully developed concentration boundary condition at the outlet, all the other boundary conditions are already implemented in the framework of OpenLB and can be readily used for this application.

Table 6.1 Boundary conditions for the coupled NSE-ADE LB model.

Position	Navier-Stokes lattice	CO_2 advection-diffusion lattice	CH_4 advection-diffusion lattice
Inlet (lower)	$\boldsymbol{u} = \boldsymbol{u}_0$ (parabolic velocity profile)	$C_1 = C_0$ (constant concentration)	$C_2 = 0$ (no concentration)

Outlet (upper)	$p = p_0$ (constant pressure, open outlet)	$C_1^y = C_1^{y-1}$ (fully developed concentration, open outlet)	$C_2^y = C_2^{y-1}$ (fully developed concentration, open outlet)
Left	Bounce-back (no slip)	Bounce-back (no flux)	Bounce-back (no flux)
Right	Bounce-back (no slip)	Bounce-back (no flux)	Bounce-back (no flux)
Solid surfaces	Bounce-back (no slip)	Langmuir adsorption	Langmuir adsorption

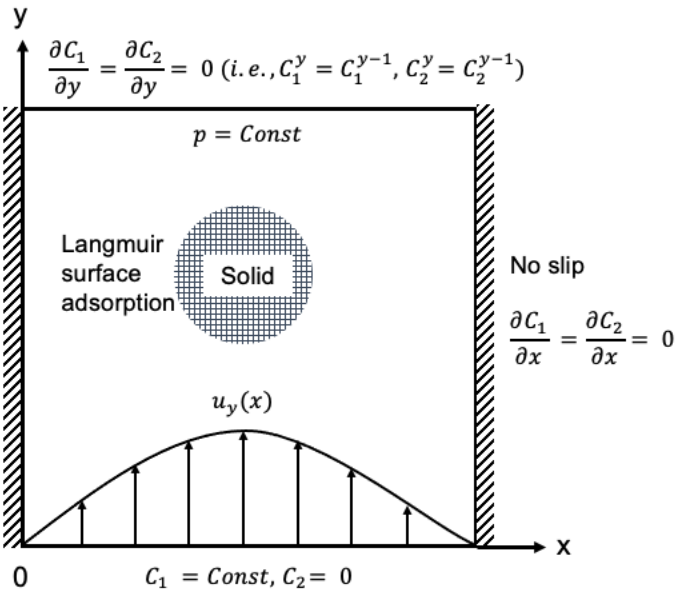

Figure 6.1 A schematic drawing of the boundary conditions in the developed LB model.

6.3 Results and discussion

The heterogeneous porous medium is created from a 2D image based on a slice of the realistic Berea sandstone rock sample (Boek and Venturoli, 2010). Similar to Zhang and Sun (2019), the rock property parameters are adjusted to match the characteristics of the shale matrix. Figure 6.2 illustrates the construction of the LB model with the coupled mass transfer process. Before being read into the LB model, the 2D image is pre-processed in MATLAB to dilate the pore space and resize it to a suitable resolution corresponding to the lattice resolution. The final

porous structure has a porosity of 0.48. We have tested the lattice spacing at resolutions of 344 × 340, 516 × 510, 774 × 765, 1161 × 1148, and 1742 × 1722 and found out that the concentration curves started to converge at 774 × 765. This lattice spacing has been selected to achieve a balance between computational accuracy and speed, which also ensures the resolution near the fluid-solid interfaces. The final pixel size is set to 3.6 nm (i.e., $\Delta x = \Delta y = 3.6\,nm$), which leads to pore sizes ranging from 20 to 180 nm as shown in Figure 6.3, consistent with the pore size distribution of the shale matrix. The pore size distribution is analysed from the 2D image using the watershed segmentation algorithm developed by Rabbani et al. (2014).

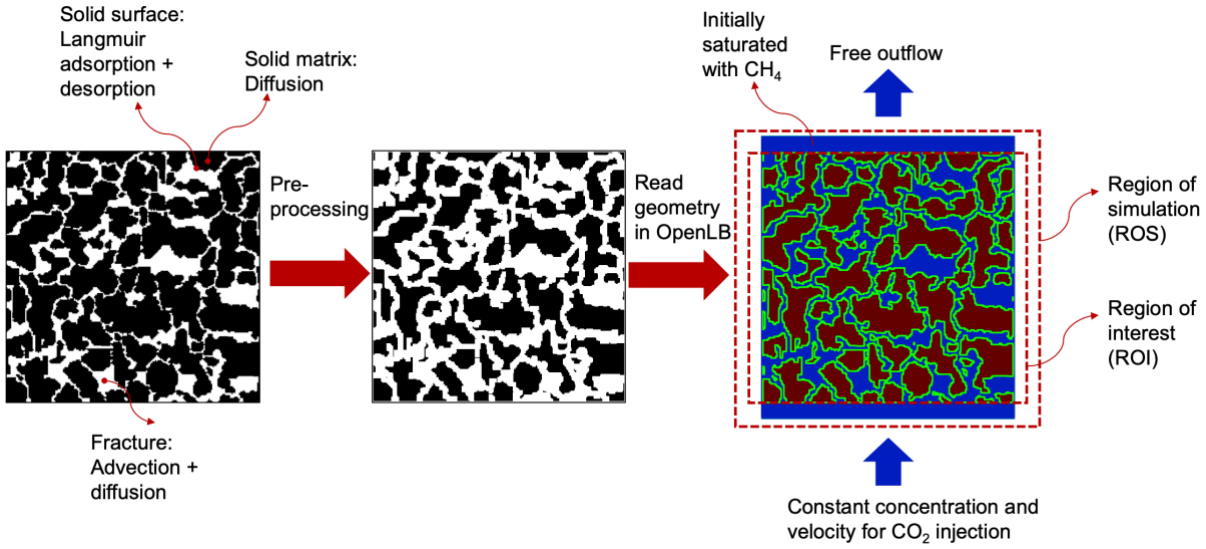

Figure 6.2 Construction of the LB model in the simulation of CO_2-CH_4 displacement.

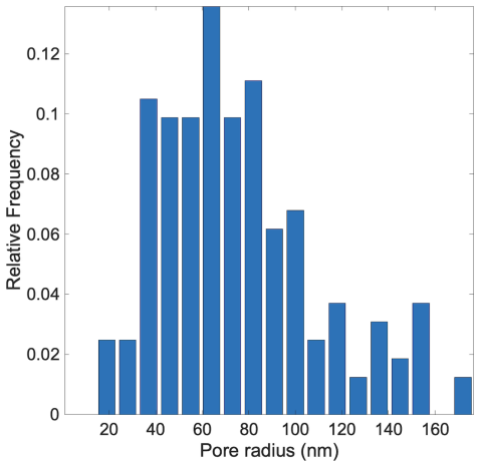

Figure 6.3 Pore size distribution of the heterogeneous shale matrix geometry.

The inlet and outlet are both extended with 50 additional rows of lattice nodes for the implementation of the boundary conditions and flow development. The number of additional rows of lattice nodes is examined to ensure the pressure drop across the simulation domain converges. The temperature in the simulation domain is set as 300 K. It is assumed that the residual CH_4 is at a depletion pressure of 1.8 MPa (0.75 kmol/m^3) and the CO_2 injection pressure is 4.3 MPa (2.31 kmol/m^3). Since both gas components have a similar viscosity under the relatively low-pressure conditions, the mixed gas interaction is neglected for simplicity, and the fictitious carrier fluid viscosity is assumed to be the average of the two. Although turbulent gas flow may occur in large natural and artificial fractures, shale matrix has extremely low permeability, and diffusion is usually considered the main gas transport mechanism in shale matrix. Herein, the simulations mainly focus on the laminar flow regime with a Reynolds number of 1.5. The local Reynolds number is estimated at 0.5-4.5 based on the pore velocity and pore size distribution. Low Reynold numbers are characterised in similar numerical studies (Yan et al., 2021; Zhao et al., 2018; Zhou et al., 2016). The maximum CO_2 and CH_4 adsorption amounts as well as the diffusion coefficients in the free space and kerogen matrix are referred from the previous MD studies (Tesson and Firoozabadi, 2018; Wu et al., 2022). The relaxation time parameters for viscosity, free diffusion, and solid diffusion are set as 1.29, 1.31, and 0.51, respectively, in the base case. They can be adjusted in the sensitivity study of diffusion coefficients according to Equations (6.7) and (6.17). The complete set of simulation parameters is described in Table 6.2, along with the conversion rules between the real and dimensionless lattice units. In this section, the effects of inter-matrix, interfacial, and intra-matrix mass transfer on the process of CO_2-CH_4 displacement are investigated in detail.

Table 6.2 Simulation parameters and scaling relationships between physical and lattice units.

Parameter	Symbol	Physical value	Lattice value	Scaling*
ROI size	L_x	2.75×10^{-6} m	774	$L_x = \Delta x \hat{L}_x$
	L_y	2.72×10^{-6} m	765	$L_y = \Delta y \hat{L}_y$

Grid size	Δx	3.56×10^{-9} m	1	-
	Δy	3.56×10^{-9} m	1	-
Timestep	Δt	6.03×10^{-12} s	1	-
Viscosity[1]	μ	5.54×10^{-7} m^2/s	0.264	$\mu = (\Delta x^2/\Delta t)\hat{\mu}$
Injection velocity	v	0.2948 m/s	0.0005	$v = (\Delta x/\Delta t)\hat{v}$
Saturated concentration[1]	C_1	2.31 kmol/m^3	3.08	$C_1 = C_2\hat{C}_1$
	C_2	0.75 kmol/m^3	1	-
Diffusion coefficient in free space[2]	D_1	5.66×10^{-7} m^2/s	0.27	$D = (\Delta x^2/\Delta t)\hat{D}$
	D_2	5.66×10^{-7} m^2/s	0.27	
Diffusion coefficient in solid[2]	D_{s1}	6.71×10^{-9} m^2/s	0.0032	
	D_{s2}	6.71×10^{-9} m^2/s	0.0032	
Adsorption rate constant[3]	k_{a1}	2.21×10^{9} m^3/kmol/s	0.01	$k_a = (C_2^{-1}/\Delta t)\hat{k}_a$
	k_{a2}	2.21×10^{9} m^3/kmol/s	0.01	
Desorption rate constant	k_{d1}	1.66×10^{7} s^{-1}	0.0001	$k_d = \Delta t^{-1}\hat{k}_c$
	k_{d2}	1.66×10^{7} s^{-1}	0.0001	
Maximum adsorption[4]	N_{m1}	6 kmol/m^3	8	$N_m = C_2\hat{N}_m$
	N_{m2}	3.08 kmol/m^3	4.1	
	N_{m2}'	0.45 kmol/m^3	0.6	

*Symbols for lattice values are expressed with a circumflex ˆ;

[1]Referenced from the US National Institute of Standards and Technology (NIST) fluid properties data (Linstrom and Mallard, 2022);

[2]Referenced from Tesson and Firoozabadi (2018). The same base value is chosen for CO_2 and CH_4 to highlight the effect of other parameters, and different diffusion rates are studied as a selectivity in Section 6.3.2;

[3]Referenced from Wang et al. (2018);

[4]Referenced from Wu et al. (2022);

6.3.1 Effect of the solid diffusion coefficient

The mass transfer process consists of the intra-matrix and inter-matrix components. Figure 6.4

shows the concentration and adsorption evolutions of CO_2 and CH_4 at three stages in the nanoporous medium with the parameters described in Table 6.2 as the base case. It can be seen that the injected CO_2 advects in the free space, and surface adsorption happens quickly even at a low gas concentration. With the concentration increasing in the pore space, CO_2 starts to evolve into solids and saturates them toward the outlet. As for CH_4, the desorption in the solids is initiated by CO_2, the desorbed CH_4 transfers into the bulk phase and flows toward the outlet under the injection induced pressure gradient. The decreased concentration in the pore space further creates a concentration gradient between the bulk and the solid, leading to more CH_4 desorption from the solid matrix.

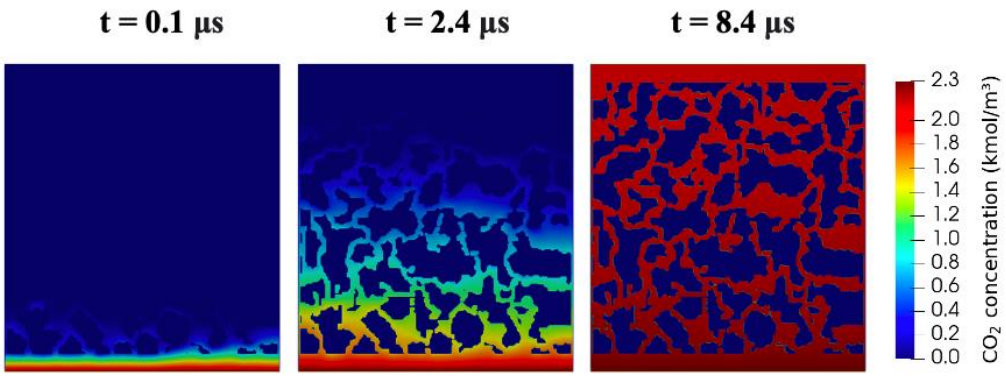

(a) CO_2 concentration

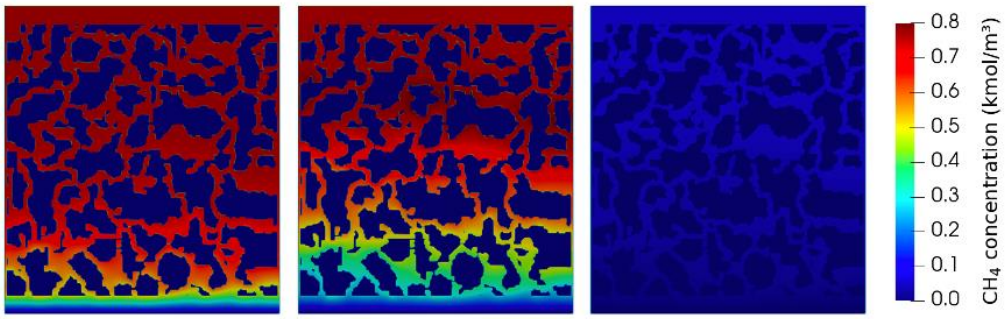

(b) CH_4 concentration

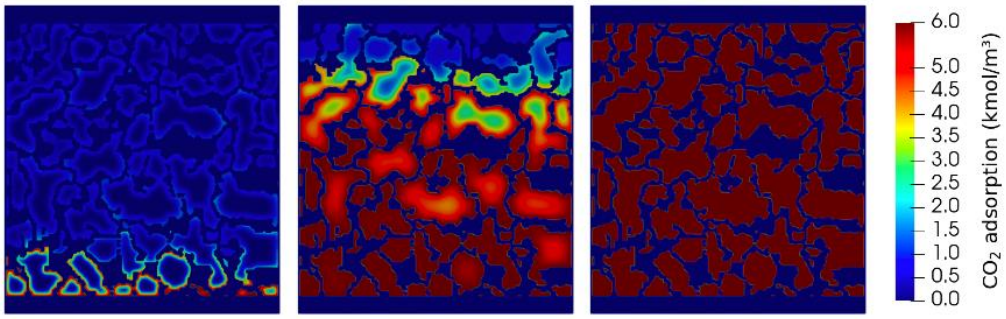

(c) CO_2 adsorption

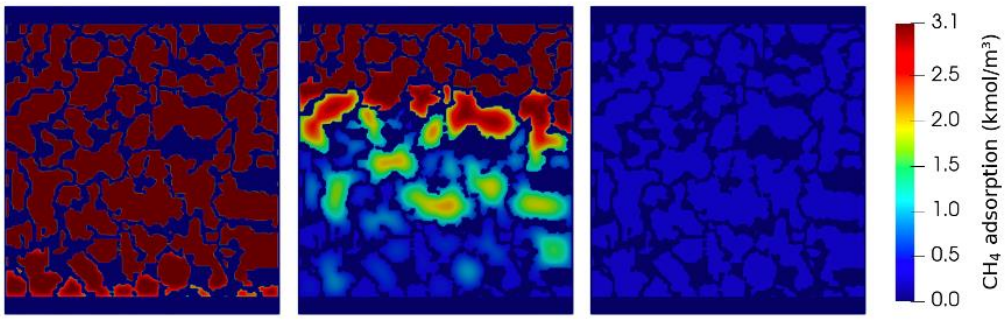

(d) CH_4 adsorption

Figure 6.4 CO_2 and CH_4 concentration (a-b) and adsorption (c-d) evolutions during the displacement at t = 0.1 μs, t = 2.4 μs, and t = 8.4 μs.

The results in Figure 6.5 are normalised by the saturated gas concentration (C_1, C_2) and maximum adsorption amounts (N_{m1}, N_{m2}). They also show the recovery ratios of free (R_f) and adsorbed (R_s) CH_4 as the total gas amount is calculated from the multiplication of average concentration/adsorption and free space/solid lattice node number. The latter is cancelled out when calculating the ratio, which then becomes the same as our normalisation. The total recovery ratio of CH_4 (free and adsorbed gases together) R_t can be easily converted from the normalised results as

$$R_t = \frac{R_f C_2 n + R_s N_{m2}(1-n)}{C_2 n + N_{m2}(1-n)} = \frac{0.36R_f + 1.6016R_s}{1.9616} \approx 0.18R_f + 0.82R_s \qquad (6.22)$$

where n is the porosity. Based on the figure, increasing the solid diffusion coefficient does not necessarily change the gas concentration and adsorption evolutions with time for both CO_2 and

CH_4 (e.g., from D_s to $10D_s$). It can be attributed to the fact that gas diffusion rates in the solids have already reached a maximum point corresponding to the adsorption and desorption reaction rates at the solid surfaces. In other words, the diffusion of adsorbed gas from the surfaces to solid interiors is limited by the surface adsorption kinetics. As the solid diffusion coefficient decreases, the intra-matrix mass transfer becomes weaker, as shown by the slower gas adsorption and desorption curves, which results in faster CO_2 saturation and CH_4 desaturation in the bulk free space. The rapid CH_4 desorption keeps the CH_4 bulk concentration stable for a longer period since the refilling from the adsorbed gas in the solids is immediate. In addition, the CH_4 desorption results in a significant gas concentration peak (>1) at the outlet, whose height increases with the increasing desorption rate.

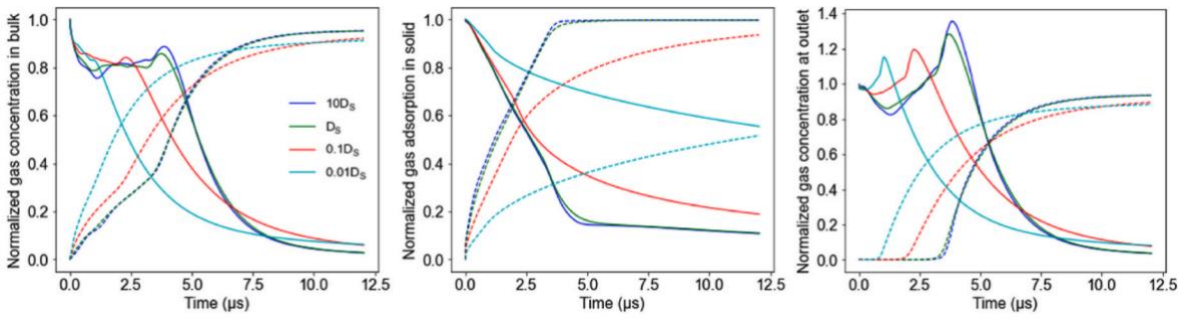

Figure 6.5 Effects of gas diffusion coefficient (D_s) for both CO_2 and CH_4 in the solid matrix on CO_2 (dotted lines) and CH_4 (solid lines) concentration, adsorption, and outflux.

6.3.2 Transport selectivity in solid matrix

Transport selectivity is widely reported in MD studies where CO_2 and CH_4 show different mass transfer rates in nanopores. Our previous study suggests that the CO_2/CH_4 transport selectivity is within the range of 1-6 depending on the nanopore size and the total mixed gas pressure (Wu et al., 2023). To investigate this effect at a large scale, we simulate the transport selectivity of CO_2/CH_4 by varying the diffusion coefficient of CO_2 in the solid matrix while keeping that of CH_4 the same. As shown in Figure 6.6a, the CO_2/CH_4 selectivity nearly has no impact on the

time-evolving gas concentration in the bulk and the gas adsorption in the solids when the solid diffusion coefficient is in the order of 10^{-9} m^2/s, which is two orders of magnitude smaller than that in the bulk free space. However, CO_2/CH_4 selectivity leads to significant differences in the bulk gas concentration and solid adsorption when the solid diffusion coefficient is decreased by two orders of magnitude (i.e., in the order of 10^{-11} m^2/s) as in Figure 6.6b. It can also be seen that the CO_2/CH_4 selectivity mainly affects the CO_2 adsorption process in the solids while slightly affecting the desorption of CH_4. High CO_2 solid diffusion rates naturally result in a faster gas adsorption process. As the CO_2 adsorption rate increases in the solids, the bulk CO_2 is consumed faster and therefore takes a longer time to achieve saturation and reach the outlet. The CH_4 desaturation process is slightly faster in the bulk free space in the beginning at higher selectivities. This is possibly because the fast desorption of CH_4 (i.e., competitive adsorption) is triggered by CO_2 adsorption at the solid boundary, and therefore the evolution of CO_2 concentration can also affect CH_4. The general results here indicate that the adsorption kinetics dominates the gas adsorption process under a fast gas diffusion rate in the solid matrix and selectivity is only non-negligible if the gas diffusion rate in solid is greatly lower than that in the bulk. It is suggested that gas separation can more easily achieve in porous media composed of low-permeable solid matrix.

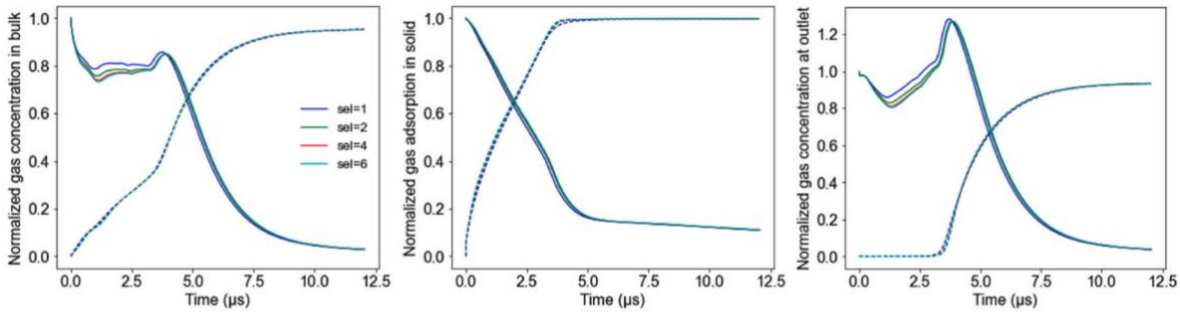

(a) $D_{s2} = 6.71 \times 10^{-9}$ m^2/s

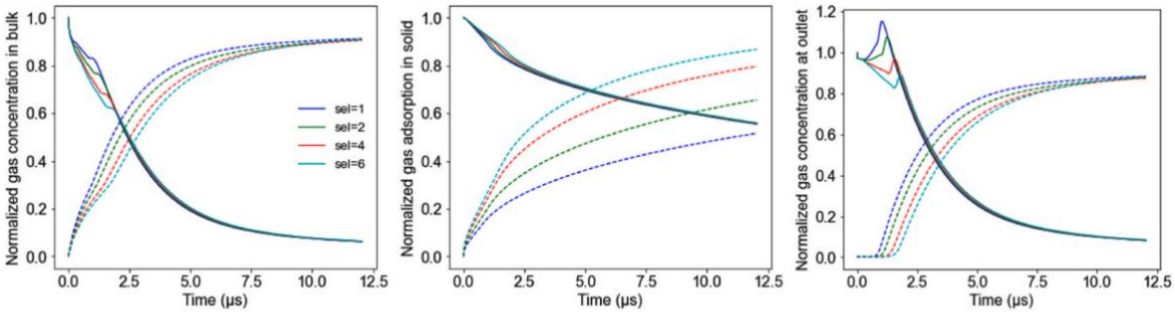

(b) $D_{s2} = 6.71 \times 10^{-11}$ m^2/s

Figure 6.6 Effects of CO_2/CH_4 transport selectivity (sel) in the solid matrix on CO_2 (dotted lines) and CH_4 (solid lines) concentration, adsorption, and outflux when (a) $D_{s2} = 6.71 \times 10^{-9}$ m^2/s and (b) $D_{s2} = 6.71 \times 10^{-11}$ m^2/s, respectively.

6.3.3 Effect of surface adsorption/desorption rates

To study the effect of surface adsorption on the process of CO_2-CH_4 displacement, we run simulations with five groups of adsorption and desorption rate constants that cover a wide range of K_a/K_d from 10^1 to 10^3. By fixing the desorption rate constant K_d, the relationships of both gas concentrations in the bulk and gas adsorption in the solid matrix to varied adsorption rates K_a are obtained, as shown in Figure 6.7a. It is noticeable that changing K_a alone does not generally affect either the CO_2 adsorption or the CH_4 desorption process in the bulk free space and solid matrix. This phenomenon suggests that the gas adsorption in the solids is limited by other mass transfer parameters such as solid diffusion coefficient and advection velocity. The Damkohler number ($Da = k_a L_x/D$) (Kang et al., 2014) compares the competition between reaction and diffusion, and it is estimated in the range of 3 to 287 based on 0.1-10K_a, which is much greater than one. Therefore, it may be a diffusion-limited state at the gas-solid interfaces under the studied conditions. When K_a is decreased to 0.1 of its base reference value, the CH_4 desorption speed increases, and the CO_2 maximum adsorption is not reached within the studied timeframe.

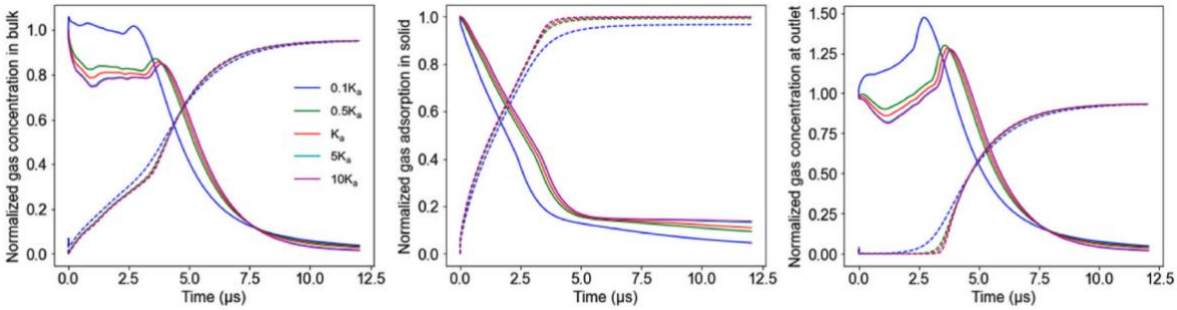

(a) Changing K_a under a fixed K_d

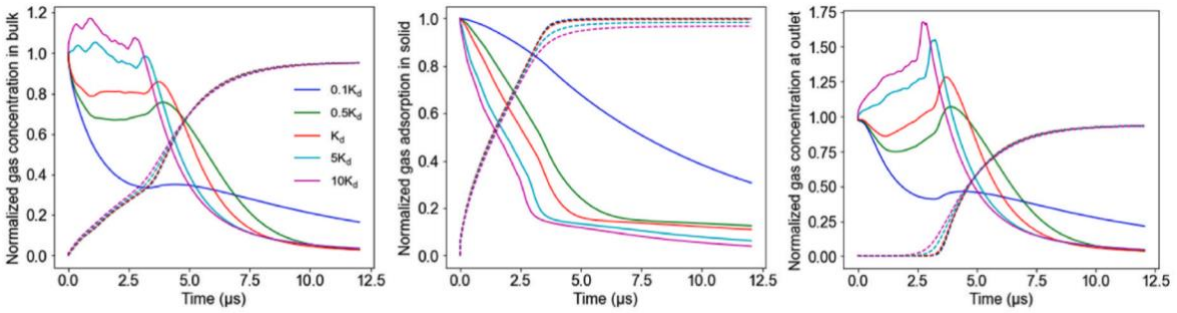

(b) Changing K_d under a fixed K_a

Figure 6.7 Effects of adsorption (K_a) and desorption (K_d) rate constants on CO_2 (dotted lines) and CH_4 (solid lines) concentration, adsorption, and outflux when (a) K_d (b) K_a are fixed, respectively.

Similarly, the desorption rate K_d has a negligible effect on the CO_2 adsorption process when K_a is fixed, according to Figure 6.7b. In comparison, K_d can greatly affect the desorption process of CH_4. As K_d increases, the CH_4 desorption from the solids becomes significantly faster since the CO_2-initiated CH_4 desorption is directly proportional to K_d (i.e., K_dC). The fast-released CH_4 goes into the bulk free space and causes higher concentration peaks, as shown in the outflux concentrations.

6.3.4 Effect of pore geometry

The effect of pore geometry on the CO_2-CH_4 displacement is investigated in four different particle-sized porous media S-1, S-2, S-3, and S-4 (Group 1) and in their duplicates with

redistributed particle positions S-1*, S-2*, S-3*, and S-4* (Group 2), generated by the quartet structure generation set (QSGS) method (Wang et al., 2007) as presented in Figure 6.8a. They are selected from a large dataset created by Germanou et al. (2018), which intends to mimic the morphological features of the shale matrix. While the artificial pore geometries may still differ from the realistic case, the QSGS offers us the flexibility to study pore geometrical parameters (e.g., porosity, particle size, and particle aspect ratio) in a controlled way while keeping the high heterogeneity similar to shale matrix. The porosity is kept at ~0.7 with varying particle numbers and sizes. The blockage ratio along the flow direction is shown in Figure 6.8b, where its fluctuation decreases with the decreasing particle size. It is important to note that simplified 2D representations may overlook complex interconnections between pores, leading to an underestimation of the blockage ratio. The original image resolution is slightly changed to fit with the LB model resolution, as described in Table 6.2. Additionally, another group (Group 3) of simulations has been performed in S-1, S-2, S-3, and S-4 with the gas injection velocity reduced to 0.2v.

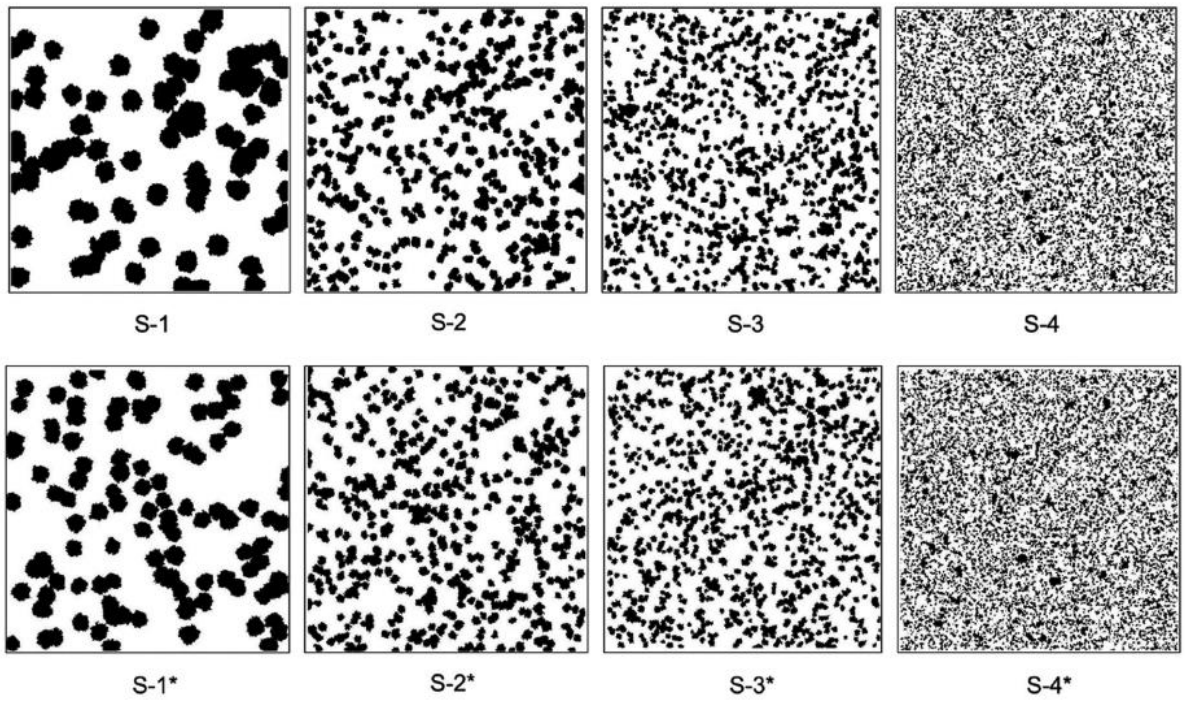

(a)

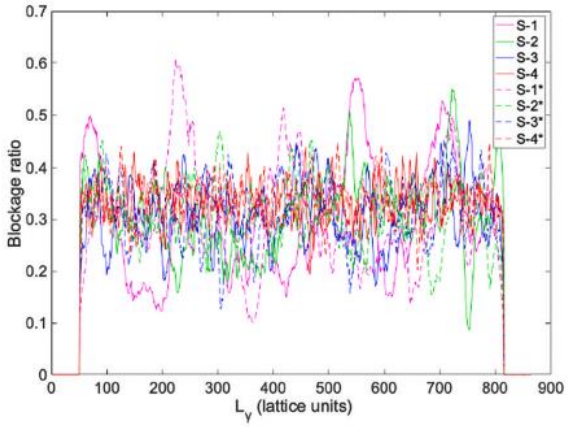

(b)

Figure 6.8 (a) Random porous media generated by the quartet structure generation set (QSGS) method (Germanou et al., 2018). The average particle sizes d_p are 91.9 nm, 46.8 nm, 33.8 nm and 15.1 nm for S-1 to S-4 and 80.4 nm, 42.9 nm, 32.5 nm, and 15.4 nm for S-1* to S-4*, as analysed by the method of Rabbani and Ayatollahi (2015). (b) Blockage ratio of S-1(*), S-2(*), S-3(*), and S-4(*) along the flow direction L_y.

The same effect of pore geometry is identified in the three groups of simulations. It is found that the rearrangement of particle distribution nearly does not affect the adsorption-desorption process while the decreased gas injection velocity slightly delays the CO_2-CH_4 displacement. As little difference is seen among the three groups of data, we only use the results from Group 1 as the representative case for the following detailed discussion on the effect of pore geometry. The results of time-evolving CO_2/CH_4 concentration, adsorption, and outflux at the outlet are included as Figures 6.S5 and 6.S6 for Group 2 and Group 3, respectively, in the supplementary materials. According to Figure 6.9, the particle size impacts both gas concentration in the bulk and gas adsorption in the solids. As the particle size decreases, the gas concentration and adsorption fronts travel slower and slower. The concentration front is also much flatter in small particle-sized porous structures such as S-3 and S-4. Figure 6.10a provides a quantitative analysis of the pore geometry effect and confirms the faster evolution of gas concentration in porous media of large particle sizes. The transient adsorbed gas amount is higher for the large

particle-sized porous structures, likely due to the decreased interparticle resistance to mass transfer. The ratio of the effective diffusion coefficient D_e to the bulk diffusion coefficient D is calculated for CO_2 according to (Mu et al., 2007; Zhou et al., 2016)

$$D_e/D = \frac{\left(\int_0^{L_x} (\frac{\partial C}{\partial y})_{y=L_y} dx\right)/L_x}{(C_{in} - C_{out})/L_y} \tag{6.23}$$

where C_{in} and C_{out} are the average inlet and outlet concentrations, respectively. A low ratio suggests more resistance during the mass transfer process in the porous medium. Additionally, permeability is calculated from Darcy's law

$$k = -\frac{\bar{v}\mu}{\nabla p} \tag{6.24}$$

where $\bar{v}$ is the average bulk velocity. When CO_2 is being injected, it first saturates the interparticle free pore space through advection-diffusion. After CO_2 is brought to the solid surfaces, gas adsorption kinetics takes place, and the adsorbed CO_2 starts to diffuse toward the central region of the solids. With the decreasing particle size, the process of CO_2 adsorption becomes slower due to the decreased permeability that constrains advection in the free pore space, consistent with the observed trend that both permeability and D_e/D decrease with the decreasing particle size in Figure 6.10b. The results here are partially consistent with the findings of Zhou et al. (2016), in which they suggest that intraparticle diffusion plays a dominant role in the mass transfer process of porous media with large solid particles, and interparticle advection-diffusion is instead more important in small particle-sized porous media. It is also mentioned that a fully developed flow field is achieved in the porous media of large particles and the gas concentration evolves more sufficiently in the pore spaces. However, they observed that the average adsorption uptake speed by the solids was in a nonmonotonic relationship with the particle size since increasing the particle size raised the intraparticle resistance at the same time. There existed an optimal point where the interparticle and intraparticle mass transfer rates were balanced with minimal total resistance. In comparison, CH_4 desorption is less sensitive to particle size change as the curves of S-1, S-2, and S-3 nearly

collapse. The reason can be that desorption occurs in the opposite direction from the solid interior to the free space and thus may be less controlled by advection. Moreover, the CO_2 breakthrough curves at the outlet in Figure 6.10c show that the CO_2-CH_4 displacement is faster in large particle-sized porous media since CO_2 arrival and CH_4 depletion occur earlier at the outlet.

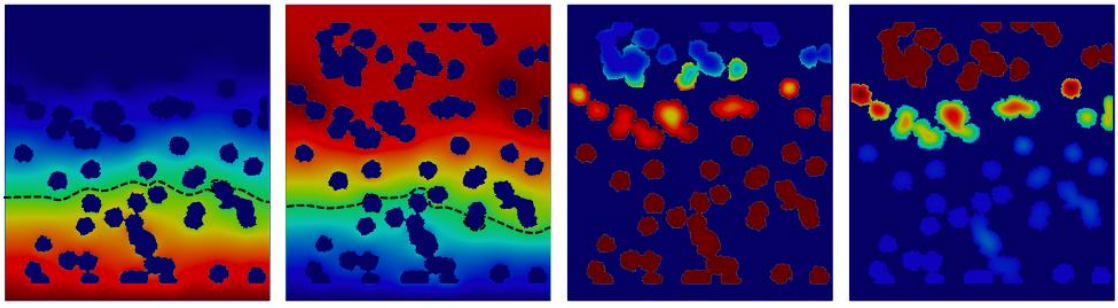

(a) S-1

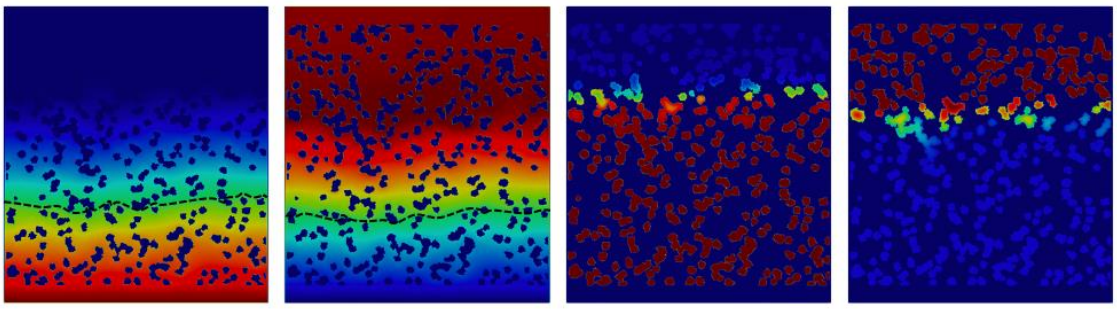

(b) S-2

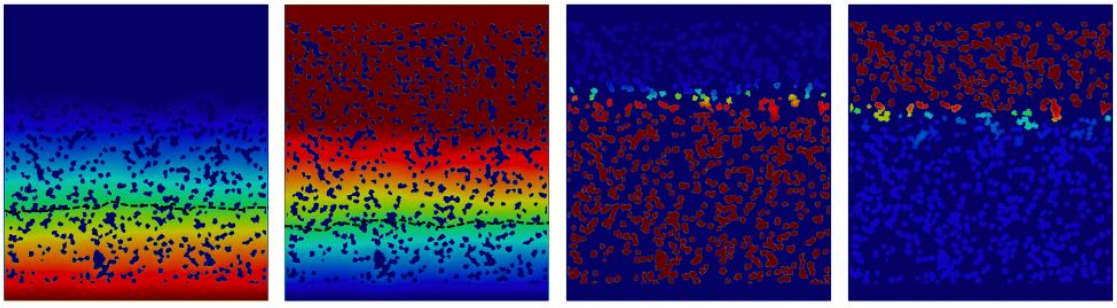

(c) S-3

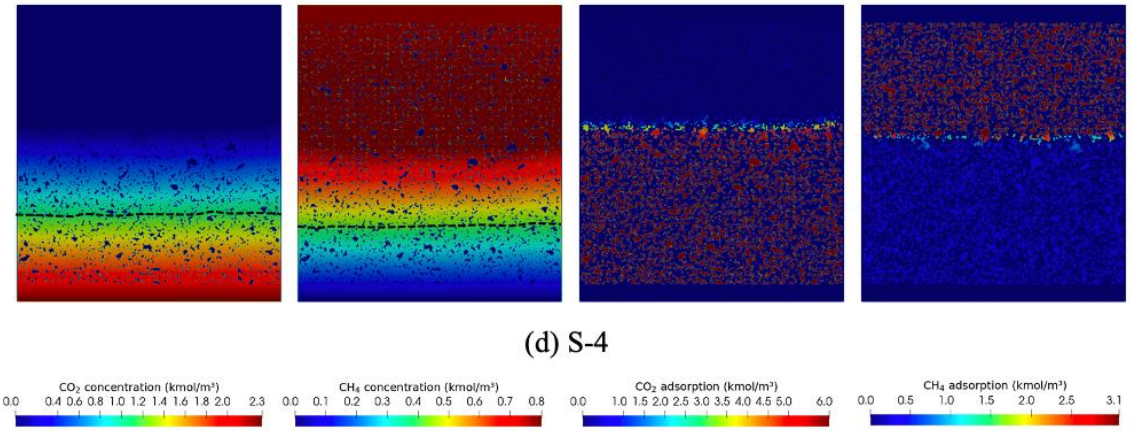

Figure 6.9 Snapshots of CO_2 and CH_4 concentration and adsorption profiles in porous structures (a) S-1, (b) S-2, (c) S-3, and (d) S-4 at t = 2.4 μs. The black dotted lines show the 0.5-saturated concentration fronts.

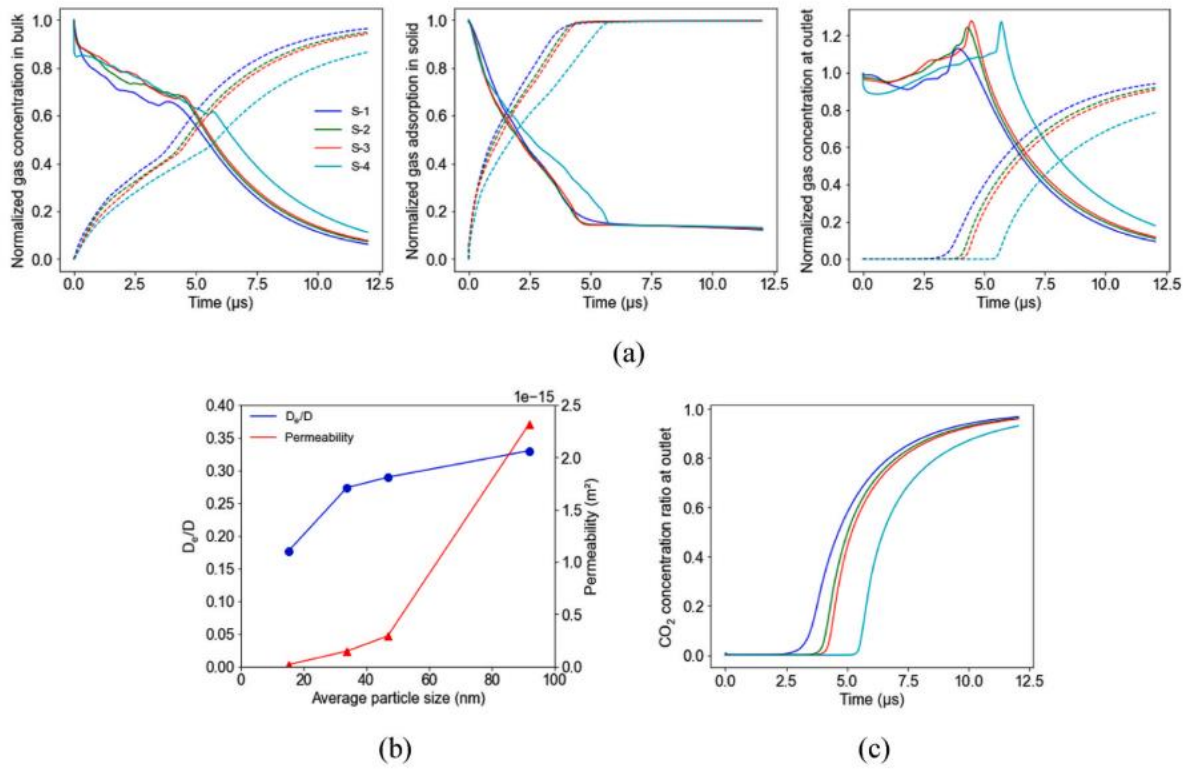

Figure 6.10 (a) Effects of pore geometry on CO_2 (dotted lines) and CH_4 (solid lines) concentration, adsorption, and outflux. (b) The effective diffusion coefficient and permeability as a function of the average particle size. (c) CO_2 breakthrough curves at the outlet.

6.4 Conclusions

In this study, we have proposed an NSE-ADE coupling scheme in the LBM to study the CO_2-CH_4 displacement in the context of CO_2-EGR in the shale matrix. The global mass transfer process consists of advection-diffusion in the bulk free pore space, surface adsorption and desorption, and intra-matrix diffusion. Compared with MD, the proposed LB model is more time-efficient and can deal with complex pore geometries at microscale. Main conclusions are:

- Gas adsorption/desorption in the solid matrix is greatly impacted by the solid diffusion rate, which subsequently affects gas concentration in the bulk free space. Changing the adsorption rate constant between 2.21×10^8 and 2.21×10^{10} m^3/kmol/s does not show a significant impact on gas adsorption or desorption while the desorption rate constant can largely control CH_4 desorption.
- The effect of CO_2/CH_4 selectivity is only pronounced in the less permeable solid matrix ($D_s = \sim 10^{-11}$ m^2/s).
- Decreasing the particle size under a given porosity can constrain advection between solids in the pore space, leading to a slower adsorption/desorption process in the solid matrix. This slow-down further causes a delayed breakthrough curve for CO_2 at the outlet.

The results suggest that the CO_2-CH_4 displacement is likely more efficient in shale composed of a few large pieces of organic matrix instead of a great number of small ones under a given porosity. More simulations are needed to establish a direct correlation between particle size and CH_4 production or CO_2 storage. Increasing the matrix diffusion and desorption rates through fracturing can directly lead to faster CH_4 production. When upscaling, care should be given to CO_2/CH_4 transport selectivity if the gas diffusion rates in bulk and solids largely vary. Apart from the rigorous validations, the key parameters are physics-based and obtained from the actual cases characterising the effect of confinement in nanoporous media. Therefore, the results are relevant to the actual process of CO_2-CH_4 displacement. The LB model herein simulates the CO_2-CH_4 displacement by separate ADEs and the gas concentration change is

assumed to not affect the viscous flow. It is recommended that the CO_2-CH_4 interaction, effect of adsorption on viscous flow, and nano-confinement should be included in future studies for more sophisticated investigation. Furthermore, the migration of gases in heterogenous porous media under given geological settings, flow rates, and injection pressures needs to be systematically studied.

Acknowledgments

This work was supported in part by the Australian Research Council through Discovery Projects (DP200101919 and DP190102954). The authors acknowledge the use of the National Computational Infrastructure (NCI) which is supported by the Australian Government, and accessed through the Sydney Informatics Hub HPC Allocation Scheme, which is supported by the Deputy Vice-Chancellor (Research), University of Sydney.

References

1. Alfarge, D., Wei, M., & Bai, B. (2020). Developments in petroleum science. *Elsevier*, 1-13.
2. Bhatnagar, P. L., Gross, E. P., & Krook, M. (1954). A model for collision processes in gases. I. Small amplitude processes in charged and neutral one-component systems. *Physical Review, 94*(3), 511.
3. Boek, E. S., & Venturoli, M. (2010). Lattice-Boltzmann studies of fluid flow in porous media with realistic rock geometries. *Computers & Mathematics with Applications, 59*(7), 2305-2314.
4. Castez, M. F., Winograd, E. A., & Sánchez, V. M. (2017). Methane flow through organic-

rich nanopores: The key role of atomic-scale roughness. *The Journal of Physical Chemistry C, 121*(51), 28527-28536.

5. Chahbani, M., Labidi, J., & Paris, J. (2002). Effect of mass transfer kinetics on the performance of adsorptive heat pump systems. *Applied Thermal Engineering, 22*(1), 23-40.

6. Chen, L., Huang, D.-B., Wang, S.-Y., Nie, Y.-N., He, Y.-L., & Tao, W.-Q. (2019). A study on dynamic desorption process of methane in slits. *Energy, 175*, 1174-1180.

7. Collell, J., Galliero, G., Vermorel, R., Ungerer, P., Yiannourakou, M., Montel, F., & Pujol, M. (2015). Transport of multicomponent hydrocarbon mixtures in shale organic matter by molecular simulations. *The Journal of Physical Chemistry C, 119*(39), 22587-22595.

8. Fang, T., Wang, M., Gao, Y., Zhang, Y., Yan, Y., & Zhang, J. (2019). Enhanced oil recovery with CO_2/N_2 slug in low permeability reservoir: Molecular dynamics simulation. *Chemical Engineering Science, 197*, 204-211.

9. Fathi, E., & Akkutlu, I. Y. (2014). Multi-component gas transport and adsorption effects during CO_2 injection and enhanced shale gas recovery. *International Journal of Coal Geology, 123*, 52-61.

10. Germanou, L., Ho, M. T., Zhang, Y., & Wu, L. (2018). Intrinsic and apparent gas permeability of heterogeneous and anisotropic ultra-tight porous media. *Journal of Natural Gas Science and Engineering, 60*, 271-283.

11. He, J., Ju, Y., Kulasinski, K., Zheng, L., & Lammers, L. (2019). Molecular dynamics simulation of methane transport in confined organic nanopores with high relative roughness. *Journal of Natural Gas Science and Engineering, 62*, 202-213.

12. He, X., Li, N., & Goldstein, B. (2000). Lattice Boltzmann simulation of diffusion-convection systems with surface chemical reaction. *Molecular Simulation, 25*(3-4), 145-156.

13. Henderson, A. (2007). The Paraview guide: A parallel visualisation application. *Kitware,*

Inc., Clifton Park, NY.

14. Huang, P., Shen, L., Maggi, F., Chen, Z., & Pan, Z. (2022). Influence of surface roughness on methane flow in shale kerogen nano-slits. *Journal of Natural Gas Science and Engineering*, *103*, 104650.

15. Huo, P., Zhang, D., Yang, Z., Li, W., Zhang, J., & Jia, S. (2017). CO_2 geological sequestration: Displacement behaviour of shale gas methane by carbon dioxide injection. *International Journal of Greenhouse Gas Control, 66*, 48-59.

16. Iddphonce, R., Wang, J., & Zhao, L. (2020). Review of CO_2 injection techniques for enhanced shale gas recovery: Prospect and challenges. *Journal of Natural Gas Science and Engineering, 77*, 103240.

17. Inamuro, T., Yoshino, M., Inoue, H., Mizuno, R., & Ogino, F. (2002). A Lattice Boltzmann method for a binary miscible fluid mixture and its application to a heat-transfer problem. *Journal of Computational Physics, 179*(1), 201-215.

18. Jiang, M., & Xu, Z. G. (2021). Pore-scale investigation on reactive flow in non-uniform dissolved porous media considering immiscible phase by lattice Boltzmann method. *Journal of Natural Gas Science and Engineering, 96*, 104280.

19. Kang, Q., Chen, L., Valocchi, A. J., & Viswanathan, H. S. (2014). Pore-scale study of dissolution-induced changes in permeability and porosity of porous media. *Journal of Hydrology, 517*, 1049-1055.

20. Klewiah, I., Berawala, D. S., Alexander Walker, H. C., Andersen, P. Ø., & Nadeau, P. H. (2020). Review of experimental sorption studies of CO_2 and CH_4 in shales. *Journal of Natural Gas Science and Engineering, 73*, 103045.

21. Krause, M. J., Kummerländer, A., Avis, S. J., Kusumaatmaja, H., Dapelo, D., Klemens, F., . . . Simonis, S. (2021). OpenLB – Open source lattice Boltzmann code. *Computers & Mathematics with Applications, 81*, 258-288.

22. Krüger, T., Kusumaatmaja, H., Kuzmin, A., Shardt, O., Silva, G., & Viggen, E. M. (2017). The lattice Boltzmann method. *Springer International Publishing.*

23. Lei, J., Ding, R., & Zhang, J. (2021). Study on seepage and adsorption characteristics of porous media containing adsorbent based on lattice Boltzmann. *AIP Advances, 11*(4), 045126.

24. Linstrom, P., & Mallard, W. (2022). NIST chemistry WebBook, NIST standard reference database number 69, *National Institute of Standards and Technology, Gaithersburg MD, 20899*.

25. Liu, L., Wang, Y., & Aryana, S. A. (2021). Insights into scale translation of methane transport in nanopores. *Journal of Natural Gas Science and Engineering, 96*, 104220.

26. Louk, K., Ripepi, N., Luxbacher, K., Gilliland, E., Tang, X., Keles, C., . . . Michael, K. (2017). Monitoring CO_2 storage and enhanced gas recovery in unconventional shale reservoirs: Results from the Morgan County, Tennessee injection test. *Journal of Natural Gas Science and Engineering, 45*, 11-25.

27. Mansoubi, H., Mansourpour, Z., & Fatemi, S. (2023). Investigation of CO_2 and CH_4 capture from syngas in adsorption process and breakthrough modelling by modified Lattice-Boltzmann mesoscale method. *Chemosphere, 325*, 138366.

28. Mu, D., Liu, Z.-S., Huang, C., & Djilali, N. (2007). Prediction of the effective diffusion coefficient in random porous media using the finite element method. *Journal of Porous Materials, 14*(1), 49-54.

29. Nan, Y., Li, W., & Jin, Z. (2020). Slip length of methane flow under shale reservoir conditions: Effect of pore size and pressure. *Fuel, 259*, 116237.

30. Peng, Z., Deng, Z., Feng, H., Liu, S., & Li, Y. (2021). Multiscale lattice Boltzmann simulation of the kinetics process of methane desorption-diffusion in coal. *ACS Omega, 6*(30), 19789-19798.

31. Peng, Z., Liu, S., Tang, S., Zhao, Y., & Li, Y. (2018). Multicomponent lattice Boltzmann simulations of gas transport in a coal reservoir with dynamic adsorption. *Geofluids, 2018*, 1-13.

32. Qin, C., Jiang, Y., Zuo, S., Chen, S., Xiao, S., & Liu, Z. (2021). Investigation of adsorption kinetics of CH_4 and CO_2 on shale exposure to supercritical CO_2. *Energy, 236*, 121410.

33. Rabbani, A., & Ayatollahi, S. (2015). Comparing three image processing algorithms to estimate the grain-size distribution of porous rocks from binary 2D images and sensitivity analysis of the grain overlapping degree. *Special Topics & Reviews in Porous Media: An International Journal, 6*(1), 71-89.

34. Rabbani, A., Jamshidi, S., & Salehi, S. (2014). An automated simple algorithm for realistic pore network extraction from micro-tomography images. *Journal of Petroleum Science and Engineering, 123*, 164-171.

35. Seta, T. (2013). Implicit temperature-correction-based immersed-boundary thermal lattice Boltzmann method for the simulation of natural convection. *Physical Review E, 87*(6), 063304.

36. Sheikholeslami, M., Gorji-Bandpy, M., & Ganji, D. (2013). Numerical investigation of MHD effects on Al_2O_3 – water nanofluid flow and heat transfer in a semi-annulus enclosure using LBM. *Energy, 60*, 501-510.

37. Tesson, S., & Firoozabadi, A. (2018). Methane adsorption and self-diffusion in shale kerogen and slit nanopores by molecular simulations. *The Journal of Physical Chemistry C, 122*(41), 23528-23542.

38. Wang, H., Chen, L., Qu, Z., Yin, Y., Kang, Q., Yu, B., & Tao, W.-Q. (2020). Modelling of multi-scale transport phenomena in shale gas production – A critical review. *Applied Energy, 262*, 114575.

39. Wang, H., Qu, Z. G., & Zhou, L. (2018). Coupled GCMC and LBM simulation method for

visualisations of CO_2/CH_4 gas separation through Cu-BTC membranes. *Journal of Membrane Science, 550*, 448-461.

40. Wang, H., Su, Y., Wang, W., Jin, Z., & Chen, H. (2022). CO_2-oil diffusion, adsorption and miscible flow in nanoporous media from pore-scale perspectives. *Chemical Engineering Journal, 450*, 137957.

41. Wang, J., Chen, L., Kang, Q., & Rahman, S. S. (2016). The lattice Boltzmann method for isothermal micro-gaseous flow and its application in shale gas flow: A review. *International Journal of Heat and Mass Transfer, 95*, 94-108.

42. Wang, J., Kang, Q., Chen, L., & Rahman, S. S. (2017a). Pore-scale lattice Boltzmann simulation of micro-gaseous flow considering surface diffusion effect. *International Journal of Coal Geology, 169*, 62-73.

43. Wang, J., Kang, Q., Wang, Y., Pawar, R., & Rahman, S. S. (2017b). Simulation of gas flow in micro-porous media with the regularised lattice Boltzmann method. *Fuel, 205*, 232-246.

44. Wang, M., Wang, J., Pan, N., & Chen, S. (2007). Mesoscopic predictions of the effective thermal conductivity for microscale random porous media. *Physical Review E, 75*(3), 036702.

45. Wang, S., Feng, Q., Javadpour, F., Zha, M., & Cui, R. (2017). Multiscale modelling of shale apparent permeability: An integrated study of molecular dynamics and pore network model. *SPE Annual Technical Conference and Exhibition*, SPE-187286-MS.

46. Wu, J., Huang, P., Maggi, F., & Shen, L. (2022). Molecular investigation on CO_2-CH_4 displacement and kerogen deformation in enhanced shale gas recovery. *Fuel, 315*, 123208.

47. Wu, J., Shen, L., Huang, P., & Gan, Y. (2023). Selective adsorption and transport of CO_2-CH_4 mixture under nano-confinement. *Energy, 273*, 127224.

48. Xia, M. (2016). Pore-scale simulation of miscible displacement in porous media using the lattice Boltzmann method. *Computers & Geosciences, 88*, 30-40.

49. Xie, W., Wang, M., Chen, S., Vandeginste, V., Yu, Z., & Wang, H. (2022). Effects of gas components, reservoir property and pore structure of shale gas reservoir on the competitive adsorption behaviour of CO_2 and CH_4. *Energy, 254*, 124242.

50. Yan, M., Zhou, M., Li, S., Lin, H., Zhang, K., Zhang, B., & Shu, C.-M. (2021). Numerical investigation on the influence of micropore structure characteristics on gas seepage in coal with lattice Boltzmann method. *Energy, 230*, 120773.

51. Yang, X., Chen, Z., Liu, X., Xue, Z., Yue, F., Wen, J., . . . Xue, Y. (2022). Correction of gas adsorption capacity in quartz nanoslit and its application in recovering shale gas resources by CO_2 injection: A molecular simulation. *Energy, 240*, 122789.

52. Yu, H., Fan, J., Chen, J., Zhu, Y., & Wu, H. (2018). Pressure-dependent transport characteristic of methane gas in slit nanopores. *International Journal of Heat and Mass Transfer, 123*, 657-667.

53. Yu, H., Fan, J., Xia, J., Liu, H., & Wu, H. (2020a). Multiscale gas transport behaviour in heterogeneous shale matrix consisting of organic and inorganic nanopores. *Journal of Natural Gas Science and Engineering, 75*, 103139.

54. Yu, H., Xu, H., Fan, J., Wang, F., & Wu, H. (2020b). Roughness factor-dependent transport characteristic of shale gas through amorphous kerogen nanopores. *The Journal of Physical Chemistry C, 124*(23), 12752-12765.

55. Zakirov, T. R., & Khramchenkov, M. G. (2022). Effect of pore space heterogeneity on the adsorption dynamics in porous media at various convection-diffusion and reaction conditions: A lattice Boltzmann study. *Journal of Petroleum Science and Engineering, 212,* 110300.

56. Zhan, S., Su, Y., Lu, M., Cai, M., Fu, J., Liu, Z., . . . Li, G. (2021). Effect of surface type on the flow characteristics in shale nanopores. *Geofluids, 2021*, 1-12.

57. Zhang, H., Moh, D. Y., Wang, X., & Qiao, R. (2022). Review on pore-scale physics of shale

gas recovery dynamics: Insights from molecular dynamics simulations. *Energy & Fuels*, *36*(24), 14657-14672.

58. Zhang, T., & Sun, S. (2019). A coupled Lattice Boltzmann approach to simulate gas flow and transport in shale reservoirs with dynamic sorption. *Fuel, 246*, 196-203.

59. Zhang, W., Feng, Q., Wang, S., Xing, X., & Jin, Z. (2021). CO_2-regulated octane flow in calcite nanopores from molecular perspectives. *Fuel, 286*, 119299.

60. Zhao, J., Yao, J., Zhang, L., Sui, H., & Zhang, M. (2016). Pore-scale simulation of shale gas production considering the adsorption effect. *International Journal of Heat and Mass Transfer, 103*, 1098-1107.

61. Zhao, T., Zhao, H., Li, X., Ning, Z., Wang, Q., Zhao, W., & Zhang, J. (2018). Pore scale characteristics of gas flow in shale matrix determined by the regularised lattice Boltzmann method. *Chemical Engineering Science, 187*, 245-255.

62. Zhao, Y., Luo, M., Liu, L., Wu, J., Chen, M., & Zhang, L. (2022). Molecular dynamics simulations of shale gas transport in rough nanopores. *Journal of Petroleum Science and Engineering, 217*, 110884.

63. Zhou, L., Qu, Z. G., Chen, L., & Tao, W. Q. (2015). Lattice Boltzmann simulation of gas-solid adsorption processes at pore scale level. *Journal of Computational Physics, 300*, 800-813.

64. Zhou, L., Qu, Z. G., Ding, T., & Miao, J. Y. (2016). Lattice Boltzmann simulation of the gas-solid adsorption process in reconstructed random porous media. *Physical Review E, 93*, 043101.

65. Zhou, W., Yang, X., & Liu, X. (2022). Multiscale modelling of gas flow behaviours in nanoporous shale matrix considering multiple transport mechanisms. *Physical Review E, 105*(5-2), 055308.

Supplementary materials for

Pore-scale lattice Boltzmann simulation of CO_2-CH_4 displacement in shale matrix

Jian Wu[a], Yixiang Gan[a, b], Zhang Shi[c], Pengyu Huang[a, d], Luming Shen[a, *]

[a] School of Civil Engineering, The University of Sydney, NSW 2006, Australia

[b] Sydney Nano Institute, The University of Sydney, NSW 2006, Australia

[b] School of Mechanical and Mining Engineering, The University of Queensland, St Lucia, QLD 4072, Australia

[d] Hard Rock Mining, CSIRO Mineral Resources, QCAT, 1 Technology Court, Pullenvale, QLD 4069, Australia

[*]Corresponding author. Email: luming.shen@sydney.edu.au

S1. Model verification

The first example shows the mass transfer process of Poiseuille flow through a plate channel, which has the upper surface as a non-slip boundary and the bottom surface as a continuous mass sink. The first-order Henry's adsorption kinetics is imposed at the bottom surface as $R = KC$. The simulation parameters are presented in Table 6.S1. The Lévêsque solution (Lévêque, 1928; Zhou et al., 2015) is plotted as a function of x to compare with the simulated concentration flux at the bottom surface ($y = 0$)

$$\tilde{C}_S = \frac{L}{C_0}\frac{\partial C}{\partial n} = 0.854\left(\frac{u_{max}L^2}{xD}\right)^{1/3} \quad (6.S1)$$

where C_0 is the inlet gas concentration, L is the channel size in the flow direction, n is the normal direction of the bottom surface, u_{max} is the maximum inlet gas velocity, D is the gas diffusion coefficient. Figure 6.S1a provides a snapshot of the simulation domain where the gas

concentration is clearly seen consumed at the bottom by surface adsorption. Figure 6.S1b shows the comparison of the Lévêsque solution with the simulated flux results. It is found that the two solutions generally agree with each other, and minor differences are only observed near the flow inlet. This example confirms the feasibility of the proposed LB model in simulating coupled mass transfer process of advection, diffusion, and surface adsorption.

Table 6.S1 Simulation parameters for gas advection-diffusion with first-order surface reaction.

L	C_0	u_{max}	D	K
200	1.0	0.06	0.1	1.0

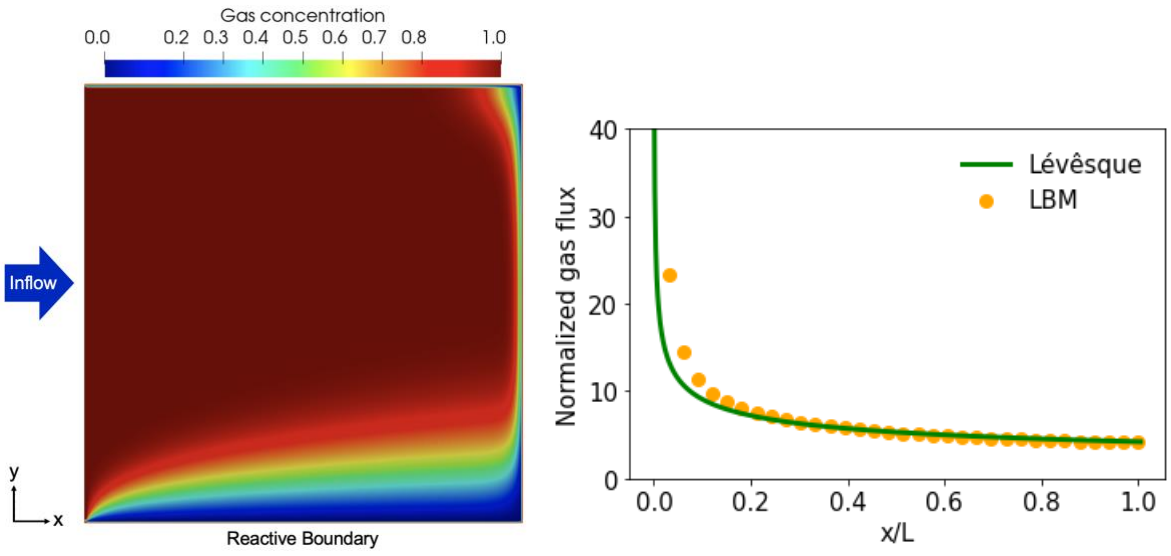

(a) (b)

Figure 6.S1 (a) Concentration contour of Poiseuille flow in a plate channel with the bottom surface acting as a first-order reactive boundary. (b) Comparison between the simulated concentration flux at $y = 0$ and the Lévêsque solution.

The second example examines the pure diffusion process driven by a concentration gradient at zero velocity inside the solid matrix. The solid sphere is exposed to a constant concentration at

the outer periphery. Gas adsorbs on the solid surface in first-order and gradually evolves into the interior of the sphere as a function of time *t* according to the following analytical solution (Zhou et al., 2015)

$$\frac{\bar{q}}{q_0} = 1 - \sum_{n=1}^{\infty} \frac{4}{r_s^2 \alpha_n^2} \exp(-D_s \alpha_n^2 t) \tag{6.S2}$$

The boundary conditions are

$$\left(\frac{\partial q}{\partial r}\right)_{r=0} = 0, \qquad (q)_{r=r_s} = KC_0 = q_0$$

where $\bar{q}$ is the average amount of gas adsorption inside the solid, C_0 is the gas concentration at the outer periphery, r_s is the sphere radius, D_s is the gas diffusion coefficient in the solid, α_n is the positive root of the first-type Bessel function of order zero. The simulation parameters are presented in Table 6.S2. Figure 6.S2 compares the simulated adsorption uptake curve to that calculated by the analytical solution Equation (6.S2), showing a perfect agreement between the two groups of data.

Table 6.S2 Simulation parameters for pure diffusion in the solid sphere.

r_s	D_s	C_0	K
28	0.02	1	0.001

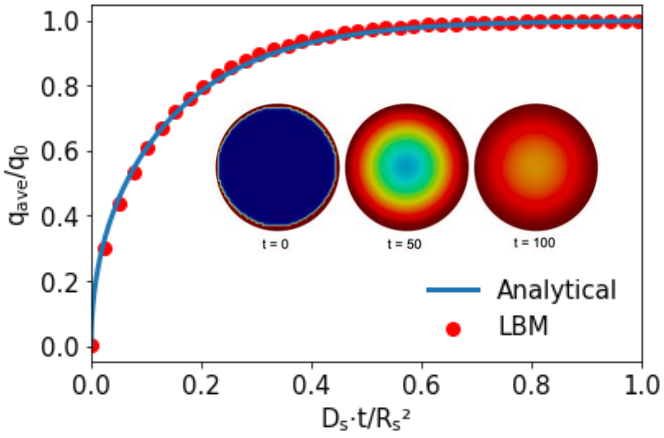

Figure 6.S2 Validation of the gas adsorption uptake curve in a solid sphere.

The third example demonstrates the validity of the proposed model in simulating the stable counter-diffusion of a binary mixture between two parallel porous plates, as illustrated in Inamuro et al. (2002). Component a is injected at a constant velocity v_a into a 200 × 200 square domain from the lower wall and exits through the upper wall. The concentration of component b is fixed at the lower and upper walls at $C_b^l = 1$ and $C_b^u = 2$, respectively. Therefore, the diffusion flux of component b is opposite to that of component a. The normalised concentration of component b ($\frac{C_b - C_b^l}{C_b^u - C_b^l}$) follows the analytical solution (Inamuro et al., 2002)

$$C_b^* = \frac{\exp(v_a y / D_b) - 1}{\exp(v_a L / D_b) - 1} \tag{6.S3}$$

where D_b is the diffusion rate of component b, and L is the domain length along y-axis. The ratio of v_a/D_b is set as 0.02. The periodic boundary condition is applied in the x-direction. It is seen that the results agree well with the analytical solution in Figure 6.S3.

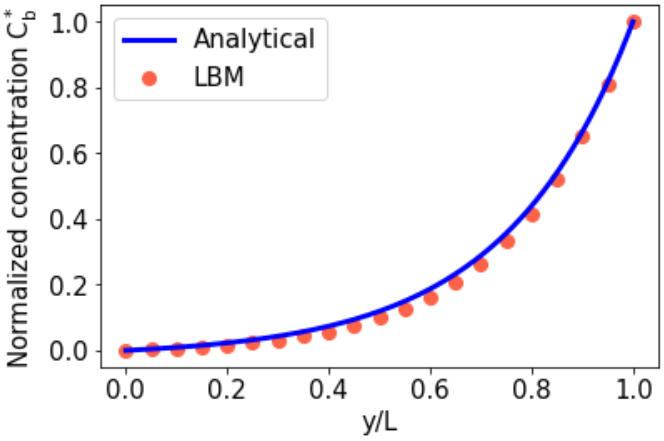

Figure 6.S3 Calculated concentration profile of component *b* along the *y*-axis ($L = 200$) in a binary fluid counter-diffusion problem.

In the fourth example, the multicomponent LBM coupling scheme is validated by comparing to the experimental data where a CO_2-CH_4 mixture flows through a 26 cm-long dispersive packed bed column of activated carbon (Mansoubi et al., 2023). The column is initially empty of any gases. At the inlet, v = 0.08 m/min, C_{CO2} = 0.2 mol/L and C_{CH4} = 0.02 mol/L. The outlet is considered open using the fully developed flow boundary conditions. Since the CO_2-CH_4 mixture is carried by H_2 (78%) at 3 bars, we used a kinematic viscosity of 8.84×10^{-5} m^2/s. The CO_2 and CH_4 diffusion rates are 2.36×10^{-5} and 1.18×10^{-5} m^2/s, respectively. The LB model relaxation parameters are 1.4, 0.74, and 0.62 for viscosity, CO_2 diffusion, and CH_4 diffusion, respectively. As our pore-scale model is not directly applicable to explicitly simulate adsorption-desorption in each solid particle inside the reaction bed at centimetre-scale, we assume a homogenous adsorption-desorption reaction across the entire domain of the column. The maximum gas adsorption amounts are selected at 4.4 and 0.64 mol/L, respectively, from the Langmuir adsorption isotherms reported by Mansoubi et al. (2023) using partial gas pressures. The gas adsorption and desorption rates in the LB model are adjusted to fit the data. The adsorption rates are 2.95×10^{-2} L/mol/s for both CO_2 and CH_4, and the desorption rates are 5.90×10^{-3} and 2.36×10^{-3} /s. The simulated CO_2 and CH_4 concentration breakthrough curves are measured at the outlet, which can successfully capture the trends observed from the

experimental data (Figure 6.S4). Note that the gas diffusion rates used in shale matrix are much smaller due to the nano-confinement.

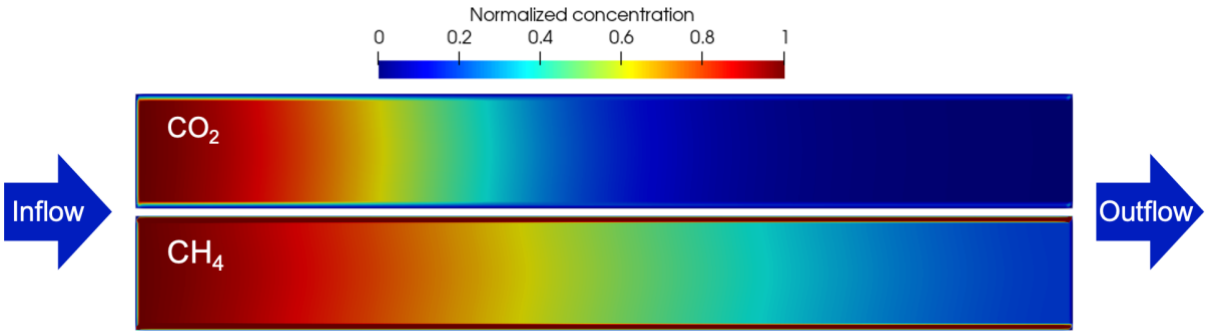

(a)

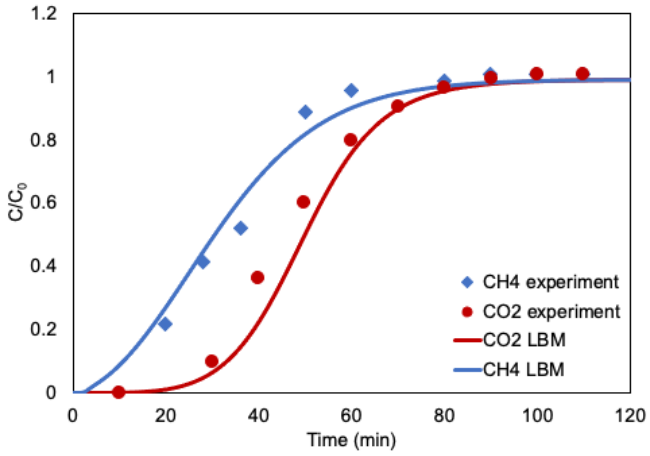

(b)

Figure 6.S4 Experimental validation: (a) Concentration profiles in the LBM simulation domain at t = 15 min. (b) Comparison of the normalised gas concentration at the outlet obtained from LBM simulation and the experimental data in Mansoubi et al. (2023) at a gas velocity of 0.08 m/min.

S2. Supplementary simulations on pore geometry

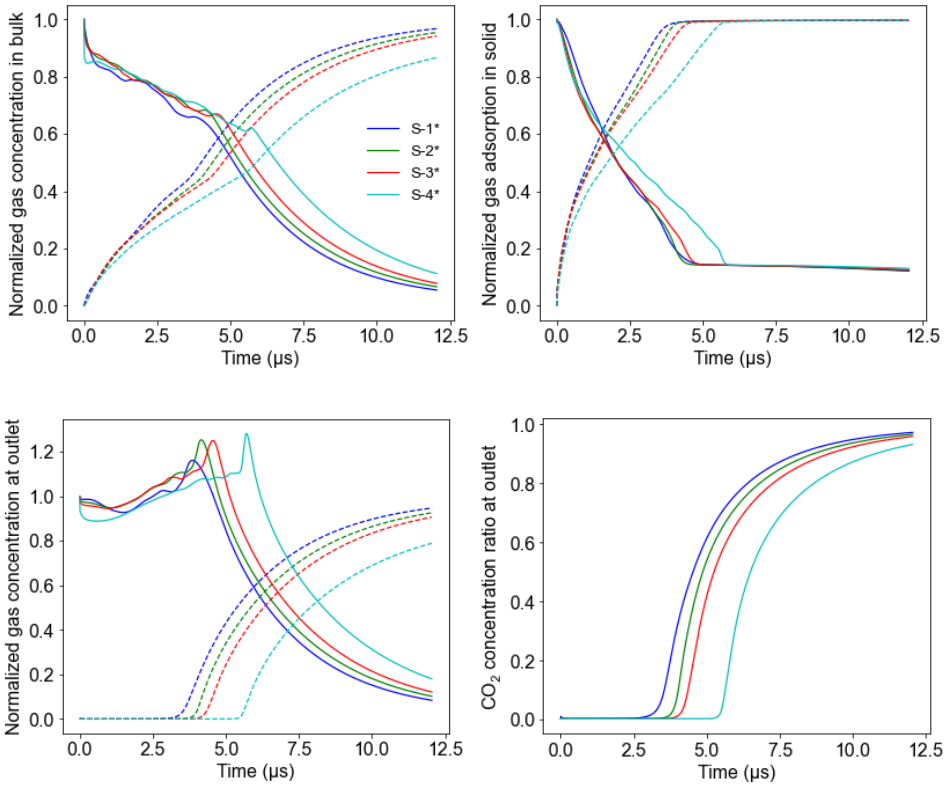

Figure 6.S5 Effects of pore geometry (S-1*, S-2*, S-3*, and S-4*) on CO_2 (dotted lines) and CH_4 (solid lines) concentration, adsorption, and outflux at the outlet.

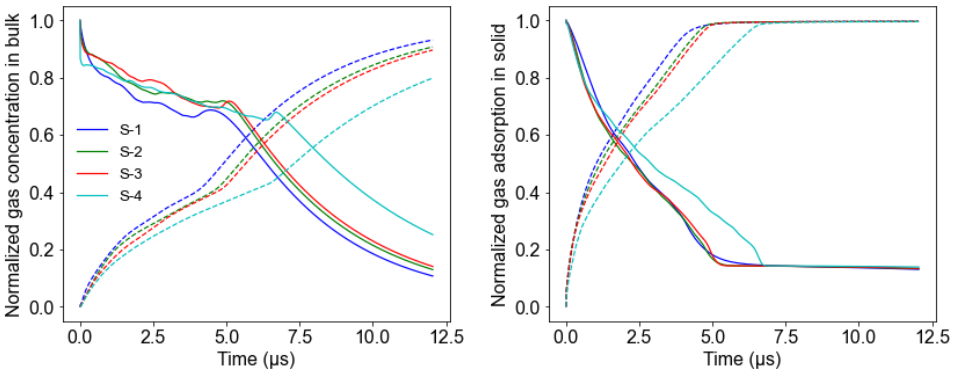

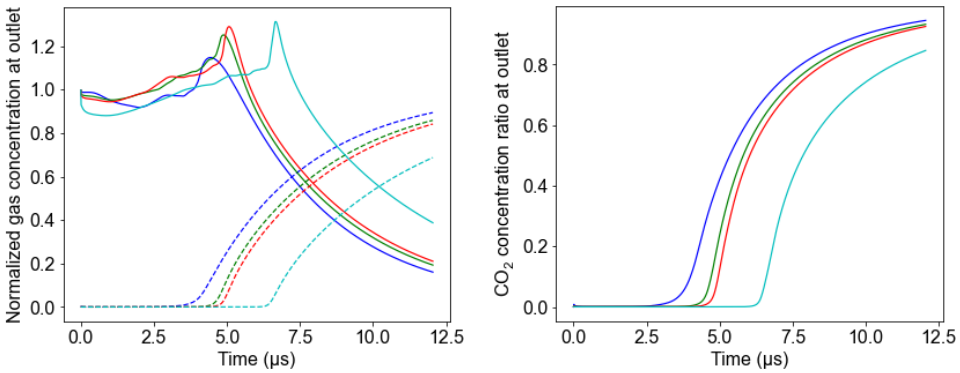

Figure 6.S6 Effects of pore geometry on CO_2 (dotted lines) and CH_4 (solid lines) concentration, adsorption, and outflux at the outlet when the gas injection velocity is *0.2v*.

References

Inamuro, T., Yoshino, M., Inoue, H., Mizuno, R., & Ogino, F. (2002). A lattice Boltzmann method for a binary miscible fluid mixture and its application to a heat-transfer problem. *Journal of Computational Physics, 179*(1), 201-215

Lévêque, A. (1928). Les lois de la transmission de chaleur par convection. *Dunod*.

Mansoubi, H., Mansourpour, Z., & Fatemi, S. (2023). Investigation of CO_2 and CH_4 capture from syngas in adsorption process and breakthrough modelling by modified Lattice-Boltzmann mesoscale method. *Chemosphere, 325*, 138366.

Zhou, L., Qu, Z. G., Chen, L., & Tao, W. Q. (2015). Lattice Boltzmann simulation of gas-solid adsorption processes at pore scale level. *Journal of Computational Physics, 300*, 800-813.

Chapter 7 Conclusions and future research

7.1 Summary and conclusions

This research studies the displacement between CO_2 and CH_4 at nano- and micro-scales in the context of CO_2-EGR. In particular, molecular simulations, including GCMC, MD, and NEMD, are adopted to investigate CO_2/CH_4 adsorption, solid deformation, and gas flow associated with nanoporous kerogen. A multiphysics model is then developed with LBM based on previous nanoscale knowledge to study the integrated process of CO_2-CH_4 displacement in complex nanoporous media. The overall results suggest that CO_2 injection is feasible for shale gas recovery and can significantly enhance adsorbed gas production after pressure drawdown, but the recovery ratio may be subject to pore size, pressure conditions, and geometrical properties. As CO_2 ratio increases in the reservoir during injection, gas mixture properties may change and manifest different flow characteristics under nano-confinement such as separation. Moreover, sorption-induced deformation is also an essential consideration as the swelling of organic matter reduces reservoir permeability and may affect CO_2 injectivity and CH_4 production rate. These nano- and micro-scale findings are expected to improve the accuracy of large-scale reservoir models. The main conclusions of the thesis are summarised below.

The GCMC-MD results in Chapter 3 indicate that CO_2 adsorption is higher than CH_4 as a single component, leading to greater swelling within the kerogen matrix. Both CO_2 and CH_4 adsorption amounts follow the Langmuir isotherm, and the induced kerogen deformation is well described by a non-linear adsorption-strain curve derived from surface free energy change under the sorption-deformation coupling condition. This derived equation can be potentially included in the continuum-scale reservoir models to improve accuracy. CO_2 injection is proven to significantly improve the production of residual CH_4 by five times after initial pressure drawdown. Higher CO_2 injection pressure facilitates the displacement efficiency, which also decreases with the increasing reservoir depletion pressure. The estimation shows that 0.13~0.6

mmol/g CH_4 can be recovered for every 1 mmol/g CO_2 sequestrated. The CO_2 storage capacity may reach ~57.6 m^3/m^3 (Barnett) and 22.8 m^3/m^3 (Eagle Ford). However, concerns about injectivity may arise as CO_2 injection is likely to cause further swelling of the depleted reservoir and reduce the production rate.

The effect of sorption-induced deformation on nanoscale methane transport is studied in Chapter 4 using NEMD. When flowing in a confined slit pore, gas molecules enter the kerogen matrix and cause swelling, resulting in narrowed flow pathway. Nanoscale gas transport consists of contributions from viscous flow and various diffusion modes. It is found that kerogen swelling mainly reduces the flux from viscous gas flow and becomes non-negligible at high pore pressure. Apparent gas permeability becomes less sensitive to such deformation as pore size increases. Calculations show that in a slit pore of size 10 Å, kerogen swelling may decrease the apparent permeability by nearly 40%. This chapter highlights the importance of understanding the dynamic permeability evolution of shale reservoirs for accurate predictions of gas production during CO_2-EGR. The derived correlation between gas permeability and matrix swelling under nano-confinement can be possibly extended to reservoir models.

CO_2 injection results in a gas flow system of CO_2-CH_4 mixture in shale reservoirs. Although the two gas components are miscible, nano-confinement may cause separation of the mixture due to different gas-wall interactions. The selective adsorption and transport of the CO_2-CH_4 mixture are studied in Chapter 5. It is revealed that CO_2 and CH_4 have different adsorption capacities and mass transfer rates in a kerogen slit pore. CO_2/CH_4 adsorption and transport selectivities are functions of pore size and pressure while nearly independent of bulk molar ratio. Surface diffusion is considered the driving factor for the mixture separation as excluding it reduces the transport selectivity. Moreover, the slit-averaged velocity of the CO_2-CH_4 mixture is found to decrease logarithmically with the increasing CO_2 molar ratio under a fixed pore pressure. These results suggest that the selective mass transport of CO_2-CH_4 in nanoporous shale reservoirs may affect predictions from large-scale simulations of CO_2-EGR if neglected.

To upscale our nanoscale investigation of CO_2-EGR to the micropore-scale, a multiphysics LB model is developed in Chapter 6. This dual-porosity model couples multiple lattices to solve Navier-Stokes and advection-diffusion equations for simulating CO_2-CH_4 displacement in 2D porous media. The key model parameters are physics-based and informed by either our previous MD studies or the literature. The results show that pore-scale CO_2-CH_4 displacement is impacted by inter/intra-solid diffusion and Langmuir adsorption kinetics at the gas-solid interfaces. An interplay exists between the advective velocity in the pore space and mass transfer rate within the solid. When porosity is fixed, decreasing the particle size can limit advection in the pore space, resulting in slower adsorption/desorption in the solid matrix. Combing with advanced image scanning and processing techniques, Australian shale samples can be studied with the LB model to preliminarily evaluate the CO_2-EGR potential prior to field test.

7.2 Recommendations for future work

This thesis investigates the fundamental physical behaviours arising from gas-gas and gas-solid interactions in the CO_2-CH_4 system at nano- and microscales. Although CO_2-EGR shows great potential in improving shale gas production, it is an intertwined multiscale and multiphysics process involving gas adsorption/desorption, nano-confinement, selective adsorption, mixture separation, adsorption-deformation coupling, flow-deformation coupling, mineral dissolution, etc. Several limitations and recommendations are discussed below for future implementations.

- This research only focuses on shale's primary organic matter – kerogen. Although it is the nanoporous structure associated with the majority of unrecovered adsorbed gas, comparisons are needed between other inorganic clay minerals such as montmorillonite, calcite, and quartz as different behaviours may manifest. This would require building different molecular models of these minerals to study gas adsorption curves arising from varied gas-solid interactions in MD.

- The adsorption selectivity between CO_2 and CH_4 is found to be a strong function of total gas pressure but not sensitive to CO_2/CH_4 partial pressure. The underlying mechanism is worth further investigating.
- Future research may consider looking into the logarithmic decrease of CO_2-CH_4 velocity versus CO_2 molar ratio observed from our MD simulations and mathematically deriving such dependence. A mathematical expression could also help identify the flow patterns of the mixture as a function of the CO_2 molar ratio.
- Shale reservoirs usually hold certain moisture contents, and immiscible two-phase flow may occur during CO_2-EGR. The effects of moisture contents on shale gas recovery and CO_2 sequestration should also be given attention. This could be simply done by adding the water phase in MD simulations. However, more difficulties are expected in LB simulations as multiphase interaction models will be required to control the interfacial tension and wettability.
- The MD studies indicate that sorption-induced kerogen deformation is important and may affect gas flow and transport. Studying the dynamic permeability during CO_2-EGR in a single pore and complex porous media is suggested. However, challenges are expected to achieve full coupling of multicomponent gas flow with deformation.
- In this study, the LB model is employed to simulate the displacement of CH_4 by CO_2 using distinct advection-diffusion equations, assuming that gas concentration alterations do not impact the viscous flow. Future research endeavours should incorporate factors such as the interaction between CO_2 and CH_4, the influence of adsorption on viscous flow, and the role of nano-confinement in more realistic 3D porous media constructed from shale samples. These additions would contribute to a more advanced and comprehensive LB model.